UNIVERSITY OF SOUTHAMPTON

FACULTY OF ENGINEERING AND PHYSICAL SCIENCES

Aeronautical and Astronautical Engineering

Aerodynamics of a Pitching Wind Turbine Blade and the Large-Scale Turbulence Impact

by

ThankGod Enatimi BOYE

A thesis for the degree of Doctor of Philosophy

March 25, 2022

UNIVERSITY OF SOUTHAMPTON

ABSTRACT

FACULTY OF ENGINEERING AND PHYSICAL SCIENCES

Doctor of Philosophy

AERODYNAMICS OF A PITCHING WIND TURBINE BLADE AND THE LARGE-SCALE TURBULENCE IMPACT

by ThankGod Enatimi BOYE

The impact of large-scale turbulence on aerodynamics is not well studied or documented, whereas the effect of high turbulence intensity is reported in many published papers. In particular, for a blade in pitching motion, which is typical in modelling non-uniform wind speed across the wind turbine height, highly unsteady incoming flows and yaw wind. This thesis conducts a research programme aimed at understanding and quantifying the effect of high pitching motion and, in particular, studying the impact of large-scale turbulence on the aerodynamic characteristics of a wind turbine blade. Firstly, large-eddy simulation (LES) of the dynamic stall of a NACA 0012 aerofoil in pitching motion at various reduced frequencies $k_{\text{red}} = 0.1$, 0.15, 0.2, 0.3 and 0.4 in smooth inflow was investigated using both 2D and 3D LES. The high pitching frequencies are within the range of the frequencies of the unsteadiness of flows around the rotating wind turbine blade at different blade span locations and close to the blade structure frequencies. It was found that the lift hysteresis loop increase as the reduced frequency increases while the peak drag coefficients decrease with the increase of the reduced frequency, and the moment coefficient showed a strong dependency on the reduced frequency. Secondly, a similar set-up as the smooth inflow was studied, but with the imposition of an efficient and divergence-free inflow turbulence condition capable of generating synthetic large-scale turbulence inside the domain. Two streamwise integral length-scales $\text{L}_\text{x} = 1c$ and $1.5c$ are studied, which represent some energetic turbulent eddies at the height of the atmospheric boundary that wind turbine operates. It was found that the effect on the maximum lift coefficient at the dynamic stall angle near the maximum angle of attack is by an average of 20% and during the downstroke is by an average of 22%, while the maximum drag and minimum moment coefficients have an average of 21% and 60%, respectively compared to the smooth inflow for $k_{\text{red}} = 0.1$. A higher pitching motion of the blade ($k_{\text{red}} = 0.2$) does not improve the aerodynamic characteristics such as the lift, drag and moment coefficients, and lift-to-drag ratio either. Finally, the dispersive shear stress and turbulent shear stress in the wake are positive and negative - suggesting flow propulsion and resistance, respectively.

Declaration of Authorship

I, ThankGod Enatimi BOYE , declare that the thesis entitled *Aerodynamics of a Pitching Wind Turbine Blade and the Large-Scale Turbulence Impact* and the work presented in the thesis are both my own, and have been generated by me as the result of my own original research. I confirm that:

- this work was done wholly or mainly while in candidature for a research degree at this University;
- where any part of this thesis has previously been submitted for a degree or any other qualification at this University or any other institution, this has been clearly stated;
- where I have consulted the published work of others, this is always clearly attributed;
- where I have quoted from the work of others, the source is always given. With the exception of such quotations, this thesis is entirely my own work;
- I have acknowledged all main sources of help;
- where the thesis is based on work done by myself jointly with others, I have made clear exactly what was done by others and what I have contributed myself;
- Parts of this work have been presented as talks at: 1.) European Turbulence Conference (ETC), Torino, Italy, 3rd - 6th September 2019; 2.) UK Fluid Conference at the University of Cambridge, 27th - 29th August 2019; and 3.) UK Fluid Conference at the University of University, 8th - 10th September 2021.
- Part of this work has been submitted for journal paper publication.

Signed:.....

Date:.....

Acknowledgements

Firstly, I am much obliged to my supervisor **Dr Zheng-Tong Xie** for his expert supervision over the past four years of this PhD research project. He helped me to have a deeper understanding of this research topic profoundly and methods in finding solutions to the research and technical problems during the period. I appreciate your support, which I must say that without it would have been like a mirage to complete this PhD degree thesis. Many thanks, **Dr Anatoliy Vorobev** for your support to secure a PhD admission into this prestigious university.

Special thanks to the researchers of the Aerodynamics and Fluid Mechanics group for their cooperation, and particularly to members of my supervisor research team - Dr. Charles Badoe, Dr Yongxin Chen, Dr Xiaolu Wang and Mr Cobum Matthew are always willing to engage in useful discussions. I do acknowledge that majority of computations were performed on supercomputer, **IRIDIS4** at the **University of Southampton**. I am very grateful for the computational resources support from the **United Kingdom Turbulence Consortium (UKTC)** under grant EPSRC/UKTC/5-6/e01-Soton-Xie/ for access to **ARCHER**, the UK National Supercomputing Service.

I want to especially acknowledge the **Petroleum Technology Development Fund (PTDF)** Nigeria for the grant (PTDF/1052/17/PHD/028) of a fully-funded PhD scholarship to be undertaken at the University of Southampton. Thank you for this very great opportunity.

Finally, a big thank you to my parents, **Capt. Anthony Adede Boye and Late Mrs Roseline F. Boye** have been the backbone support to my education and professional career right from the onset. Special thanks to my siblings Mrs Ebi Obiyomi, Mrs Faith Oghosa, Mr Ayibanimiworo Boye and their families, my nephew Mr Timi Biebo and friends for their prayers and support. A warn hearth greetings to Mrs Oghenefejiro Boye, for her moral support. I appreciate my friends and colleagues, Dr Beatrice Sankah and Dr Kamaluddeen Garba, for been always there to engage in intellectual and lively discussions during the PhD journey.

Above all, I thank **God (Jehovah)** almighty because you helped me to wear the highest academic crown on my head by your grace and mercies upon my life and family.

Contents

List of Figures

List of Tables

NOMENCLATURE

Roman symbols

A	surface area vector	[m^2]
a_{ij}	amplitude tensor	[m s^{-1}]
bj	digital filter coefficient	[.]
c	chord	[m]
C_L	lift coefficient $\left(\frac{L}{\frac{1}{2}\rho U_\infty^2 Ac}\right)$	[.]
C_D	drag coefficient $\left(\frac{D}{\frac{1}{2}\rho U_\infty^2 Ac}\right)$	[.]
C_f	skin friction coefficient $\left(\frac{\tau_w}{\frac{1}{2}\rho U_\infty^2}\right)$	[.]
CFL	currant number	[.]
C_M	moment coefficient $\left(\frac{M}{\frac{1}{2}\rho U_\infty^2 Ac}\right)$	[.]
C_{MTS}	model constant in MTS SGS model	[.]
$C_{(r)}$	correlation function	[.]
C_T	model constant in MTS SGS model	[.]
C_p	pressure coefficient $\left(\frac{p_0 - p_\infty}{\frac{1}{2}\rho U_\infty^2}\right)$	[.]
C_p'	pressure coefficient fluctuation	[.]
C_ε	SGS constant	[.]
C_{SGS}	constant in SGS model	[.]
C_{SGS}^2	constant in SGS model	[.]
C_{XC}	model constant	[.]
D	drag	[N m$^{-1}s^{-2}$]
e	exponential	[.]
exp	exponential	[.]
f	frequency	[Hz]
i, j	vector 1, 2, 3	[.]
I	integral length scale	[m]
K_{es}	estimate SGS kinetic energy	[m$^2 s^{-2}$]
K_{SGS}	SGS kinetic energy	[m$^2 s^{-2}$]
k_{red}	reduced frequency	[.]
L	lift	[N m$^{-}1s^{-2}$]
L_{ij}	resovled turbulent stress tensor	[m$^2 s^{-2}$]

l_o	largest scale eddy	[m]
l	cell centre distance to nearest boundary	[m]
L_x, L_y, L_z	integral length scale x,y, and z	[m]
L_{xij}	integral length scale stress tensor	[m]
M	moment	[N $m^{-1}s^{-2}$]
M_{ij}	SGS stress tensor at filter level	[m^2s^{-2}]
n	number of time step	[.]
R	computational domain radius	[m]
r	radius of the blade (see Fig. 1.5)	[m]
$R(\phi)$	correlation coefficient	[.]
Re	Reynolds number	[.]
R_{ij}	Reynolds stress tenor	[m^2s^{-2}]
p	pressure	[N $m^{-1}s^{-2}$]
p_∞	freestream dynamic pressure	[N $m^{-1}s^{-2}$]
s	span	[m]
St	Strouhal number $\left(\frac{fc}{U_\infty}\right)$	[.]
t	time	[sec.]
T	characteristic time	[sec.]
T	number of flow pass through (see Fig. 4.4)	[.]
TI	turbulence intensity	[%]
$u_{i(t)}$	instantaneous velocities vectors	[m s^{-1}]
u_τ	frictional velocity	[m s^{-1}]
$u'_{i(t)}$	instantaneous turbulent fluctuations	[m s^{-1}]
u^+	non-dimensional velocity	[.]
$\tilde{u}_i$	phase velocities vectors	[m s^{-1}]
$\hat{u}_i$	phase fluctuations	[m s^{-1}]
U_i	mean velocity	[m s^{-1}]
U_∞	freestream velocity	[m s^{-1}]
U_γ	yawed velocity	[m s^{-1}]
$\mathbf{u}$	velocity components vector	[m s^{-1}]
V_C	cell volume	[m^3]
W	computational domain wake length	[m]
x	distance / coordinate direction	[m]
x_1	centre of the first cell distance at the streamwise direction of wall	[m]
w	wall (aerofoil)	[m]
x^+	non-dimensional distance at the streamwise direction of wall	[.]
y	coordinate direction	[m]
y_1	centre of the first cell height of wall	[m]

y^+	non-dimensional distance normal to the wall	[.]
z	coordinate direction	[m]
z_1	centre of the first cell distance at the spanwise direction	[m]
z^+	non-dimensional distance in spanwise direction of the wall	[.]

Greek symbols

α	angle of attack	[°]
α_0	mean angle of attack	[°]
α_1	pitching amplitude	[°]
∂_c	boundary layer thickness	[m]
π	pi	[rad]
Δ	cutoff width	[m]
ε_{SGS}	dissipation rate of SGS kinetic energy	[$m^2 s^{-3}$]
$\bigtriangledown\cdot$	divergent operator	[.]
ϕ	general scalar property	[m s^{-1}]
ϕ	Yaw angle (see Fig. 1.4)	[°]
Ψ	phase angle	[°]
Ψ_n	phase angles average over the entire cyeles	[°]
γ	diffusivity coefficient	[.]
ν	kinematic velocity	[$m^2 s^{-2}$]
ν_{SGS}	subgrid-scale kinematic viscosity	[$m^2 s^{-1}$]
$\prod$	statistical operator	[.]
μ	dynamic viscosity	[kg m s^{-2}]
μ_{SGS}	subgrid-scale dynamic viscosity	[kg m s^{-2}]
ρ	fluid density	[kg $m^{-1} s^{-3}$]
ρ_∞	freestream density	[kg $m^{-1} s^{-3}$]
η	smallest scale eddy	[m]
ω	angular velocity	[rad/s]
Ω_{ij}	vorticity magnitude	[rad/s]
$\bar{S_{ij}}$	average strain rate of t	[.]
τ	shear stress / time lag	[$m^2 s^{-2}/s$]
τ_w	wall shear stress	[$m^2 s^{-2}$]
$\tau_{_{Tp}}$	dimensionless peak total shear stress	[.]
$\tau_\star$	dimensionless turbulent shear shear stress	[.]
$\tau_{\star b}$	dimensionless turbulent shear shear stress of the blade	[.]
τ_{ij}^r	residual (or SGS stress tensor)	[$m^2 s^{-2}$]

Δt	time-step	[.]

Over symbols

$\widetilde{\phi}$	local convective scalar (see Eq. 4.1)
$\bar{\phi}$	filtered (see Eq. 3.1)
$\widetilde{\ }$	phase averaged operator (see Eq. 6.3)
$\langle\phi\rangle$	assembly average operator (see Eq. 6.2)
β	pitch angle (see Fig. 1.4)
β_m	constant of differencing scheme (see Eq. 4.1)

List of Acronyms

ABL	Atmospheric boundary layer
AR	Aspect ratio
Ave.	Averaged
BC	Boundary condition
BEM	Blade element method
CD	Central differencing
CFD	Computational fluid dynamics
CPU	Central processing unit
DES	Detached Eddy simulation
DNS	Direct numerical simulation
Ds	Domain span
Eq.	Equation
Exp.	Experiment
FVM	Finite volume methods
HAWT	Horizontal axis wind turbine
HSF	Hybrid forward stepwise
IRENA	International Renewable Energy Agency
LE	Leading edge
LES	Large-eddy simulation
LEV	Leading edge vortex
$N-S$	Navier-Stokes Equations
M1	Mesh 1
M2	Mesh 2
M3	Mesh 3
$3DM1_1$	3D Mesh 1
$3DM1_2$	3D Mesh 2
$3DM1_3$	3D Mesh 3
MAV	Micro air vehicle
MTS	Mixed Time Scale
N_z	Number of grid points in the span
PDE	Partial differential equation
PDF	Probability density function

PIMPLE	PISO + SIMPLE
PISO	Pressure implicit with splitting of operation
PT	Pass through
RANS	Reynolds Averaged Navier-Stokes
SDFM	Synthetic Digital Filtering Method
SIMPLE	Semi-implicit method for pressure-linked equation
SGS	Sub-grid-scale stresses
SMT	Static mesh test
SRM	Strong Recycling method
SRFM	Synthetic Random Fourier Method
SVFM	Synthetic Volume Forcing Method
ST	Static
TE	Trailing edge
TEV	Trailing edge vortex
TKE	Turbulent Kinetic Energy
UD	Upwind differencing
USA	United States of America
VAWT	Vertical axis wind turbine
XC	Xie and Castro inflow condition
XCDF	Xie and Castro Divergence-free inflow condition
WRM	Weak Recycling Method
WT	Wind tunnel
1D	1 dimensional
2D	2 dimensional
3D	3 dimensional

Chapter 1

Introduction

1.1 Introduction

The fact that surround the uncertainty of fossil fuel sustainability for world energy demand in the future [27] is real. There are even more uncertainties with the growing world population. According to the United Nations report of 2017, that estimated 7.6 billion people with a growth rate of 1.1% per year [28, 29]. Indeed, with the growing population, man will continue to crave more energy consumption for domestic and industrial needs. The quest of improving energy sustainability and arguably damping the effects of the high reliance on fossil fuel by the growing world populations, thus, renewable energy has been identified as a feasible source of alternative energy supply.

The International Renewable Energy Agency (IRENA) [1] projected 36% steady growth in wind power contributions for electrical power sector from 2015 to 2050 [1] (Fig. 1.1). This forecast indicates a large potential market for wind turbines with a new prospect for wind power investment. Governments and private investors are intensifying their investment in wind turbine technology because wind turbines have shown great success recently among other renewable energy sources [30]. Therefore, improving the competitiveness of wind turbines through cost reduction with innovative aerodynamic design [31], and prolong its service life poses significant challenges for wind turbine development.

Wind turbine for electricity generation has a long history [31, 32, 33, 34], but only in the last decade has it generated the significant amount of commercial energy [30]. The slow development of wind turbines is due to two main factors. Firstly - strong dependence on oil fuels, and secondly - inaccurate prediction of the wind load on the blade, which has a direct effect on the wind turbine performance [30]. Considering the latter, prediction of the wind load on a wind turbine blade requires a good understanding of the aerodynamic forces on solid structure (the wind turbine blade) [31, 32, 33, 34]. Aerodynamics is usually integrated with models for

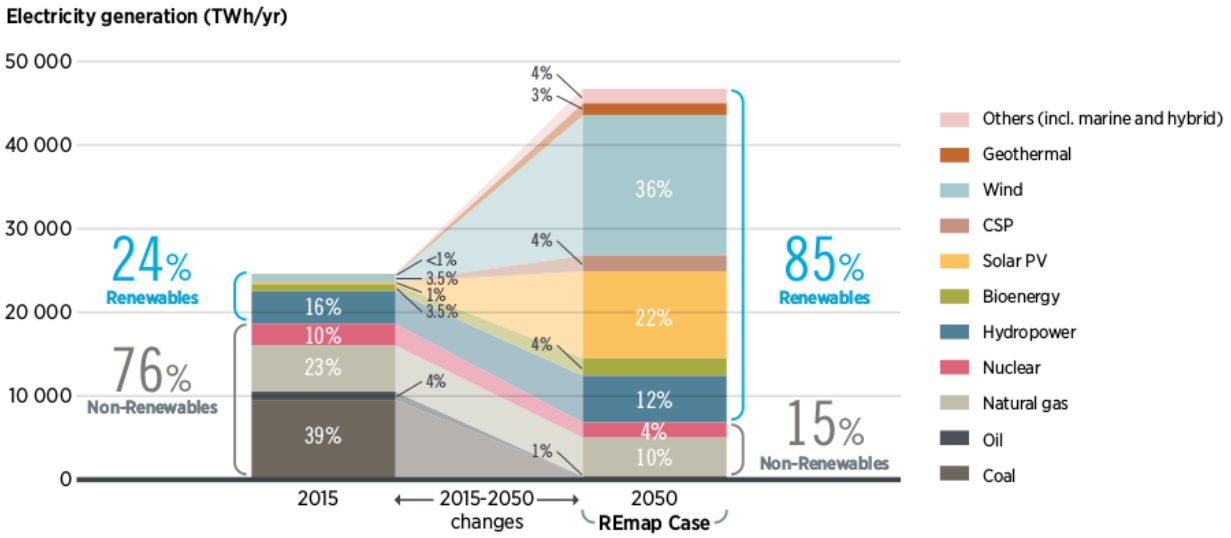

Figure 1.1: Breakdown of electricity generation, by source (TWh/yr)[1]

wind conditions and structural dynamics. The prerequisite for a competitive wind turbine blade design, development, and optimisation requires accurate predictions of its performance and structural deflection with an integrated aeroelastic model.

1.1.1 Large-scale turbulence

The need to reduce the cost of energy wind turbine produce, modern wind turbines are designed with rotor disc diameter greater than 100 m and hub height over 200 m [35]. At this height above the ground level, wind turbines are more exposed to atmospheric weather scale conditions such as high wind speed greater than 25 m/s and large-scale turbulence in the atmospheric boundary layer (ABL) [10].

Indeed, wind turbines are designed to operate in turbulent atmospheric boundary layers. Turbulence is one of the critical transport processes and is sometimes used to define the boundary layer. Stull, [10] defines turbulence as the gustiness superimposed on the mean wind and can be visualised as consisting of irregular swirls of motion called eddies. Usually, turbulence consists of many different scales of eddies superimposed on each other [10]. These various sizes of eddies possess relative strengths in different length scales that define the turbulence spectrum [10], which is shown in Fig. 1.2 and detailed discussions in relation to large-eddy simulation is presented in Chapter 3.

The large-scale turbulence or integral length-scale (average eddy size) is determine temporally and spatially using the expression of Eq. (1.1) for auto-correlation function (the average of the product of the random variable evaluated at two times) and Eq. (1.2) for two-point correlation function (the average of the product of the random variables evaluated at two points) respectively.

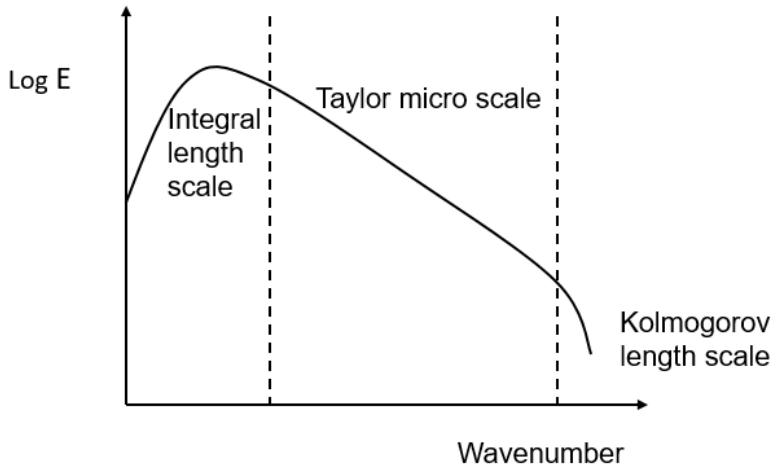

Figure 1.2: Typical turbulence scales/spectrum

$$R(u') = R(\tau) = \frac{\frac{1}{T}\int_0^T u'(t) \times u'(t+\tau)dt}{\frac{1}{T}\int_0^T u'^2(t)dt} \tag{1.1}$$

$$R(u_1'u_2') = \frac{\frac{1}{T}\int_0^T u_1'(t) \times u_2'(t)dt}{\sqrt{\bar{u_1'^2}} \times \sqrt{\bar{u_2'^2}}} \tag{1.2}$$

where R is the correlation coefficient, τ is the time lag, u' is the instantaneous turbulent fluctuations, u_1' and u_2' are the instantaneous turbulent fluctuations at two different points, T is the total time and t is the time.

Turbulent eddies in the ABL are usually much greater than the wind turbine-blade chord length [36]. The turbulence length scales in the ABL ranging from 0.01 to 500 m and eddies greater than the chord length are considered large-scale unsteadiness [36]. In reality, meteorological conditions change can generate energetic large-scales unsteadiness such as vortices or wind gusts which may damage or completely destroy the wind turbine blades [37] (see Figs. A.1 and A.2). These variable loading due to turbulent winds (Fig. A.3) could lead to serious fatigue accumulation on the turbine blades resulting in premature and long-term failures of the blade structural integrity [38].

In this thesis, the definition of large-scale turbulence referred to streamwise integral length-scale (L_x) greater than or equal to the blade chord length. The turbulent length scale within the defined eddy size is generated in a computational domain to study the impact of large-scale turbulence on the wind turbine aerodynamic characteristics. The study focuses on the dynamic stall phenomenon of pitching wind turbine blades under the influence of large scales turbulence and high turbulence intensity (TI). Fig. 1.3 shows a conceptual frame of the core research interest of the present study.

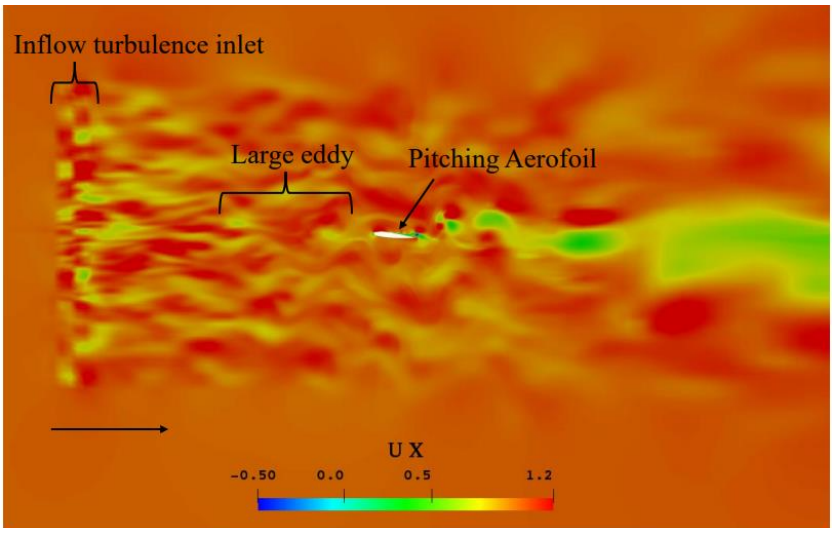

Figure 1.3: Flow field of stremwise velocity with large-isotropic turbulence in the computational domain.

1.1.2 Dynamic stall in large-scale turbulence

The dynamic stall in large-scale incoming turbulence has not been studied rigorously, and is not fully understood. In particular, flow over a pitching aerofoil suitable for modelling rotating wind turbine blade, although, for static aerofoils, considerable experimental and numerical studies for the effects of freestream turbulence on the aerodynamic characteristics has been carried out. Detailed discussions is contained in Subsection 2.3.2. There are a few experimental studies of the effect of freestream turbulence on a pitching aerofoil/blade and even fewer numerical studies [39]. This could be due to technical difficulties in measuring the surface pressure accurately during the dynamic stall process for an experimental study - particularly for high reduced frequency. A numerical simulation would involve huge computational costs overheads.

The researchers who have studied turbulence effects on the dynamic stall of a pitching aerofoil focused on high turbulence intensity and small integral length scale $L_x \leq 0.3c$, where is the chord [40, 4, 22]. They have roughly inferred that an increase of the turbulent intensity increased the lift coefficient, particularly during the downstroke of the aerofoil motion. However, research on the effect of large-scale turbulence on the dynamic stall of a pitching turbine blade is scarce in the literature.

1.1.3 Why study large-scale turbulence?

Stack 1931 [41] mentioned that the effect of the large-scale structure changes on the aerodynamics characteristics of aerofoil/blade is of greater importance than the effects of the high turbulence intensity changes. It is not surprising that only

trivial efforts were given to unravel Stack [41] postulation. This could be that researchers gave more attention to the effect of turbulent intensity and small-scale turbulence over the years than large-scale turbulence. The reasons are due to the relative ease to increase the turbulence intensity and generate small eddies that are much smaller than the chord length of an aerofoil/blade in an experiment of a wind tunnel, and less computational cost when using a numerical approach for such a study. Therefore, a salient question arises, how to bridge the knowledge gap (i.e., large length-scale turbulence effect) within our current numerical and experimental capability?

In recent times, the few studies of the effect of large-scale turbulence on the aerodynamics performance of a static aerofoil could not provide a consensus view. For example, [13] reported that large-scales eddies comparable in size to the chord length significantly improves the aerodynamic performance of the static-blade by increasing the lift coefficient and the overall lift-to-drag ratio for all angles of attack except 0°. This opposes [42] report, which showed that large-scale turbulence has a negative impact on the aerodynamic performance of an aerofoil by reducing the lift-to-drag ratio at all angles of attack except 4°. In addition, [43] reported that an increase in integral length-scale adversely affects the lift performance, whereas [12, 44] argued that an increase in integral length-scale rendered an increase in lift. Furthermore, [45] reported that an increase in integral length-scale enhances the probability of occurrence of short separation bubbles close to the leading edge of the aerofoil. These different views were drawn from wind tunnel measurements except for [42] which is a numerical study - LES. The details of the settings for these studies are in Subsection 2.3.2.

The lack of consensus-views of large-scale turbulence effect on the aerodynamics performance of static aerofoil raised more questions than answers.Therefore, further investigations are required, in particular, using a numerical study (LES) to produce more evidence to support one of the sides of the arguments. Indeed, new results of dynamic motion blade that accounts for pre-stall and post-stall of a static-blade would significantly contribute to reaching a global consensus for the effect of large-scale turbulence on aerodynamic of the wind turbine blade.

This PhD thesis focuses on a blade section oscillating in pitching motion, commonly used to model a wind turbine blade in operation. The pitching motion occurs due to rotation across the non-uniform mean wind speed of the wind turbine height, the highly unsteady incoming flows, yawed winds, and blade torsional motion [e.g. 21, 32, 4]. Thus, the need arises to investigate by accessing the impact of large-scale turbulence on the aerodynamic characteristics and performance of modern large wind turbine blades. The research outcomes would significantly contribute towards achieving a consensus of the effect of large-scale turbulence from a dynamic motion blade perspective. In emphasis, there is little or no study of the impact of large-scale turbulence greater than the chord length (e.g. $c = 1$ m) on the

aerodynamic characteristics of a pitching blade in the literature. Table 2.3 in Chapter 2 summarised the recent available literature that reported on turbulence (small-scale) effect on a pitching aerofoil.

Substantial understanding of the impact of large-scale freestream turbulence is crucial for pitching aerofoil/blade because of the need for the innovative aerodynamic design of modern large wind turbine blades and other similar rotating machinery applications such as Helicopter, micro air vehicles (MAVs) etc. In addition, when the inflow over an oscillating blade experience the effect of unsteadiness and vortex shad from the others.

1.2 Aim and objectives of this research

This PhD thesis aims and focuses at investigating the impact of large energetic eddies of streamwise integral length-scale greater than or equal to wind turbine blade chord-length. The numerical investigation involves applying an inflow turbulence generator to produce energetic large-scale turbulence inside the computational domain for large-eddy simulation. The outcome of the research project would reveal a novel understanding of the effect of large-scale turbulence on wind turbine aerodynamics.

The objective of this work are to:

- To conduct smooth inflow (laminar flow) investigation for high reduced frequencies $k_{\text{red}} = 0.1, 0.15, 0.2, 0.3$ and 0.4 that correspond to the first torsional frequency mode of a large wind turbine blade. This is to understand the high pitching rate effect on wind turbine aerodynamics. The smooth inflow study would also form the baseline simulations and validation data for the large-scale inflow turbulence investigation.
- To obtain new results for the impact of large-scale turbulence on wind turbine blade aerodynamic characteristics. Large-scale turbulence will be prescribed inside the computational domain by applying an in-house divergence-free synthetic inflow turbulence generator for LES denoted as XCDF. The streamwise integral length-scale $\mathrm{L_x}$ ranging from $1c$ to $1.5c$ will be simulated to underpin the validity of the findings for this new numerical investigation. The $k_{\text{red}} = 0.1$ and 0.2, which is synonymous with the unsteady flows will be examined to understand the influence of the blade's pitching motion on the impact of large-scale inflow turbulence on its aerodynamics under the deep dynamic stall.
- Provide qualitatively and quantitatively data of the vortex structures from the dynamic stall process of the pitching blade interaction with incoming energetic large-scale turbulence to unfold the role it plays to the effect on the aerodynamic force coefficients of a pitching wind turbine blade.

– Provide new data for dispersive shear stress and turbulent shear stress in the wake of the pitching blade to establish the total turbulent shear stress in the wake flow of a wind turbine.

1.3 Motivation

The flow conditions over a wind turbine blade is a crucial factor in its performance. Thus, a critical consideration for the aerodynamic analysis of the wind flow surrounding the blade is inevitable to develop a robust design of wind turbine blades capable of withstanding harsh weather conditions, e.g. wind gusts or large vortices. The simulation of unsteady flow over a wind turbine blade would provide a novel understanding of turbulent flows phenomena, which is relevant for improving wind turbine blade geometrical design and structural fitness.

This research work is also motivated by focusing on blade oscillating in pitching motion similar to wind flow over wind turbine blade at a yawed angle (Fig. 1.4). This causes the different angles of attack at the top and bottom blades of the wind turbine per revolution. Physically, the wind direction and conditions change spontaneously in time during harsh weather conditions. Incoming wind approaching the wind turbine blade in a sinusoidal flow pattern or yawed wind is illustrated in Fig. 1.4.

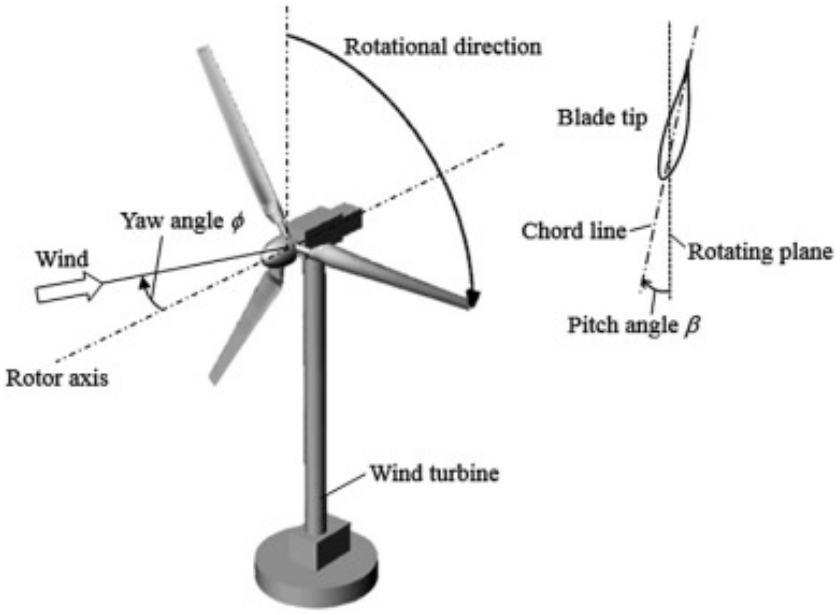

Figure 1.4: Definition of the yaw angle Ψ and the blade pitch angle β. The yaw angle Ψ is defined between the wind turbine rotor shaft and the free stream flow direction. The blade pitch angle is defined as the angle between the chord at the tip of the blade and the rotor surface respectively, [2].

The pitching motion concept of mean velocity over the rotating wind turbine blades aligns with the descriptions by other authors that have conducted research in

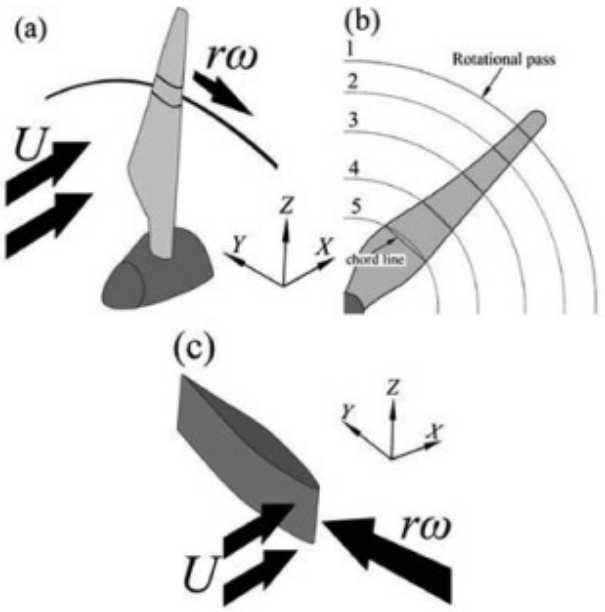

Figure 1.5: Schematic of wind turbine. (a) A rotor blade which rotates with rotational velocity of r; (b) rotational pass and chord line in different sections through the rotor blade; (c) section of blade at radius of r, [3].

related topics of wind turbine applications [e.g. 2, 3, 46, 4]. This inflow pattern is considered a pitching motion of the mean wind over the wind turbine blades sections during operation (Fig. 1.5), which motivate the modelling of the mean wind pitching motion to a pitching blade in a computational domain setting.

1.4 Structure of the report

This PhD thesis is structured in chapters as follows. Chapter 2 proceed with the literature review topics that relate to turbulence and wind turbine aerodynamics in the view to identify a specific research gap within this research space. Then, important issues and questions for these topics were raised. In addition, the challenges of numerical modelling of large-scale turbulence were discussed, with the strategy to overcome them. Chapter 3 presents the methodology, which includes discussions of large-eddy simulation theory, modelling, boundary conditions, and followed by the justification for the synthetic inflow turbulence method adopted to generate large-scale turbulence for the study.

Chapter 4 presents the mesh generation and sensitivity tests for the mesh and the LES sub-grid scale (SGS) models conducted in 2D and 3D simulations for a static NACA 0012 aerofoil to kick start the numerical experiments. The surface forces such as pressure and skin-friction coefficients are used to verify and validate the selected mesh quality and contributions of the SGS viscosity for different LES models tested. In Chapter 5, smooth inflow simulations were performed for the aerodynamics of a pitching wind turbine blade at high reduced frequencies. This

study bridges the research gap of the effect of pitching motion at high reduced frequencies on the aerodynamics of a wind turbine blade under a deep dynamics stall, which is scarce in the literature. The aerodynamics forces coefficients and phase angles, boundary layer on the blade suction surface and dynamic stall vortices are analysed. In addition, the effectiveness of 2D LES be an efficient alternative for studying a section of a pitching wind turbine blade at high reduced frequencies was discovered for the first time.

In Chapter 6, turbulence inflow boundary condition (XCDF) is applied to investigate the impact of large-scale turbulence on pitching wind turbine blade aerodynamics for $k_{\text{red}} = 0.1$ and 0.2, and with different streamwise integral length scales $L_x = 1c$ and $1.5c$. This study bridges the research gap for the effect of large-scale turbulence compared to the small-scale turbulence effect on pitching wind turbine aerodynamics for the first time. The aerodynamics forces coefficients and performance, leading-edge vortex were analysed and discussed. Additionally, with new results of the dispersive shear stress, turbulent shear stress and total stress in the wake. Furthermore, the preliminary simulations in 2D LES to test the viability of this PhD thesis topic are presented in Appendix B. Finally, in Chapter 7 the major points and findings of this doctoral thesis are summarised with a general conclusion. In addition, recommendations were made for future research works.

1.5 Highlights of this doctoral thesis

The novel aspects and scientific contributions to knowledge from this PhD thesis are listed as follows:

- Chapter 5 present the novel features of the effect on the aerodynamics of a pitching wind turbine blade at high reduced frequencies. As the reduced frequency increase from 0.1 to 0.4, the lift hysteresis loop curve increases significantly during the upstroke and downstroke pitching motion. In addition, the lift coefficient during the upstroke loses its linearity at a higher reduced frequency, e.g. 0.4. The peak drag coefficients are reduced noticeably for a higher frequency. A strong dependency on the reduced frequencies was evident in the blade moment. Pitching motion at the high reduced frequency (e.g. 0.4) significantly enhances the suppression of leading-edge vortex during the upstroke and delays the reattachment of the boundary layer until a very low angle of attack in the downstroke. In addition, the effectiveness of 2D LES be an efficient alternative for studying a section of a pitching wind turbine blade at high reduced frequencies was discovered for the first time.

  The provided more accurate aerodynamic force coefficients at various angles of attack, and reduced frequencies and the gained more understanding of

physics from this study, can be used for improvement in the parameterisation of the operational blade element method (BEM).

Part of the work in this chapter was presented at UK Fluid Conference at the University of Cambridge, 27th - 29th August 2019 [47], and at the European Turbulence Conference (ETC), Torino, Italy, 3rd - 6th September 2019 [48]. The results of this chapter were also reported in a scientific paper by **T.E. Boye** and Z.T. Xie, "Aerodynamics of a pitching wind turbine blade at high reduced frequencies", Journal of Wind Engineering and Industrial Aerodynamics, vol. 223, 104935, 2022 [49].

– New understanding of the impact of large-scale turbulence on pitching wind turbine blade aerodynamic performance revealed for the first time to the best of the author's knowledge in Chapter 6. The large-scale turbulence significantly impacts the lift, drag and moment coefficients during the upstroke and downstroke of the pitching blade motion for reduced frequency 0.1. The large-scale turbulence does not enhance the lift and drag coefficients at a higher reduced frequency of 0.2. The moment coefficient has the most impact by large-scale turbulence for both the two reduced frequencies studied and makes the aerodynamic centre of the blade independent of the blade motion due to the given turbulence conditions.

  The leading-edge vortex is adversely impacted by the incoming large-scale turbulence, which affects the aerodynamic characteristics and performance of the wind turbine blade. In addition, for the first time, a pitching motion blade point of view using LES has been provided on the conflicting experimental results for the effect of large-scale turbulence on static aerofoils in the literature. Furthermore, the dispersive shear stress and turbulent shear stress in the wake of the pitching wind turbine blade has indicated flow propulsion and resistance, respectively.

  The new phenomena of large-scale inflow turbulence derived from this study provide a novel understanding needed to enhance the development of the innovative aerodynamic design for modern large wind turbine blades by possibly improving their capability to withstand critical turbulent wind loading during their operational lifespan. In addition, the current study contributes relevant data of large-scale turbulence not seen in the literature to the turbulence research communities in the development of theoretical models for wind turbine research in this aspect.

  Part of the work in this chapter was presented in a conference paper published in the book of abstract (06A-1) by **T.E. Boye** and Z.T. Xie, UK Fluids Conference, University of Southampton, 8th - 10th September 2021 [50]. In addition, the results in Chapter 6 were used to prepare a manuscript by **T.E. Boye** and Z.T. Xie "Impact of Large-Scale Turbulence on a Pitching Wind Turbine Blade Aerodynamics" to be submitted for paper publication in the

Journal of Wind Engineering and Industrial Aerodynamics within the first quarter of 2022.

Chapter 2

Literature review of the thesis

In this chapter, the review of relevant topics of wind turbine aerodynamics for the current research topic is carried out, especially on large wind turbine blades. Fig. 2.1 shows a concise view of some major topics in wind turbine aerodynamics that are of interest to the study.

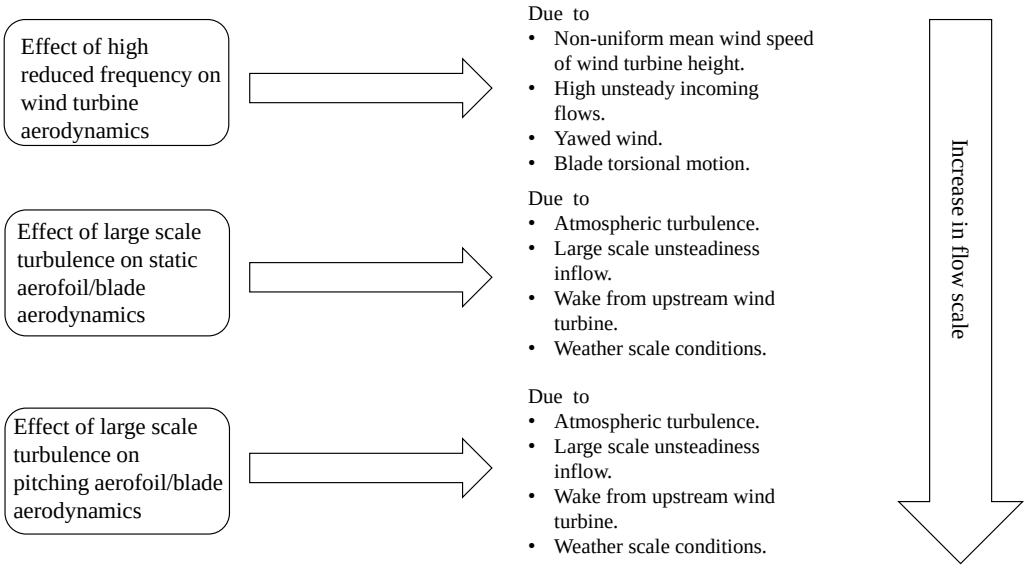

Figure 2.1: Topics in wind turbine aerodynamics (in box): their reason of study/ causes

2.1 CFD and experimental modellings

Computational fluid dynamics (CFD) and experimental studies are vastly utilised to predict and analyse the effect of turbulent flow on wind turbine blade aerodynamics. However, the latter is usually the implementation of typical wind tunnel test procedures and the results, which may serve as validation data for the formal.

As computer power increases, CFD has continued to gain utilisation for turbulent flow prediction and analysis of aerodynamic forces due to its reliability, capability to simulate complex geometry and numerous boundary conditions in a flow domain with relatively low cost [51, 52].

Many researchers and engineers have used the CFD method to study different flows phenomena on a wind turbine blade, with significant successes recorded in the last two decades. In 2003, Ravergy et al. [53] successfully conducted CFD simulations using the LES technique to predict the transition process and its interaction with the wake dynamics for a subsonic blade turbine configuration. Jimenez et al. (2007) [54], used a developed CFD code for LES and focused on the drag forces of a wind turbine wake and their LES results agreed well with experimental and analytical correlation data. Robert et al. (2010) [55], presented combined experimental and computational studies to investigate the aerodynamic performance of a small-scale vertical axis wind turbine (VAWT). The work includes 2D and 3D simulations, in which the results are compared with experimental data for validation, which shows good agreements.

Kim and Xie [4] in 2016 arguably for the first time successfully demonstrated the capability of CFD by the use of the LES approach to predict highly separated flows at the deep dynamic stall of a pitching aerofoil as shown in Fig. 2.2. Among other many works, relevant literature that has successfully applied CFD simulations for the investigation of turbulent flows on wind turbine aerodynamics [56, 57, 58, 59].

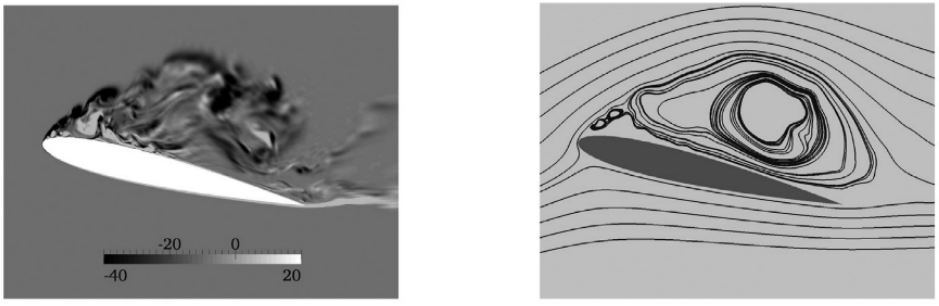

(a) z-vorticity (b) Streamlines

Figure 2.2: Snapshots of the instantaneous flows (z-vorticity) over a pitching NACA 0012 airfoil at the middle section of the span, at α =23.3^o ($\alpha(t)$ =10^o + 15^{o}sin(ωt)) Re = 135,000, k_{red} = 0.1 [4].

It is to be noted that CFD method (LES technique) forms the basis of the implementation of the research objectives. Available numerical and experimental data will be used for the validation of the obtained numerical solutions. The expected findings would provide a novel understanding of the high reduced frequencies effect and the impact of large-scale turbulence on the aerodynamic characteristics and performance of the wind turbine blade.

2.2 Causes of dynamic stall of pitching aerofoil/blade

Unsteady flows over wind turbines affect performance and yield crucial aerodynamic phenomena such as dynamic stall, which is the significant stall delay beyond the static stall point of aerofoils or wings [5, 21]. The dynamic stall is associated with a series of vortices generated, shed or reattached. An aerofoil in pitching motion is a typical example used for modelling of dynamic stall phenomenon for wind turbine and other similar applications.

Modelling dynamic stall of an aerofoil in pitching motion for smooth inflow has been carried out in many previous studies for wind turbine aerodynamics and other similar applications. Experimental [5, 60, 21] and numerical [61, 62, 63, 64, 46, 4] studies provide very good insights on this topic, with a focus on leading-edge vortex (LEV), surface boundary layer mechanism, and unsteady aerodynamic loading induced by generation, growth, convection and detachment of LEVs during the dynamic stall procedure. Given the complexity of the highly unsteady flows and their interaction with turbulence, some challenges are still present today, and further research is required. These include effect of high reduced frequency on the generation and shedding of LEVs, aerodynamic coefficients and interaction of LEVs with large inflow eddies.

Typically unsteady inflow conditions that lead to dynamics stall includes large-scale unsteadiness, atmospheric boundary layer, wind shear, tower shadow, gust, yawed flow (when the wind is not normal to the rotating plane of a turbine) and wakes from an upstream turbine in the wind farm. Detailed descriptions of the dynamic stall events, e.g. a pitching NACA 0012 aerofoil at reduced frequency $k_{\text{red}} = 0.15$, $Re = 2.5 \times 10^6$ and angle of attack $(\alpha) = 15^{\circ} + 10^{\circ}(\omega t)$ is shown in Fig. 2.3 in a progressive order.

Carr et al. (1988) [5], reported that all pitching aerofoils practically experienced a full development dynamics stall. The sequence of dynamic stall should start at point (a) in Fig: 2.3. The boundary layer is thin, and there is no discernible change in the inviscid flow of the aerofoil, which initiates stall delay. The reversed flow develops from the trailing edge and continues towards the leading edges as incidence increases while the flow within the viscous layer remains attached at point (b) in Fig. 2.3. At this point, the viscous flow cannot remain attached; an energetic vortex appears at the leading edge at (e) in Fig. 2.3. This produced vortex refers to as a leading-edge vortex (LEV).

The LEV enlarges and then convects rapidly downstream, the LEV creates a low-pressure region over the aerofoil that increased the lift slop see ((e) – (h) in Fig. 2.3), and the LEV remains at the aerofoil suction surface, inducing strong pitching-moment effects on the aerofoil (point (f) and (i) in Fig. 2.3), which produces the phenomenon called a dynamic stall. By the time the LEV passes the pithing pivot point, the pitching moment begins to drop, referred to as moment-stall see (g) in

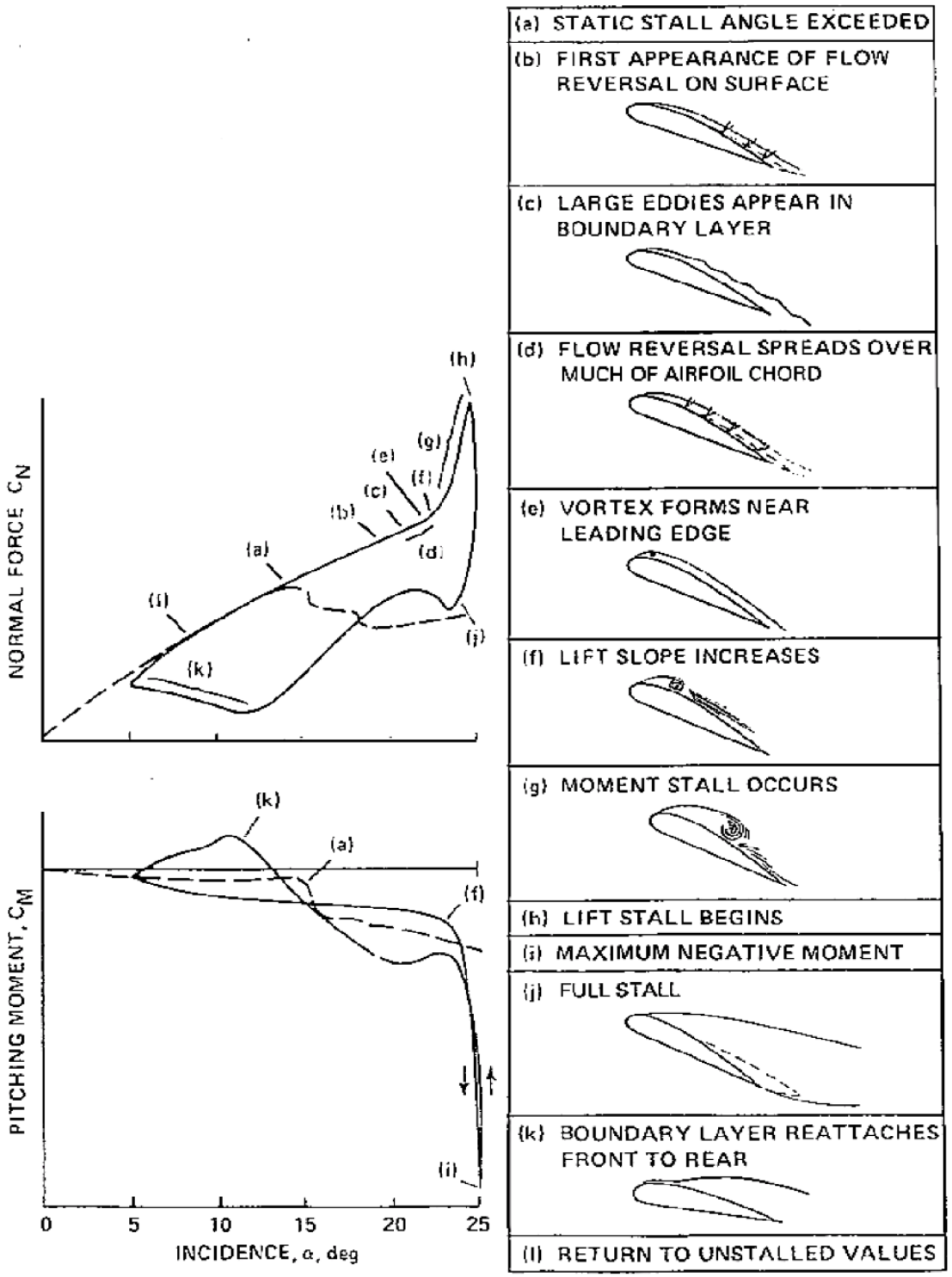

Figure 2.3: Events of dynamic stall on NACA 0012, $k_{\text{red}} = 0.15$, $Re = 2.5 \times 10^6$, angle of attack $(\alpha) = 15^\circ + 10^\circ(\omega t)$ [5].

Fig. 2.3. Therefore, the flow is fully separated from the trailing edge. The flow becomes reattached as incidence passes the lowest angle of attack.

Dynamic stall of an oscillating aerofoil in pitching motion has been studied extensively experimentally, and a reasonable amount of investigations is done numerically within the aviation and wind energy research communities [5, 60, 21, 63, 64, 46]. However, little research on the effect of large-scale freestream turbulence on the dynamic stall has been conducted, in particular, for wind energy applications. Some relevant research works on flow over a pitching aerofoil are discussed before the review for the effect of freestream turbulence on the dynamic stall, which is the focal interest of the current study.

McCroskey et al. (1976) [65], conducted an experimental investigation on the dynamic stall of a NACA 0012 aerofoil. This study focus was to examine the different boundary layer separation observed from different aerofoils, the general effect of the vortex shedding phenomenon at different frequencies, and the leading-edge geometry on the lift force and pitching moment coefficients. The factor that affects the dynamic stall includes aerofoil geometry, pitching frequency, pitching amplitude, and Reynolds number. In addition, the flow reversal and flow separation locations are notably different on a pitching aerofoil compared to a static aerofoil and occur at almost the same point.

Lee and Gerontakos (2004) [21], provides insight into the nature of the unsteady boundary-layer events as stalling mechanisms at work in different stages of the dynamic stall process. The reduced frequency of an oscillating aerofoil is of high significance, and only a small value reduction is required to delay the onset of the various boundary-layer events. In addition, the static-stall mechanism is due to the bursting of a leading-edge laminar separation bubble compared to oscillating aerofoil, which the dynamic stall is due to the sudden turbulence boundary layer breakdown at a short distance downstream of the leading-edge. The dynamics of the leading edge vortex during the dynamic-stall on a pitching aerofoil is reported in [66, 67].

In order to get a solid understanding of the principle of dynamic stall, the relation between the rotation period (time unit) of the blade as well as the time scale for the flow passing over each turbine blades section should be considered as shown in Figs. 1.4 and 1.5. This relation is known as the reduced frequency k_{red}, which is defined as:

$$k_{\text{red}} = \frac{\omega c}{2U_{\infty}}, \tag{2.1}$$

where ω is the pitching frequency, c is the chord length and U_{∞} is the freestream velocity.

2.2.1 Wind turbine operates in high pitching frequencies

Indeed, researchers [68, 39, 69] reported that the pitching motion impacts significantly on the dynamic stall process, and the reduced frequency (k_{red}) expressed in Eq. (2.1) is a principal non-dimensional parameter [65, 5]. It is to be noted that very little work about the effect of high reduced frequency (e.g. $k_{\text{red}} \geq 0.3$) on the dynamic stall is published in the literature. Some recently published papers, e.g. [70] report the effect of very high reduced frequency (e.g. ≥ 3) at much lower Reynolds numbers for different applications.

Future horizontal axis wind turbine (HAWT) blades could span over 100 m, and the cut-in and cut-out wind velocities are usually 5 m/s and 25 m/s respectively [71, 4]. The blade torsional frequencies of this type of wind turbine in operation range from 5.2 to 7.0 Hz [32], of which the reduced frequencies k_{red} are less than 1. Unsteady flow around the rotating wind turbine blade (e.g. at different blade span locations) yields a wide range of reduced frequencies, leading to various coinciding dynamic stall events (Fig. 2.4). Leishman [72] states that "under yawed wind conditions the 1/rev fluctuations in the component of flow velocity normal to the blade can occur at reduced frequencies greater than 0.1 and significantly higher inboard on the blade", and also comments that transient changes of angle of attack due to the blade passage through the tower shadow could result in an effective reduced frequency k_{red} exceeding 0.2. These results in oscillating wind loading could largely amplify the response at the primary torsional modes and consequently affect the performance and service life of the blades. The latter is because the high-frequency torsion results in the rapid accumulation of fatigue loads on the blades.

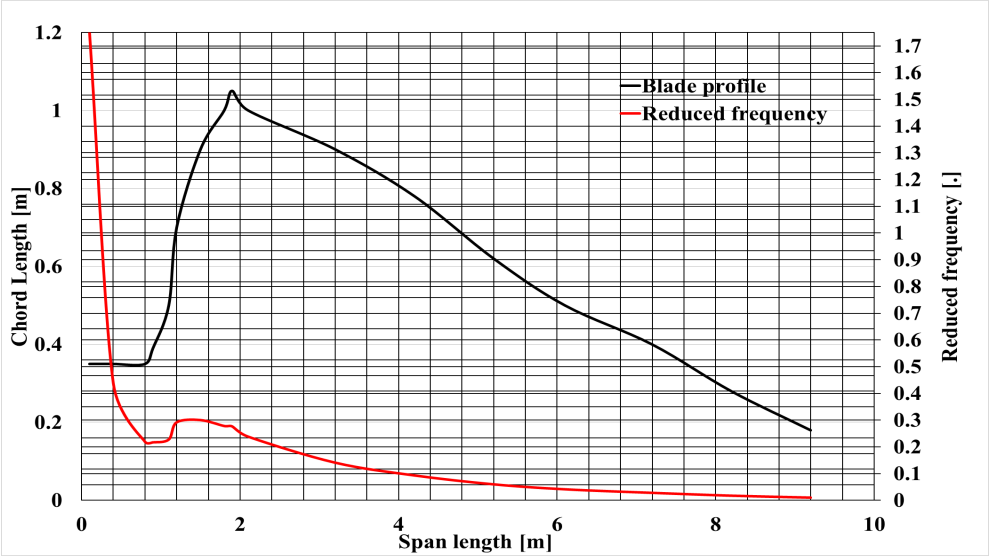

Figure 2.4: The Northern Power Systems (NPS) 100 kw 9.2-meter Wind Turbine blade profile and it corresponding reduced frequencies along the blade radius. See appendix A for detailed information of the blade parameters. Only the blade geometry data is obtained from [6].

Fatigue loads, due to aerodynamic force variation such as cyclic forces on the wind turbine blades are accumulated primarily within the blade's transition region (e.g. in Fig. 2.4 at span length $x = 0.6$ m and morphing via a non-linear chord variation up to $x = 1.8$ m) [73]. The root and transient sections of the wind turbines blades are regions where failures most likely to occur as reported in [6, 73] structural integrity studies (see Fig. A.1 appendix A). These regions of the blades are usually dominant with high reduced frequencies flows. Table A.2 in Appendix A, provides details for the reduced frequencies, freestream velocity, period and eddy size, derived from Northern Power Systems (NPS) 100 kW, 9.2-meter wind turbine blade profile obtained from [6].

2.2.2 Numerical approaches for dealing with high reduced frequencies

For reduced frequency $k_{\text{red}} \leq O(0.01)$, the flow can be considered steady or quasi-steady while for that one order of magnitude higher, the flow is considered unsteady [72, 74]. Wind turbine operates more frequently in highly unsteady wind environments than in steady winds [75, 76, 72, 74]. These raise a question whether only considering 'quasi-steady' reduced frequencies is enough for wind turbine blade design in operation conditions. Thereby, more research on unsteady winds and their impacts should be carried out.

The blade element-momentum (BEM) technique [32] is widely used for the prediction of wind turbine aerodynamics and its performance in steady and unsteady winds, because of its high efficiency. The parameterization scheme and settings of the BEM are based on using aerodynamic coefficients of 2D static aerofoil at a series of angle of attacks in steady flows, which are usually obtained through 2D Reynolds-Average Navier–Stokes (RANS) [77, 78, 79] or wind tunnel experiments. The accuracy of the BEM for unsteady problems is intrinsically debatable.

In addition, unsteady Reynolds-Average Navier–Stokes (URANS) [e.g. 63] approaches have a very limited capability to model flow at the stall angle of attack, which is highly unsteady flow. This is because URANS has an inherent problem to deal with a genuine unsteady flow that does not has a gap between the non-turbulence unsteadiness and turbulent eddies in the power spectrum [e.g. 80]. An example of the spectrum gap is the scale separation between the large-scale non-turbulence unsteadiness (e.g., large-scale unsteady motions) and the large-scale turbulence motions (e.g. due to external forcing) is shown Fig. 2.5.

Large-eddy simulation (LES) and detached eddy simulation (DES) are more capable to capture the 3D dynamic stall features compared with the URANS approaches and are more computationally expensive. LES is chosen in this study, as it is aimed at the understanding of the interaction of the pitching motion of a wind turbine blade at high reduced frequencies and the generated large vortices.

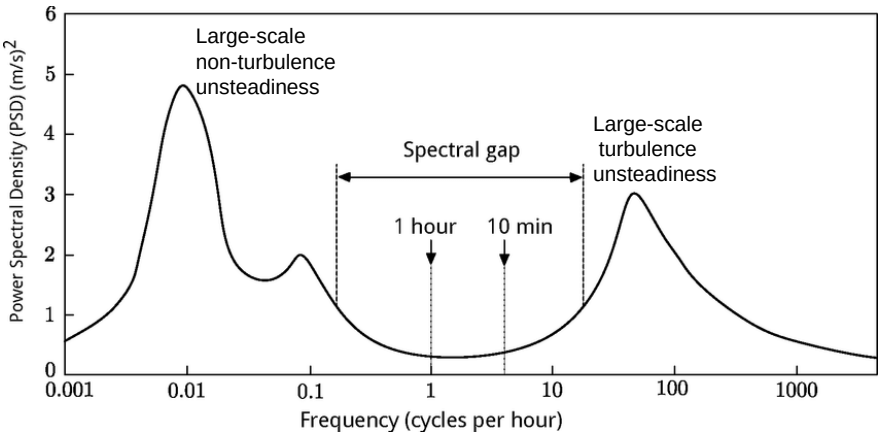

Figure 2.5: Reproduction of the van der Hoven energy spectrum of wind [7]

This is also because it is being possible to access high-performance computing facilities. This does not imply that the use of URANS or DES for more practical applications is not valid. Indeed, with hope, the LES data can be useful for the future improvement of URANS or DES.

2.2.3 A summary of the published reduced frequencies and Reynolds numbers

Table 2.1 shows an non-exhaustive list of relevant experimental and numerical studies in the literature on the effect of reduced frequency of a pitching aerofoil under dynamic stall. Visbal and Shang (1989) [81] found that a change of the maximum lift was associated with the pitching frequency and the pitching axis location. Tuncer et al. [61] suggested that the leading-edge vortex (LEV) played a dominant role in the dynamic stall process, and the formation of the LEV delayed to a high angle of incident as the reduced frequency increased.

Amiralaei et al. [83] observed from their laminar model that the reduced frequency, pitching amplitude and Reynolds number have significant effects on the maximum lift coefficient and the hysteresis loop at very small Reynolds numbers $5.5 \times 10^2 - 5.0 \times 10^3$ (Table 2.1). However, [89, 90, 91, 92] conclude that the Reynolds number effect is of secondary importance at a higher Reynolds number, e.g. $Re = 1.0 \times 10^3 - 1.0 \times 10^6$. Guillaud et al. [86] stated in their LES study that the LEV life-time decreased with an increase in reduced frequency at Re $= 10^4$. Table 2.1 evidently shows there is a requirement for studies on large reduced frequencies (e.g. greater than 0.2). This is explored in Chapter 5.

Table 2.1: A non-exhaustive list of relevant studies on the effect of reduced frequency on aerodynamics of pitching aerofoil. k_{red} is reduced frequency, $\alpha_0[^\circ]$ is the mean angle of attack and $\alpha_1[^\circ]$ is the pitching amplitude (Eq. 5.6).

References	**Methods**	$k_{\mathbf{red}}$	**Re**	**Aerofoil**	**Domain**	$\alpha_0[^\circ]$	$\alpha_1[^\circ]$
Visbal and Shang [81]	DNS laminar	0.1 - 0.6	4.5×10^4	NACA 0015	2D	0 - 60	-
Tuncer et al. [61]	URANS	0.1 - 0.25	1.5×10^6	NACA 0012	2D	15	10
Choudluri and Knight [82]	DNS laminar	0.05 - 0.2	1×10^4 & 1×10^5	NACA 0012	2D	0 - 15	4.75
Lee and Gerontakos [21]	Experiment	0.025 - 0.1	1.35×10^5	NACA 0012	3D	10	15
Amiralaei et al. [83]	DNS laminar	0.1 - 0.25	5.5×10^2 - 5×10^3	NACA 0012	2D	0	2 - 10
Wang et al. [63]	URANS	0.1 - 0.15	1.35×10^5	NACA 0012	2D	10	15
Gharali and Johnson [84]	URANS	0.026 - 18	10^4 - 10^6	S809	2D	8	10
Kim and Xie [4]	LES	0.025 - 0.1	1.35×10^5	NACA 0012	3D	10	15
Sharma asn Poddar [23]	Experiment	0.01 - 0.5	2×10^5	NACA 0015	3D	10	15
Leknys et al. [85]	Experiment	0.05 - 0.2	2×10^4	NACA 0021	3D	0 - 60	-
Guillaud et al. [86]	LES	0.025 - 0.4	2.1×10^4	NACA 0012	3D	10	10
Li et al. [87]	URANS	0.01 - 0.12	3×10^5	DU91- W2-250	2D	10	10
Eslami et al. [88]	Experiment	0.0 - 0.12	0.45×10^6	SC-0410	3D	7.05	15.65
Huang et al. [22]	LES	0.05 - 0.2	1.35×10^5	NACA 0012	3D	10	15

2.3 Effect of turbulence on wind turbine aerodynamics

The height of a modern large wind turbine is within the range of 50 m to 70 m tall above ground level, with blades approximately 50 m long, which operates within the atmospheric boundary layer show in Fig. 2.6 (a). The Scientific-American [8] reported that the alliance of six institutions led by researchers at the University of Virginia are designing the world's largest offshore wind turbine about 500 m tall above sea level with blades span of 200 m long show in Fig. 2.6 (b). In addition, the CNBC [93, 94] also reported that general electric (GE) renewable energy company has laid out plans to develop what it says will be the world's largest and most powerful offshore turbine, the "Haliade –X" at 260 m tall above sea level with 107 m long blades. Let us assume these ambitions comes to fruition then these could mean that large wind turbines will be operating at micro alpha scale [10], (e.g. the vertical height $>$ 200 m of the atmospheric boundary layer) , which typically contains larger eddies compared to micro beta scale (e.g. the vertical height $<$ 200 m of the atmospheric boundary layer), where modern large wind turbine operates. Therefore, should wind turbines operate at these heights, this would create critical structural dynamics and aerodynamic challenges on the blade constantly interacting with large-scale turbulence in the ABL.

Generally, the lower surface of the ABL is characterised as always turbulence with small eddies - high turbulence intensity [95]. However, the upper scale of the ABL is typically dominant with large eddies - low turbulent intensity [95, 96]. Moreover, the impact of turbulence is an unavoidable factor in wind turbine aerodynamics. Different turbulence length scales and turbulence levels results in the complex aerodynamic phenomena of the blade [96]. Therefore, investigation of the effect of large-scale turbulence on wind turbine blade aerodynamics can not be over-emphasised.

Another critical point is that within the wind turbine plant, the wind turbine performance and structural dynamics are usually driven by the turbulence atmospheric winds with the wakes from upwind wind turbine blades [97]. Some of the eddies in the wake of the upwind wind turbine blade may be greater than the chord length of the downwind wind turbines blades. These may contribute excessively to the fluid-structures fatigue loading on the wind turbine blade downwind. Therefore, the need to have a clear understanding of the fluid-structures characteristics of the atmospheric boundary layer is critical. These are important for effective prediction and modelling of the impact of turbulence on the aerodynamic performance of a wind turbine. The next Subsection 2.3.1 presents a brief overview of the atmospheric boundary layer characteristics before reviewing large-scale turbulence flows and their effects on wind turbines blade aerodynamics.

(*a*)

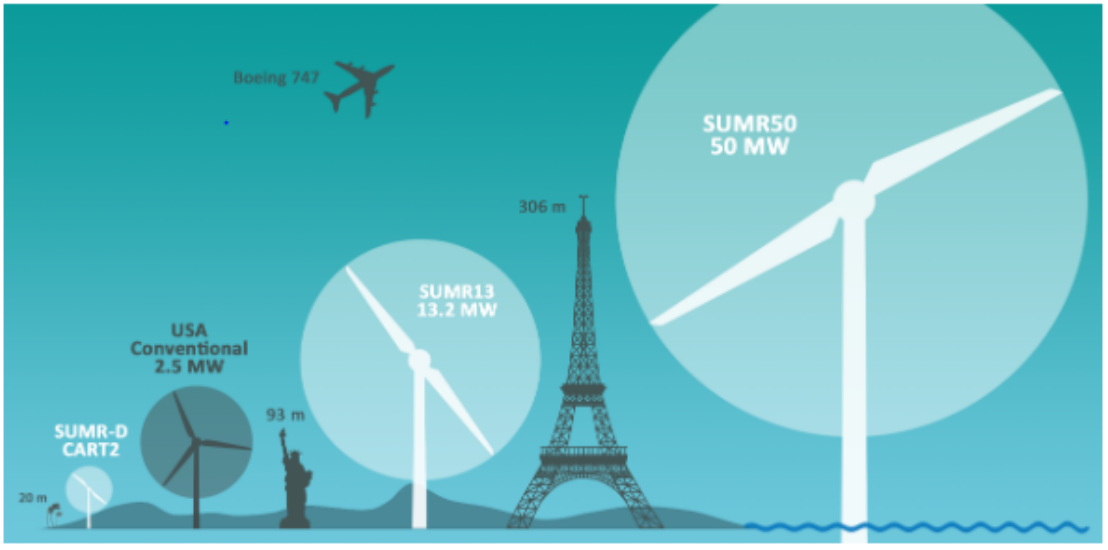

(*b*)

Figure 2.6: (a) Modern wind turbine, (b) evolution of futuristic of wind turbines. [8]

.

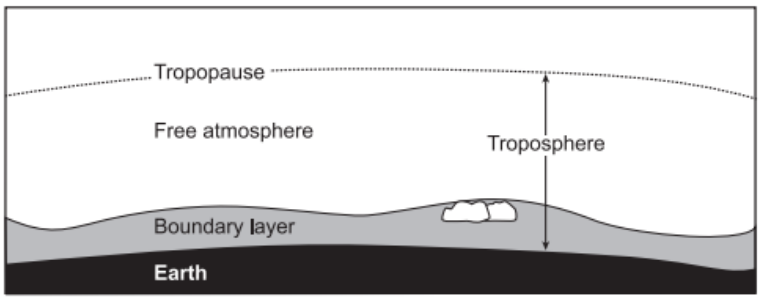

(*a*)

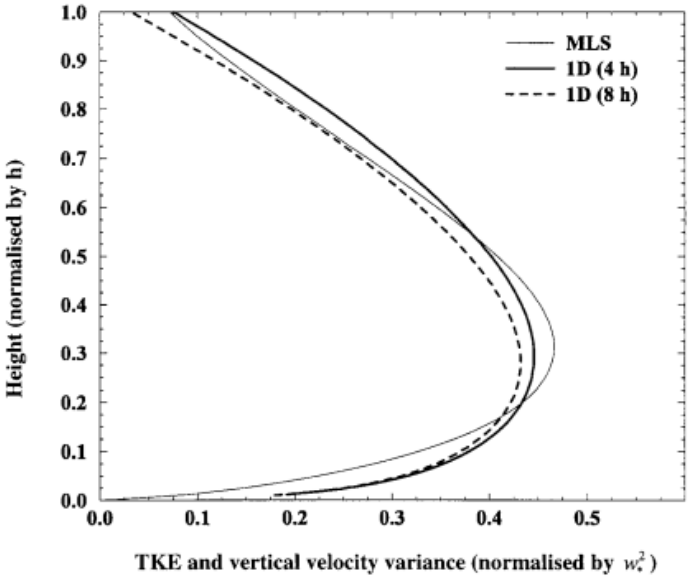

(*b*)

Figure 2.7: (a) The structure of the atmosphere [9], (b) Normalised profiles of turbulent Kinetic energy from 1-D model (hourly means at hours 4 and 8) and vertical velocity variance from mixed-layer scaling [10, 9] h is assumed to be the height.

2.3.1 Turbulence atmospheric boundary layer

The earth surface is the boundary to the atmosphere. Transport processes at this boundary modify the lowest 100 to 3000 m of the atmosphere, creating what is referred to as boundary layer [10]. Fig. 2.7 shows the typical structure of the atmosphere and the boundary layer. Stull (1988) [10], defined the boundary layer as that part of the troposphere that is directly influenced by the presence of the earth's surface and responds to surface forcing with a timescale of about an hour or less. Turbulence is one of the important transport processes and it is sometimes used to define the boundary layer.

Figure 2.7 (a) shows the division of the atmosphere into two layers. First is the boundary layer near the surface, while the other is the free atmosphere. The top of the surface, the boundary layer is usually ∼1 km, but it may be less, e.g. ∼ 100 m depending on the wind and thermodynamic properties of air near the surface. The tropopause height is ∼ 10 to 12 km in the tropics [10, 98]. The wind properties near the surface are determined mainly by the surface friction and vertical temperature gradient. The characteristics of the rest of the atmospheric boundary layer are variable shearing stress, and the wind properties are influenced by the surface friction, temperature gradient and rotation of the earth. Fig. 2.7 (b) shows the vertical profile of turbulent kinetic energy (TKE) of 1D boundary-layer model of a case of dry atmospheric convection (hourly means at hours 4 and 8) [9] and together with the vertical velocity variance from mixed-layer scaling of Stull, 1988 [10]. Both were normalised by w_*^2, which is the convective velocity scale. Some of the significant characteristics of the boundary layer compared with the free atmosphere are enumerated in Table. 2.2.

Table 2.2: Comparison of boundary and free atmosphere characteristics [10].

Property	Boundary Layer	Free Atmosphere
Turbulence	Almost continuously turbulent over it whole depth.	Sporadic CAT in thin layers of large Horizontal extent.
Friction	Strong drag against the earth's surface. Large energy dissipation.	Small viscous dissipation.
Wind	Near logarithmic wind speed profile in the surface layer. Sub-geostrophic, cross-isobaric flow common.	Wind nearly geostrophic.

- About 50% of the atmosphere's kinetic energy is dissipated in the boundary layer.
- Turbulence and gustiness affect the architecture for the design of structures.
- Wind turbine extract energy from the boundary layer winds.
- Wind stress on the sea surface is the primary energy source for ocean currents.

Examine Table. 2.2, one will notice that the boundary layer properties directly affects the wind turbine performance and the effect may even more severe for large wind turbine irrespective of the site of location due to large-scale turbulence contained in the micro alpha scale (> 200 m) height of atmosphere boundary layer.

2.3.1.1 Turbulence scales and motion

Turbulence motions range in size from the width of the flow to much smaller scales, which become progressively smaller as the Reynolds number increases [11]. The

motion size has a wide range of spatial and temporal scales relative to Reynolds number. The ratio between the largest scale eddy (l_o), i.e. production region and the smallest scale eddy (η), i.e. dissipation region scales which can be assumed to be statistically homogeneous isotropic turbulence is expressed in Eq. 2.2 [99].

$$\frac{l_o}{\eta} = O\left(Re^{\frac{3}{4}}\right) \tag{2.2}$$

The above equation similarly expresses the numbers of grid points scales in $O\left(Re^{\frac{9}{4}}\right)$ that may be required for a three-dimensional turbulence flow to resolve all dynamics of motion in a numerical solution. The energy and anisotropy eddies are distributed among the various scales of motion. Details of the different physical processes occurring in the scales are in [11] and schematically show in Fig. 2.8. Definitely, in aeronautics and wind turbine aerodynamics, high Reynolds numbers in order of $O(10^8)$ are reached [99]. Thus, resolving all the ranges of scales of turbulence at a practical Reynolds number is not feasible from a computational point of view, even with the increasing power of super-computers nowadays. In that case, the parameterisation/modelling of turbulence helps to upset this limitation.

The term 'parameterisation or modelling' can be considered as the method used for decomposing the turbulence scales. However, this is solely depending on the decomposing approach employed. For example, if the flow is decomposed into mean and fluctuating parts through integral averaging functions then, the parameterisation or modelling method is known as the Reynolds Averaged Navier-Stokes (RANS) approach. On the other hand, if the whole range of spatial and temporal scales of the turbulence must be resolved in a computational mesh without any form of decomposing the turbulence scales. It is referred to as direct numerical simulation (DNS).

Alternatively, if the flow is decomposed into large and small eddies through a filtering procedure then, the modelling method is called large-eddy simulation (LES). The scales separation between the large and small scales in the turbulence motion is the fundamental concept in LES. The repeating terms in this chapter are the $'large'$ and $'small'$ are similarly used with $'large' \Longleftrightarrow filtered \Longleftrightarrow resolved'$ and $'small \Longleftrightarrow unresolved \Longleftrightarrow sub-grid'$ as depicted in Fig. 3.1 Chapter 3.

From the computational cost point of view, LES lies between the Reynolds-stress models and Direct Numerical Simulation (DNS) and developed due to the limitations of each of these approaches [11]. Because the large-scale unsteady motions are represented explicitly in LES and can be more accurate and reliable than Reynolds-stress (RANS) models for flows, in which large-scale unsteadiness is significant such as the flow over bluff bodies [11] dynamic motion of slender bodies [63, 62, 100] including unsteady separation and vortex shedding. Detailed discussions of the LES method in Chapter 3.

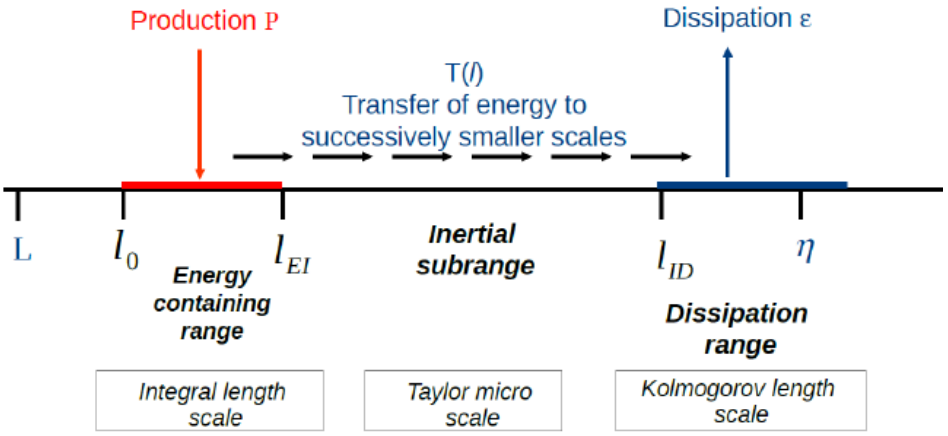

Figure 2.8: Schematic diagram of different length scales and ranges in turbulence motion (Cascade) at high Reynolds number [11].

2.3.2 The effect of large-scale turbulence on static aerofoil/blade aerodynamics

The investigation of the effect of freestream large-scale turbulence flow (isotropic and shear-free) on wind turbine aerodynamics is to simplify the research problem in the current study. In reality, turbulent wind in ABL is usually anisotropic with shear force properties. This research topic aims to understand the impact of large-scale turbulence in the ABL, with the integral length scale greater than the wind turbine blade chord length.

In 1931 Stack [41], performed a wind tunnel experiment of the effect of different turbulence intensities and length-scales (Reynolds numbers) on the aerodynamics performance with five different aerofoils includes NACA 0006, NACA 0021, the Clark Y, the USA 35-A and the USN PS.6. The study aimed to investigate discrepancies in the test results from different wind tunnels. The report stated that the maximum lift increased as the turbulence level increased. It also showed that the effect of large-scale aerodynamics characterises of aerofoils are of greater importance than the effect of the high turbulence level. In the same vein, Hancock and Bradshaw (1983) [101] reported that both turbulent intensity and length-scale of near isotropic free-stream turbulence affect skin friction.

Ames and Plesniak (1997) [102], an experimental study examined the influence of large-scale, high-intensity turbulence on vane aerodynamic losses with Reynolds number, Re = 800,000. A simulated combustor was used to produce moderate and high intensity of 8.3% and 12.0% of relative large integral length-scale of 2.34 cm and 3.36 cm turbulence. The sizes of eddies are presumed to be in the order of the vane chord length. The vane chord length is 14.493 cm, and the span is 7.816 cm. They found that elevated free-stream turbulence has a significant effect on the

wake growth, broader and smaller peak velocity deficits (i.e, velocity deficits are the deference between the mean streamwise velocity profiles and the freestream velocity). In addition, the Reynolds stresses profiles exhibited asymmetry in peak amplitudes about the wake centreline, which was attributed to differences in the evolution of the boundary layers on the pressure and suction surfaces of the vanes. Thus, freestream turbulence strongly affects eddy diffusivities.

Sicot et al. (2006) [103], investigated the fluctuation of the separation point of the static aerofoil (NACA 654-421) with chord length 7 cm and the span 30 cm under high turbulence level up to 16% using pressure measurements and flow visualisation (particle image velocimetry). The main objective of the research was to study the characteristics of unsteady loads induced by Karman vortex shedding. The results showed that the lift and drag peaks at the same frequency due to the asymmetry of the configuration, which shows no effect of the turbulent level on the Karman vortex shedding frequency. Nevertheless, Sicot et al. did not mention the size of the length-scale generated by using a maximum grid with dimension (Mesh, M = 0.36 m, Beam cross-section l = 0.12 m).

An experimental study to investigate the effects of turbulent intensity and integral length-scale of the asymmetric aerofoil (S1223, chord length 0.1524 m, span width ratio of 5 of the chord) was performed by Coa (2010), [104]. The focus is to examine the independent effects of low to moderate turbulence intensity and integral length-scale at Reynolds number (55,000 $\leq Re \leq$ 100,000). Turbulence intensity (TI) are 4.1% and 9.5%, and integral length-scale 0.021 m and 0.032 m were employed for the experimental study. They found that the independent roles of the integral length-scale with turbulence intensity 4.1% delayed the stall of the aerofoil, and the wake profiles became wider at the stall region with the increased integral length-scale from 0.14 m to 0.23 m. This implies that a smaller integral length-scale under low turbulence intensity 4.1% delays the boundary layer separation on the aerofoil suction surface. When the turbulence intensity was increased to 9.5%, the effect of different length scales from 0.08 m to 0.15 m only resulted in subtle changes in the lift and drag.

Perhaps, if a larger length scale that is sufficiently greater than the chord length was used for the study, it could have given clarity to the subtleness of the effect of length-scale with high turbulence intensity on the aerofoil aerodynamic coefficients.

Mahmoodilari et al. (2012) [43], conducted experimental and numerical studies in 2D flow (URANS). The research aims to investigate the significance of turbulence (turbulence intensity and length-scale) on wind turbine blade performance. The NACA 4705 static aerofoil profile with a chord length of 0.06 m and span of 0.4 m. Reynold number (40,000 $\leq$ Re $\leq$ 75,000) and length-scale ranging from 0.15 m to 0.21 m were prescribed for the study. The results confirmed the well-known effect of turbulent intensity on aerofoil performance that any slight increase of the turbulence intensity would improve the lift coefficient noticeably. However, an increase

in integral length-scale can substantially diminish aerodynamics performance, but the drag coefficient is not significantly affected.

The conclusion in [43] opposes the findings of the effect of integral length-scale of other authors who have conducted similar studies with similar turbulence length-scale of the same order although with different aerofoil types.

The effect of freestream turbulence on the flow around an S809 wind turbine blade was investigated experimentally using 2D particle image velocimetry (PIV) measurement by Torres-Nieves and Maldonado [105]. The aim of the study was the effect of a large turbulence length-scale on a smooth and rough surface over a static aerofoil with chord length 0.25 m and a span of 1.22 m. Reynolds number Re = 185,000, TI up to 6.14%, and integral length scale of 0.321 m. The two angles of attack considered for the experiment are the pre-stall (0°) and the post-stall (16°). They found that turbulence significantly reduces the aerodynamic efficiency (i.e. lift-to-drag ratio from 4.896 to 0.908) when the flow is fully attached and produces higher loads and fatigue on the blades. However, when the flow is mostly stalled, the effect is reversed. The aerodynamic performance is slightly improved by 5% due to the presence of freestream turbulence. This improvement is due to freestream turbulence observed at a post-stall angle of attack at (16°). In addition, their results show evidence of complex flow dynamics between the boundary layer scales and the freestream turbulent scales when relatively large length-scale turbulence is present at different angles of attack.

The complex dynamics between the boundary layer scales structure and the free stream turbulent scales structure in various angles of attack observed in [105], would be interesting to get more insights, especially for dynamic motion aerofoil.

More recently, researchers involved in micro air vehicles (MAVs), small remotely controlled or autonomous aircraft that fly slowly ($\leq$ 20 m/s) and very close to the Earth's surface are beginning to show a keen interest in the investigation of larger-scale freestream turbulence. Their interests are urged based on the demand to study flow structures over MAVs aerofoils at a much lower Reynold number (50,000 $\leq$ Re $\leq$ 200,000), and MAVs is much smaller compared with the integral length scales present in the atmospheric boundary layer [12] in which it operates.

Ravi et al. (2012) [12], carried out an experimental study to examine the individual influence of intensity and longitudinal integral length scales of the order to a typical MAVs with flat thin aerofoil profile at low Re = 75,000. The aerofoil chord length (0.15 m) with span width (0.9 m) resulting in an aspect ratio of 6. The wind tunnel test generated turbulence intensity TI (7.15% $\leq TI \leq$ 12.6%) and longitudinal integral length scales L_x = 0.14 m, 0.22 m, 0.15 m, 0.21 m and 1.3 m, which were used for the study. Fig. 2.9, shows the dimensional and normalised spectrum for all turbulence conditions generated as part of the study. They found that turbulence intensity and longitudinal integral length-scale

turbulence had an opposing influence on the lift curve slope, with an increase in both shows an increase in maximum lift and significantly delayed the stall. In addition, the influence of the TI and L_x on the pitching moment coefficient was considerable only at higher angles of attack.

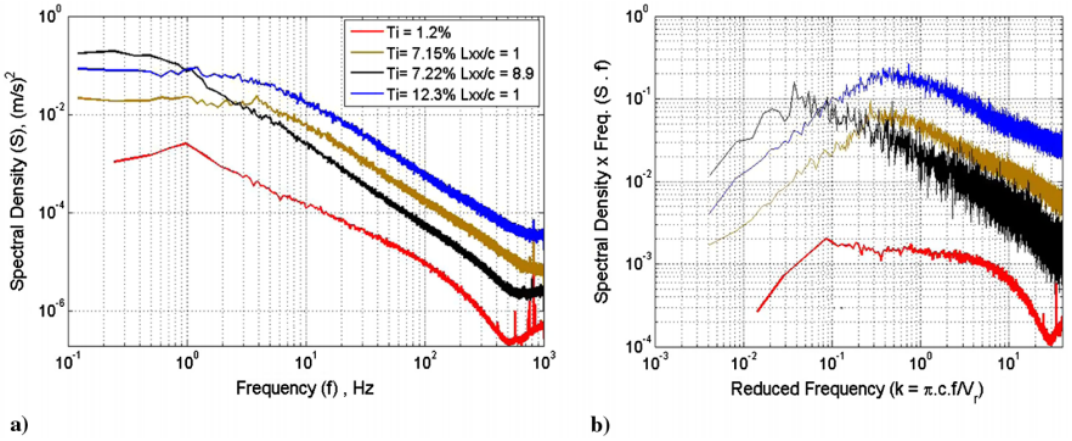

Figure 2.9: (a) Dimensional and (b) partially normalized spectra of the velocity fluctuations in difference conditions [12].

Herbst et al. (2018) [106], conducted an experimental investigation similar to [44], using SD7003 aerofoil with a chord length of 0.2 m and span of 0.8 m. The turbulence intensity is 10% and vary length scales of 0.1 m, 0.2 m and 0.4 m, and Re = 60,000. They found that increasing the integral length scale raises the probability of a short separation bubble to the leading edges. A Short separation bubble may imply that the lift coefficient would be affected.

It will be of great interest to look deeper at the specific impact of large-scale turbulence on the aerofoil surface at Reynold number one order of magnitude higher. Perhaps, if the effect of the turbulence intensity and especially large length-scale will exhibit similar flow phenomenon for a thick symmetrical aerofoil popular in the wind turbine applications.

An extension of the study [12] with the same turbulence conditions was presented in [44]. This paper focused on the individual influence of turbulence intensity and integral length scale on the transient-lift, pressure drag, pitching moment, and rolling moment experienced by thin flat aerofoil. They found that an increase in integral length-scale also rendered an increase in lift and pressure drag fluctuations. Also, the rolling moment fluctuation was smaller at the longer length scales, and there was an increase in force fluctuations at a longer length scale. They attributed the force fluctuations at a longer length scale to the higher peak energy present at lower frequencies. In addition, [44] acknowledged that detailed quantitative information on the persisting flow structures over the aerofoil under the different turbulence conditions could not be obtained.

Indeed, a numerical method such as LES can offer a better alternative in capturing important quantitative data of the persisting flow structures, which is challenging for experimental studies to obtain.

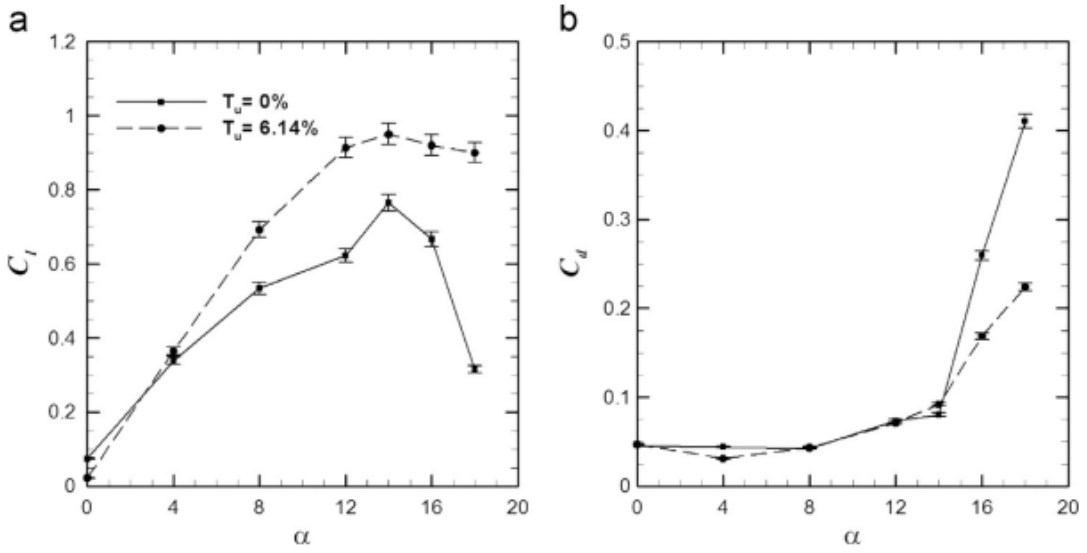

Figure 2.10: Aerodynamics coefficients: (*a*) Lift coefficient and (*b*) Drag coefficient, α is the angle of attack [13].

In wind energy applications, investigation of the effect of very large-scale turbulence has begun to gain strong interest compared to the previous decades. This growing interest in studying large-scale turbulence within the wind energy research community is due to the increasing demands for the design and manufacture of large wind turbines for low-cost electricity generation.

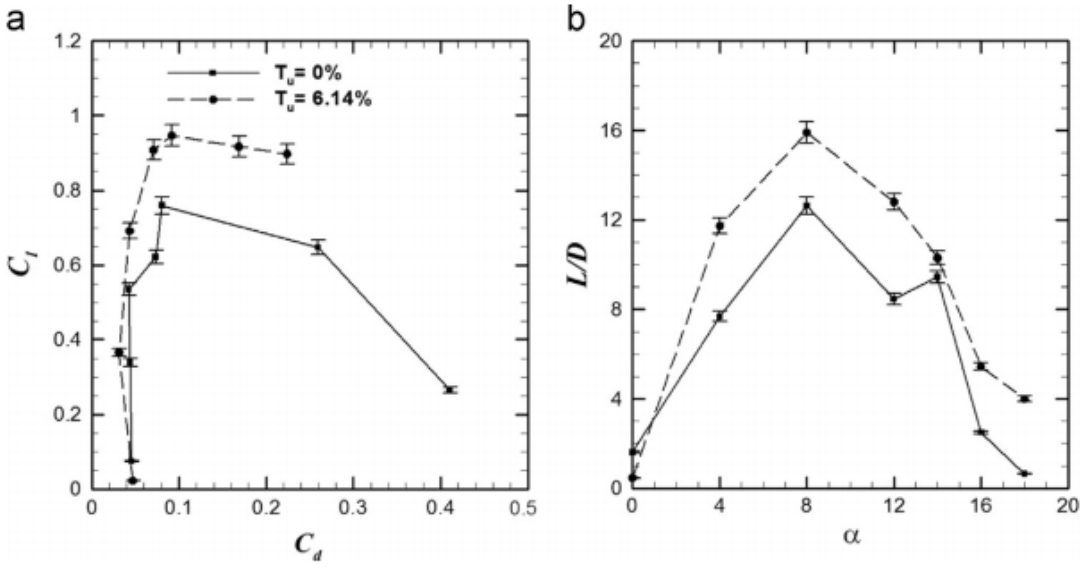

Figure 2.11: Aerodynamics coefficients: (*a*) Drag polar and (*b*) Lift –to- Drag ratio, α is the angle of attack [13].

For example, Maldonado et al. (2015) [13], performed a wind tunnel test with the objectives to study the impact of freestream turbulence with a large length-scale on the aerodynamics performance of an S809 aerofoil suitable for horizontal axial wind turbine (HAWT) at Re = 208,000. Turbulence conditions used for the experiments are 6.4% and 60% of the aerofoil chord length (0.15 m) for the turbulence intensity and integral length scale, respectively. The aerofoil chord length = 0.25m and span = 1.22 m. The range of angles of attack tested from 0 to 20 degrees on a static position. They found that large eddies comparable in size to the chord length significantly improve the aerodynamic performance of the blade, and the overall lift to drag ratio for all angles of attack expect 0° shown in Figs. 2.10 and 2.11. They, however, caution that freestream turbulence - integral length-scale could improve the wind turbine power, but the blade must be designed to withstand the larger mean and fluctuating aerodynamic loads and thus cyclic stresses due to the turbulence.

The various authors' works reviewed in this subsection suggests that a reasonable amount of investigations has been done to study the effect of turbulence intensity and large-scale turbulence for static aerofoils, in which the majority are experimental studies. However, there is no consensus conclusion yet on this important topic for static aerofoil. In particular, for the effect of large-scale turbulence. Therefore, the need arises to employ an advanced numerical method, such as LES, an high fidelity numerical technique combining with a turbulent inflow generator to simulate the effect of large integral length scales. It has become necessary because this will provide a numerical point of view on the conflicting experimental studies conclusions.

2.3.3 The effect of large-scale turbulence on pitching aerofoil/blade aerodynamic

A modern large wind turbine blade is coupled with a pitching control mechanism to enhance its operation. By controlling the variable pitching angle of the blade, the blade's rotational speed can be kept to generate rated electric power [107]. In addition, a wind turbine blade with a pitching control system enhances the reduction of aerodynamic loading, which relieves the torque on the rotor shaft and prevents the rotor from shutdown during highly unsteady flow, which can also reduce the loads on the turbine tower [108]. A pitching system on a large wind turbine blade can reduce the detrimental effect of fatigue on the blade-root compering with a stiff blade (i.e. blades with an increased natural frequency) [109]. However, the dynamic stall is inevitable to occur even with such a pitching controlling system on the wind turbine blade during unsteady wind conditions.

Apart from the pitching motion of the wind turbine blade as described above, the fundamental reasons for considering pitching aerofoil of the current study for the

investigation of the impact of large-scale turbulence on wind turbine aerodynamics are as follows:

- Physically, the incoming wind changes direction spontaneously and approaching the wind turbine blade at different rotational speeds at a yawed angle. Thus, the flow will resemble a pitching motion on the wind turbine blade surface. A conceptual sketch of the incoming yawed's wind approaching the aerofoil was shown in Subsection 1.3(Figs. 1.4 and 1.5).
- As earlier stated in Subsection 1.3 and shown in Fig. 1.5. The high wind speed at the upper region of the atmospheric boundary layer, e.g. ≥ 0.25 km, will produce a high angle of attack on the top blade. At the lower region where the wind speed is low, e.g. ≤ 0.05 km of the boundary layer will produce a low angle of attack to the lower blades. Note that modern large wind turbine blades diameter are ≥ 100 m. Therefore, each wind turbine blade rotating in periodicity will change to a different angle of attack due to the wind mean velocity profile it moves across.
- Wind turbine blades oscillating in pitching motion in unsteady wind experience physical flow phenomena that affect the aerodynamics performance. Therefore, a solid understanding of the effect of unsteady wind is crucial for pitching blade aerodynamics because the innovative aerodynamic design of modern large wind turbine blades is of more importance nowadays. When a pitching blade experienced wind unsteadiness or large vortex structure shedding at a high angle of attack, this would cause a physical flow phenomenon known as **dynamic stall**.

2.3.3.1 Large-scale freestream turbulence on the dynamic stall of a pitching aerofoil

In wind turbine aerodynamics, the effect of turbulence on the dynamic stall of a wind turbine blade is an important topic to study. This is because the wind turbine blade experienced unsteady wind conditions differently at each rotating blade. Dynamic stall event is characterised by the rotating frequency of the wind turbine (Fig. 1.5.

The literature shows that dynamic stall does occur on a wind turbine blade. Although, the wind turbine blade does not rotate fast enough to pass through such a vivid chaotic phenomenon as compared to helicopter rotor blades, which the dynamic stall phenomenon is first observed [5]. The dynamic stall can still occur due to a dynamic inflow, atmospheric turbulence, and a blade in pitching motion (see Subsection 2.2). In principle, the dynamic stall phenomenon is the same irrespective of the application, and the reduced frequency (k_{red}) expressed in Eq. (2.1) is a principal non-dimensional parameter [65, 5].

As mentioned in Section 2.3.2, wind turbine operates in the atmospheric boundary layer, which is always turbulent. A little or no research has been conducted for the effect of freestream turbulence on pitching wind turbine blades, particularly for large-scale turbulence based on the available literature. Table 2.3 shows a summary of researchers who have attempted to investigate the effect of turbulence on the dynamic stall of a pitching aerofoil. The majority of these studies focused on the effects of high turbulence intensity and small-scale turbulence.

The effect of large-scale turbulence on static aerofoil aerodynamic performance could not be underpinned, because of contradicting experimental conclusions from researchers who have studied this research problem. One school of thought augured with their results that large integral length-scale improve aerodynamic performance while the others opposed the former positions with their data.

In the case of an aerofoil/blade with dynamic motion such as pitching motion, the effects of large-scale turbulence on the aerodynamics performance can not be proven because little or no study is available in the literature for this specific research problem. However, the literature of static aerofoil cases, which is conflicting may give ambiguous clues of what to expect in the case of a pitching aerofoil under the influence of large-scale inflow turbulence.

2.3.4 The effect of reduced frequency on dynamic stall under large-scale freestream turbulence

The reduced frequency k_{red} as defined in Eq. 2.1 is also another critical parameter that could influence the unsteady flow structure of a dynamic stall event on an aerofoil either in laminar or turbulence flows. However, the turbulence intensity and eddy size can determine the degree of effect on the aerodynamic performance of a pitching aerofoil relative to reduced frequency.

In the case of laminar flow, the effect of reduced frequencies was characterised by the stall delay as a result of laminar separation bubble diminishing and boundary layer suppression for $k_{\text{red}} \leq 0.1$ [21, 4] and the LEV convective speed is not dependent on the aerofoil motion in $k_{\text{red}} \leq 0.1$. It was also reported that within this range of reduced frequencies, the maximum peak of the LEV increases as the reduced frequencies increases, these also reflect in their maximum lift coefficients.

The effects of reduced frequencies in the case of turbulence flow have some similarities with that of laminar flow. Turbulence intensity promotes the delay of the dynamic stall as reduced frequencies grow [14] and the turbulence effect is more pronounced at a high reduced frequency. Also, the circulation (LEV) value for laminar flow increased rapidly before attaining the peak value and dropped sharply for the higher reduced frequencies compared with that of turbulent flow.

Table 2.3: Summery of literature on the effect of turbulence on dynamic stall of an pitching airfoil, $\boldsymbol{\alpha_0}$ and $\boldsymbol{\alpha_1}$ are mean angle of attack and pitching amplitude respectively, **AR** aspect ratio, $\boldsymbol{L_x}$ integral length-scale and $\boldsymbol{TI}$ turbulent intensity. wT^* is the wake turbulence from a static cylinder.

Authors	**Method**	$k_{\mathbf{red}}$	**Re**$[10^6]$	$TI[\%]$	c **[m]**	$L_x/\mathbf{c}$	**AR**$[z/\mathrm{c}]$	**Airfoils**	$\alpha_0[^\circ]$	$\alpha_1[^\circ]$
Amandolese and Szechenyi (2004)	Exp.	0.0183 - 0.183	≈ 1	1.1 - 7.5	0.5	0.24	3.2	NACA $63_4 - 421$	8 - 20	2 - 8
Wang et al. [15]	DES	0.10	0.135	0.08	0.15	0.4	0.375	NACA 0012	10	15
Kim and Xie [4]	LES	0.025 - 0.1	0.135	5 - 10	1	0.3	0.5	NACA 0012	10	15
Yu et al. [14]	Exp.	0.09 - 0.27	0.0045	0.5 - 6.9	0.01	0.03	0.3	NACA 0015	0	30
Gandhi et al. [39]	DNS	0.16, 0.25	0.044	wT^*	1	wT^*	-	NACA 0012	15	10
Algozino [110]	Exp.	0.005 - 0.025	0.023 -0.053	0.5 - 1	0.1	0.5	0.4	Flat-plat	0.2	0 - 45
Huang et al. [22]	LES	0.2	0.15	5	1	0.15	1	NACA 0012	15	10

These turbulence effects observed are from the study [14] that conducted an experimental investigation of the effect of reduced frequency and freestream turbulence with $0.09 \leq k_{\text{red}} \leq 0.27$ and of $0.5\% \leq TI \leq 6.9\%$ respectively (Fig. 2.12).

Gandhi et al. (2017) [111] conducted a numerical study that investigated the effect of reduced frequencies on a pitching aerofoil in wake turbulence of an oscillating round cylinder for $0.16 \leq k_{\text{red}} \leq 0.25$. The simulation results show an increase in overall lift peak and drag forces at $k_{\text{red}} = 0.25$ compared to that of $k_{\text{red}} = 0.16$ in both laminar and turbulence flow cases. Thus, increase the stall delay from higher pitching amplitude leads to delay detachment of the LEV and flow separation characterised with high pitching moment. In addition, the secondary LEV was not found at $k_{\text{red}} = 0.25$. Although, there was a rapid drop of the already attained peak value of the aerodynamic coefficients as the first LEV detaches from the suction side of the aerofoil [86, 111, 14]. The unsteady dynamic flow structure that results from increased reduced frequency suggests a significant fatigue impact on the service life of a wind turbine blade and other similar rotating machinery.

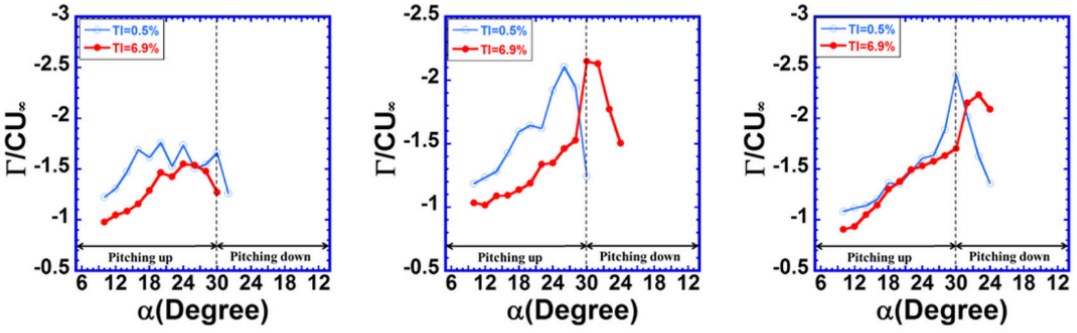

Figure 2.12: The dimensionless circulation (Γ/CU_∞) varies with angle of attack and reduced frequency [14].

The observed effects of different reduced frequencies on the dynamic stall of an aerofoil oscillating in pitching motion in turbulence flow were small-scale turbulence. It is unclear if the same phenomenon is possible or a new flow physics will emerge with the influence of large-scale turbulence. Therefore, it is imperative to investigate the effect of the reduced frequency with large-scale turbulence since the realistic size of eddies in the ABL where futuristic large wind turbine will operate could be much greater than its chord length. Note that substantial effort will be focused on high reduced frequencies because they are synonymous with high flow unsteadiness, which is typical during harsh weather conditions.

2.3.5 Numerical approach of turbulence on pitching aerofoil/blade

Many researchers conduct numerical investigations using the Reynolds Averaged Naiver-Stokes (RANS) approach for pitching blade flow problems. However, the

literature shows that RANS turbulent models cannot adequately predict the aerodynamic hysteresis for the complex flows associated with the LEV and unsteady aerodynamic loads particularly, during the downstroke in a deep stall [62, 100, 63]. Prediction of the effect of large-scale turbulence using a numerical method such as URANS would not be suitable for modelling dynamic stall either because of the same reason discussed in Subsection 2.2.2.

Wang et al. (2012) [15] carried out a numerical study of turbulence modelling of deep dynamic stall of NACA 0012 aerofoil with chord length $c = 0.15$ m and span of 0.375 m using detached eddy simulation (DES) for the computation at $Re = 1.35 \times 10^5$. The turbulence intensity and integral length-scale prescribed are 0.08% and 0.06 m, respectively. Table 2.3 detail the simulation settings while Fig. 2.13 shows DES results compared with experimental data. It is hard to give a clear-cut assessment of the turbulence effect in this specified case because the turbulence properties prescribed in the simulation are significantly small. Nevertheless, the 2D DES prediction of the aerodynamic forces shows good agreement with experiment data while the 3D DES failed to show any significant improvement of the 2D DES predictions [15].

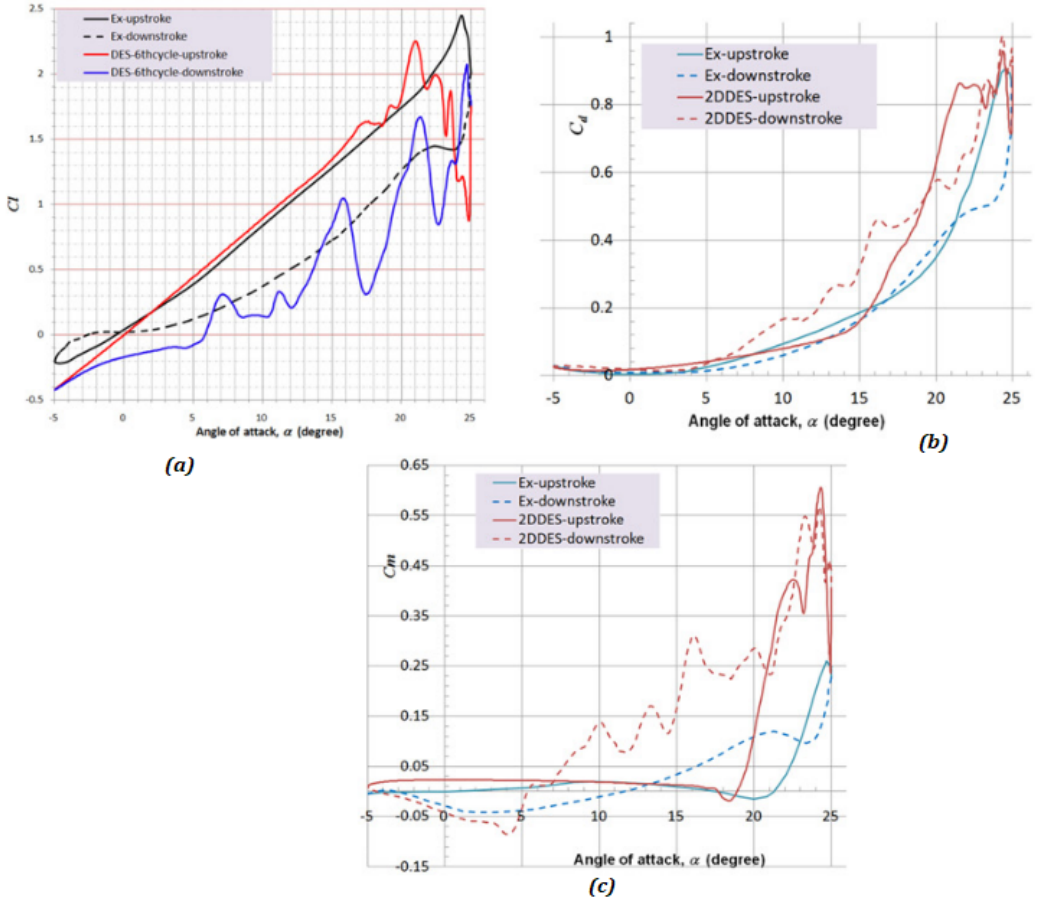

Figure 2.13: Lift, drag and moment coefficients of six numerical pitching cycles using DES $k_{red} = 0.1$ [15].

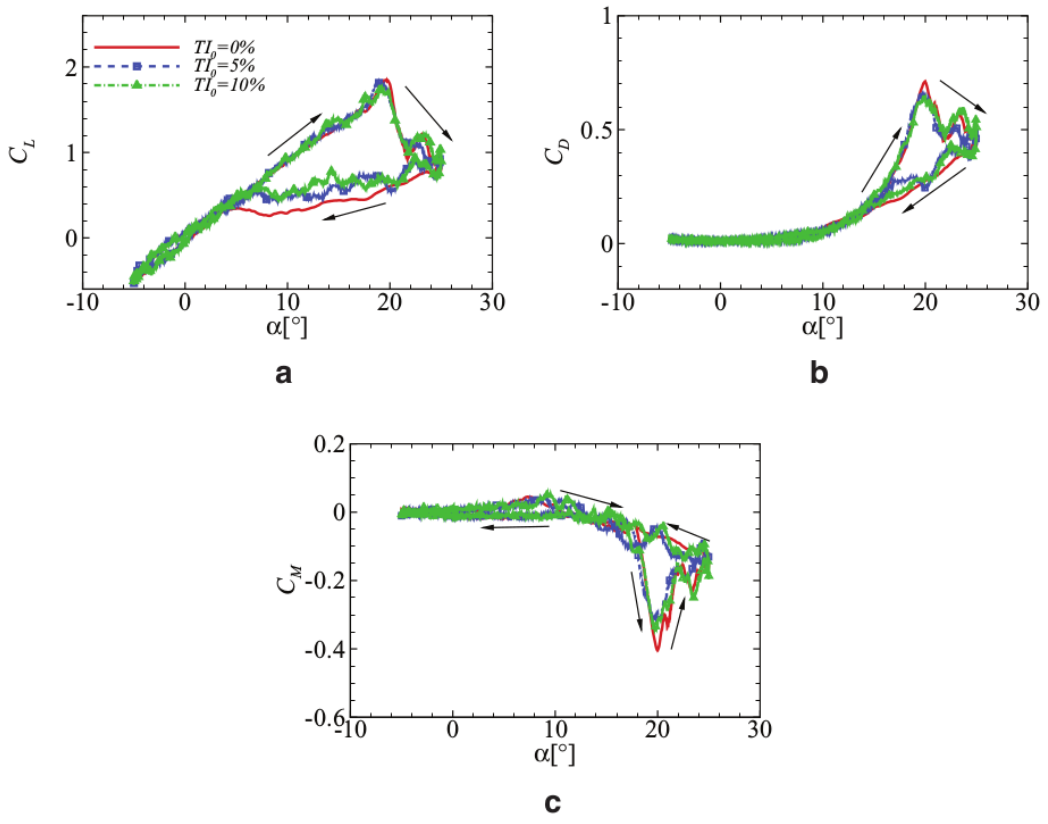

Figure 2.14: Effect of freestream turbulence on lift, drag and moment coefficients. $k_{\text{red}} = 0.05$. The turbulence intensities prescribed at the inlet TI are 5% and 10% while TI at -1c upstream near the lead-edge of the aerofoil are 4.5% and 6.3% respectively, [4].

Kim and Xie (2016) [4], arguably for the first time using a divergence-free inflow generation code for LES known as XCDF [26] to model the effect freestream turbulence on dynamics stall of pitching NACA 0012. They focused more on the effect of the turbulence intensity with a small length scale in the order of the chord length see Table 2.3. Fig. 2.14 shows the effect of turbulence intensity and small length-scale. They found that an increase in the turbulence intensity increases the lift coefficient by approximately 50%, particularly on the downstroke at a low reduced frequency, $k_{\text{red}} = 0.05$.

At this time, it is unclear if such impact can be observed from similar parameters of inflow turbulence [4] at higher reduced frequencies. Furthermore, the large-scale freestream turbulence effect on the dynamic stall is not well studied, particularly in wind energy applications. Therefore, it is of great interest to investigate the impact of large energetic eddies larger than the wind turbine blade section, which is significantly important because of the physical application benefits to large wind turbine blade aerodynamics design and structural dynamics.

It is interesting to note that in this literature review of this thesis, there is no

experimental or numerical work at Reynolds number $Re = 1.3 \times 10^5$ or higher that have studied the effect of integral length scale $L_x \geq 1c$ on the dynamic stall of an aerofoil/blade oscillating in a pitching motion for high reduced frequencies $k_{red} \geq 0.1$ to best of the author's knowledge. **Therefore, the focus here will be aiming to attempt and explore these significant research gaps by using a high fidelity numerical technique such as LES and applying a divergence-free inflow turbulent condition superimpose on the velocity flow field in the computational domain for this vital research area for wind turbine applications.**

2.3.6 Research questions and issues raised

The issues and questions raised in this chapter in Sections 2.2 and 2.3 which includes:

1.) The issue of lack of data for the effect of high reduced frequency for pitching wind turbine blades.

2.) The research gap issues of large-scale turbulence impacting the dynamic stall of a pitching wind turbine blade at high pitching motion.

3.) The issue of the significance to investigate large-scale turbulence effect on the aerodynamic characteristics of pitching blades for the physical application for futuristic large wind turbine development.

These are all crucial issues that need serious consideration for the development of innovative aerodynamical design for modern large wind turbine blades that would be more capable of withstanding extreme conditions. Therefore, these issues raised facilitates the following **research questions** that make up the road map to deliver the current PhD research topic aim and objectives in Section 1.2:

- Can the advanced numerical method such as Large-eddy simulation predicts the flow structures of high reduced frequency of a pitching aerofoil under deep dynamic stall phenomenon? Could the numerical solutions be reliable since data of high reduced frequencies for pitching aerofoils/blades are scarce in the literature? Attempt to provide answers for this research question is presented in Chapter 5.
- What is the magnitude of the impact of the energetic large-eddies greater than the chord length of a pitching wind turbine blade on the aerodynamic characteristics and performance? A preliminary study in 2D LES is presented in Appendix B. Indeed, this very challenging research question is tackled in Chapter 6, Section 6.5.
- What is the reduced frequency effect on the dynamic stall of pitching wind turbine blade section under the influence of large-scale turbulence? Attempt

to provide answers to this research is also presented in Chapter 6, Subsection 6.5.2.

– How does the wind turbine blade motion influence the dispersive stress, shear stress and total turbulent shear stress in the wake? Attempt to provide answers to this research novel question is also presented in Chapter 6, Section 6.6.

It should be noted that the computational resources needed to undertake this type of numerical study pose the challenges of efficient delivery of the research outcomes within the limited time frame of this PhD research project. However, the best attempt and strategies are deployed for delivering this PhD research aim and objectives on schedule.

2.4 Potential challenges for this research topic

In general, fluid mechanics is a physical science attempting to understand and predict flow motions. One of the most challenging problems of the discipline yet unresolved is predicting the behaviour of turbulence interacting with objects. These are the primary source of drag and noise in aeronautics and could cause physical damage to components due to their chaotic/random flow orientation and energy production [11]. These flows are certainly complex to analyse because of their wide range of length scales interacting non-linearly and simultaneously and with their transport phenomena.

2.4.1 Challenges of large-scale turbulence numerical modelling

In a wind tunnel experiment for turbulence flow, it is almost impossible to generate large-scale turbulence (e.g. ≥ 1 m) comparable to the ones in the ABL, where the large wind turbine operates. However, using an active grid to generate turbulence in a wind tunnel, the size of large eddies generated is still tiny compared to the realistic size of large eddies existing in the ABL. These expose a critical limitation of wind tunnel experiments. In contrast, computational fluid dynamics (CFD) offers the possibility to generate large-scale eddies comparable to the range of large eddies size in the ABL using the inflow turbulence condition technique. The implementation is usually in the LES or DNS method, which involves a great expense of computational resources compared to LES.

The massive computational resources required to model the large-scale turbulence numerically is one of the main challenges confronting the computational method of this specific research. The large-scale structures characteristics include low-frequency and slow convection in the flow field, and this would require additional

computational resources to make the calculations get to reasonable converged solutions. Moreover, the inflow large eddies need to be spatially and temporally resolved in the for LES. Refined grid elements should be used to discretised critical areas of interest, e.g. near the wall surfaces and the wake, to capture important flow physics. The total mesh size may be up to ten - hundreds of millions of grid elements, which makes the calculations very expensive, challenging, and time-consuming.

Possible reasons for the effect of large-scale turbulence data of a pitching wing is scarce in the literature could be as a result of the following:

- Numerical modelling of large-scale turbulence is expensive and need a supercomputer to perform the simulations.
- Large-eddy simulation (LES) is time-consuming because all the large scale turbulence in the flow domain needs to be revolved while the small scale ($\sqrt{\Delta x}$) structures are removed using some filter function procedures.
- Pitching motion of the wind turbine blade takes a long computational time to complete one cycle of the blade motion, particularly for low pitching rates.
- Implementation of the inflow condition in the flow domain requires painstaking and skilfully design mesh at the inlet plane location where the inflow boundary condition is superimposed on the computational domain.
- The difficulty for adequate implementation of the synthetic turbulence generation code for generating coherent structures at the inlet plane, and consistency of the prescribed turbulence intensity and length scale in the domain.
- The current limitation of a wind tunnel to generate large-scale turbulence (e.g. $L_x \geq 1$ m) either with the use of passive grid or active grid methods for the turbulent eddies generation comparable to the ones in the ABL, where wind turbines operate.

2.4.2 Strategies to overcome the research challenges

Some of the significant challenges confronting the execution of the PhD research topic was identified in the preceding subsection, which must be addressed to ensure effective and efficient modelling of the impact of large-scale turbulence on wind turbine blade aerodynamics. Therefore, practical and novel strategies must be developed and implemented to achieve substantial research outputs within the limited time frame of the research project.

The strategies developed were focused on efficient computational required to achieve the research objectives while simplifying the research tasks without compromising the quality of the simulation results. Therefore, the following strategies are employed to overcome the challenges of this research project:

- To get a quick insight into this research topic, 2D LES was employed for the initial simulations because it is very efficient to calculate large-scale inflow turbulence impacting a pitching aerofoil. The results help determine if it is worth carrying on with the research topic due to expensive simulations that will involve using 3D LES simulations with other technical issues, which has limited research in this specific area for decades.
- Reduce frequencies synonymous with unsteady wind flows over wind turbine blades in the ABL are examined using 3D LES. Thus, it assures the scope of the numerical investigations to a large extent and achieves robust research outcomes with reasonably affordable computing resources for 3D LES.

2.5 Chapter summary

In this chapter, a summary of topics for wind turbine aerodynamics relevant to this PhD thesis was highlighted and shown in Fig: 2.1.

A thorough literature search and literature review for the effect of turbulence on wind turbine aerodynamics was carried out. The literature review revealed the current trend of futurities wind turbines and their challenges operating in the atmospheric boundary layer up to the micro alpha scale ($\geq$ 200 m height) and during harsh weather conditions. Furthermore, the literature review also showed that the study of large scale freestream turbulence is not well studied or documented due to two significant reasons. Firstly, due to the limitation of the wind tunnel tests been unable to generate large eddies comparable to the energetic eddies contained in ABL where large wind turbines operate. Secondly, due to the massive computational resources required for the numerical modelling of large-scale turbulence using LES or DNS.

Moreover, the researchers who have studied the effect of large-scale turbulence on static blade section experimentally has opposing conclusions. This contradiction needs a numerical approach to confirm a position. Moreover, the consistency of scientific findings is very important. Also, the necessity to investigate the impact of large-scale turbulence of a blade oscillating in pitching motion for physical application for the development of futuristic wind turbine blades can not be over-emphasised.

The reviewed literature further revealed significant research gaps in the current research topic. In other words, there is no numerical (LES) study of the impact of large-scale greater than the chord length ($c = 1$ m) on a pitching wind turbine blade aerodynamics to the best of the author's knowledge. Hence, vital research questions were raised on the influence of large-scale turbulence on the dynamic stall of pitching blades for a range of reduced frequencies synonymous with unsteady wind flows. In addition, available literature on the effect of freestream turbulent

(small-scale) and moderate turbulent intensity on a pitching aerofoil is collected and tabulated for concise view in Table 2.3.

The potential challenges confronting the current research topic are cautiously acknowledged. However, the need to develop strategies to overcome the challenges for the efficient and effective execution of the research project is recognised. Therefore, practical approaches are suggested in strategically tackling and overcoming these challenges.

Chapter 3

Methodology: Large-eddy simulations, concepts, modelling and inflow boundary conditions

3.1 Introduction

The methodology employed for the present study was the large-eddy simulation (LES) computational approach. This method has shown strong reliability in simulating turbulent flow with large length scales and scales separation with high fidelity of the numerical results [4, 112, 59]. LES offers the necessary modelling tools and capability needed to execute the PhD research project that aims to assess impacting energetic large-eddies in ABL on wind turbine blade aerodynamics. Therefore, to demonstrate an understanding of the working principles of the large-eddy simulation technique, the sub-grid filtration concept, governing equations, modelling and inflow boundary conditions for LES are discussed. Furthermore, the justification of the adopted inflow turbulence conditions is presented in this chapter.

As briefly discussed, the turbulent scales and motion in Sub-subsection 2.3.1.1 in Chapter 2, in LES, the dynamics of the large-scale turbulence motion, which are not universal in scale, are affected by the flow geometry and inlet conditions and are explicitly computed, while simple models are used to represent the influence of the smallest scale turbulence, which is assumed to be statistically universal in scale. Thus, compared to DNS, the huge computational cost of explicitly representing the small-scale motions is avoided. Fig. 3.1 shows a typical filtering procedures/operation for the LES method.

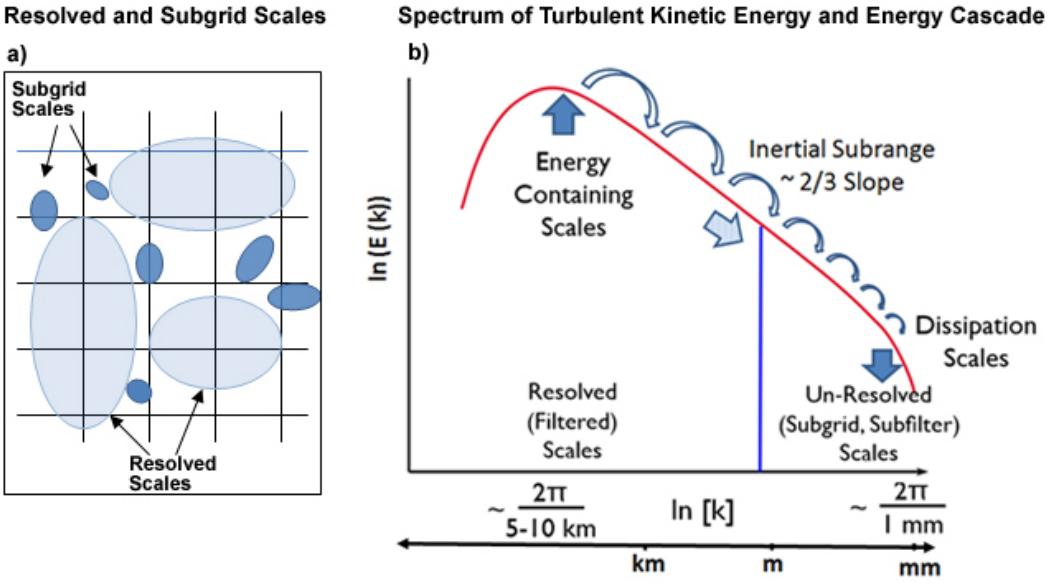

Figure 3.1: (a) Schematic of physical differences between resolved and sub-grid structure and (b) spectrum of turbulence kinetic energy and cascade. The blue line marks the delimiting line between the LES resolved scale and the sub-grid scale[16].

Contrary to time-averaging, LES uses a spatial filtering operation to separate the larger and smaller eddies. The method begins with the selection of a filtering function and a certain cutoff width aimed at resolving the unsteady flow computation for all those eddies with a length scale greater than the cutoff width. Hence, the next spatial filtering operation is performed on the time-dependent flow equations.

3.2 Spatial filtering of Unsteady Navier-Stokes equations

Filters are simple separation devices in electronics and process applications [113] that are designed to split (cutoff width $\triangle$) of an input into a desirable, retained part and undesirable, rejected part. In this case, to separate the large and small scales Leonard (1974) [114] introduced a filter operator that can be applied to the velocity vector fields ϕ, which can be rewritten as in Eq. (3.1).

3.2.1 Filtering functions

The general definition of spatial filtering operation for LES is by means of a filter function $G(\mathbf{x}, \mathbf{x}^{'}, \Delta)$ as follows:

$$\bar{\phi}(\mathrm{x}, t) \equiv \int_{-\infty}^{\infty} \int_{-\infty}^{\infty} \int_{-\infty}^{\infty} G(\mathbf{x}, \mathbf{x}^{'}, \Delta) \phi(\mathbf{x}^{'}, t) dx_1^{'} dx_2^{'} dx_3^{'} \tag{3.1}$$

where $\bar{\phi}(\mathbf{x}, t)$ = filtered function; $\phi(\mathbf{x}^{'}, t)$ = original (unfiltered function) and Δ = filter cutoff width.

Equation (3.1) indicates that filtering is an integration, similar to time-averaged in the development of RANS equations. Particularly in LES, the integration is carried out in time, but in a three-dimension space, in which filtering is a linear operation stated by Versteeg and Malalasekera (2007) [113]. The three popular forms of filtering functions used for LES three-dimensional calculations are:

– Top-hat or box filter:

$$G(\mathbf{x}, \mathbf{x}^{'}, \Delta) = \begin{cases} 1/\Delta^3 & \left|x - x^{'}\right| \leqslant \Delta/2 \\ 0 & \left|x - x^{'}\right| > \Delta/2 \end{cases} \tag{3.2}$$

– Gaussian Filter:

$$G(\mathbf{x}, \mathbf{x}^{'}, \Delta) = \left(\frac{\gamma}{2\pi^2}\right)^{\frac{3}{2}} \exp\left(-\gamma \frac{\left|x-x^{'}\right|^2}{\Delta^2}\right) \tag{3.3}$$

typical value for parameter $\gamma = 6$

– Spectral cutoff:

$$G(\mathbf{x}, \mathbf{x}^{'}, \Delta) = \prod_{i=1}^{3} \frac{\sin\left[(x_i - x_i^{'})/\Delta\right]}{(x_i - x_i^{'})} \tag{3.4}$$

The top-hat or box filter is commonly used in finite volume implementation of LES. The Gaussian and Spectral cutoff filters are preferred in the turbulence research literature. The spectral filtering method (i.e. Fourier series to describe the flow variables) gives a sharp cutoff in the energy spectrum at a wavelength of (Δ/π). In turbulence flow research where scale (large and small eddies) separation is of importance, the spectral method is more attractive, although it is not feasible for general-purpose CFD according to [53]. Generally, choosing the cutoff width (Δ) for LES filtering operation is critical; however, the most common selection method of choosing Δ should be of the same order as the grid size. In 3D computation the length, width and height of the grid cells cutoff width (Δx), (Δy) and (Δz) respectively is often accounted as the cube root of the grid cell volume:

$$\Delta = \sqrt[3]{\Delta x \Delta y \Delta z} \tag{3.5}$$

In practice, the Gaussian filter is always used in combination with a Spectral Fourier cutoff [17]. Fig. 3.2 shows a typical difference between the filters function defined to test the function, and the spectra of the filtered variables are shown in Fig. 3.3. Just as the top-hat and Gaussian smooth out the large-scale fluctuations together with the small-scale fluctuations, which in contrast to the Spectral cutoff filter, affects the scales below the cutoff wavelength.

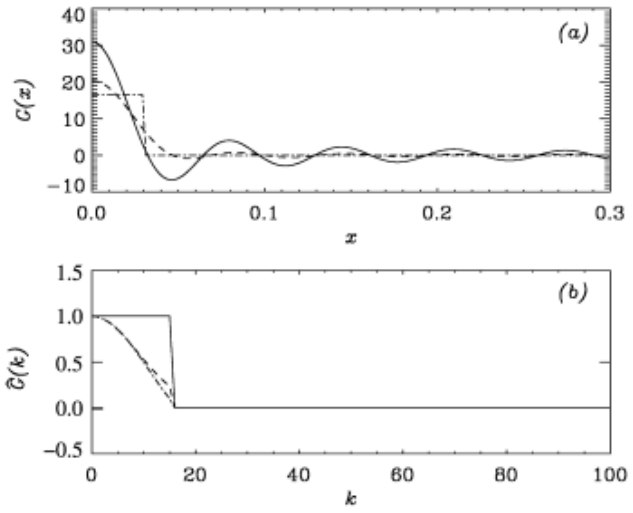

Typical filter functions. —— sharp Fourier cutoff; – – – truncated Gaussian; –·– top hat. (a) real space; (b) Fourier space.

Figure 3.2: Typical Filter functions [17]

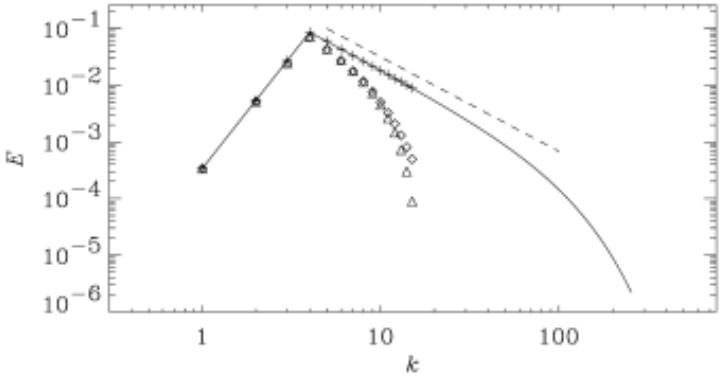

Filtering of a test function. —— Unfiltered; + sharp Fourier cutoff; ◇ Gaussian; △ top hat; – – – $k^{-5/3}$.

Figure 3.3: Filtering test function [17]

3.2.2 Filtered Unsteady Navier-Stokes equations

By use of the filtering methods introduced in the preceding section, the filtered Navier-Stokes $(N-S)$ equations can be derived. Using the Cartesian coordinates so that the velocity vector $\mathbf{u}$ has $u-, v-, w-components$. The incompressible unsteady $N-S$ equations are the following:

$$\bigtriangledown .\mathbf{u} = 0 \tag{3.6}$$

$$\frac{\partial(u)}{\partial t} + \bigtriangledown.(u\mathbf{u}) = -\frac{\partial p}{\partial x} + \mu \bigtriangledown.(\bigtriangledown(u)) \tag{3.7a}$$

$$\frac{\partial(v)}{\partial t} + \bigtriangledown.(v\mathbf{u}) = -\frac{\partial p}{\partial y} + \mu \bigtriangledown.(\bigtriangledown(v)) \tag{3.7b}$$

$$\frac{\partial(w)}{\partial t} + \bigtriangledown.(w\mathbf{u}) = -\frac{\partial p}{\partial z} + \mu \bigtriangledown.(\bigtriangledown(w)) \tag{3.7c}$$

Considerable further implication of the algebra is possible to use the filtering function:

$$G(\mathbf{x}, \mathbf{x}^{'}) = G(\mathbf{x} - \mathbf{x}^{'}) \tag{3.8}$$

Equation (3.8) can be used throughout the computational domain. The filter function G is independent of position x, uniform function and its linearity enable the manipulation of the filtering operations. Thus, it is possible by changing the orders of the filtering and differentiation with respect to time or space vice-versa. Note that the **commutative property** for the filtering operation can be express as in Eq. (3.9). Detailed expression and demonstration on the commutation action are discussed in [113, 11].

$$\overline{\frac{\partial \phi}{\partial x}} = \frac{\partial \bar{\phi}}{\partial x} \tag{3.9}$$

Performing filtering on Eq. (3.6) yields to the **LES continuity equation** for the incompressible unsteady $N - S$ equations. Note that this study would be based on incompressible flow computations:

$$\bigtriangledown.\bar{\mathbf{u}} = 0 \tag{3.10}$$

The overbar in Eq. (3.10) and all following equation in this section indicates a filtered flow variable.

$$\frac{\partial(\bar{u})}{\partial t} + \bigtriangledown.(\overline{u\mathbf{u}}) = -\frac{1}{\rho}\frac{\partial \overline{p}}{\partial x} + \nu \bigtriangledown.(\bigtriangledown(\bar{u})) \tag{3.11a}$$

$$\frac{\partial(\bar{v})}{\partial t} + \bigtriangledown.(\overline{v\mathbf{u}}) = -\frac{1}{\rho}\frac{\partial \overline{p}}{\partial y} + \nu \bigtriangledown.(\bigtriangledown(\bar{v})) \tag{3.11b}$$

$$\frac{\partial(\bar{w})}{\partial t} + \bigtriangledown.(\overline{w\mathbf{u}}) = -\frac{1}{\rho}\frac{\partial \overline{p}}{\partial z} + \nu \bigtriangledown.(\bigtriangledown(\bar{w})) \tag{3.11c}$$

where ν is the fluid kinematic viscosity.

Solving the above set of Eq. (3.10) and (3.11a - c) will yield the filtered velocity field $\bar{u}$, $\bar{v}$, $\bar{w}$ and the pressure field $\bar{p}$. The problem to compute for the convective terms of the form $(\bigtriangledown.(\overline{\phi\mathbf{u}}))$ on the left hand side arise. Since we know velocity field $\bar{u}$, $\bar{v}$, $\bar{w}$ and the pressure field $\bar{p}$, the convective terms can be rewritten as:

$$\bigtriangledown.(\overline{\phi\mathbf{u}}) = \bigtriangledown.(\bar{\phi}\bar{\mathbf{u}}) + (\bigtriangledown.(\overline{\phi\mathbf{u}}) - \bigtriangledown.(\bar{\phi}\bar{\mathbf{u}})) \tag{3.12}$$

In Eq. (3.12), the first term on the right hand can be calculated from filtered $\bar{\phi}-$ and $\bar{\mathbf{u}}-$ fields and the second term could be replaced with a model. By substituting Eq. (3.12) into Eq. (3.11a - c) and rearrangement yields the **LES momentum equations**:

$$\frac{\partial(\bar{u})}{\partial t} + \bigtriangledown.(\bar{u}\bar{\mathbf{u}}) = -\frac{1}{\rho}\frac{\partial \overline{p}}{\partial x} + \nu \bigtriangledown .(\bigtriangledown(\bar{u})) - (\bigtriangledown.(\overline{u\mathbf{u}}) - \bigtriangledown.(\bar{u}\bar{\mathbf{u}})) \tag{3.13a}$$

$$\frac{\partial(\bar{u})}{\partial t} + \bigtriangledown.(\bar{v}\bar{\mathbf{u}}) = -\frac{1}{\rho}\frac{\partial \overline{p}}{\partial x} + \nu \bigtriangledown .(\bigtriangledown(\bar{v})) - (\bigtriangledown.(\overline{v\mathbf{u}}) - \bigtriangledown.(\bar{v}\bar{\mathbf{u}})) \tag{3.13b}$$

$$\underbrace{\frac{\partial(\bar{w})}{\partial t}}_{\text{(I)}} + \underbrace{\bigtriangledown.(\bar{w}\bar{\mathbf{u}})}_{\text{(II)}} = \underbrace{-\frac{1}{\rho}\frac{\partial \overline{p}}{\partial x}}_{\text{(III)}} + \underbrace{\nu \bigtriangledown .(\bigtriangledown(\bar{w}))}_{\text{(IV)}} - \underbrace{(\bigtriangledown.(\overline{w\mathbf{u}}) - \bigtriangledown.(\bar{w}\bar{\mathbf{u}}))}_{\text{(V)}} \tag{3.13c}$$

From the above Eqs. (3.13a - c), the Term (I) are the change in time of the filtered $x-$, $y-$ and $z-$ momentum. Terms (II) and (IV) are convective term and diffusive fluxes of filtered $x-$, $y-$ and $z-$ momentum. Term (III) are the gradients in the $x-$, $y-$ and $z-$ direction of the filtered pressure field. The last Term (V) is caused by the filtering operation similar to Reynolds tensors in RANS Momentum equations. The term (V) can be referred to as a divergence of a set of stresses τ_{ij}. In suffix notation the i-component of these terms can be written as follows:

$$\bigtriangledown.(\overline{u_i\mathbf{u}} - \bar{u}_i\bar{\mathbf{u}}) = \frac{\partial \bar{u}_i\bar{u} - \bar{u}_i\bar{u}}{\partial x} + \frac{\partial \bar{u}_i\bar{v} - \bar{u}_i\bar{v}}{\partial y} + \frac{\partial \bar{u}_i\bar{w} - \bar{u}_i\bar{w}}{\partial x} = \frac{\partial \tau_{ij}}{\partial x_j} \tag{3.14a}$$

$$\text{where } \tau_{ij} = \overline{u_i\mathbf{u}} - \bar{u}_i\bar{\mathbf{u}} = \overline{u_iu_j} - \bar{u}_i\bar{u}_j \tag{3.14b}$$

The τ_{ij} commonly terms the Sub-grid-scale stresses (SGS). A substantial portion of these stresses is attributable to the convective momentum transport due to interaction between the unresolved or SGS eddies.

The LES SGS stresses contributions to the flow field can be determined with the aid of decomposition of flow variable as follows:

$$\phi(\mathbf{x}, t) = \bar{\phi}(\mathbf{x}, t) + \phi^{'}(\mathbf{x}, t) \tag{3.15}$$

where $\phi^{'}(\mathbf{x}, t)$ is consider as unresolved spatial variations at a length scale smaller than the filter cutoff width.

now the LES SGS stresses can be written as follows:

$$\tau_{ij} = \overline{u_iu_j} - \bar{u}_i\bar{u}_j = \underbrace{(\overline{\bar{u}_i\bar{u}_j} - \bar{u}_i\bar{u}_j)}_{\text{(A)}} + \underbrace{\overline{\bar{u}_iu_j^{'}} + \overline{u_i^{'}\bar{u}_j}}_{\text{(B)}} + \underbrace{\overline{u_i^{'}u_j^{'}}}_{\text{(C)}} \tag{3.16}$$

Thus, the SGS stresses contain three groups of contributions:

- Term (A), **Leonard stresses** (L_{ij})

  $L_{ij} = \overline{\bar{u}_i \bar{u}_j} - \bar{u}_i \bar{u}_j$, these are solely due to effects at resolved scale. Leonard (1974) [114]

- Term (A), **cross -stresses** (C_{ij})

  $C_{ij} = \overline{\bar{u}_i u_j'} + \overline{u_i' \bar{u}_j}$, these are due to interactions between the SGS eddies and the resolved flow [115].

- Term (C), **LES Reynolds stresses** (R_{ij})

  $R_{ij} = \overline{u_i' u_j'}$. These are caused by convective momentum transfer due to interactions of SGS eddies and are modelled with SGS turbulence model.

  Thus, the SGS stresses Eq. (3.16) must be modelled like in the case of RANS. Commonly used SGS modelled are discussed in the proceeding Section 3.3.

3.3 Subgrid-scale modelling

The primary principle of LES is predicated upon intentionally leaving the smallest-scale fluid structures unresolved. Thus, fewer computational resources are utilised than those required in DNS Georgiadis (2010) [116]. The filtered $N-S$ Eqs. (3.13a - c) are solved, giving rise to sub-grid stresses in Eq. (3.16), which represent the effect of unresolved structures, and which must be modelled in classic ways. It is commonly assumed that the smallest-scale eddies are relatively isotropic so, that simple subgrid model are generally utilised to account for their effects.

3.3.1 Smagorinsky-Lilly SGS model

The widely used choice for this representation is in terms of an eddy viscosity, which requires specification of both length and velocity scales, along with a Boussinesq stress/strain relationship. It was first suggested by Smagorinsky (1963) [117]. Just as the smallest turbulent eddies are almost isotropic, then the expectation of the Boussinesq hypothesis might provide a good description of the effects of the unresolved eddies on the resolved flow. For this reason, in Smagorinsky's SGS model, the local SGS stresses R_{ij} are taken to be proportional to the local rate of strain of the resolved flow:

$$\bar{S}_{ij} = \frac{1}{2}\left(\frac{\partial \bar{u}_i}{\partial x_j} + \frac{\partial \bar{u}_j}{\partial x_i}\right) \tag{3.17}$$

Therefore, the **LES Reynolds stresses** R_{ij} for the Smagorinsky (1963)[117] is applied as follows:

$$R_{ij} = -2\mu_{SGS}\bar{S}_{ij} + \frac{1}{3}R_{ii}\delta_{ij} = -\mu_{SGS}\left(\frac{\partial \bar{u}_i}{\partial x_j} + \frac{\partial \bar{u}_j}{\partial x_i}\right) + \frac{1}{3}R_{ii}\delta_{ij} \tag{3.18}$$

The dynamic SGS viscosity μ_{SGS} represent the constant of proportionality, which has a dimension Pa s. The term $\frac{1}{3}R_{ii}\delta_{ij}$ ensures that the sum of the modelled normal SGS stresses is equal to the kinetic energy of the SGS eddies.

The above model Eq. (3.18) i.e. (R_{ij}) is commonly used together with the Leonard stresses L_{ij} and cross-stresses C_{ij} in the latest version of the finite volume method [113], in the literature of LES research as reviewed by Meinke and Krause in (Payret and Krause, 2000) [118]. The entire stress τ_{ij} is modelled as one entity through a **SGS turbulence model**:

$$\tau_{ij} = -2\mu_{SGS}\bar{S}_{ij} + \frac{1}{3}\tau_{ii}\delta_{ij} = -\mu_{SGS}\left(\frac{\partial\bar{u}_i}{\partial x_j} + \frac{\partial\bar{u}_j}{\partial x_i}\right) + \frac{1}{3}\tau_{ii}\delta_{ij} \tag{3.19}$$

The Smagorinsky - Lilly SGS model also assumes that in terms of one length scale and velocity scale which defines the kinematic SGS viscosity and the dimensions (m/s) is related to the dynamic SGS viscosity by $\nu_{SGS} = \mu_{SGS}/\rho$. Thus, the size of the SGS structures is determined by the detail of the filtering function, and the length scale is chosen with the filter cutoff width $\triangle$. Therefore, the velocity scale is expressed as a product of the filter cutoff width $\triangle$ and the average strain rate of the resolved flow $\triangle \times \mid \bar{S} \mid$, where $\mid \bar{S} \mid = \sqrt{2\bar{S}_{ij}\bar{S}_{ij}}$. Thus, the SGS viscosity is computed as follows:

$$\mu_{SGS} = \rho(C_{SGS}\triangle)^2 \mid \bar{S} \mid = \rho(C_{SGS}\triangle)^2\sqrt{2 \mid \bar{S}_{ij} \mid \bar{S}_{ij} \mid} \tag{3.20}$$

where C_{SGS} = constant

and $\bar{S}_{ij} = \frac{1}{2}\left(\frac{\partial\bar{u}_i}{\partial x_j} + \frac{\partial\bar{u}_j}{\partial x_i}\right)$

The model constant is a critical value for the SGS viscosity. From the literature, the values of the C_{SGS} are between 0.17 and 0.21 as suggested by Lilly (Jan. and Nov. 1966) [119]. Other values of $C_{SGS} = 0.19 - 0.24$ was also suggested by [120] after conducting critical reviewed of C_{SGS} values of other authors works. Although Deardorff (1970) [121] reported that the C_{SGS} values earlier suggested by Lilly is not effective because it caused excessive damping and also suggested that $C_{SGS} = 0.1$ is most appropriate for internal flow type computations such as channel flow. Thus, the difference in C_{SGS} values characteristically affect the mean flow strain or shear and that a more sophisticated approach or case-by-case adjustment of the C_{SGS} value might require to achieve fruitful LES modelling.

3.3.2 Higher-order SGS model: Transport-equation SGS model

An higher-order SGS model is consider as the transport-equation SGS model which is based on the idea of estimating the velocity scale of $\triangle \times \mid \bar{S} \mid$, which is considered to be more representative of the velocity of the SGS eddies, i.e. the square root of the SGS turbulent kinetic energy $\sqrt{k_{SGS}}$ [113] as defined in Eq. (3.21). This

is used as an additional transport equation to calculate the (k_{SGS}) and the SGS eddies (μ_{SGS}).

$$\mu_{SGS} = \rho C'_{SGS} \triangle \sqrt{k_{SGS}} \tag{3.21}$$

$$\text{where } C'_{SGS} = \text{constant}$$

To consider the effect of transport properties such as convection, diffusion, production and destruction on the SGS velocity scale, the distribution of (k_{SGS}) in the transport equation is determined as:

$$\frac{\partial \rho k_{SGS}}{\partial t} + \nabla.(\rho k_{SGS} \bar{\mathbf{u}}) = \nabla. \left[\frac{\mu_{SGS}}{\sigma_k} \nabla (k_{SGS}) \right] + 2\mu_{SGS} \bar{S}_{ij} . \bar{S}_{ij} - \rho \varepsilon_{SGS} \tag{3.22}$$

The rate of dissipation ε_{SGS} of SGS turbulent kinetic energy is related to the velocity and length scales as:

$$\varepsilon_{SGS} = C_\varepsilon \frac{k_{SGS}^{\frac{3}{2}}}{\triangle} \tag{3.23}$$

$$\text{where } C_\varepsilon = \text{constant},$$

The model constant $C_\varepsilon = 0.93$ [11]. This is the LES equivalent of a one-equation RANS turbulence model such as the one used in the two-layer $k - \varepsilon$ model for the viscous-dominated near-wall region. Performance for the transport equation model has been demonstrated on homogeneous isotropic turbulent [113], and a turbulent boundary layer Shcmidt (1989) [122].

3.3.3 Avanced SGS models

Bardina et al. (1980) [123] proposed a method to compute local values of C_{SGS} based on the application of two filtering operations, considering the SGS stresses to be proportional to the stresses due to eddies at the finest resolved scale, and defined as:

$$\tau_{ij} = \rho C' (\overline{\bar{u}_i \bar{u}_j} - \bar{\bar{u}}_i \bar{\bar{u}}_j) \tag{3.24}$$

where C' is an adjustable constant and factor in the brackets, which can be evaluated from twice-filtered resolved flow field information. They suggested that adding the damping term into the smagorinsky models Eqs. (3.19) and (3.20) stabilises the calculations, which then results in what is called **Mixed Model**:

$$\tau_{ij} = \rho C' (\overline{\bar{u}_i \bar{u}_j} - \bar{\bar{u}}_i \bar{\bar{u}}_j) - 2C^2_{SGS} \triangle^2 \mid \bar{S} \mid \bar{S}_{ij} \tag{3.25}$$

The value of the constant C' depends on the cutoff width used for the second filtering operation.

Germano (1986) [124] proposed a different decomposition of turbulent stresses, which formed the basis of the **Dynamic SGS model**. The model was established in [125] for the computation of local values of C_{SGS}. The decomposition of turbulence stresses was carry-out with the difference of the SGS stresses, which involves two different filtering operations with cutoff widths $\triangle_1$ and $\triangle_2$ respectively, and defined the resolved flow data as:

$$\tau_{ij}^{(2)} - \tau_{ij}^{(1)} = \rho L_{ij} \equiv (\overline{\bar{u}_i \bar{u}_j} - \bar{\bar{u}}_i \bar{\bar{u}}_j) \tag{3.26}$$

The bracketed superscripts (1) and (2) indicate filtering at cutoff widths $\triangle_1$ and $\triangle_2$.

The Dynamic SGS model is modelled using Smagorinsky's model Eqs. (3.19) and (3.20) assuming that the constant C_{SGS} is the same for the two filtering operations and can be expressed as:

$$L_{ij} - \frac{1}{3} L_{kk} \delta_{ij} = C_{SGS}^2 M_{ij} \tag{3.27a}$$

$$M_{ij} = -2\triangle_2^2 |\ \bar{\bar{S}}\ |\ \bar{\bar{S}}_{ij} + 2\triangle_1^2 \overline{|\ \bar{S}\ |\ \bar{S}_{ij}} \tag{3.27b}$$

The least-square approach to computing the local value of C_{SGS} was proposed by Lilly (1992) [126]:

$$C_{SGS}^2 = \frac{\langle L_{ij} M_{ij} \rangle}{\langle M_{ij} M_{ij} \rangle} \tag{3.28}$$

The angular brackets $\langle\rangle$ indicates an averaging procedure. This model was found to produce high variable eddy viscosity fields, including regions with negative values. This problem was remedy by performing an averaging operation in time and space depending on the nature of the flow.

3.3.3.1 Mixed-time scale SGS model

More recently, Inagaki et al. (2005) [127] proposed a new SGS model called the **mixed-time scale model (MTS)**. Just as the model is related to the scale similarity hypothesis suggested by [123], which assumes that the statistical structure of the tensor based on the subgrid-scale is similar to that of the smallest (still larger than SGS) resolved scale.

$$\nu_{SGS} = C_{MTS} K_{es} T_S, \tag{3.29}$$

$$K_{es} = |\ \bar{u}_i - \bar{\tilde{u}}_i\ |^2, \tag{3.30}$$

$$T_S^{-1} = \left(\frac{\triangle}{\sqrt{K_{es}}} \right)^{-1} + \left(\frac{C_T}{|\ \bar{S}\ |} \right)^{-1} \tag{3.31}$$

Where C_{MTS} and C_T are 0.5 and 10 respectively and ($\tilde{}$) in Eq. (3.30) is the explicit filter operator. K_{es} is the estimated SGS kinetic energy by using the explicit filtered scale, $\tilde{\triangle}$, and the ratio between the explicit and cutoff width is $\tilde{\triangle}/\triangle = 2$ in general. The estimated SGS kinetic energy guarantees that ν_{SGS} is close to zero in laminar flow as $\bar{u}_i = \tilde{\bar{u}}_i$ in Eq. (3.31), and it is a harmonic average of the characteristic time scales between the cutoff ($\triangle$ / $\sqrt{K_{es}}$) and large ($1/\mid \bar{S} \mid$) scale [127].

The wall damping function and spatial averaging procedures seen in the dynamic SGS model are not required for the MTS, and it is suitable for transitional flow due to the estimated SGS kinetic energy in Eq. (3.30). Note that the MTS model was implemented in OpenFoam and tested in channel flow and aerofoil flows [25, 128, 129] and buffet body such as long-span bridge and high rise buildings flows [130, 131].

3.4 Initialisation and boundary conditions for LES

In LES computations, solving the unsteady Navier-Stokes equation requires imposing the appropriate boundary conditions (BC). Typical boundary conditions impose for a well-bounded LES problem are the initial condition, inflow boundary (laminar or turbulence) conditions and wall boundary condition.

3.4.1 Initial condition

Initialisation is very important for LES. Begin from an initial state, the solutions must be developed from a sufficiently long time so that transitional flows are eliminated from the computational flow field, and an equilibrium turbulent state is achieved [116]. The transitional flow to turbulence have to be removed entirely, else the temporal averaging and statistical qualities may be contaminated. The remover of transients is a difficult task because to determine exactly when the flow is fully developed to turbulence. Thus, evolving solutions for a very long time will mitigate the effect of the initial transitions but at the expense of using more computational resources.

3.4.2 Inflow boundary conditions

There are several ways to generate turbulence inflow conditions, and none of them is a trivial task to implement [116, 132]. The discussion of some of the popular methods for inflow turbulence condition generation is in the following subsections. Nevertheless, more attention is exerted on the synthetic turbulence condition approach due to its attractive features for engineering applications viewpoint and the peculiarity of the current study.

The implementation of inflow boundary condition is very challenging [132], since the inlet flow properties are convected downstream, and inaccurate specification of the inflow boundary condition can seriously affect the simulation solution [113]. Convective flow typical for aerodynamics, inflow condition intensely influences the quality of the results. Direct numerical simulation (DNS) and Large-eddy simulation (LES) both methods resolve the unsteady, three-dimensional and energy-containing (large) eddies. In the case of laminar flow (steady), it is natural for the velocity profile to accommodate the inlet conditions in the flow field. However, this is a contrast for turbulent inflow, which needs appropriate details of the fluctuating velocity motion [133, 116]. The turbulence inflow conditions are essential to generate atmospheric turbulence for wind engineering applications. Thus, investigating the impact of large-scale atmospheric turbulence on wind turbine aerodynamics, an efficient turbulence inflow generation method is necessarily required to reduce significantly the computational cost that would be involved in the LES calculations.

The approaches involve for inflow turbulence generation are typically Recycling and Synthetic inflow turbulence generation. Both inflow turbulence generation consists of several methods of generating inflow turbulence for DNS and LES computations. The Recycling inflow turbulence generation includes first the Strong Recycling method (SRM) and the other the Weak Recycling Method (WRM). The Synthetic inflow generation method consists of the Synthetic Random Fourier Method (SRFM), Synthetic Digital Filtering Method (SDFM) and Synthetic Volume Forcing Method (SVFM). These methods have been practically applied for incompressible and compressible flow problems in various fields such as in environmental flows, compressible boundary layers, rough surface boundary layers, as well as wind engineering applications including aerodynamics of buildings and aerofoils [56, 132]. A comparative review conducted by Wu (2017) [132] presented the progress of inflow turbulence generation over the past quarter-century and spotlighted the pending issues.

3.4.2.1 Recycling/Rescaling inflow turbulence generation method

Spalart (1987) [134] for the first time, introduced the recycling/rescaling method. Lund et al. (1996) [135] proposed a simplified version for incompressible flows and was later extended to compressible flow by Sagaut et al. (2004) [136]. The implementation of this method involves the extraction of profiles data at some location downstream of the inflow boundary. The data is separately rescaled in the inner and outer layer and reintroduced into the inflow plane. The flow between the inner and outer boundaries must be initially and artificially perturbed to ensure the generation of small-scale structures. The merit of this method is that the inflow is treated implicitly as part of the global simulation. The approximating of the

rescaling is one of the demerits of the rescaling method. Also, the significant spatial distance that is required in the recycling boundaries to help in de-correlate the solutions between inner and outer boundaries usually increasing the computational resources [116]. Enhancement and extension of the other recycling methods such as Extension of weak Recycling to Compressible Boundary layers, Extension of Weak Recycling to Rough Surface Boundary Layers and Extension of Weak Recycling to Environment Flows were reviewed in detail in [132].

3.4.2.2 Synthetic inflow turbulence generation method

Synthetic turbulence can be referred to as some form of disturbance that could be superimposed upon assumed steady flow profile at the inflow boundary [116]. These disturbances can be specified from analytical representation, sometimes from DNS data profile [132, 137, 133]. Implementation of this method, the flows characteristically reaches its equilibrium state downstream of the inflow. It should be noted that using this method, the construction of the computational domain is essential to allow simple alignment of the inflow conditions inlet plane [116]. An acceptable range of the disturbance values is required. Thus, if the values are too small, turbulence will not be generated or supported. Also, if the values are too large, it will result in unphysical flow behaviour [116].

In most cases, the simplest method to generate turbulence is to specify measured mean velocity distributions and to superimpose Gaussian random perturbations with the correct turbulent intensity, but this ignores the cross-correlation between velocity components (Reynolds stresses) and two-point correlation (i.e. spatial coherence) in real turbulence flow [113]. Jarrin [138] found that in synthetic inflow turbulence generation, the downstream distance of the inlet for realistic fluctuations to develop is 3000 wall units. However, [26] augured that the length of the upstream region to develop turbulence is impractical because the associated computational cost involved would outweigh that of the part in which is of interest.

Moreover, Xie and Castro [137] proposed an efficient digital-filter-based generation of inflow conditions that take into account to satisfy prescribed integral length scale and Reynolds-stress-tensor. It is a competitive class for the digital filtering method of the synthetic inflow turbulence generation [139]. The proposed inflow turbulence condition method accounts for the cross-correlation between Reynolds stresses and spatial coherence in real turbulence to some considerable extent. This method is one of the SDFM with an attractive feature of significantly reduces computational cost [132]. Kim et al. (2013) [26] slightly modified the inflow condition of [137] for an incompressible solver to satisfy the continuity equation in order the reduce artificial pressure fluctuation. The modification was necessary because the inlet 2D plane of the inflow turbulence generation method [137] produces artificial large pressure fluctuations causing some downstream effect. The reduction of

undesirable pressure fluctuation satisfies the divergence-free condition [26]. The divergence-free inflow condition is not commonly imposed in the SDFM, and the work of [26] provides a credible implementation [132, 133].

It should be noted that from an engineering point of view, the SDFM is more attractive to apply than the SRFM inflow turbulence generation because of its ability to impose a two-point spatial correction directly in the inlet plane compared to the SRFM which is done indirectly through an energy spectrum [132, 140]. Furthermore, the SDFM inflow turbulence generation is straightforward in implementation. Thus, these fascinating features of the SDFM for engineering applications are obtainable in [137, 26] inflow turbulence generators, and importantly, the significant reduction of computational cost makes them even more attractive [139] to apply for large-scale turbulence structures comparing to other inflow turbulence generators.

3.4.3 Wall conditions

In LES computation, the no-slip boundary condition is prescribed on the wall (aerofoil) in the computational domain. This condition is appropriate to use if the LES filtered $N-S$ equations (see Eq. 3.13a - c) are integrated with the wall, which requires fine grid cells near the wall. The wall resolution conditions for LES [116] are:

$$50 \leqslant \Delta x^{+} \leqslant 150,\ \Delta y^{+}_{Wall} < 1, 15 \leq \Delta z^{+} \leq 40 \tag{3.32}$$

The values in Eq. (3.32) are relevant for the "flat plate" configuration, the x^{+} direction is the streamwise, the y^{+} direction is normal to the wall is cross-flow, and the z^{+} direction is spanwise and assume to be homogeneous. These wall conditions could be adopted for aerofoils such as NACA 0012 since it is close to flat plate shape and theoretical concept.

3.4.3.1 Wall boundary layer theory

The boundary layer theory has a strong influence on mesh generation. It provides information for the turbulent layer boundary thickness, and the wall function, y^{+} can be estimated. The boundary layer thickness δ_c can be estimated theoretically for aerofoil chord (c) at small angle of attack as:

$$\delta_c = 0.37c(Re)^{-0.2} \tag{3.33}$$

The law of the wall state that the average velocity of a turbulence flow over a specific range is directly proportional to the logarithmic function of distance from

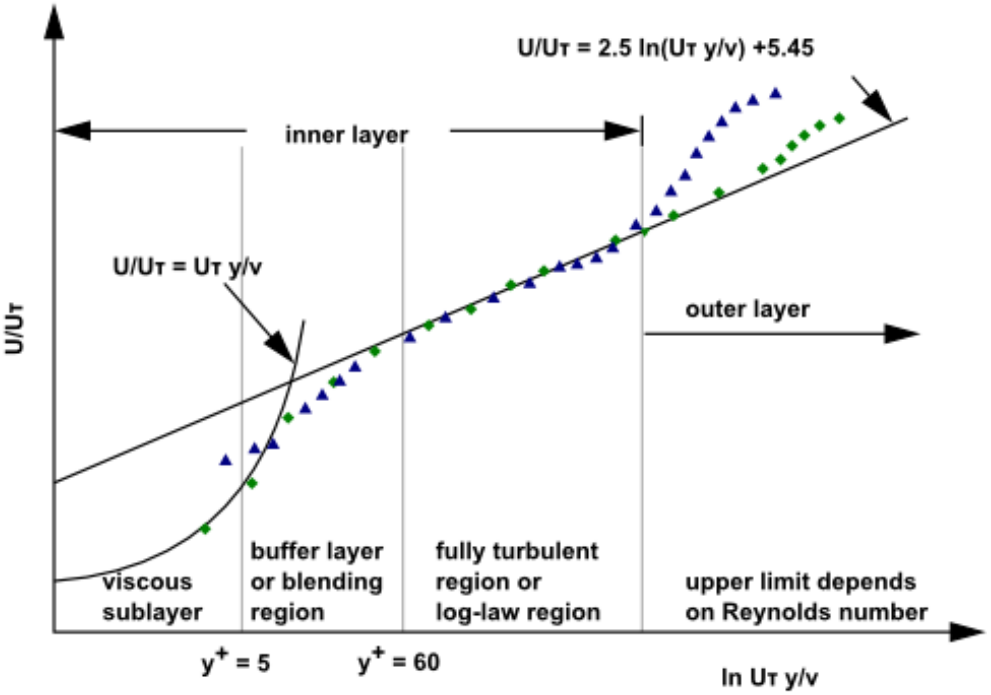

Figure 3.4: Turbulence boundary-layer and 'law of the wall' [18]

that point to the wall. Typically, the laminar and turbulent boundary layers are the two types of boundary layers that exist in fluid flow on a surface. The turbulent boundary layer is one of the interests, and it's categorised into three parts. This includes the viscous linear sub-layer, the log-law layer and the outer layer. Fig. 3.4 shows a pictorial view of the turbulent boundary layer velocity profile and the law of the wall.

3.4.3.2 Viscous sub-layer

The viscous sub-layer is the region where fluid at the wall is assumed to be stationary and turbulent eddy motion should, therefore, be zero. The viscous shear dominates this region near the wall ($y^+ < 5$) in the absence of turbulent shear stress effects. The shear stress is presumed to be equal to the wall shear stress throughout the layer, and these can be expressed linearly as:

$$u^+ = y^+ \tag{3.34}$$

where u^+ and y^+ are defined as:

$$u^+ = \frac{u}{u_\tau} \tag{3.35}$$

$$y_1^+ = \frac{u_\tau y_1}{\nu} \tag{3.36}$$

Similarly, the x^+ and z^+ are important as to the resolution of the turbulent boundary layer mesh quality as that of y^+, and they are defined as follows:

$$x_1^+ = \frac{u_\tau x_1}{\nu} \tag{3.37}$$

$$z_1^+ = \frac{u_\tau z_1}{\nu} \tag{3.38}$$

where:

y_1 - centre of the first cell height of wall.

x_1 - centre of the first cell distance at the streamwise direction of wall.

z_1 - the centre of the first cell distance at the spanwise direction of the wall.

u_τ - frictional velocity defined as $\left(\sqrt{\frac{\tau_w}{\rho}}\right)$

ν - kinematic viscosity

y_1^+ - the non-dimensional distance normal to the wall, similar for x_1^+ and z_1^+ for the stream-wise and cross-flow directions respectively.

The dimensionless quantities, u^+ and y_1^+, defines the velocity and vertical distance from the boundary layer, respectively. Thus, to estimate the frictional velocity theoretically, u_τ can be estimated for an aerofoil as:

$$u_\tau = \sqrt{0.0296 Re^{-0.2}} [141] \tag{3.39}$$

3.4.3.3 Log-law layer

Between the viscous sublayer and outer, there is a region where both the viscous and turbulence effects are dominant, which is between $y^+ \sim 30$ and $y^+ \sim 400$. The shear stress is assumed to be constant and equal to the wall shear stress and varying with increasing distance from the wall. The logarithmic relation of the wall is as follows:

$$u/u_\tau = 2.5 \mathrm{In}(\frac{u_\tau y_1}{\nu}) + 5.5 \, [18] \tag{3.40}$$

the values in Eq. (3.40) are constants.

3.4.3.4 Buffer layer

The buffer layer can be referred to as the transition region, $6 < y^+ < 30$. In this region, neither the viscosity nor Reynolds stresses is dominant, which the flow is very complex. Thus, there is no simple stress-strain relation founded. Any

computational simulation that the y^+ falls within this region gives a large number of errors.

Apart from the turbulent boundary layer theory, other vital factors to consider for high-quality mesh generation includes aspect ratio and orthogonal skewness. The aspect ratio (AR) of quadrilateral elements is a measure of the stretching of cell and is usually defined by $\frac{\Delta x}{\Delta y}$ (or the inverse relation depending, which one is above 1). An AR = 1 represents a perfect square, while an AR approaching zero represents a very irregular quadrilateral. Therefore, in LES, it is recommended to keep AR $\leq$ 20 in critical areas such as the aerofoil surface, AR = 1 around the leading and trailing edge. The skewness of a cell in the mesh can primarily affect the accuracy and destabilise the solution.

3.4.3.5 Dynamic mesh

The pitching motion on the aerofoil in the computational domain is initiate using the PimpleDyMFoam solver in OpenFOAM [142]. The PimpleDyMFoam solver is dictated for dynamic motion flow problems, whereas the PimpleFoam solver is for static flow simulation. Note that PimpleDymFoam solver shear the same algorithm characteristics with PimpleFoam without dynamic motion boundary condition.

The pitching motion of the aerofoil would be enabled by the use of the dynamic mesh technique for the mesh's cells in the near-aerofoil region to accommodate the deformation of the domain resulting from the aerofoil motion. In the PimpleDyM-Foam solver, the pre-defined sequence of dynamic mesh, which accommodates the aerofoil motion is controlled by recalculation of relative nodal positions at each time step according to a pre-defined boundary motion and diffusivity γ. The conservation equation of an arbitrary moving control volume V_C of a property ϕ can be expressed as:

$$\frac{d}{dt}\int_{V_C}\phi dV_C + \int_A d\mathbf{A}.(\mathbf{u_v} - \mathbf{u_b})\phi = \int_{V_C} \bigtriangledown.(\Gamma \bigtriangledown \phi)dV_C \tag{3.41}$$

Where $\mathbf{u_v}$ is the vertex velocity, $\mathbf{A}$ is the front surface area vector and $\mathbf{u_b}$ is the boundary velocity vector at the interface cell, and Γ is the diffusivity coefficient.

Therefore, When the vertex velocity, $\mathbf{u_v}$ of the control volume is specified, the local boundary velocity, $\mathbf{u_b}$ is obtained through interpolation. While, the Laplacian operator with a diffusivity, γ in Equation 3.42 [19] is used to control the vertex motion.

$$\bigtriangledown .(\gamma \bigtriangledown \mathbf{u_v}) = 0. \tag{3.42}$$

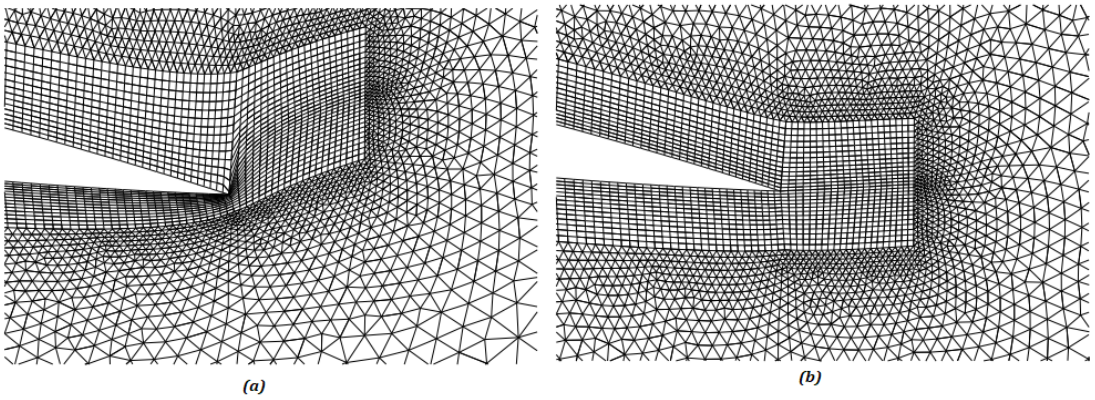

Figure 3.5: The impact of diffusivity, γ, on the mesh quality surround the trialling edge of a moving aerofoil. (a) γ = constant, (b) γ = quadratic [19].

Thus, the boundary conditions for Eq. 3.42 are calculated from the preceding boundary motion of the moving wall. Subsequently the vertex position at time $\mathbf{n+1}$ is updated using vertex velocity, $\mathbf{u_v}$

$$\mathbf{x^{n+1}} = \mathbf{x^n} + \mathbf{u_v}\Delta\mathbf{t}. \tag{3.43}$$

A constant diffusivity is used for a static mesh computation whereas, for a dynamic mesh computation, the diffusivity could be linear, quadratic or exponential; and it is dependent on the mesh quality surround the moving wall. Moreover, the diffusivity has a substantial effect on the mesh deformation. Jasak and Tukovic [19] examined the influence of the diffusivity on the mesh quality of the trailing edge of moving aerofoil. The various diffusivity investigated are:

$$\gamma = contant, \tag{3.44}$$

$$\gamma = \frac{1}{l}, linear; \tag{3.45}$$

$$\gamma = \frac{1}{l^2}, quadratic; \tag{3.46}$$

$$\gamma = e^{-l}, exponential, \tag{3.47}$$

where l is the cell centre distance to the nearest selected boundary. The study of [19] reported that the quadratic diffusivity, γ enhances the superiority of the mesh quality compared to the other types. For this reason, quadratic diffusivity is adopted for this current study. The constant and quadratic deformation, γ are depicted in Fig. 3.5.

3.5 XC and XCDF synthetic inflow generation for LES

As earlier mentioned in subsection 2.3.5 and later subsection of subsection 3.4.2. A synthetic inflow turbulence generation approach denoted as XC [137], imposes correlations using an exponential function to satisfy the prescribed space and time integral length scales. The XC synthetic inflow turbulence generation is a synthetic digital filtering method for LES with incompressible flow solvers.

3.5.1 XC synthetic inflow generation

The inlet velocities are defined as:

$$u_i = U_i + a_{ij} u_{*,j}, \tag{3.48}$$

where $i, j = 1, 2, 3$, u_i is an instantaneous velocity, which is imposed at the inlet boundary, U_i is a prescribed mean velocity, a_{ij} is a prescribed tensor (Eq. 3.49) and $u_{*,j}$ is an auto-correlated fluctuation satisfying the prescribed integral length scales, but with a zero mean, zero cross-correlations and a unit variance. Lund et al. [135] suggested a form of a_{ij}, using Cholesky decomposition of the prescribed Reynolds stress tensor, R_{ij}:

$$a_{ij} = \begin{pmatrix} \sqrt{R_{11}} & 0 & 0 \\ R_{21}/a_{11} & \sqrt{R_{22} - a_{21}^2} & 0 \\ R_{31}/a_{11} & (R_{32} - a_{21}a_{31})/a_{22} & \sqrt{R_{33} - a_{31}^2 - a_{32}^2} \end{pmatrix}. \tag{3.49}$$

This 3×3 matrix builds scaling and cross-correlations based on $u_{*,j}$ in Eq. (3.49). To impose correlations on random sequences, the XC approach employed an exponential function instead of a Gaussian function used in the early digital-filter based methods. This digital filter method was used to generate spatial correlations,

$$\psi_m = \sum_{j=-N}^{N} b_j r_{m+j}, \tag{3.50}$$

where $N = 2n$, $n = I/\Delta x$, is grid size and I is integral length scale. ψ_m is the intermediate velocity field and rj is a one-dimensional random number sequence with a zero mean and a unit variance. ψ_m is a one-dimensional number sequence with a zero mean, a unit variance and spatial correlations. Note that the subscripts, m, j , are the position indices. The model constant b, j is estimated as:

$$b_j = \frac{b_j^{'}}{\left(\sum_{l=-N}^{N} b_l^{'2}\right)^{1/2}} \text{ where } b_j^{'} = \exp\left(-\frac{\pi\,|j|}{2n}\right) \tag{3.51}$$

By applying Eq. (3.50) spatial correlations are generated on a two-dimensional space, defined as:

$$\psi_{m,l} = \sum_{j=-N}^{N} \sum_{k=-N}^{N} b_j b_k r_{m+j,\, l+k.} \tag{3.52}$$

Note that only one slice of 2D data, $\psi_{m,l}$, at each time step can be generated and it is correlated with the velocity at the previous time level using,

$$u_{*,i}(t+\Delta t) = u_{*,i}(t)\ \exp\ \left(-\frac{C_{XC}\Delta t}{T}\right) + \psi_i(t)\left[1-\exp\ \left(-\frac{2C_{XC}\Delta t}{T}\right)\right]^{0.5}, \tag{3.53}$$

where the model constant $C_{XC} = \pi/4$ and T is the Lagrangian time scale which is estimated using $T = I/U$. Thus, I is the turbulent integral length scale and U is the mean convective velocity. In Eq. (3.53) the subscript i denote a vector index, i.e. i = 1,2,3. The procedure in Eq. (3.53) effectively imposes an exponential correction in the streamwise direction. These Eqs. (3.48) - (3.53) are used to generate synthetic turbulence in the XC method [137]. Note that, the integral length scale, L_x, depend on each velocity component and direction as defined in Eq. (3.54). The correlation function modelled in the XC method is $C(r) = \exp\left(-\frac{\pi r}{2L_x}\right)$, but [26] suggested using a correlation function as $C(r) = \exp\left(-\frac{\pi r}{4L_x}\right)$. Since the integral length scale is defined as the enclosed area of the correlation function, using this give a better fit compared to XC, and this was implemented in the improved XC method [137], denoted as XCDF [26] and satisfies the divergence free condition.

$$L_{xij} = \int_0^{rij,0.1} C_i(r\hat{e}_j)dr, \tag{3.54}$$

The XC method generates synthetic inflow turbulence by using Eqs. (3.48) - (3.53). It should be noted that one attractive feature of this method is the use of exponential correlations in the streamwise direction, which significantly reduces the computational cost compared to the early digital filter-based approaches. XC method is a combination of the digital filter method and the forward stepwise methods and is also denoted Hybrid Forward Stepwise (HFS) approach [4].

As previously mentioned, Kim et al. [26] imposes the divergence-free condition of the XC inflow turbulent generation approach known as the XCDF. Furthermore, implementation of the XCDF inflow condition involves the insertion of synthetic turbulence fluctuations into the source term of the Poisson equation in one of the corrector steps after the predictor step of the PISO solver for the unsteady flows. Therefore, this model does not require solving for additional Poisson equations to achieve divergence-free conditions. These slight modifications of the modelling procedure and correlation functions improved, and it does not require additional CPU time to achieve this condition.

However, the limitation of the XCDF particularly, the maximum error at the inlet plane when the synthetic turbulence is imposed for the velocity, one order higher than the truncation errors, while the maximum error for the pressure is less than one order higher than the truncation error [26]. Nevertheless, the maximum error of the pressure is considered ineligible for the overall accuracy of the XCDF inflow condition method.

3.5.2 Justification for adopting the XCDF method of inflow turbulence generation

The current study aimed at modelling large energetic eddies impacting on a blade oscillating in the pitching motion. This involved generating streamwise integral length-scale $\geq$ the aerofoil chord length of $1c$ in the computational domain. Again, one of the main challenges confronting this research area is the difficulty to generate large energetic eddies $\geq$ 1 m in a conventional wind tunnel, or the enormous computational cost required to resolve all the energetic large eddies that convecting downstream and filter-out the small-scale structures using LES. Similarly, if DNS is considered for the simulation of the same turbulence scales as it was for LES. Then the already enormous cost of computational will increase exponentially because all the turbulence scales (large to small) will be wholly revolved, which can amount up to the order 10^{13} gird elements in the computational domain which is impractical considering the available computational resources.

In the bid to tackle this challenge, an inflow turbulence generation suitable for practical implementation for engineering applications without incurring additional computational cost is of utmost desire. Hence, in that case, the XCDF inflow turbulence condition for LES and incompressible solver offers a plausible implementation. Apart from being a very efficient method, its ability to impose two-point spatial correction and Reynolds-stress-tensor directly in the inlet plane [132] justifies its suitability for the current engineering research problem.

Moreover, the XCDF satisfies the divergent-free condition. On the whole, the adoption of the XCDF inflow turbulence generation to apply for the present study is a decision researched based on the critical comparative review conducted by [132] over inflow turbulence generation methods. Likewise, the XCDF was applied to various engineering problems such as peak loading and surface pressure for high rise buildings, long-span bridge aerodynamics, free-stream turbulence on the dynamic stall for wind turbine aerodynamics and 2D LES study of heaving wing aerodynamics by researchers, which includes Daniels et al. (2013 and 2015) [131, 143], Kim and Xie (2016) [4], and Wang and Xie [129] respectively with good agreement with results in the literature.

3.6 Chapter summary

The governing equations, filtering concepts, sub-grids scale modelling, initial condition, boundary conditions, inflow turbulence conditions for LES were discussed in detail to give a background and clear understanding of turbulence and its modelling procedures.

The combination of the LES method with the synthetic inflow turbulence generation method (e.g. XCDF) for the execution of the overall research objectives is promising. Adopting the XCDF inflow turbulence condition for the current study is due to its attractive features discussed in Subsection 3.5.2, and its applicability for engineering flow problems is justified in the Subsection.

The XCDF is carefully applied for the execution of the current research project objectives stated in Section 1.2, while the challenges discussed in Section 2.4 are taken into cognisance. All computations are carry-out and supported with the University of Southampton super-computer **Iridis4** and the UK super-computer **Archer.**

The next chapter introduced the mesh design and construction, mesh sensitivity study and LES sub-grid (SGS) model verification and validation.

Chapter 4

Mesh generation, preliminary sensitivity study and LES subgrid models verification

4.1 Introduction

The solutions to a flow problem - velocity, pressure, aerofoil aerodynamic characteristics are defined at a nodal point inside each cell. The accuracy of a CFD solution is governed by the number of cells in the mesh. In general, the larger the number of cells, the better the solution accuracy. However, as the number of cells in the mesh increases, the cost of computer resources of the calculation increases. Haven these in mind, painstaking design and construction of the domain mesh is inevitable.

This chapter presents the mesh generation, preliminary sensitivity study for the meshes and LES subgrid stress (SGS) models verification. Large-eddy simulations are performed in the 2D and 3D flow domains to rigorously test the independence of the meshes and to verify different LES SGS models. To kick-start, the research numerical works of the LES methodology and its conditions discussed in Chapter 3. This was applied during the design and construction of the computational domain meshes and the specification of the appropriate boundary conditions as well. These preliminary steps and crucial activities of the CFD method are presented in Section 4.2.

Firstly, static aerofoil in 2D LES is used to commence the preliminary mesh sensitivity study. Secondly, the SGS models verification are presented in Sections 4.3 and 4.4 respectively. The surface force coefficients on aerofoil surfaces (e.g. pressure coefficient (C_p) and skin-friction coefficient (C_f)) are quantities to be the focus for determining a high-quality mesh and a suitable SGS model for the current study. In addition, the aerodynamic forces - lift, drag and moment coefficients

were analysed, for further verification of the SGS model selection, also presented in Section 4.4. Thirdly, a mesh convergence test in 3D LES was conducted for the spanwise z - direction on different domain span lengths, presented in Section 4.5.

Finally, concluding remarks and the chapter summary are presented in Section 4.6.

Part of this work was presented in a conference paper by **T.E. Boye** and Z.T. Xie , UK Fluids, University of Cambridge, 27th -29th August 2019 [47], and European Turbulence Conference (ETC), Torino, Italy, 3rd - 6th September 2019 2019 [48].

4.2 Mesh generation

The mesh generation and domain construction are crucial parts of CFD simulations. There must be high-quality cells with a high mesh density surrounding the aerofoil to capture critical flow physics in the turbulent boundary layer region. The high denser mesh around the aerofoil surface must be fine enough to extend to the wake region at the trailing edge to capture the small eddies in the wake region. This is more critical for LES, which requires high resolution to resolve the grid-size eddies spatially in the domain and to satisfy the LES wall resolution conditions as discussed in Subsection 3.4.3.

Due to the simplicity of the geometry (aerofoil - a cross-section of a wind turbine blade), the structured mesh strategy is used for the mesh generation inside the domain. Construction of the C-mesh type - a hybrid of O-mesh type and H-mesh type, is developed for the computation. The use of this C-mesh is due to the advantage that it has an O-mesh type upstream to ensure high-quality mesh at the curvature of the aerofoil and H-mesh type downstream in the wake region. Therefore, this makes the mesh resolve well effectively by producing low skewed cells when the mesh transit from O-mesh type to H-mesh type on the aerofoil surfaces and also have high-quality mesh in the wake region. In most cases, the hybrid C-type mesh is adequate for laminar inlet simulations. However, a C-type mesh superimposed on an H-type mesh domain is best for applying turbulence inflow conditions [116].

The hybrid C-grid mesh is used for the static aerofoil mesh sensitivity test and the mesh is denoted as static mesh test (SMT). As a result, a mesh denoted as SMT_{2D} is generated for the 2D LES computation details in (Table. 4.1) of the preliminary convergence study. It is to be noted that grid 'static' denoted as ST_{2D2} in (Kim, 2013)[25], also detailed in Table 4.1 was adopted as the reference 2D LES data. Because, mesh ST_{2D2} resolution around the aerofoil surfaces is much higher compared to current SMT_{2D}. This approach is to enhance the effectiveness and efficiency of the mesh sensitivity study to minimise computational cost.

Table 4.1: Summary of the computational domain size in-unit c of the chord length with the number of grid points for the static 2D aerofoil. N_{up} and N_{low} are the number of points in the suction and pressure side of the aerofoil, respectively. N_R, N_W and N_z, denotes the number of points in the inlet radius, wake and spanwise direction respectively. R, W and Z denotes the radius of the inlet, wake and spanwise length, respectively. Mesh ST_{2D2} adopted from [25].

	SMT_{2D}	ST_{2D2}
R/c	20	22
W/c	33	33
Z/c	n/a	n/a
N_R	234	200
N_W	125	66
N_{up}	367	733
N_{low}	193	211
N_z	1	1

4.2.1 Domain meshing for smooth inflow simulation

Generation of the hybrid C-mesh for the static 2D aerofoil was in Pointwise V18.0R1 - an advanced meshing software suitable to design and construct structured and unstructured meshes. In Pointwise work-space: first, a NACA 0012 geometry is generated with the aid of a customised script capable to generate most NACA aerofoil profiles. The required number of points (see Table. 4.1) are distributed systematically around the upper and lower surfaces of aerofoil geometry for meshing and generating structured cells in the domain.

Figure 4.1 (a) shows an example of hybrid C - H type structured mesh constructed and Fig. 4.1 (b) shows a sketch of the computational domain (not to scale) and the partition of multiple blocks of structured mesh. Table 4.1 shows more details of the domain mesh. The domain radius R is split into two parts - the inner (near the airfoil) and outer parts. The length of the former is c forms a sub-C-block around the aerofoil and is discretised into 100 points for current mesh SMT_{2D}. The centre of the first cell from the wall (aerofoil) y_1 is calculated with the LES wall conditions (Subsection 3.4.3) in mind. The discretisation of the domain radius R in the outer C-block region is further stretched with 134 points for mesh SMT_{2D}. The aerofoil is rotated to assume a geometric angle of attack 10° at the domain origin, which is within the twisted angles for most twisted blades of wind turbine [73]. The aerofoil chord length $c = 1$ m. BC1, BC2 denoted the inlet boundary, while BC3, BC4 for the outlet boundary shown in Fig. 4.1 (b).

These processes involved in the mesh generation in Pointwise is not trivial. However, adequate for the construction of O-grid to H-grid hybrid mesh-type. The mesh quality such as cell skewness, aspect ratio, grid point and distribution were

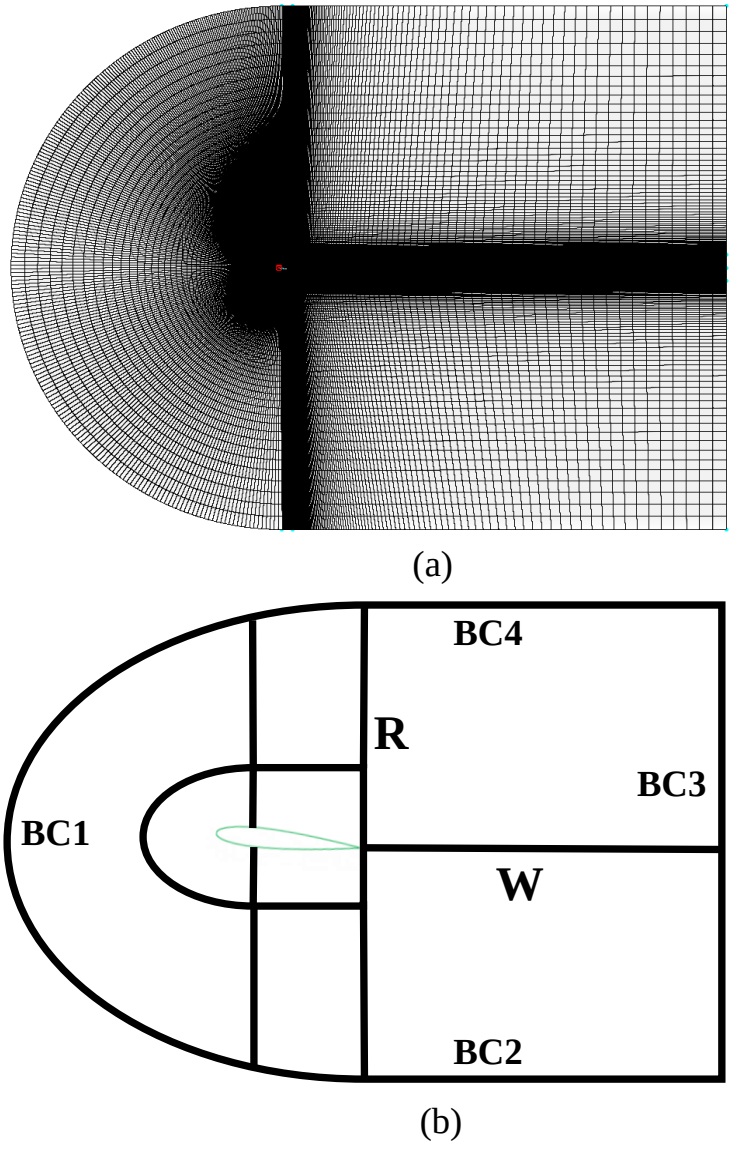

Figure 4.1: (a) Hybrid C - H type mesh, (b) a sketch of computational domain (not to scale) and the partition of multiple blocks of structured mesh. R: domain radius, W: wake length. BC1, BC2, inflow boundary condition. BC3 and BC4, outflow boundary conditions. More in Table 4.2

carefully checked and examined using the robust quality check features available in pointwise V18.0R1.

The grid growth/expansion ratio is 1.05 for mesh SMT_{2D}. The maximum boundary layer thickness (Eq. 3.33) at the trailing edge of mesh SMT_{2D} was estimated to be $0.038c$ at zero degree angle of attack. The centre of the first grid point is placed at $y_1 = 3 \times 10^{-4} c$ near both of the leading edge and trailing edge, which correspond to $y_1^+ \leq 2.1$ using (Eq. 3.36). In critical areas such as near the aerofoil surfaces, the grid aspect ratio $\Delta x/\Delta y \leq 10$ is ensured in mesh SMT_{2D}. For mesh

ST_{2D2} [25] the first off-wall grid point was placed at $y_1 \approx 1{\times}10^{-4}c$ near the leading edge and $y_1 \approx 3{\times}10^{-4}c$ near the trailing edge.

4.3 Numerical settings / mesh convergence test in 2D static aerofoil

The mesh sensitivity tests to check the independence of the meshes (detailed in Table 4.1) of the numerical solutions is conducted. A Reynolds number $Re = 1.35 \times 10^5$ based on the chord length c, freestream velocity U_∞ and kinematic viscosity ν, was applied for the static aerofoil simulation. The time step $\triangle t$ was set to 3×10^{-4}, which satisfied the condition of the mean courant number $(CFL) = \frac{U_\infty \triangle t}{\triangle x} \leqslant 1$, where $\triangle x$ is the smallest cell in the streamwise direction of the grid. The boundary conditions were applied, as shown in Fig. 4.1 (b) and detailed in Table 4.2. The no-slip boundary condition is imposed on the aerofoil surface. The time-averaging was performed approximately over $25T$ for mesh SMT_{2D} case, where $T = n\triangle t/c$, where c is the chord length, n is the number of time step. For the reference mesh ST_{2D2} [25] averaging was conducted over $10T$.

The transient incompressible solver in OpenFOAM 2.3.0 is used, and the PIMPLE algorithm is employed for the pressure-velocity coupling. The decision to use the PIMPLE algorithm is based on its robustness and efficiency. This algorithm combines the SIMPLE and PISO algorithms capable of accommodating a larger time-step, for example, if $CFL > 1$. Also, a second-order implicit scheme is applied for the temporal discretization, and the bounded second-order (Gamma) differencing scheme (γ) a hybrid scheme developed by Jasak et al. (1999) [144] is used for the convective term.

The Gamma differencing scheme (γ) is a blending between upwind differencing (UD) and the central differencing (CD) schemes [144]. To establish a smooth transition, the blending between from UD and CD should be used over the interval $0 < \tilde{\phi}_c < \beta_m$. The γ factor has been selected to vary linearly between $\phi_c = 0$ and $\phi_c = \beta_m$ according to:

$$\gamma = \frac{\tilde{\phi}_c}{\beta_m} \tag{4.1}$$

where β_m is a constant of differencing scheme, approximated to 0.16 [145]. $\tilde{\phi}$ is the local convective scalar. More details of the Gamma differencing scheme (γ) in [144].

Again, to save CPU time, the mesh convergence test in the streamwise and crosswise directions were performed in the 2D domain without the SGS model (see Subsections 3.3.1 and 3.3.3). Setting the SGS model constant to zero in this case of mesh SMT_{2D}, which is to ensure similar settings to that of the reference mesh ST_{2D2} [25]. To obtain reasonable convergence of the numerical solutions of the

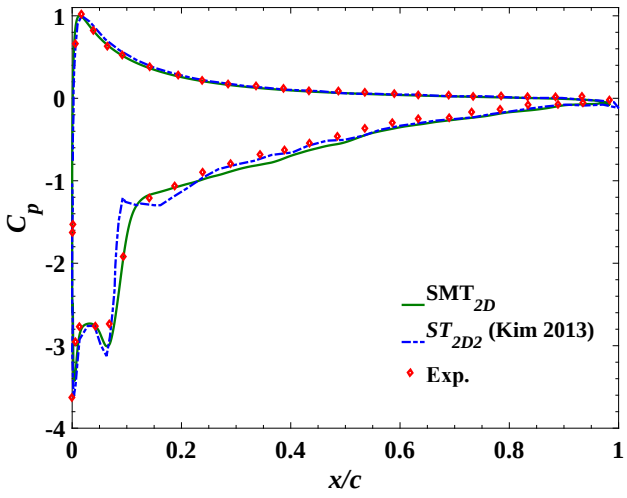

(a)

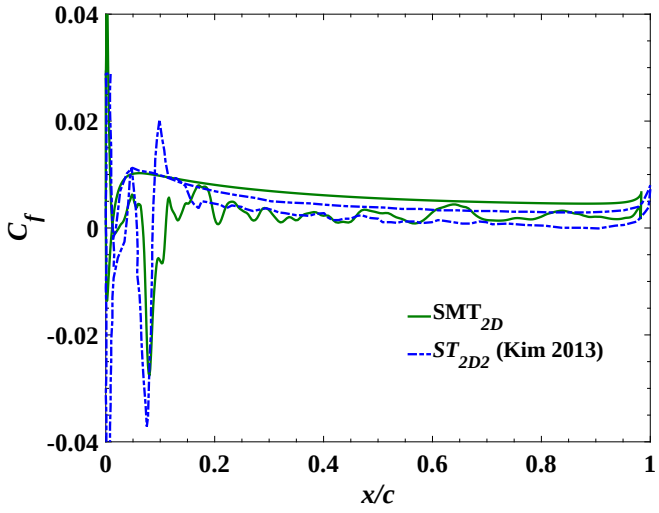

(b)

Figure 4.2: The effect of resolution on the aerofoil surface force. (a) Pressure coefficients, (b) skin friction coefficients, 2D static aerofoil at $\alpha = 10°$, Exp. [20].

Table 4.2: Summary of the boundary conditions (**BC**) for the 2D static aerofoil. U_∞ is the free stream velocity, and $\partial/\partial n$ is the derivative to the boundary.

BC1	**BC2**	**BC3**	**BC4**
$u_i = U_\infty$, $\partial p/\partial n = 0$	$u_i = U_\infty$, $\partial p/\partial n = 0$	$\partial u_i/\partial n = 0$, $p = p_\infty$	$\partial u_i/\partial n = 0$, $p = p_\infty$

mesh SMT_{2D} comparable to that of the reference case mesh ST_{2D2}, the number of grid points were increased until the surface force coefficients converge to the reference data in simulations.

Figure 4.2 shows the pressure and skin-friction coefficients for mesh SMT_{2D} case, referenced ST_{2D2} case [25] and experimental data [20], they have very good agreement with each other. This is vital to carry out further sensitivity study using the mesh for case SMT_{2D} to examine the effect of SGS models on the numerical solutions.

4.4 LES SGS model sensitivity study and validation in 2D static aerofoil

Due to the influence of SGS models on the numerical results for LES discussed in Section 3.3. It is imperative to conduct a sensitivity study for different SGS models to objectively select an SGS model to demonstrate more confidence in the adopted SGS model of the current LES study. The SGS model sensitivity study involves the verification of two SGS models, which includes the smagorinsky model [117] and the Mixed time scale (MTS) model [127], and a test case (SMT_{2D}) without an SGS model. The model constant for that Smagorinsky model test case was $Cs = 0.065$, which is slightly lower than $Cs = 0.1$ for channel flow as suggested by [121] while that of the MTS model were $C_{MTS} = 0.03$ and $C_T = 10$, a modified model constants by Krishnan et al. (2009) [146].

It is expected that a suitable SGS model and high-quality mesh should be capable of predicting very well the laminar separation bubble reattachment and the transition point phenomena over the aerofoil suction surface at 10° incidence at a moderate Reynolds number $Re = 1.35 \times 10^5$. In addition, this would provide a framework to choose an SGS model that has less effect on the numerical solutions. This is important because the aim of this research work focuses on the modelling of a wing in pitching motion usually involves a complex flow phenomenon such as dynamic stall, which is associated with highly unsteady flows, boundary layer flow separation, series of vortices generation. In addition, the leading edge vortex interacts with incoming large-scale eddies. These are crucial physical flow fundamentals to capture. The study of the dynamic stall in smooth inflow and large-scale inflow turbulence are presented in the proceed chapters.

It should be noted that the numerical settings for all the SGS model test cases are similar to that of the mesh SMT_{2D} case in Section 4.3. To obtain the mean aerodynamic forces, averaging started once the lift coefficient reached a statistically converged state and time-averaging was conducted over $25T$. The similar boundary conditions of case SMT_{2D} shown in Fig. 4.1 and Table 4.2 are imposed on all of

the SGS model test cases. In emphasis, mesh SMT_{2D} was used for the different SGS test cases that were studied.

4.4.1 Discussion of SGS model contribution to the numerical solution

Figure 4.3 shows the verification and validation of the pressure coefficient Cp and skin-friction coefficient Cf for the different SGS model test cases. The pressure coefficients Cp in Fig. 4.3 (a) show that the MTS SGS model case (SMT_{2D} MTS model) and case without SGS model (SMT_{2D} without SGS model) match very well with each other except that of the Smagorinsky SGS model (SMT_{2D} Smagorinsky model). Both SMT_{2D} without SGS model and SMT_{2D} MTS model have a good agreement with the experimental data [20].

The peak of the separation bubble near the leading edge of the aerofoil at $x/c \approx 0.1$ shown in Fig. 4.3 (a) for cases SMT_{2D} without SGS model, SMT_{2D} Smagorinsky model and SMT_{2D} MTS model have a percentage difference of 7.14%, 17.64%, and 0.71% respectively, compared to that of the reference data [20]. The little discrepancy seen between experimental data and the SMT_{2D} MTS model case is due to the effect of the SGS viscosity, which does not affect the case SMT_{2D} without the SGS model. The difference of the peak Cp between case SMT_{2D} without SGS model and that of case SMT_{2D} MTS model is 6.4% while the SMT_{2D} Smagorinsky model differ by 26% compared to the SMT_{2D} without SGS model.

The large discrepancy seen in the separation bubble peaks between SMT_{2D} smagorinsky SGS model compared to those of case SMT_{2D} without SGS model and SMT_{2D} MTS model is attributed to the excessive SGS viscosity (νSGS) dissipation [121] near the aerofoil surfaces. Thus, suppressing the separation bubble significantly and under-predicts the peak of the separation bubble in case SMT_{2D} smagorinsky SGS model (see Fig. 4.3 (a)). The 6.4% difference seen between case SMT_{2D} MTS model and SMT_{2D} without SGS model is small compared with SMT_{2D} smagorinsky SGS model. This implies that the MTS SGS model dissipates much less νSGS near the aerofoil surface, which confirms the observation in the literature. Badoe et al. (2019) [147] showed that the MTS model is preferable to wall adapting eddy-viscosity (WALE) model because it dissipated the νSGS near the wall region gives a more accurate prediction. It should be noted that the 2D LES predictions of SMT_{2D} without the SGS model and SMT_{2D} MTS SGS model match very well with the experimental data because the laminar separation bubble for the static aerofoil at α 10° is a quasi-2D structure.

Figure 4.3 (b) shows the effects on the skin-friction coefficients Cf distribution around the aerofoil. The predicted reattachment points of the separation bubble near the leading edge for cases SMT_{2D} without model, SMT_{2D} smagorinsky model and SMT_{2D} MTS model were at $x/c = 0.12$, 0.18 and 0.11 respectively. It is to be

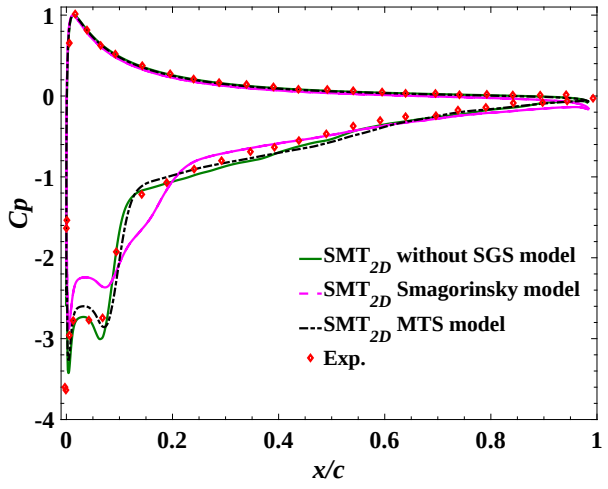

(*a*)

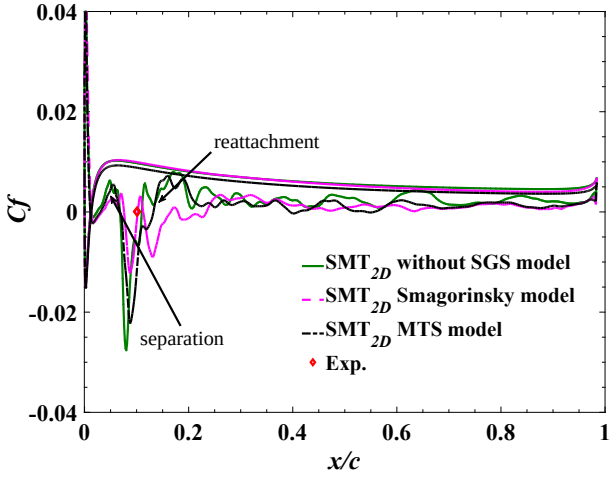

(*b*)

Figure 4.3: The effect of SGS models. (a) pressure coefficients, (b) skin friction coefficients, 2D static aerofoil at $\alpha = 10°$, Exp. [20].

noted that the SMT_{2D} MTS model predicted the reattachment point very closer to that of the reference data at $x/c = 0.1$ [20].

Table 4.3: Verification of SGS models effects on the aerodynamic performance of the static aerofoil at $\alpha = 10°$. The subscript ave. and max donates the averaged and maximum lift, drag coefficients and lift-to-drag ratio.

Case	$C_{Lave.}$	C_{Lmax}	$C_{Dave.}$	C_{Dmax}	$C_{Lave.}/C_{Dave.}$
SMT_{2D} without SGS model	0.87	1.04	0.055	0.0873	15.81
SMT_{2D} Smagorinsky model	0.813	1.04	0.075	0.117	10.84
SMT_{2D} MTS model	0.876	1.08	0.058	0.093	15.10

The aerodynamic performance of the static NACA 0012 aerofoil at 10° angle of attack is shown in Table. 4.3, which includes the averaged and maximum coefficients of lift, drag and lift-to-drag ratio for all SGS models tested in the section. The averaged lift-to-drag ($C_{Lave.}/C_{Dave.}$) shown in Table 4.3 provided swift insight into the aerodynamic performance of the static aerofoil for the different LES SGS models. For the case of SMT_{2D} smagorinsky model, the $C_{Lave.}/C_{Dave.}$ indicates a low aerodynamic performance compared to the other two cases, which is attributed to excessive turbulence dissipation near the wall. This is a typical characteristic of the Smagorinsky SGS model for wall-bounded flow in the literature.

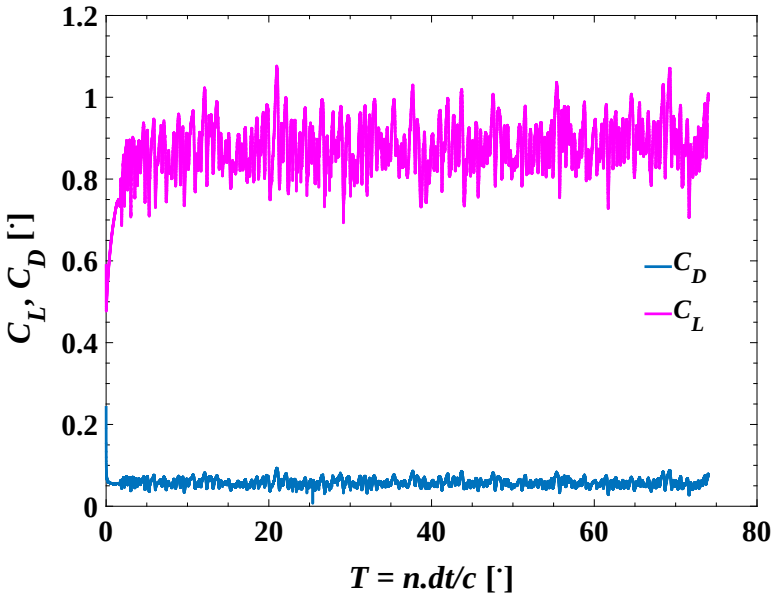

Figure 4.4: Time history coefficients of lift and drag at $\alpha = 10°$, mesh SMT_{2D} and MTS SGS model. T is the number of flow pass-through, n is the number of time step (dt or $\triangle$t), simulation time step normalised with the chord length (c).

The time history of a converged lift and drag coefficients for case SMT_{2D} MTS SGS model is shown in Fig. 4.4.

Figure 4.5 shows snapshots of the instantaneous streamwise velocity, pressure, and mean streamwise velocity and pressure contours for mesh SMT_{2D} MTS model. It is evident that the mesh SMT_{2D} MTS model can adequately capture the critical aerodynamic phenomena on the suction side of the aerofoil surface. The separation bubble near the leading edge is well captured on both the streamwise instantaneous and mean - velocities as well as pressure contours.

Figures 4.6 and 4.7 shows snapshots of a two-dimensional instantaneous vorticity structures and a section of the velocity streamlines respectively, of the static aerofoil at $\alpha = 10°$. The reverse flow in the boundary layer that started from the trailing edge is well observed in Fig. 4.6, and the separation bubble near the

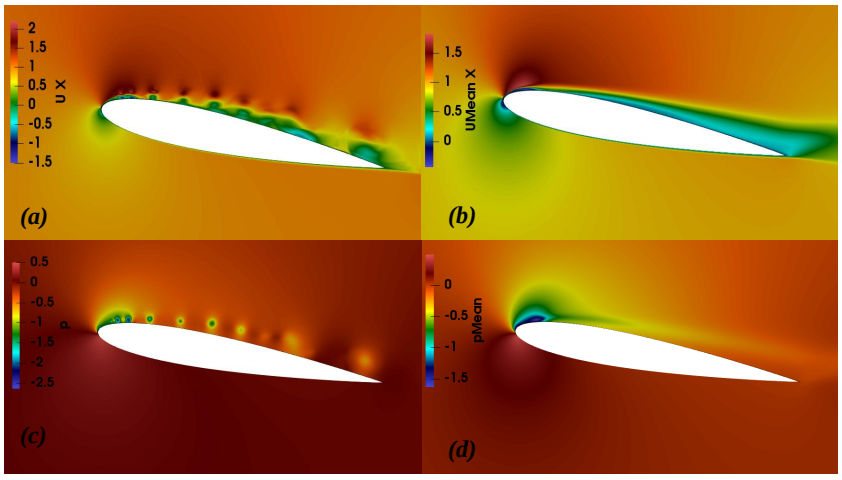

Figure 4.5: (a) instantaneous streamwise velocity , (b) mean streamwise velocity , (c) Instantaneous pressure distribution and (d) mean pressure distribution. $Re = 135,000$ at $\alpha = 10°$, mesh lift and drag at $\alpha = 10°$, mesh SMT_{2D} MTS model.

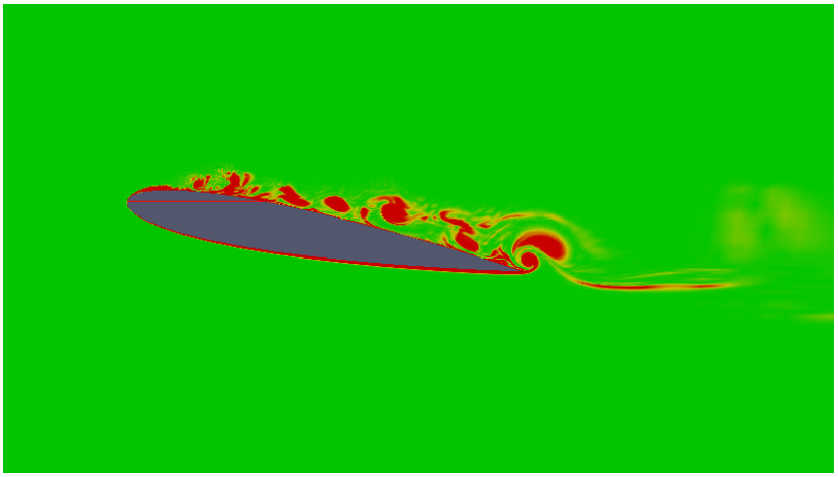

Figure 4.6: Instantaneous vorticity at $Re = 135,000$ and $\alpha = 10°$, mesh SMT_{2D} MTS model.

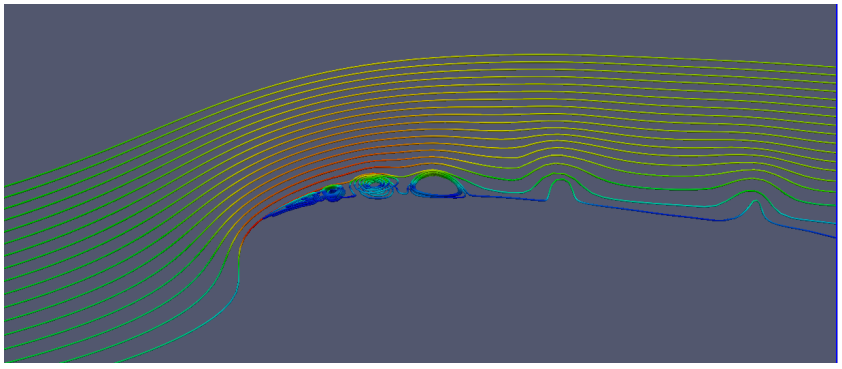

Figure 4.7: 2D LES: Streamline of the Instantaneous vorticity magnitude at the leading edge of the NACA 0012 at $Re = 135,000$ and $\alpha = 10°$, mesh SMT_{2D} MTS model.

leading edge of the aerofoil is evident in Fig. 4.7. This is an indication that the boundary layer is adequately resolved both in streamwise and crossflow directions of mesh SMT_{2D}, which is vital to further study for a three-dimensional (3D) mesh with spanwise resolution.

4.5 Mesh convergence test in 3D static aerofoil

The 3D simulations for static aerofoil at $\alpha = 10°$and a similar $Re = 135{,}000$ was conducted for the spanwise resolution sensitivity test. The same numerical settings and boundary conditions in Table 4.2 used in the preceding section were adopted for the 3D simulations. On the lateral sides of the domain, the periodic boundary condition is imposed. The MTS SGS model is adopted for the large-eddy simulations in this section. The coordinates x, y, and z with the origin at the leading edge of the aerofoil represented the streamwise, crossflow and spanwise directions, respectively.

The mesh SMT_{2D} was extruded in the spanwise z direction with 30 and 60 grid points to generate meshes SMT_{3D1} and SMT_{3D2} respectively. For meshes, SMT_{3D1} and SMT_{3D2} the centre of the first cell near the aerofoil surface (mesh SMT_{2D}) was reduced to $y_1 = 2 \times 10^{-4}$ at both the leading and trailing edges, which correspond to $y_1^+ \approx 1.43$. Again, mesh SMT_{2D} was extruded in the spanwise z direction with 30 and 60 grid points to generate another set of mesh e.g., SMT_{3D3} and SMT_{3D4}, respectively. The details of the meshes grid points used to resolve the 3D computational domains are summarised in Table 4.4.

Table 4.4: Summary of the computational domain size in-unit c and the number of grid points for 3D static aerofoil. N_{up} and N_{low} are the number of points in the suction and pressure side of the aerofoil, respectively. Note N_z is the number of points in the spanwise direction. R, W and Z are the radius, wake and spanwise length respectively. y_1^+ is the non-dimensional height centre of the first cell normal to the aerofoil surface.

	SMT_{3D1}	SMT_{3D2}	SMT_{3D3}	SMT_{3D4}
R/c	20	20	20	20
W/c	33	33	33	33
Z/c	0.5	0.5	0.5	0.5
y_1^+	1.43	1.43	2.14	2.14
N_R	234	234	234	234
N_W	125	125	125	125
N_{up}	367	367	367	367
N_{low}	193	193	193	193
N_z	30	60	30	60

To obtain the mean aerodynamic forces averaging started once the lift coefficient attained a statistically converged solution, and the time-averaging was performed

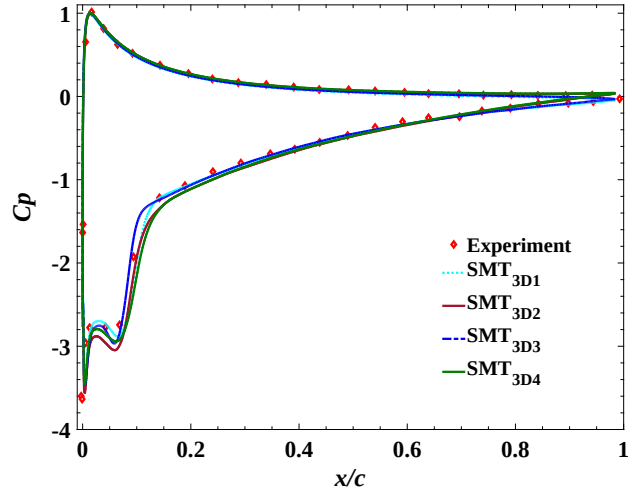

(*a*)

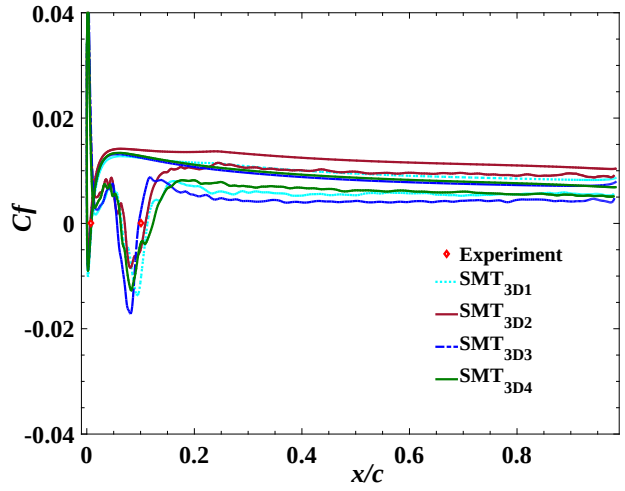

(*b*)

Figure 4.8: 3D LES mesh sensitivity test for static aerofoil: effect of wall normal resolutions (y_1^+) and spanwise resolution. (a) Pressure coefficients, (b) skin friction coefficients. $Re = 135,000$ and $\alpha = 10°$, Exp. [20].

over $15T$. The spanwise average was conducted to obtain the aerofoil pressure coefficient and skin friction coefficient in this section.

Figure 4.8 shows the effect of the spanwise and y_1^+ resolutions on the pressure coefficients Cp and skin-friction coefficients Cf for all cases SMT_{3D1}, SMT_{3D2}, SMT_{3D3} and SMT_{3D4}. Fig.4.8 (a) shows that all the cases of the pressure coefficients Cp have very good agreements with the experimental data [20]. An average of 5% difference is obtained between the LES data (Cp_s) and experimental measurements. Fig. 4.8 (b) shows the skin-friction coefficients Cf for all cases, and the reattachment points agrees reasonably to that of the experimental data

reattachment point. Nevertheless, SMT_{3D3} produced a better prediction of the reattachment point at $x/c = 0.09$, which is very closer to the reference data at $x/c = 0.1$ compared to the other mesh cases. This results in an average of 10% difference.

It can be concluded that the effect of resolutions in the spanwise direction and wall-normal resolutions on the pressure coefficients Cp and skin friction coefficients Cf of static aerofoil for all the 3D-domains cases are small compared to the reference data in the study.

4.6 Chapter summary

The grid sensitivity study conducted objectively identified the suitability of mesh SMT_{2D} streamwise and crossflow directions resolutions are of high quality and capable of capturing important flow physics for the current study. The mesh SMT_{2D} is a hybrid C-H type mesh that fit for flow simulation with a laminar inlet (smooth flow). The turbulence boundary layer theory for the wall conditions was applied for the design and construction of mesh SMT_{2D} that ensures the non-dimensional first cell height normal to the wall (aerofoil) y^+ is placed within the viscous sub-layer region. Appropriate boundary conditions were imposed on the inlet, outlet and lateral sides of the computational domains.

The 2D LES simulations were conducted to study the effect of mesh resolutions and different SGS models on the aerodynamic forces of a NACA 0012 static aerofoil. To develop a high-quality mesh and to select an adequate SGS model for the LES study. It was found that mesh SMT_{2D} is of high quality and was used for the SGS model sensitivity test. The MTS SGS model produced a better prediction of the separation bubble peak with 0.71% of the pressure coefficient and the reattachment point with 9% of the skin-friction coefficient compared to the wind tunnel measurementS at Reynolds number Re = 135,000 and angle attack $\alpha = 10°$.

Furthermore, the analysis of the aerodynamic performance of the different SGS models sensitivity test showed consistently high performance of the MTS SGS model with an average lift-to-drag ratio of 15.10 compared to the Smagorinsky SGS model with an average lift-to-drag ratio was 10.84. The Smagorinsky SGS model low performance was attributed to excess turbulence dissipation near the aerofoil surface. The discrepancy between the case without SGS model and the MTS SGS model was attributed to the difference in SGS viscosity (νSGS) treatment of both models. Therefore, this study shows that the effect of the MTS SGS model on the numerical solution is significantly less than the Smagorinsky SGS model.

The mesh SMT_{2D} was used to generate 3D meshes by extrusion in the spanwise direction to study the effect of the resolution in domain span. Four new 3D meshes

were generated and used to study the effect of the spanwise and near-wall resolutions. They are denoted as SMT_{3D1}, SMT_{3D2}, SMT_{3D3} and SMT_{3D4} respectively. Their spanwise averaged pressure coefficients and skin friction coefficients have good agreement with the reference data. This implies that the effect of spanwise resolutions of all the 3D simulations is of good quality compared to the reference data. Nevertheless, mesh SMT_{3D3} and SMT_{3D4} predicted very close pressure coefficients and skin-friction coefficients compared to the reference data. These meshes will be further explored in the next chapter.

Indeed, the grid sensitivity study and LES SGS model verification and validation have delivered high-quality meshes, and the identification of a less dissipative SGS model (MTS model) that can be used to simulate highly unsteady flows such as dynamic stall of a wing or aerofoil oscillating in pitching motion in the proceed chapters.

Chapter 5

Smooth inflow: Aerodynamics of a pitching wind turbine blade at high reduced frequencies

5.1 Introduction

In recent decades researchers and engineers have shown growing interest in studying flows around wind turbine blades to improve their performance. The study in this chapter focused on the effect of various pitching frequencies induced on wind turbine blade sections at different span locations. Unsteady flows over wind turbines affect performance and yield crucial aerodynamic phenomena such as dynamic stall, which is the significant stall delay beyond the static stall point of aerofoils or wings [5, 21]. The dynamic stall is associated with a series of vortices generated, shed or reattached. A wing or aerofoil in pitching motion is a common example used to model the dynamic stall phenomenon for a wind turbine.

The review in Chapter 2, Subsubsection 2.2 highlights that a complete understanding of the effect of reduced frequency on the dynamic stall is urgently needed, in particular for high pitching frequency and amplitude. In addition, the growing interest in modem HAWT promotes studies on the effect of a high reduced frequency close to the blade structure frequencies [32].

Therefore, this chapter aims to understand the interaction of the pitching motion of a wind turbine blade at high reduced frequencies and the generated large vortices. In particular, high pitching frequencies (e.g., reduced frequencies, $k_{\text{red}} = 0.2$ to 0.4.) are studied, within the frequency range of the unsteadiness of flows around the rotating wind turbine blade at different blade span locations, and close to some of the blade structure frequencies. The mean angle of attack $\alpha_0 = 10°$, and high pitching amplitude $\alpha_1 = 15°$. It was found that such research is scarce in the literature. To the best of the author's knowledge, the efficiency and effectiveness

of 2D LES for the highly unsteady flows are validated with the 3D LES results and wind tunnel measurements for the first time.

5.1.1 Outline of this chapter

In this chapter, the author numerically investigated the effect of high reduced frequencies on the aerodynamics of a pitching aerofoil under a deep dynamic stall at a moderate Reynolds number. The numerical settings is presented in Section 5.2. Firstly, the author verified the 2D LES approach rigorously compared with the 3D LES results and validated with other numerical data and wind tunnel measurements in the literature, which were reported in Sections 5.3 and 5.4 respectively. Secondly, 2D and 3D LES of aerodynamic coefficients for $k_{\text{red}} = 0.2$, 0.3 and 0.4 at high amplitude $\boldsymbol{\alpha_1} = 15^\circ$ were carried out and presented in Section 5.5. Finally, the author analysed the effect of reduced frequency on aerodynamic coefficients, the LEV structure, the local boundary layer and the dimensionless vortex shedding frequency (i.e. Stroual number, $St = fc/U_\infty$) in the Subsections of Section 5.5. The conclusions and scientific contributions of this chapter are summarised in Section 5.6.

Part of this work was presented in a conference paper by **T.E. Boye** and Z.T. Xie, UK Fluids, University of Cambridge, 2019 [47], and European Turbulence Conference ETC, 2019 [48]. The results of this chapter were also reported in a scientific paper by **T.E. Boye** and Z.T. Xie, "Aerodynamics of a pitching wind turbine blade at high reduced frequencies", Journal of Wind Engineering and Industrial Aerodynamics, vol. 223, 104935, 2022 [49].

5.2 Numerical settings

The governing equations are the unsteady filtered incompressible Navier-Stokes equations (see Eq. 3.13a-c), and it is re-written in Einstein's notation in this chapter:

$$\frac{\partial \bar{u}_i}{\partial x_i} = 0 \tag{5.1}$$

$$\frac{\partial \bar{u}_i}{\partial t} + \frac{\partial \bar{u}_i \bar{u}_j}{\partial x_j} = -\frac{1}{\rho}\frac{\partial \bar{p}}{\partial x_i} + \frac{\partial}{\partial x_j}\left(\nu \frac{\partial \bar{u}_i}{\partial x_j} - \tau_{ij}^r\right), \tag{5.2}$$

where '¯' denotes a filtered quantity, $\bar{u}_i$ the filtered velocities, $\bar{p}$ the filtered pressure, ρ the density, and ν the kinematic viscosity. τ_{ij}^r is the subgrid-scale (SGS) stress tensor, and is modelled below:

$$\tau_{ij}^r = \overline{u_i u_j} - \bar{u}_i \bar{u}_j \tag{5.3}$$

$$\tau_{ij}^{r} = -2\nu_t \bar{S}_{ij} + \frac{1}{3}\delta_{ij}\tau_{kk}, \tag{5.4}$$

where the Kronecker delta $\delta_{ij} = 1$ for $i = j$, otherwise $\delta_{ij} = 0$; ν_t is the SGS viscosity, and $\bar{S}_{ij}$ is the rate-of-strain tensor for the resolved scales defined by

$$\bar{S}_{ij} = \frac{1}{2}\left(\frac{\partial \bar{u}_i}{\partial x_j} + \frac{\partial \bar{u}_j}{\partial x_i}\right). \tag{5.5}$$

Recall the outstanding performance of the mixed-time scale (MTS) SGS model [127] in the SGS models verification and validation in Chapter 4, subsection 4.4. Hence, the MTS SGS model is thus adopted. The MTS model was used for simulations of flows past a pitching aerofoil [4] and a bluff body [131].

5.2.1 Adopted numerical settings

Figure 5.1 illustrates the pitching NACA 0012 aerofoil at various phase angles. The pitching pivot is placed at $0.25c$ from the leading edge of the aerofoil. The pitching motion is described in Eq. 5.6,

$$\alpha(t) = \alpha_0 + \alpha_1 sin(\omega t), \tag{5.6}$$

where $\alpha_0 = 10°$ is the mean angle of attack, $\alpha_1 = 15°$ is the pitching amplitude, ω is the aerofoil angular velocity, and t is the time of the aerofoil pitching motion.

A Reynolds number $Re = 1.35 \times 10^5$ based on the chord length c, freestream velocity U_∞ and kinematic viscosity ν, was used in the current work. It is within the range of Reynolds number for small and medium wind turbines. The primary reason for choosing NACA0012 aerofoil at this Reynolds number is because of the rich available published data [e.g. 21, 4, 22]. For 3D simulations with the viscous-sublayer resolved, the number of grid points for a problem at a Reynolds number one order of magnitude greater than the current used one, is more than two orders of magnitude greater than the current number of grid points 10^7 (Table 5.2), considering that the required number of grid points is proportional to $Re^{\frac{9}{4}}$ as discussed in subsection 2.3.1.1. This is not practical for a 3D LES of modelling a pitching wind turbine blade. For dealing with such flows at a much larger Reynolds number, it was explore in this study the capability of 2D LES, which is much computationally cheaper than 3D LES and intrinsically more accurate than URANS.

[148] showed that the aerodynamic performance (e.g. lift-to-drag ratio) transition of a steady aerofoil takes place at the critical Reynolds number 70,000, at which the lift-to-drag ratio increases more than one order of magnitude. At a greater Reynolds number, such an increase is much smaller. The Reynolds number used in

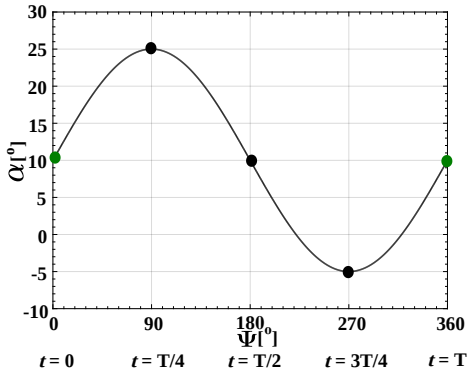

(a)

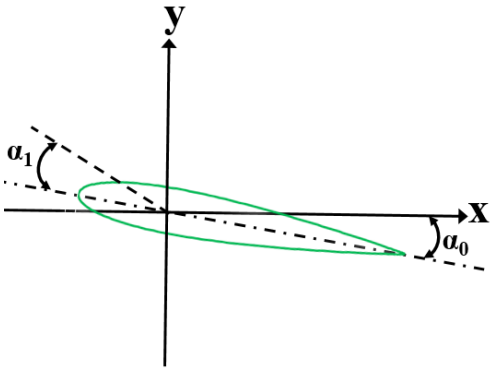

(b)

Figure 5.1: A sketch of pitching aerofoil motion. (a) the angle of attack (α) as a function of phase angle (Ψ), where t is the time, T is the period of the pitching cycle. (b) a pitching aerofoil at neutral position (see Eq. 5.6).

the current study is twice the critical Reynolds number, and one would not expect a significant change of aerodynamic performance beyond this Reynolds number.

Horizontal axis wind turbines (HAWT) aerofoils are typically thick and cambered. Nevertheless, [149] reported that the effect of the shape of a pitching aerofoil does not appear to be dominant over the pitching motion for the dynamic stall. [5] reported that the dynamic stall hysteresis loops for both chambered and symmetric aerofoils are very similar.

There are few published papers on the Reynolds number effect on pitching aerofoil. It is to be noted that [150] is on a ramp-type pitching motion, which is in a rotation speed starting from a statistically stationary solution with zero angular velocity to an eventual constant angular velocity. The rotation speed is "nearly 0.35 convective time unit (c/U_∞) per degree of rotation", which is extremely slow and more a quasi-stationary motion. In these settings, it is perhaps not surprising that

Table 5.1: Parameters of pitching aerorfoil

Profile	NACA 0012
Re	1.35 $\times 10^5$
α_0	10°
α_1	15°
k_{red}	0.1, 0.15, 0.2, 0.3 and 0.4

that the results show the sensitivity of the dynamic stall process to investigated Reynolds numbers 0.2×10^6, 0.5×10^6, 1.0×10^6.

Most published papers [e.g. 89, 90, 91, 151, 92] on this topic investigate periodically pitching motion of an airfoil, which differs substantially from [150]. The fluid dynamics of the former is affected by the preceding oscillation cycles, whereas the latter is affected more by the turbulent transition, which is dependent on the Reynolds number. [89] tends to agree that the effect of Reynolds number on two-dimensional oscillating airfoils is small. [90] state that the effect of Reynolds numbers in these problems is of secondary importance. [91] conclude that "average thrust estimates based on the DPIV data (Reynolds number 1,100) confirm the trends established by the force and power experiments at Reynolds number 40,000". [92] compare the data at Re numbers 10^5 and 10^6, and state that the same physic processes are observed. These confirm that the Reynolds number effect on a periodically pitching airfoil is of secondary importance, assuming the pitching motion is not too slow, e.g. $k_{\text{red}} \geq 0.1$. Further research should be pursued in what conditions the Reynolds number effect is important for these problems.

Therefore, the data generated in the current study is beneficial for fundamental research, and can be used as reference data for the study of pitching wind turbine blade at much higher Reynolds numbers. Table 5.1 shows the five reduced frequencies that were examined in this chapter.

Considering the robustness and efficiency, the PIMPLE algorithm of OpenFOAM 2.3.0 was employed for the pressure-velocity coupling in LES [142], with two outer iterations, and three pressure correctors. A second-order implicit scheme was used for the temporal discretization, and the bounded Gamma differencing scheme [144] was used for the convective term. The time step Δt was set to 9.5×10^{-4} s that satisfied the mean courant number $CFL \leq 1$ and the maximum $CFL \leq 3$ for all the cases simulated. The pitching periods for reduced frequencies $k_{\text{red}} = 0.1$, 0.15, 0.2, 0.3 and 0.4, are respectively $T = 31.41$ s, 20.94 s, 15.7 s, 10.47 s and 7.85 s, resulting in a very small ratio $\Delta t/T$ ranging from 3.02×10^{-5} to 1.21×10^{-4}. It is to be noted that the time step used in the current study is 1/5 of that in [4] for the same reduced frequency $k_{\text{red}} = 0.1$. Given that these data and the previous work show a time step convergence, hence it would not be necessary to carry out further sensitivity tests for time step.

The dynamic mesh technique [19], discussed in Subsection 3.4.3.5 was adopted for wing/aerofoil pitching motion in the simulation, which allows the deformation of the grid cells in the near-wall (aerofoil) region resulting from the aerofoil motion. To be specific, the setting of the quadratic diffusivity, $\gamma = \frac{1}{l^2}$ (Eq. 3.46) was applied for local deformation of grid cells in the near-aerofoil region because, it's enhances the superiority of the mesh quality [19], where l is the cell centre distance to the nearest selected boundary.

5.2.2 LES in a 2D flow domain for pitching aerfoil

Albeit it has limits, the 2D LES approach can be useful for highly unsteady flow problems [152], because it is fast and inexpensive compared to 3D LES [153]. Bouris and Bergeles [152] reported that the 2D LES demonstrated high-quality results than URANS for modelling large-scale quasi-2D flow passing a square cylinder.

Flow around a pitching aerofoil in a deep stall at an angle of attack $\alpha \geq 20°$can be considered being more similar to that around a bluff body than a thin aeofoil. Badoe et al. [154] reports that the LEV of an heaving aerofoil at the pre-stall angle of attack resembles quasi-2D, while 3D structures begin to emerge as the aerofoil approaches the post-stall angle of attack. This could support applying 2D LES for pitching aerofoil. Nevertheless, little is reported in the literature for application of 2D LES of a pitching aerofoil. Thereby it is of great interest to assess the effectiveness of 2D LES, e.g. through a comparison with 3D LES for this application.

5.3 Baseline simulations

Figure 4.1a Subsection 4.2.1 shows an example of hybrid C - H type structured mesh constructed in Pointwise V18.0R1. Fig. 4.1b also in Subsection 4.2.1 shows a sketch of computational domain (not to scale) and the partition of multiple blocks of structured mesh, while Table 5.2 shows more details of the domain and the mesh. Note that the mesh SMT_{2D} in Chapter 4 is denoted as mesh M1 a in this chapter.

The mesh convergence test was conducted using three 2D meshes denoted M1, M2 and M3, and three 3D meshes that were extruded in the spanwise z direction from the 2D mesh M1, denoted $\mathrm{3DM}_1$, $\mathrm{3DM}_2$ and $\mathrm{3DM}_3$ (details in Table 5.2). The first grid height $y_1 = 3.0 \times 10^{-4}c$, which corresponds to $y_1^+ = 2.1$, with a cell size growth ratio 1.05, 1.035 and 1.037 for M1, M2, and M3 respectively. The maximum boundary layer thickness at the trailing edge was estimated (Eq. 3.33) to be $0.038c$ at zero degree angle of attack. In critical areas such as near the aerofoil surfaces, the grid aspect ratio $\Delta x/\Delta y \leq 10$ is ensured in all meshes.

Table 5.2: A summary of the computational domain size in unit c and number of grid points for the pitching aerofoil. R, W and s are the radius, wake and span lengths respectively (Fig. 4.1). N_{up} and N_{low} are number of points in the suction and pressure sides of aerofoil respectively. N_z denotes the number of points in the spanwise direction of the 3D meshes. C_T denotes total number of cells in the domain. Note: **M1**, **M2** and **M3** are 2D while **3DM1**$_1$, **3DM1**$_2$ and **3DM1**$_3$ are 3D dynamic meshes.

	M1	**M2**	**M3**	**3DM1**$_1$	**3DM1**$_2$	**3DM1**$_3$
R/c	20	20	20	20	20	20
W/c	33	33	33	33	33	33
s/c	n/a	n/a	n/a	0.5	1.5	3
N_R	234	234	234	234	234	234
N_W	125	125	125	125	125	125
N_{up}	367	519	733	367	367	367
N_{low}	193	272	384	193	193	193
N_z	1	1	1	60	60	120
C_T	186,528	240,120	315,752	11,005,152	11,005,152	22,196,832

The computational domain and the 2D mesh of M1 were extruded in the spanwise direction z for $0.5c$, $1.5c$ and $3c$, discretised into 60 (3DM$_1$), 60 (3DM$_2$) and 120 (3DM$_3$) points respectively. Note that the resolution of these 3D meshes in the cross-wing directions was slightly greater than that in [4] and the smooth flow mesh in [22], while the spanwise resolutions of 3DM$_2$ and 3DM$_3$ were similar to the 'PC5' mesh in [4], and that of 3DM$_1$ was close to the smooth flow mesh in [22] For mesh 3DM$_1$, it is the same as mesh SMT$_{3D3}$ in Chapter 4.

The mesh sensitivity study was carried out at reduced frequency $k_{\text{red}} = 0.1$. The aerofoil neutral position was set geometrically at $10^\circ \uparrow$ in the domain. The symbols '$\uparrow$' and '$\downarrow$' denote the pitching-upstroke and pitching-downstroke motion respectively. The maximum y_1^+ is less than 5, which occurs approximately at the stall angle, where the LEV detaches from the aerofoil upper surface.

Appropriate boundary conditions (BCs) are imposed on the computational domains shown in Fig. 4.1(b) also in Subsection 4.2.1. No-slip boundary conditions are imposed on the aerofoil surface. Inflow boundary conditions were imposed on boundaries BC1 and BC2. Outflow boundary conditions were imposed on boundaries BC3 and BC4. Symmetric boundary conditions were imposed on the lateral boundaries, which substantially speeded up the simulations compared to using periodic boundary conditions. This might not be surprising as the former yielded more narrow band matrices for solving a set of linear equations in the implicit scheme, and confirmed the same concluding remark in [155]. [4] argued that simulations of pitching aerofoil were much less sensitive to the lateral boundary conditions compared to those of a static one, because the flows were more dominant by the pitching motion.

It should be noted that the symmetry boundary condition was used for the 3D simulations only because period boundary conditions (cyclic) settings were difficult to implement for dynamic mesh simulations of pitching motion of an aerofoil in OpenFoam 2.3.0. An alternative to the cyclic boundary condition known as Arbitrary Mesh Interface (cyclicAMI) was successfully implemented on the pitching-aerofoil dynamic mesh but caused the simulations to run extremely slow. This is due to updating the flow fields of previous deformed cells to the following deforming cells at the lateral sides of the domain during the aerofoil motion. These procedures of the cyclicAMI reduce the speed of the simulation over 100 times compared with the symmetry condition.

The significant inefficiency of the cyclicAMI boundary observed using the pimpimDynFoam for the pitching aerofoil motion made the symmetry condition the best computational-cost effective option despite its inherent attributes. Furthermore, given that the final chosen span of the domain was three times chord, any effects of the lateral boundary conditions were smaller than those on flows around a shorter span blade [e.g. 4, 22].

5.3.1 Mesh sensitivity study - 3D dynamic mesh

The 2D simulations were initialised for ten cycles of oscillation Fig. 5.2 (a), while the 3D simulations were initialised for one cycle of oscillation only, because after the first cycle the peak-to-peak changes of the lift hysteresis loop curves were insignificant from cycle to cycle shown in Fig. 5.2 (b), this was because the aerodynamic forces were calculated over the span in a high resolution, as well as in the chord direction. The subsequent twenty-four cycles of 2D simulations and three cycles of 3D simulations were used for the post-processing. These time durations for the 3D simulations were respectively the same as those in [4, 22]. It is to be noted that the span lengths of the wind turbine blade in $3DM_2$ and $3DM_3$ were respectively twice and triple of that in the 'PC5' mesh [4] and the smooth flow mesh [22].

The $3DM_3$ settings were used for most of the simulations in the study, and were expected to yield better-converged data than those in the previous research in the literature. It was observed that the deviation between the phase-averaged lift hysteresis loop and those individual cycles was small for most phase angles at k_{red} = 0.1 and 0.2 (Fig. 5.3). The phase-averaged quantity at a phase angle (i.e. Ψ, Eq. 5.6) is that calculated from averaging the data at the same phase angle from all periodic cycles of pitching motion.

Figure 5.4 shows the effect of the mesh resolution on the phase-averaged lift (C_L), drag (C_D) and moment (C_M) coefficients. The cases M1, M2 and M3 show no evident difference of the force coefficients in the upstroke and downstroke. The difference is about 1% at the peak region near the maximum angle of attack,

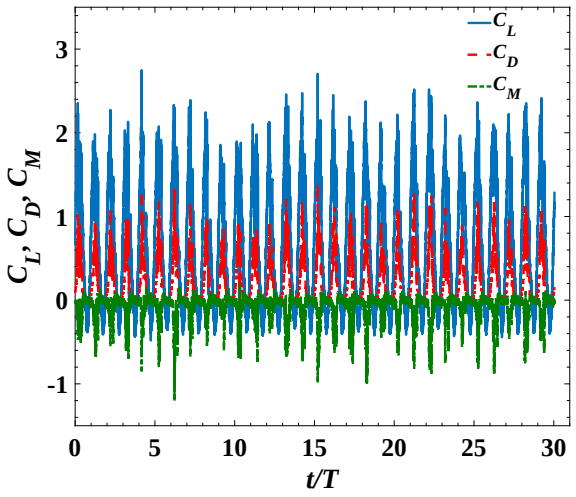

(*a*)

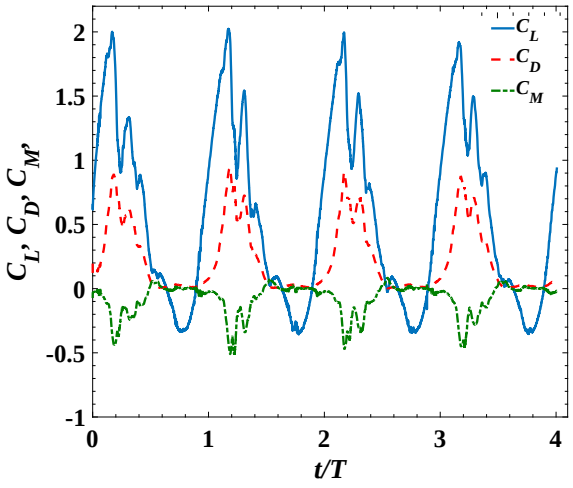

(*b*)

Figure 5.2: Number of pitching cycles of the aerodynamic force coefficients. (a) 2D simulation mesh **M1**, (b) 3D simulation mesh $3DM_2$. T is Time-period per cycle and t is run-time.

and is within 2.5% at $\alpha \geq 20° \downarrow$. Overall, the 2D results are independent of the resolutions in cases M1, M2 and M3.

The cases $3DM_1$, $3DM_2$ and $3DM_3$ in Fig. 5.4 show a reasonable comparison with a maximum difference 12% at $\alpha \approx 17° \downarrow$. This could be owing to the different resolutions in the spanwise direction, and the shorter phase-averaging compared to the 2D cases. The difference between the peak values near the maximum angle of attack is within 3%. The difference between the cases $3DM_3$ and $3DM_2$ is much smaller than with the case $3DM_1$. Indeed, an crucial conclusion from the mesh sensitivity tests is that the mesh in $3DM1_3$ is fine enough, and span length $3c$ in $3DM1_3$ is great enough to accommodate chord-length scale eddies. Thereafter, M1

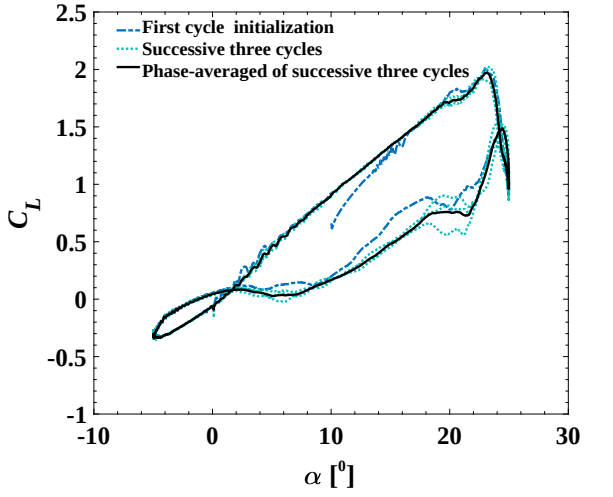

(a)

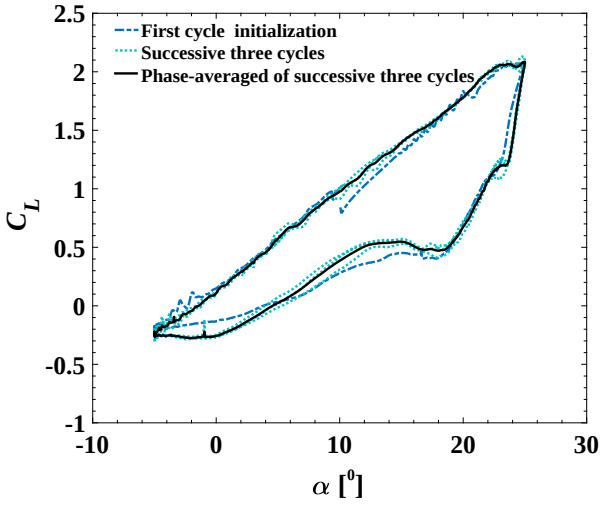

(b)

Figure 5.3: The first initialisation cycle, the successive three cycles, and the phase-averaged lift hysteresis loop. (a) $k_{\text{red}} = 0.1$ (mesh 3DM_2), (b) $k_{\text{red}} = 0.2$ (mesh 3DM_3).

and 3DM1_3 settings were adopted respectively for 2D and 3D simulations for the rest of the study.

Figure 5.4 shows evident differences in peak lift coefficients near the maximum angle of attack and during the downstroke regime between the 2D and 3D cases. This is attributed to the fact that the 2D cases do not account for the large eddy (e.g. LEV) variation across the span at a high angle of attack. The LEV, which dominates the dynamic stall at $k_{\text{red}} = 0.1$, forms and detaches earlier in 2D cases compared to 3D cases. Overall, 2D simulations produced a good prediction for the linear region during the upstroke, produced fair dynamic stall phenomena, and yielded a greater lift coefficient during the downstroke.

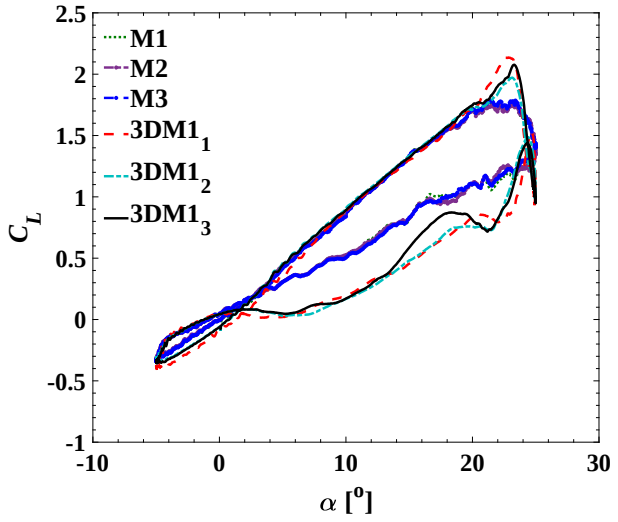

(*a*)

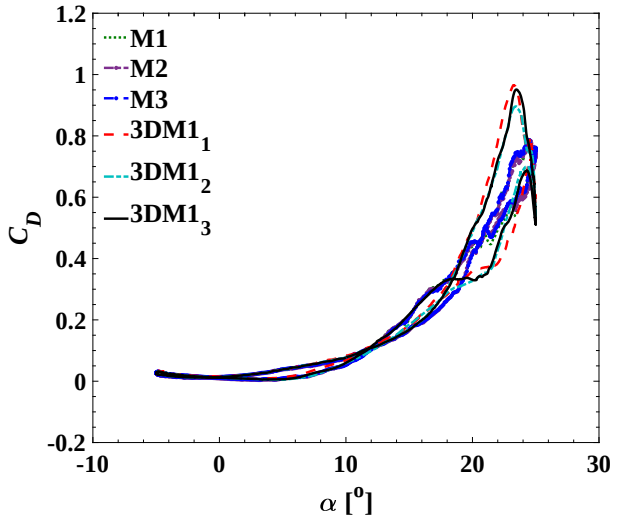

(*b*)

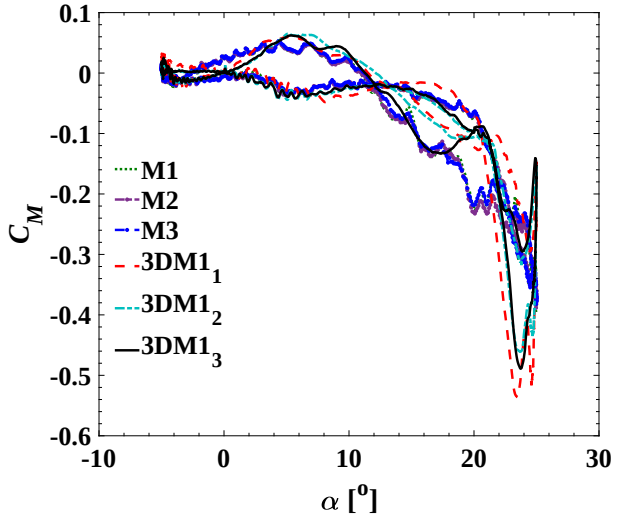

(*c*)

Figure 5.4: Verification of mesh resolution at $k_{\text{red}} = 0.1$. (a) Lift, (b) drag, (c) moment coefficients.

The differences of the drag and moment coefficients between the 2D and 3D simulations are small, with an exception at the stall angle. It is to be noted that the 2D LES results are slightly better than the 2D URANS data in [63]. Again, for dealing with genuine unsteady flows, the URANS approach is only valid and therefore accurate for those having an evident gap in the power spectrum between the large non-turbulent unsteadiness and turbulent eddies, whereas the 2D LES approach does not have this constraint. The 2D LES does not resolve the flow details in the spanwise direction, however gains a speedup more than one order of magnitude faster than the 3D LES. In summary, the 2D LES is potentially a compromise when both resolving the shed quasi two-dimensional vertices and computational efficiency are of interest.

Table 5.3: Average aerodynamic coefficients per pitching cycle, $k_{red} = 0.1$.

Mesh	C_{Lave}	C_{Dave}	C_{Mave}
M1	0.66	0.23	-0.083
M2	0.66	0.23	-0.085
M3	0.66	0.23	-0.083
$3DM1_1$	0.58	0.23	-0.078
$3DM1_2$	0.57	0.23	-0.079
$3DM1_3$	0.56	0.23	-0.077

Table 5.3 shows the averaged aerodynamic coefficients per pitching cycle for both the 2D and 3D simulations of all the meshes. The difference between the 2D averaged lift, drag and moment coefficients (C_{Lave}, C_{Dave}, C_{Mave}) and those of the 3D results are averagely 14.64%, 0% and 6.21% respectively. Overall, the effect of mesh resolution on the averaged aerodynamic force coefficients per pitching cycle is small by comparison between the 2D meshes and those of the 3D meshes.

5.4 Validation for a pitching aerofoil at different reduced frequencies

Table 5.4 shows the specifications of the validation cases. Figure 5.5 shows comparison of aerodynamic coefficients between the present simulations and the reference LES [22] and experiment [21] at $k_{red} = 0.1$. The present 3D results agree very well with the reference LES predictions [22]. They are also in good agreement with the wind tunnel measurements [21], except for the lift and moment at maximum $\alpha \uparrow$ and at $\alpha \geq 20°\downarrow$.

It is to be noted that the moment is based on the pitching pivot at $0.25c$ from the LE, where is the force centre of an aerofoil is usually located. This means that the moment coefficient is usually very small and extremely sensitive to any small variation of aerodynamics. This is confirmed in Fig. 5.5 (b) for $\alpha \leq 20°\uparrow$. At the

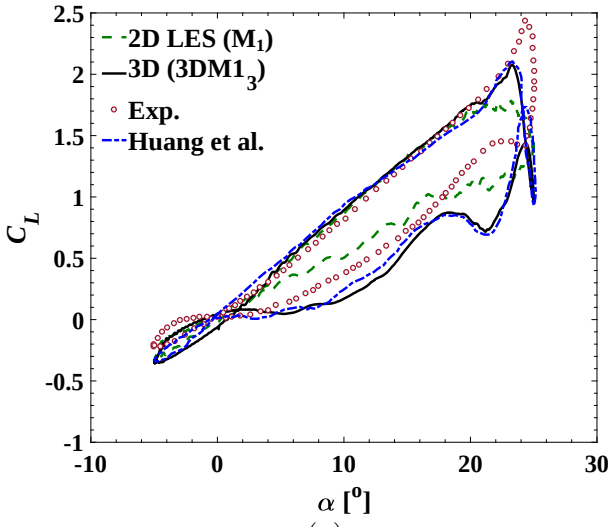

(*a*)

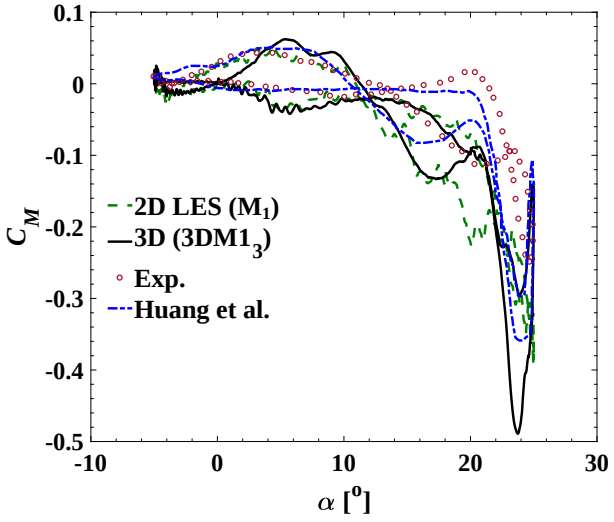

(*b*)

Figure 5.5: Phase averaged aerodynamic forces at $k_{\mathrm{red}} = 0.1$. (a) Lift coefficient, (b) moment coefficient. Exp., experimental data [21], Huang et al, LES data [22].

Table 5.4: Settings of validation cases. WT, wind tunnel; LES, large-eddy simulations.

References	**Aerofoil**	$k_{\mathbf{red}}$	*Re* **& Methods**
Lee and Gerontakos [21]	NACA0012	0.1	1.35 $\times 10^5$ WT
Sharma and Poddar [23]	NACA0015	0.15	2.0 $\times 10^5$ WT
Huang et al. [22]	NACA0012	0.1	1.35 $\times 10^5$ LES

stall angle $\alpha = 23°\uparrow$, the C_M suddenly drops to the lowest peak and immediately recovers to a 'normal' small absolute value (also see Fig. 5.13), due to an LEV having grown to mature and shed. This could yields large oscillating torsional force of the wind turbine blade.

The present 3D LES predicted the LEV shed at $23°\uparrow$, which was similar to the LES data in the literature [4, 156, 157, 22]. However, the experiment [21] predicted the LEV shed at nearly 25°. This leads to a visible difference in the aerodynamic coefficients between the experimental data and the present LES data and the numerical data in the literature [4, 156, 157, 22]. Kim and Xie [4] explain that this discrepancy is likely due to the technique limit in the experiment, in particular for high reduce frequencies (i.e. $k_{\text{red}} \geq 0.1$). [21] stated that "the effect of the length of the Tygon tubing was a simple time constant delay on all pressure signals with frequency above 2.95 Hz, which rendered a limited reduced frequency k_{red} of 0.0993 at $U_1 = 14ms^{-1}$ or Re $= 1.35 \times 10^5$ in the present experiment".

Figure 5.5 also shows the 2D LES predictions of the aerodynamic coefficients for $k_{\text{red}} = 0.1$. The lift hysteresis loop at the linear region agrees well with the experimental measurements and 3D LES data except at the maximum peak lift coefficient. Also, a discrepancy is evident in the early part of the downstroke. This is because at the maximum angle of attack and in the early stage of downstroke, the separated flow (e.g. the shed LEV) is more three dimensional compared to at smaller angle of attack. It was noticed that the 2D LEV peaks at a high angle of attack in the hysteresis loop varied more evidently from cycle-to-cycle in the time series (see Fig. 5.2 (a)) compared to the 3D data. This perhaps is not surprising as in the 2D LES any pressure distribution in the chord-wise direction is forced to be identical in the spanwise direction, whereas in the 3D LES at the maximum angle of attack the pressure distribution is not uniform but more random. 30 cycles for phase average of 2D LES data largely improve the convergence of the phase average; on the other hand, the long-term average smooths out the peak lift. The 2D LES predicts the dynamic stall angle approximately at $23°\uparrow$, which is consistent with those of the 3D LES data in Fig. 5.5.

Figure 5.6 shows a comparison of the lift and moment coefficients at $k_{\text{red}} = 0.15$ between the present 2D and 3D LES and that of experimental data [23]. Both the 2D and 3D LES data of lift C_L and moment C_M are in a reasonable agreement with the experimental data. The C_L for the 3D LES case indicates similar phenomena of the first and second LEVs shed in the early stage of downstroke at reduced frequencies, $k_{\text{red}} = 0.1$ (Fig. 5.5 a), and $k_{\text{red}} = 0.15$ (Fig. 5.6 a). Both the wind tunnel measurements [23] and the 2D LES data did not show an evident phenomenon of the second LEV shed in the early stage of downstroke. It is deduce that for the 2D LES case, the 2D flow separation after the first LEV shed is greater than that in the more accurate 3D LES, and makes the influence of the second LEV much smaller and hard to discern. It is to be noted that the wind tunnel set-up [23]

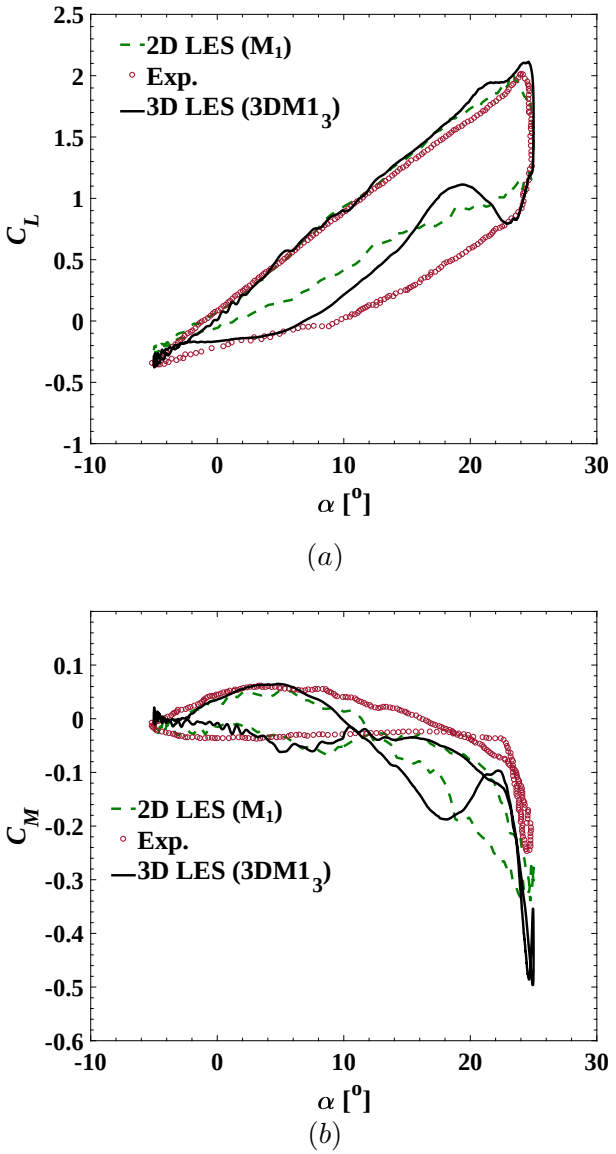

Figure 5.6: Phase averaged force coefficient at $k_{\text{red}} = 0.15$. Lift (a), and moment (b). Exp. [23].

has a 10% geometrical blockage, which might have an adverse impact on accuracy in the early stage of downstroke. It is difficult to speculate any further why the experimental lift hysteresis loop curve has larger 'memory' (the area in the lift hysteresis loop) during the downstroke compared to the LES data. Nevertheless, the key features of the C_L and C_M hysteresis loops and peak lift coefficient are well captured by the 2D and 3D LES compared to the experimental data at k_{red} = 0.15.

In summary, the validation for $k_{\text{red}} = 0.1$ and $k_{\text{red}} = 0.15$ is promising. The numerically estimated force coefficients agree well with the reference data. The key features of deep dynamic stall of a pitching aerofoil are captured adequately.

The success of validation is vital for carrying out further studies on the effect of reduced frequency.

5.5 Effect of high reduced frequency on aerodynamic forces and vortices

For a deep good understanding of the complex flow around a pitching wing, the focus of the chapter is to study the vortex dynamics at high pitching frequencies and its impact on the aerodynamic forces. Given the great computational cost and the massive datasets, simulation, visualisation and analysis of vortex dynamics in a full pitching cycle are non-trivial. To compromise this, LES was carried out both in 2D and 3D in the study, while more analysis was focused on the 2D LES due to the simplicity.

5.5.1 Effect on aerodynamic forces

Figure 5.7 (a - c) shows the lift, drag and moment coefficients in 3D LES at $k_{\text{red}} =$ 0.2, 0.3 and 0.4 respectively. Figure 5.7 (a) shows that the lift coefficient C_L at k_{red} = 0.4 has noticeable high values in the entire cycle compared to that at $k_{\text{red}} = 0.2$ and 0.3. The increase of lift coefficient at $k_{\text{red}} = 0.4$ is within 22% and 8% during the upstroke and 64% and 32% during the downstroke compared to $k_{\text{red}} = 0.2$ and 0.3, respectively. For $k_{\text{red}} \geq 0.3$, the upstroke curves lose their linearity, which is consistent with data at very high reduced frequency and very lower Reynolds number [70]. Overall, Figure 5.7 (a) shows a considerable increase of the lift during the pre-stall and post-stall angle of attack as the reduced frequency increases. The author speculate that a greater lift coefficient at $k_{\text{red}} = 0.4$ is due to the higher pitching kinetic energy resulting in more energetic LEVs. A sharp drop of the lift coefficient C_L at the maximum angle of attack $\downarrow$ for $k_{\text{red}} = 0.2$ is evident in Fig. 5.7 (a). This indicates a sudden detachment of the first LEV, which is similar to that observed at $k_{\text{red}} = 0.1$ (Fig.5.5 (a)) and 0.15 (Fig. 5.6 (a)). It is crucial to note that such a phenomenon is not visible for $k_{\text{red}} \geq 0.3$.

Figure 5.7 (b) show the effect of reduced frequency on drag coefficient C_D, which is less compared to that on the lift coefficient C_L Figure 5.7 (a). Nevertheless, the peak of drag coefficient C_D at $k_{\text{red}} = 0.4$ decreases by 13% and 26% compared to at reduced frequencies $k_{\text{red}} = 0.3$ and 0.2, respectively. Again, this is owing to the difference of the first LEV detachment. The peak drag coefficients decrease evidently with an increase of the reduced frequency, this is also consistent with all simulated results of the drag coefficients shown in Fig. 5.8. Indeed, the influence on the drag coefficient of high reduced frequency is visible.

The discrepancy of the moment coefficients C_M for different reduced frequencies in Fig. 5.7 (c) is distinct. The global minimum C_M values are -0.51, -0.39 and -0.32,

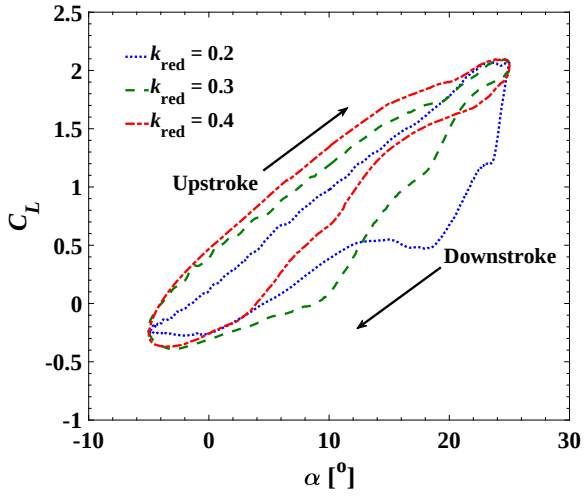

(*a*)

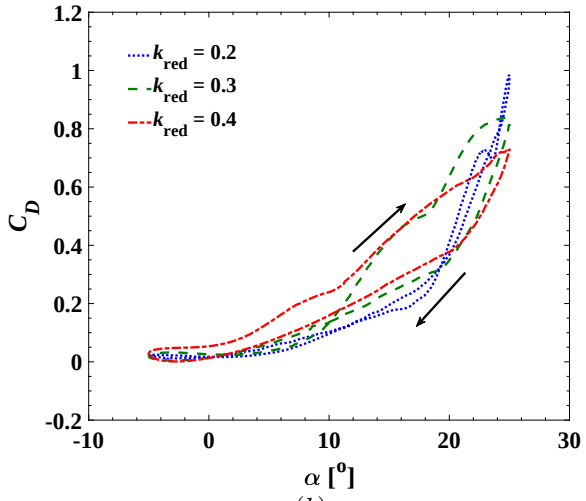

(*b*)

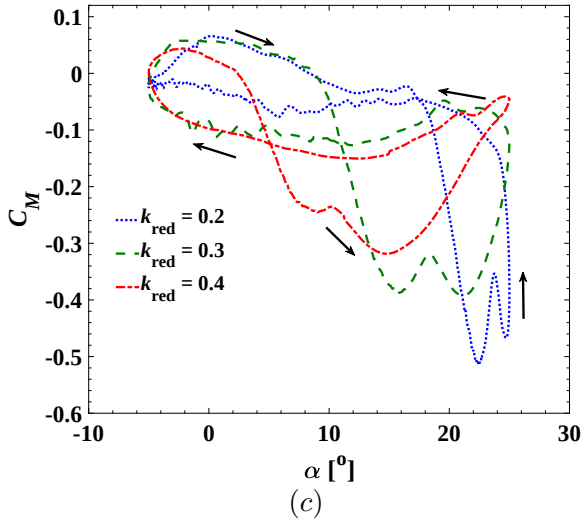

(*c*)

Figure 5.7: Effect of reduced frequency on the phase averaged aerodynamic coefficients for 3D simulations: (a) lift, (b) drag, (c) moment.

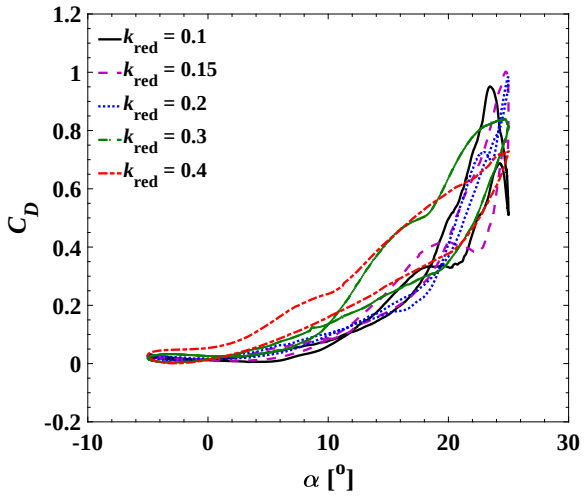

Figure 5.8: Effect of reduced frequency on the phase averaged drag coefficients for 3D simulations.

which occur at $\alpha \approx 22.5°$, 21.1° and 15.0° for $k_{\text{red}} = 0.2$, 0.3 and 0.4 respectively. Given that the lift and drag coefficient shown in Fig. 5.7 (a, b) are only weakly dependent on the reduced frequency, whereas the moment coefficient is strongly dependent on the reduced frequency, it can be deduce that the reduced frequency significantly affects the position of the aerodynamic force centre on the aerofoil. Overall, the data shown in Fig. 5.7 can draw a conclusion that the aerodynamic force coefficients change substantially at a high reduced frequency, e.g. $k_{\text{red}} = 0.4$.

5.5.1.1 Comparison of aerodynamic coefficients between 2D and 3D LES

Figures 5.9, 5.10 and 5.11 shows a comparison of phase-averaged lift, drag and moment coefficients between 2D and 3D LES at reduced frequencies, $k_{\text{red}} = 0.2$, 0.3 and 0.4, respectively. Overall, the 2D data agree well with the 3D data.

Figure 5.9 (a) shows an evident discrepancy of lift coefficients C_L from 23°↓ to 16°↓ for $k_{\text{red}} = 0.2$. Again this is because in the early stage of downstroke the flow is 3D-flow dominant at low reduced frequencies (also see Figs. 5.5 and 5.6). Such a discrepancy is not visible at $k_{\text{red}} = 0.3$ and 0.4 (Fig. 5.9 (b)). Figure 5.10 (a - c) shows a better agreement of drag coefficient between the 2D and 3D LES.

Figure 5.11 (a - c) also shows reasonable agreement of the moment coefficients between the 2D and 3D LES, except at the global minimum peaks, which the 2D LES values are optimistically predicted, especially at $k_{\text{red}} = 0.2$ and 0.3 Fig. (5.11 (a - b)).

The good agreement between the 2D and 3D LES suggests that 2D LES could be a promising compromise for pitching aerofoil applications in terms of efficiency and

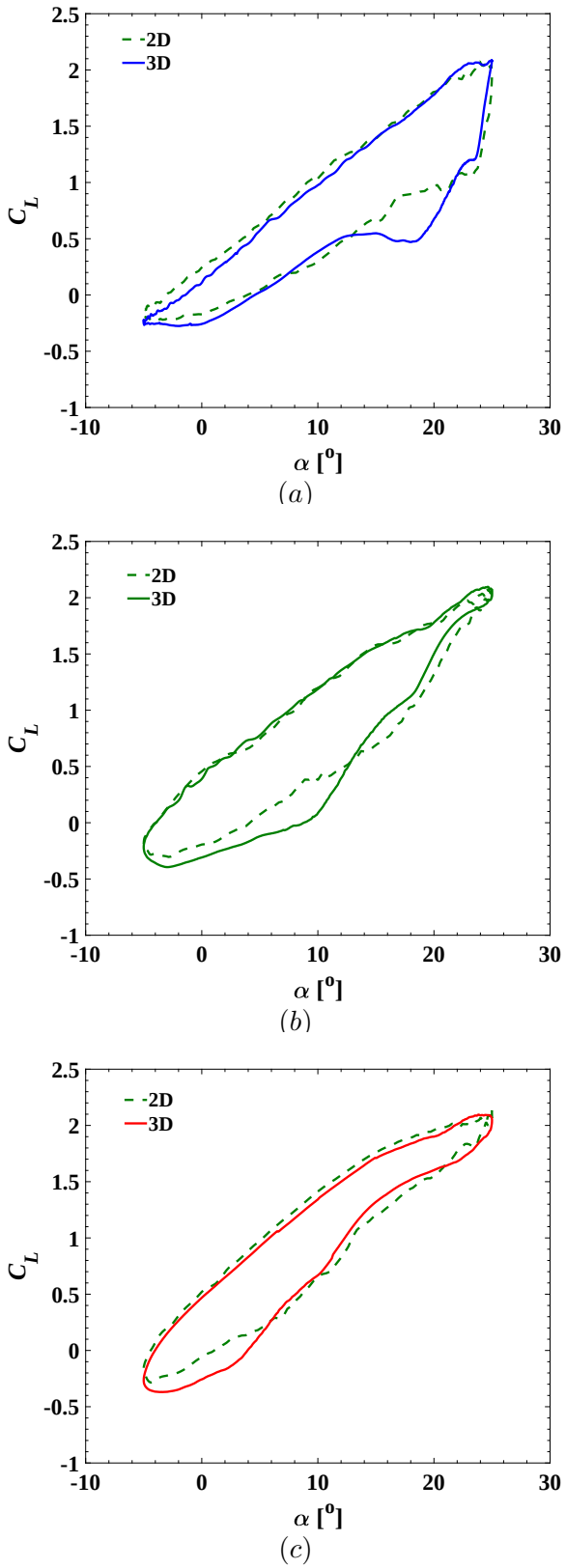

Figure 5.9: Comparison of phased-averaged lift coefficients between 2D and 3D. (a) $k_{\text{red}} = 0.2$, (b) $k_{\text{red}} = 0.3$. (c) $k_{\text{red}} = 0.4$.

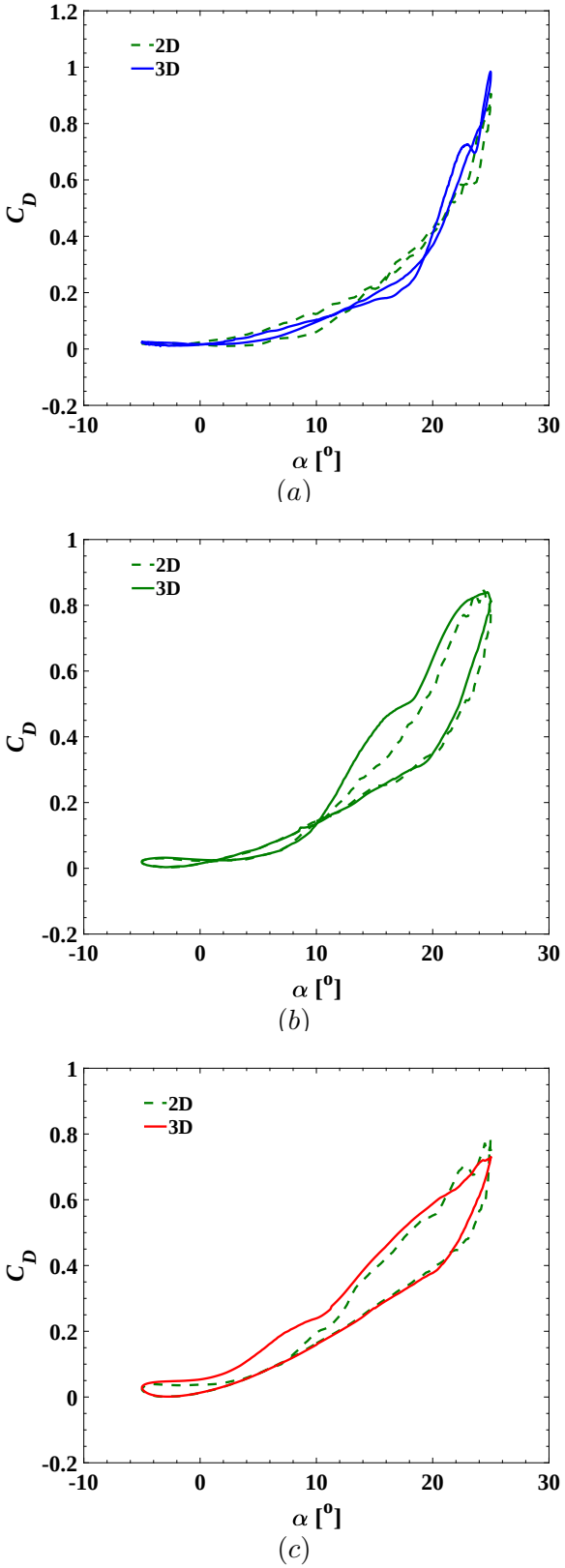

Figure 5.10: Comparison of phased-averaged drag coefficients between 2D and 3D. (a) $k_{\text{red}} = 0.2$, (b) $k_{\text{red}} = 0.3$. (c) $k_{\text{red}} = 0.4$.

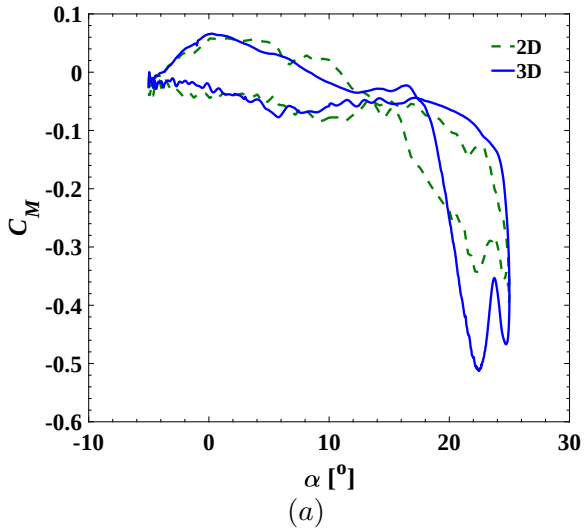

(*a*)

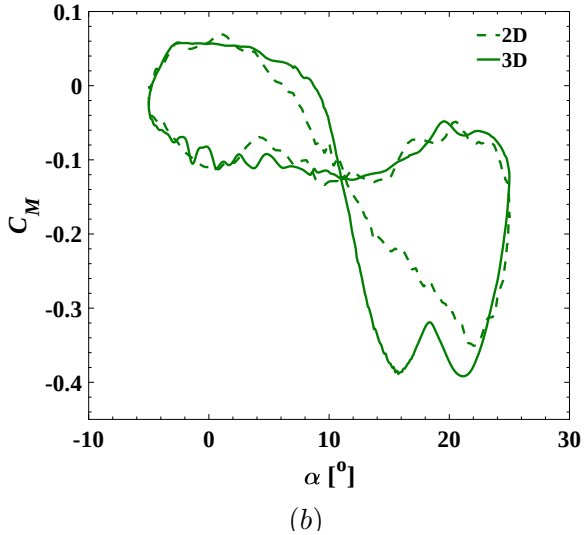

(*b*)

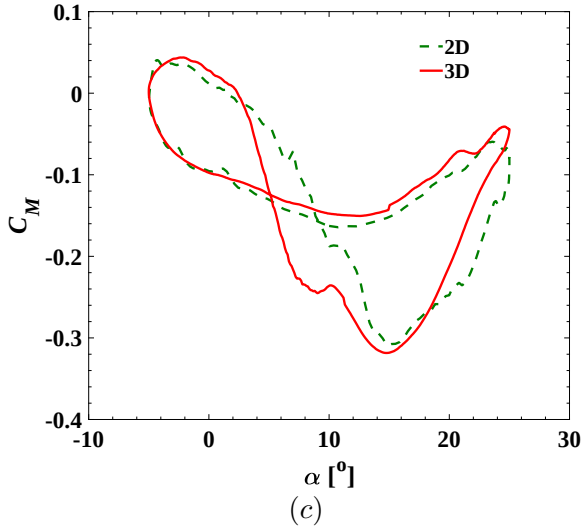

(*c*)

Figure 5.11: Comparison of phased-averaged moment coefficients between 2D and 3D. (a) $k_{\text{red}} = 0.2$, (b) $k_{\text{red}} = 0.3$. (c) $k_{\text{red}} = 0.4$.

accuracy. The 2D LES is more effective for a high reduced frequency, e.g. $k_{\text{red}} = 0.4$. This is because the LEVs are suppressed on the aerofoil suction side at a high reduced frequency (see Fig. 5.16), and the flow can be considered as quasi-2D.

5.5.1.2 Lift and moment coefficients against phase angle

Figures 5.12 and 5.13 respectively show phase-averaged lift and moment coefficients against phase angle Ψ in 2D and 3D LES. The phase angles at which LEVs were shed in 2D LES in Fig. 5.12 (a) match the respective ones in 3D LES in Fig. 5.12 (b). Nevertheless, the local peaks in 3D LES shown in Fig. 5.12 (b) are more visible than those in 2D LES in Fig. 5.12 (a), in particular for $k_{\text{red}} = 0.1$, which are consistent with Figs. 5.5, 5.6 and 5.9. Fig. 5.12 (b) shows three evident local peaks respectively at phase angle $\Psi = 62.4°\uparrow$, $108°\downarrow$ and $147°\downarrow$ for $k_{\text{red}} = 0.1$, indicating that three LEVs were shed.

Compared to the other reduced frequencies, the substantial rise of lift coefficient C_L in the last stage of upstroke and the early stage of downstroke for $k_{\text{red}} = 0.3$ and 0.4 is because the LEVs were still attached at high angle of attack. Fig. 5.12 (a, b) shows an overall increase both in the upstroke and downstroke regimes with an increase of reduced frequency. The curves for different reduced frequencies are in evidently different shape and magnitude, confirming again that the formation, growth, convection and shedding of LEVs are largely affected by the reduced frequency.

Figure 5.13 shows moment coefficients C_M against phase angle at different reduced frequencies in 2D and 3D LES. Both 2D and 3D data show that the global minimums of moment coefficient C_M occur at higher phase angle (downstroke) for a greater reduced frequency. The discrepancy of moment between the 2D and 3D data in Fig. 5.13 is greater than that of lift in Fig. 5.12. This is again because the moment is also dependent on the location of the force centre.

An inference of Figs. 5.12 and 5.13 is that dynamic stall occurs at higher phase angle towards the downstroke as the reduced frequency increases. This suggests that the large vortices during dynamic stall are sensitive to the pitching motion. The LEVs formed at the leading edge extract kinetic energy from the pitching aerofoil. The pitching motion at a high reduced frequency delays LEVs' detachment, subsequently delays the dynamic stall towards the pitching downstroke region, and increases the peak lift. In emphasis, the pitching motion plays a more dominant role on the aerodynamics at a high reduced frequency.

One-to-one comparison between the 2D and 3D LES phase-averaged lift and moment coefficients in phase angle Ψ for $k_{\text{red}} = 0.1$ and 0.2 are shown in Fig. 5.14, and k_{red} 0.3 and 0.4 (Fig. 5.15). Both the 2D and 3D LES phase-averaged C_L and C_M match very well with each other in their respective phase angles for all the reduced frequencies, except for the local peaks at high phase angles Ψ in the 3D

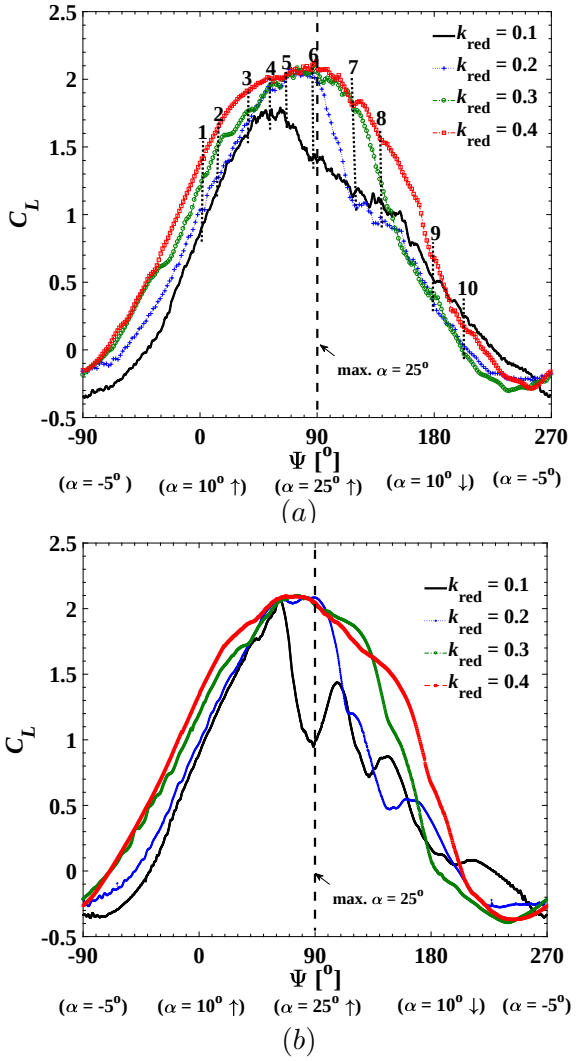

Figure 5.12: Phase-averaged lift coefficients versus phase angles. (a) 2D data with a vertical dash line at the middle indicates the aerofoil maximum $\alpha = 25°$at phase angle $\Psi = 90°$, while the dot vertical lines with assigned numbers across the curves correspond to the snapshots in Fig: 5.23, 1: $\alpha = 10.3° \uparrow$, 2: $\alpha = 13° \uparrow$, 3: $\alpha = 18.8° \uparrow$, 4: $\alpha = 21.7° \uparrow$, 5: $\alpha = 23.3° \uparrow$, 6: $\alpha = 24.9° \uparrow$, 7: $\alpha = 23.8° \downarrow$, 8: $\alpha = 20° \downarrow$, 9: $\alpha = 10° \downarrow$, 10: $\alpha = 4° \downarrow$. (b) 3D data.

LES of low $k_{\text{red}} = 0.1$ shown in Fig. 5.14 (a). Again, this is due to any pressure distribution in the chord-wise direction is forced to be identical in the spanwise direction, whereas in the 3D LES at the high phase the pressure distribution is not uniform.

Overall, the phase-averaged moment coefficients C_M in Figs. 5.14 and 5.15 show very good agreement between the 2D and 3D LES in the entire phase angles Ψ for all the reduced frequencies. The discrepancies observed in the global minimum moment coefficients at $k_{\text{red}} = 0.2$ and 0.3 (Figs. 5.14 (b) bottom, and 5.15 (a) bottom) is due to the settings, which the moment is very sensitive to. Figure 5.15 (b) shows that both the 2D and 3D LES phase-averaged C_L and C_M agree very

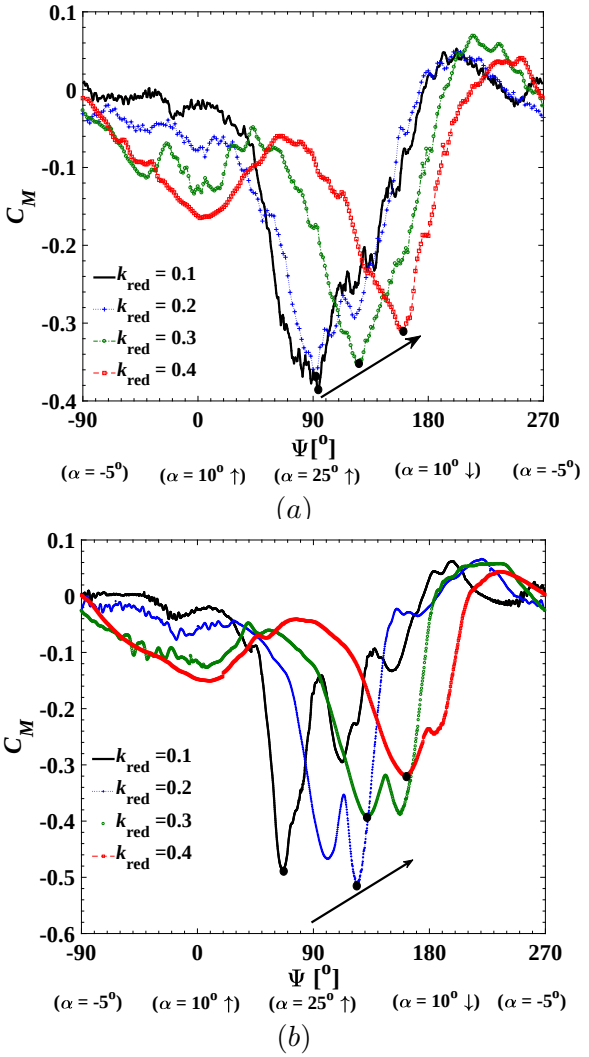

Figure 5.13: Phase-averaged moment coefficients versus phase angles Ψ . The solid black dots on the peaks of the moment coefficients indicate their global minimum at each reduced frequency k_{red}. The black arrow shows the shift of the global minimum towards high phase downstroke. (a) 2D, (b) 3D.

well with each other in the entire phase of the aerofoil pitching cycle. These again confirm that 2D LES effectiveness increase as the reduced frequency increases from a lower $k_{\text{red}} = 0.1$ to a higher $k_{\text{red}} = 0.4$.

5.5.1.3 Comparison of vorticity contours in 2D and 3D simulations

Fig. 5.16 shows a comparison between vorticity contours in 2D LES and those on the mid-span plane in 3D LES for $k_{\text{red}} = 0.1$, 0.2 and 0.4. The phase angles $\Psi = 65.8°\uparrow$ (i.e. ID = 5 in Fig. 5.12) and $86.5°\uparrow$ (i.e. ID = 6 in Fig. 5.12) are respectively at the dynamic stall angle and near to the maximum angle of attack.

The vortices in the 2D LES resemble well those in the 3D LES. However, there are some difference between them. For $k_{\text{red}} = 0.1$ (Fig. 5.16 (left column)), the

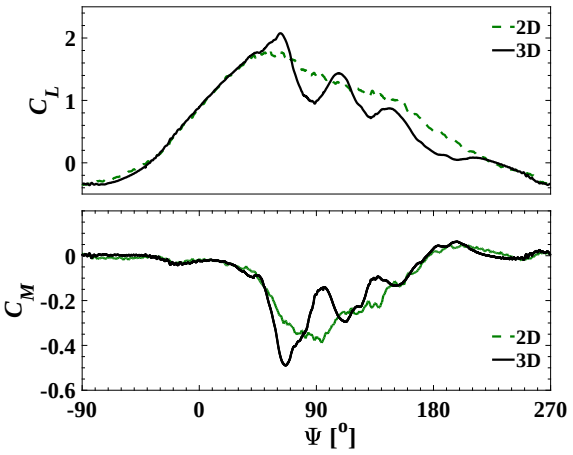

(*a*)

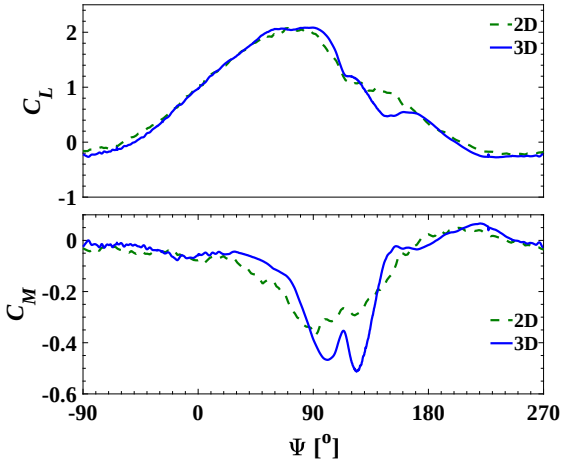

(*b*)

Figure 5.14: Comparison of phase averaged lift and moment coefficients versus phase angles. (a) $k_{\text{red}} = 0.1$, (b) $k_{\text{red}} = 0.2$

2D vortices are more concentrated, regular, and seem slightly smaller, and the 3D LEVs are more dispersed, more chaotic, and seem slightly larger. For $k_{\text{red}} = 0.4$ (Fig. 5.16 (right column)), the LEVs are much thinner in the cross-flow direction while longer in the streamwise direction in both the 2D and 3D LES, compared to those for $k_{\text{red}} = 0.1$. For $k_{\text{red}} = 0.2$, the vortex is transient in shape between the other two. Similar comparison of vorticity contours between the 2D and 3D LES at the other phase angles (not shown) were observed. These confirm that 2D LES can provide reliable data, and is a compromise to 3D LES.

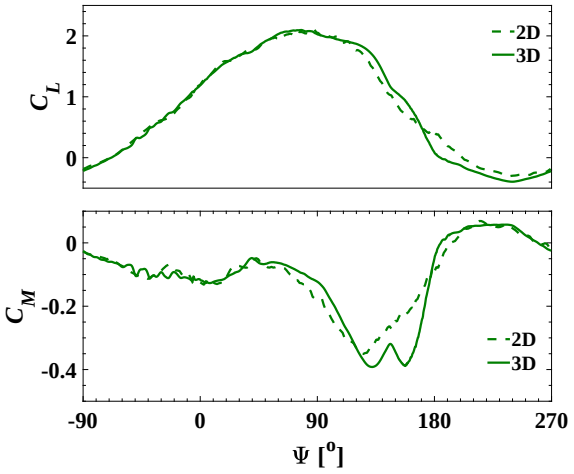

(a)

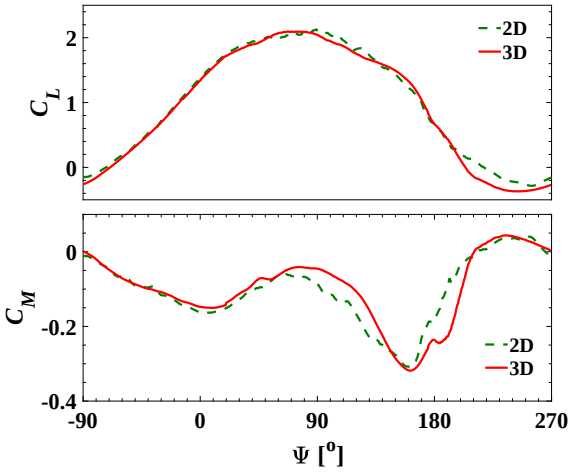

(b)

Figure 5.15: Comparison of Phase averaged lift and moment coefficients versus phase angles. (a) $k_{\text{red}} = 0.3$, (b) $k_{\text{red}} = 0.4$.

5.5.2 Comparison of required computational resources between 2D and 3D LES

Figure 5.17 shows the required computational resources used for the 2D case (mesh M3) and 3D case ($3DM_3$). The 3D and 2D cases required respectively 256 CPUs (cores) running for 520 wall-clock hours, and 16 CPUs running for 420 wall-clock hours, resulting in a 3D-to-2D efficiency ratio approximately 1/20. Note that the 2D case required at least ten cycles for initialisation and twenty cycles for obtaining converged statistics, whereas the 3D case required at least one cycle for initialisation and three cycles for averaging. These data suggest that the much computationally cheaper 2D LES is an alternative affordable approach when only limited computer resources are available.

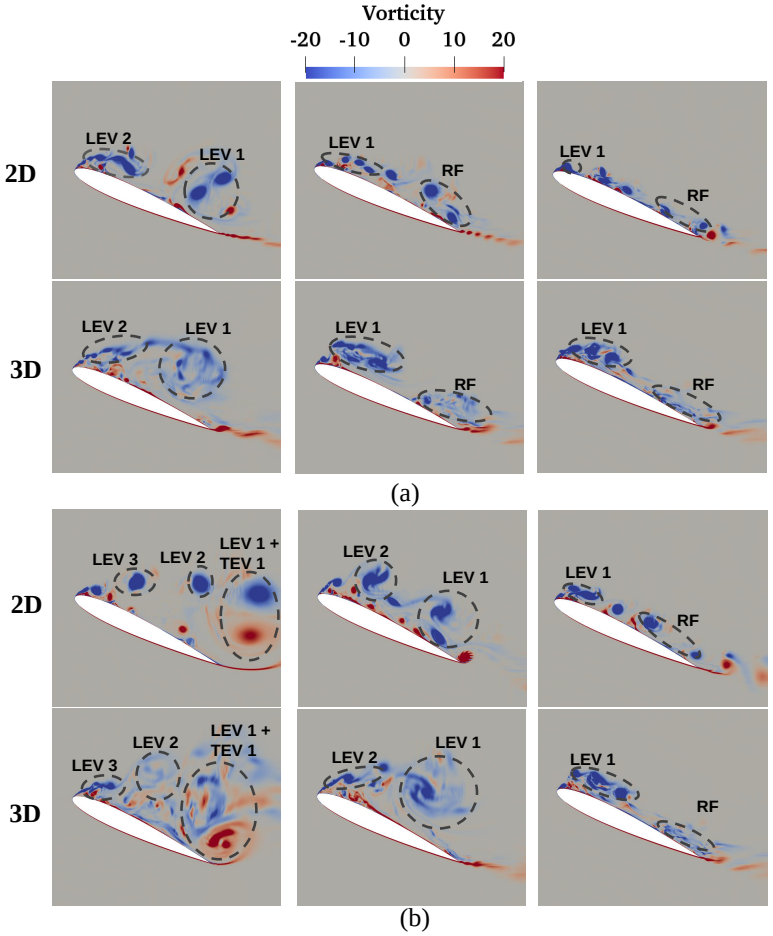

Figure 5.16: Instantaneous vorticity contours normalised by c and U_∞ in 2D and 3D simulations. **LEV**, **TEV** and **RF** denote leading edge vortex, trailing edge vortex and reverse flow respectively. (a) $\Psi = 65.8° \uparrow$ (i.e. ID=5 in Fig. 5.12) , (b) $\Psi = 86.5° \uparrow$ (i.e. ID=6 in Fig. 5.12). (left) $k_{\text{red}} = 0.1$, (middle) 0.2, (right) 0.4.

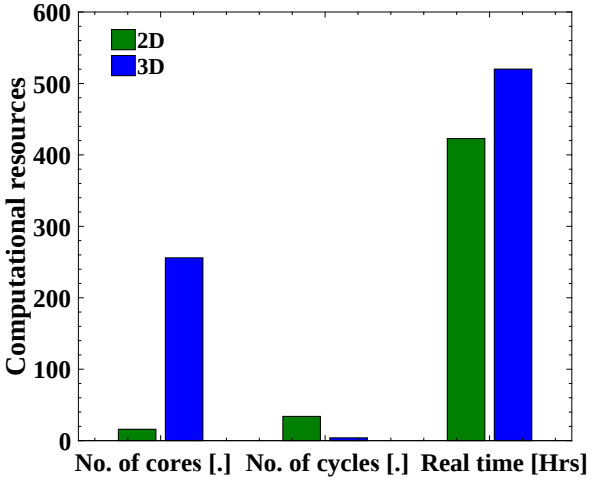

Figure 5.17: Required computational resources for the 2D case (M3) and the 3D case ($3DM_3$).

5.5.2.1 The aerofoil surface forces

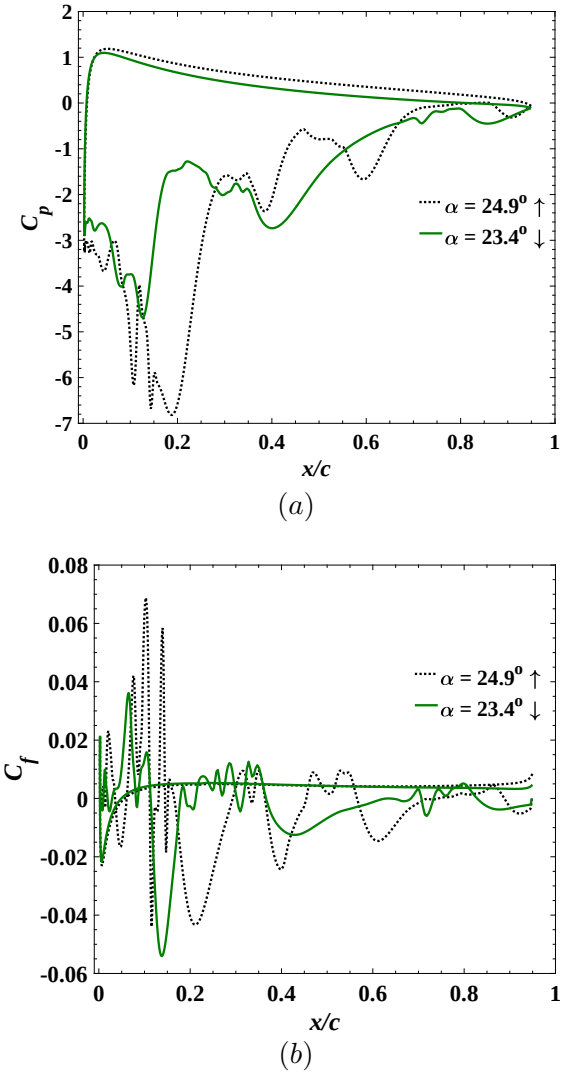

Figure 5.18: (a) Pressure coefficients for 2D simulation, (b) Skin friction coefficients. $k_{\text{red}} = 0.4$.

In order to further demonstrate that the LEV remains attached near the dynamic stall angle for higher reduced frequency both in the up - and down - strokes, aerofoil surface force is analysed in the subsection.

Figure 5.18 shows the pressure coefficients (C_p) and skin friction coefficients (C_f) at $k_{\text{red}} = 0.4$, which again confirm that the stall occurs at the turning point (i.e. $\Psi = 90°$) between the upstroke and downstroke regions (Ref. Fig. 5.12). It was also observed that at a high angle of attack $\alpha = 23.8° \downarrow$ and at $k_{\text{red}} = 0.4$, the LEVs remain attached near the leading edge (see Fig. 5.23) resulting in a high lift coefficient, which was different from at a lower reduced frequency (e.g. $k_{\text{red}} = 0.2$) shown in (Fig. 5.19). At similar angles of attack for $k_{\text{red}} = 0.2$ (Fig. 5.19) a

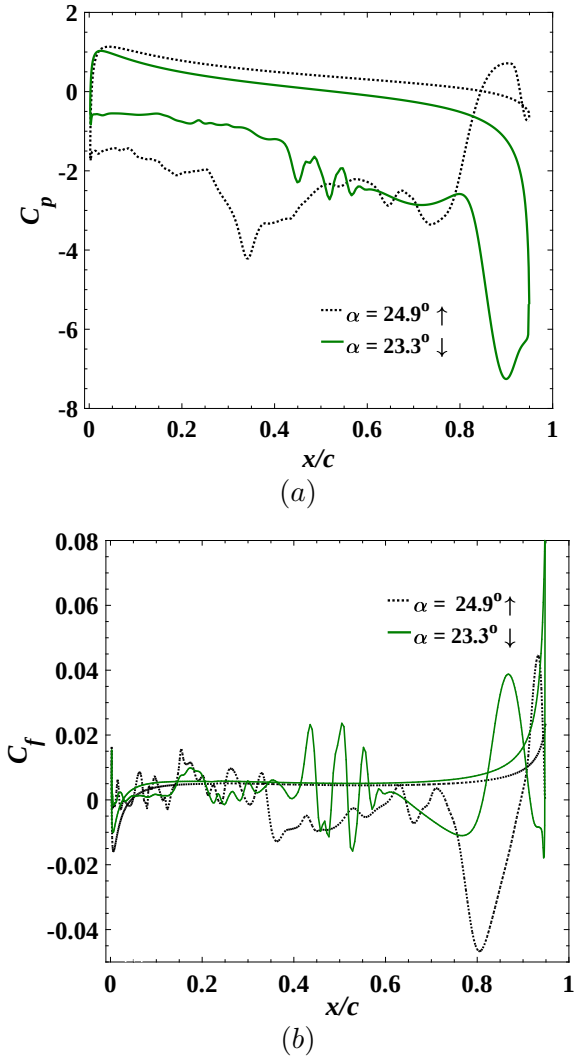

Figure 5.19: (a) Pressure coefficients, (b) Skin friction coefficients. $k_{\text{red}} = 0.2$.

plateau was seen near the lead edge of the aerofoil while at the trailing edge the LEVs shed is evident.

5.5.3 Effect on separation point and reversed flow region

Figures 5.20 and 5.21 shows the velocity profiles within and immediately above the boundary layer on the suction side of the aerofoil for static case, $k_{\text{red}} = 0.1$, $k_{\text{red}} = 0.2$ and $k_{\text{red}} = 0.4$ respectively at $\alpha = 10°$. The position of the aerofoil is at the natural phase angle $\Psi = 0°$. The velocity profiles for $k_{\text{red}} = 0.1$, $k_{\text{red}} = 0.2$ and $k_{\text{red}} = 0.4$ are phased-averaged data over three pitching cycles, while the velocity profiles for the static case are converged time-averaged data. The data that is shown in Figs. 5.20 and 5.21 suggest that the leading edge separation bubble in the boundary layer flow is affected by the reduced frequency.

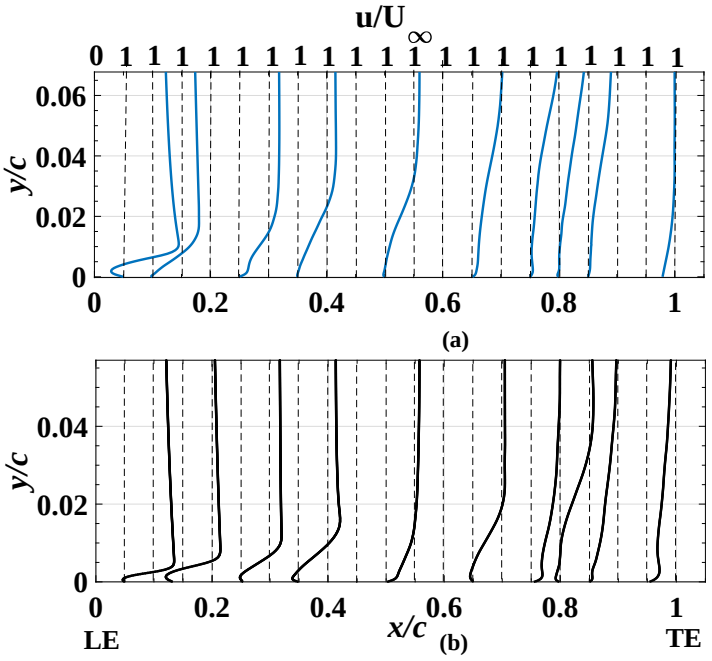

Figure 5.20: Boundary layer velocity profiles on the suction side on the aerofoil at $\alpha = 10° \uparrow$ for 2D simulation. (a) Static case and (b) $k_{\text{red}} = 0.1$. LE and TE denotes leading edge and trailing edge respectively.

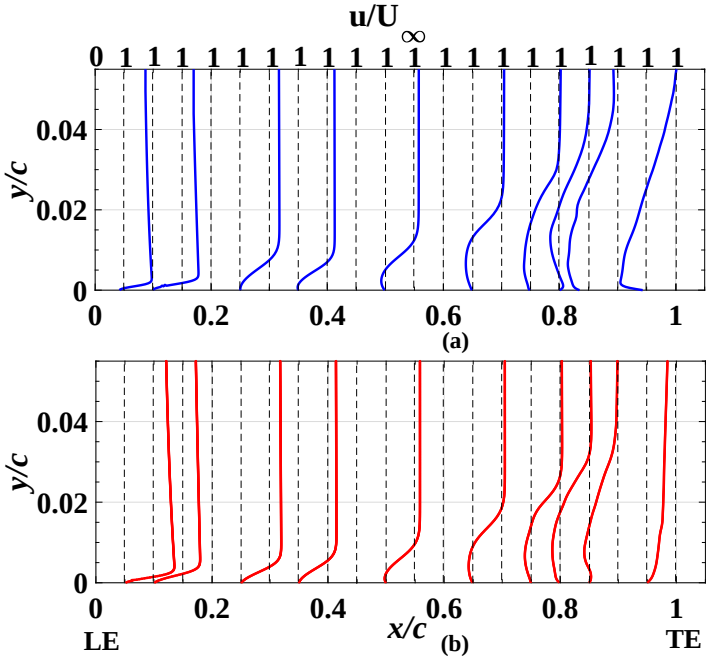

Figure 5.21: Boundary layer velocity profiles on the suction side of the aerofoil at $\alpha = 10° \uparrow$ for 2D simulation. (a) $k_{\text{red}} = 0.2$ and (b) $k_{\text{red}} = 0.4$. LE and TE denotes leading edge and trailing edge respectively.

It was noticed that the location of the separation bubble near the LE shifts downstream towards the mid-chord vicinity at $\alpha = 10°\uparrow$ as the reduced frequency increases (Fig. 5.21). The substantial shift of the separation point near the leading edge to the mid-chord is attributed to the increased angular velocity of aerofoil motion as the reduced frequency increase. This means that increased aerofoil motion directly influence the separation point at the pre-stall angle of attack.

In order to further understand the effect of the reduced frequency on the boundary layer flow, the boundary layer thickness is define to be the height from the aerofoil surface to where the local velocity is 90% of the freestream velocity U_∞. Fig. 5.22 shows boundary layer thickness profiles. Note that in Fig. 5.22, the lower and upper error bars caps on each data points are the estimated boundary layer thickness respectively, based on the 85% and 95% of the freestream velocity U_∞.

Figure 5.22 shows that the pitching motion substantially suppresses the growth of the boundary layer compared to that of the static aerofoil. The significantly suppressed boundary layer at the leading edge is attributed to the upstroke motion of the aerofoil. Such an effect at the leading edge increase as the reduced frequency increases. Downstream from the leading edge of the aerofoil, the effect of the reduced frequency shows a very complicated trend, which might be owing to the phased-averaged data being sampled only from three pitching cycles, which may yield considerable errors.

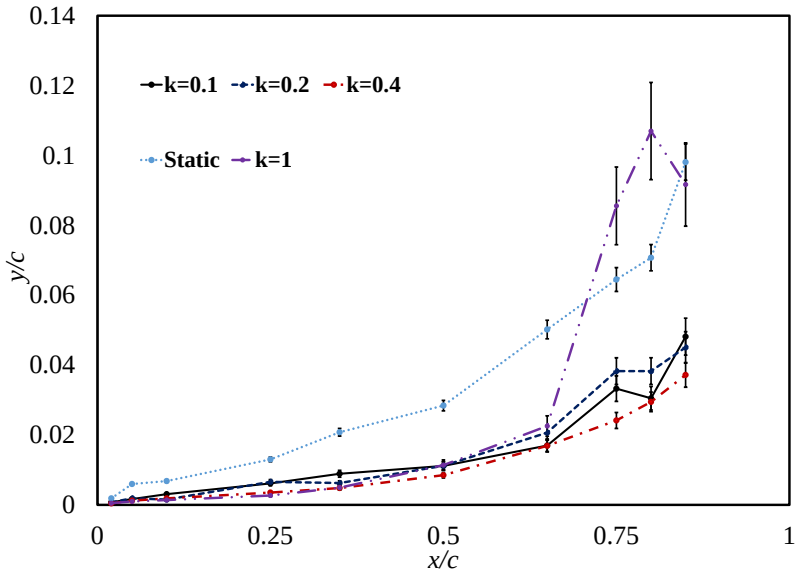

Figure 5.22: The boundary layer thickness of the aerofoil at static and in pitching motion at $\alpha = 10°$ for 2D simulation.

5.5.4 Effect on the vortex dynamic

Snapshots of instantaneous vorticity and velocity streamlines super imposed with pressure coefficients contours in 2D LES for $k_{\text{red}} = 0.1$ (left), 0.2 (middle) and 0.4

(right) are shown in Figs. 5.23 and 5.24. The 2D data was used instead of 3D LES data because the former are much easier for analysis and indeed much clear (see Fig. 5.16). The Identification numbers (ID = 1,2...10) in Fig. 5.23 respectively correspond to the IDs marked with vertical dot-lines in Fig. 5.12 (a).

1. $\alpha = 10°$ at $\Psi = 0°\uparrow$. Figs. 5.23 and 5.24 shows that the boundary layer begins to separate for $k_{\text{red}} = 0.1$ and 0.2. For $k_{\text{red}} = 0.4$, the boundary layer flow is well attached from the leading edge (LE) to near the trailing edge (TE). The separate bubble are suppressed in all the cases.

2. $\alpha = 13°$ at $\Psi = 13°\uparrow$. Figs. 5.23 and 5.24 shows that the vortices (reverse flow) in the boundary layer near the TE continued to grow and roll-up for $k_{\text{red}} = 0.1$ and 0.2, whereas for $k_{\text{red}} = 0.4$ no sign of reverse flow is visible on the upper surface. A wide area with negative pressure coefficient is evident for $k_{\text{red}} = 0.4$ on the suction surface in Fig. 5.24, which indicates an earlier increase of the lift coefficient at $\Psi = 13°$compared to $k_{\text{red}} = 0.1$ and $k_{\text{red}} = 0.2$.

3. $\alpha = 18.8°$ at $\Psi = 37.3°\uparrow$. Figs. 5.23 and 5.24 shows that the vortices in the boundary layer at the TE increase in size and roll-up for $k_{\text{red}} = 0.1$, but in a slower pace and smaller size for $k_{\text{red}} = 0.2$. For $k_{\text{red}} = 0.4$ vortices begin to appear in the boundary layer, and more visible near the TE.

4. $\alpha = 21.7°$ at Ψ 53.3 $\uparrow$. Figs. 5.23 and 5.24 shows that the reverse-flow vortices in the boundary layer near the TE merge with other vortices at the mid-chord for $k_{\text{red}} = 0.1$, which causes a slight lift drop (Fig. 5.12 (a) ID 4). The first LEV remains attached, and a large trailing edge vortex (TEV) becomes evident. For $k_{\text{red}} = 0.2$, multiple vortices are visible in the boundary layer and an energetic LEV starts to emerge and grow. For $k_{\text{red}} = 0.4$, the growth of vortices is suppressed due to the more energetic pitching motion during the upstroke.

5. $\alpha = 23.3°$ at $\Psi = 65.8°\uparrow$. Figs. 5.23 and 5.24 shows that the first LEV sheds into the shear layer, which causes the lift coefficient to drop sharply (i.e. dynamic stall) for $k_{\text{red}} = 0.1$ (Fig. 5.12 (a) IDs 5 - 6). More vortices emerge and convect on the suction side of the aerofoil for both $k_{\text{red}} = 0.2$ and 0.4. However, the vortices and the boundary layer are still evidently suppressed at this phase angle for $k_{\text{red}} = 0.4$. Pitching motion at high reduced frequencies significantly enhances suppression of the LEVs during the upstroke.

6. $\alpha = 24.9°$ at $\Psi = 86.5°\uparrow$. Figs. 5.23 and 5.24 shows that the first LEV (the largest one with negative vorticity) induces and interacts with the first TEV (with positive vorticity) for $k_{\text{red}} = 0.1$. Such interaction slows down the convection of the two counter-rotating vortices being shed into wake. The second and third LEVs detached from the aerofoil resulting in a fully separated boundary layer flow on the suction side, which causes a continuous drop of the lift coefficient (Fig. 9 (a) ID 6). For $k_{\text{red}} = 0.2$, the first and second LEVs convect rapidly downstream and detach from the aerofoil, which triggers the dynamic stall (Fig. 5.12 (a) ID 6).

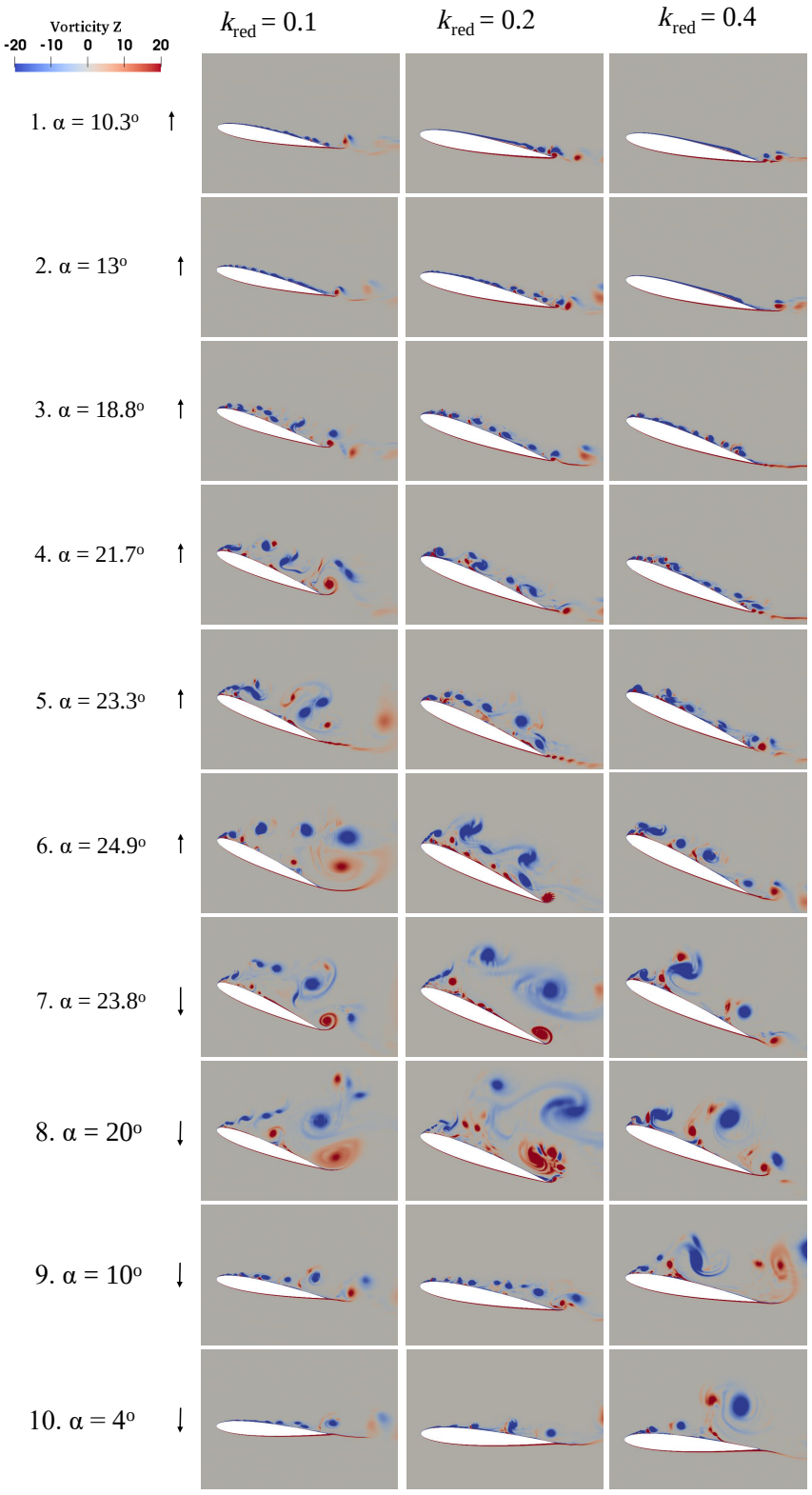

Figure 5.23: Instantaneous vorticity contours normalised by c and U_∞, for $k_{\text{red}} =$ 0.1 (left), 0.2 (middle) and 0.4 (right). The Identification numbers (ID=1,2...10) respectively correspond to IDs (1,2...10) marked with dot-lines in Fig. 5.12 (a).

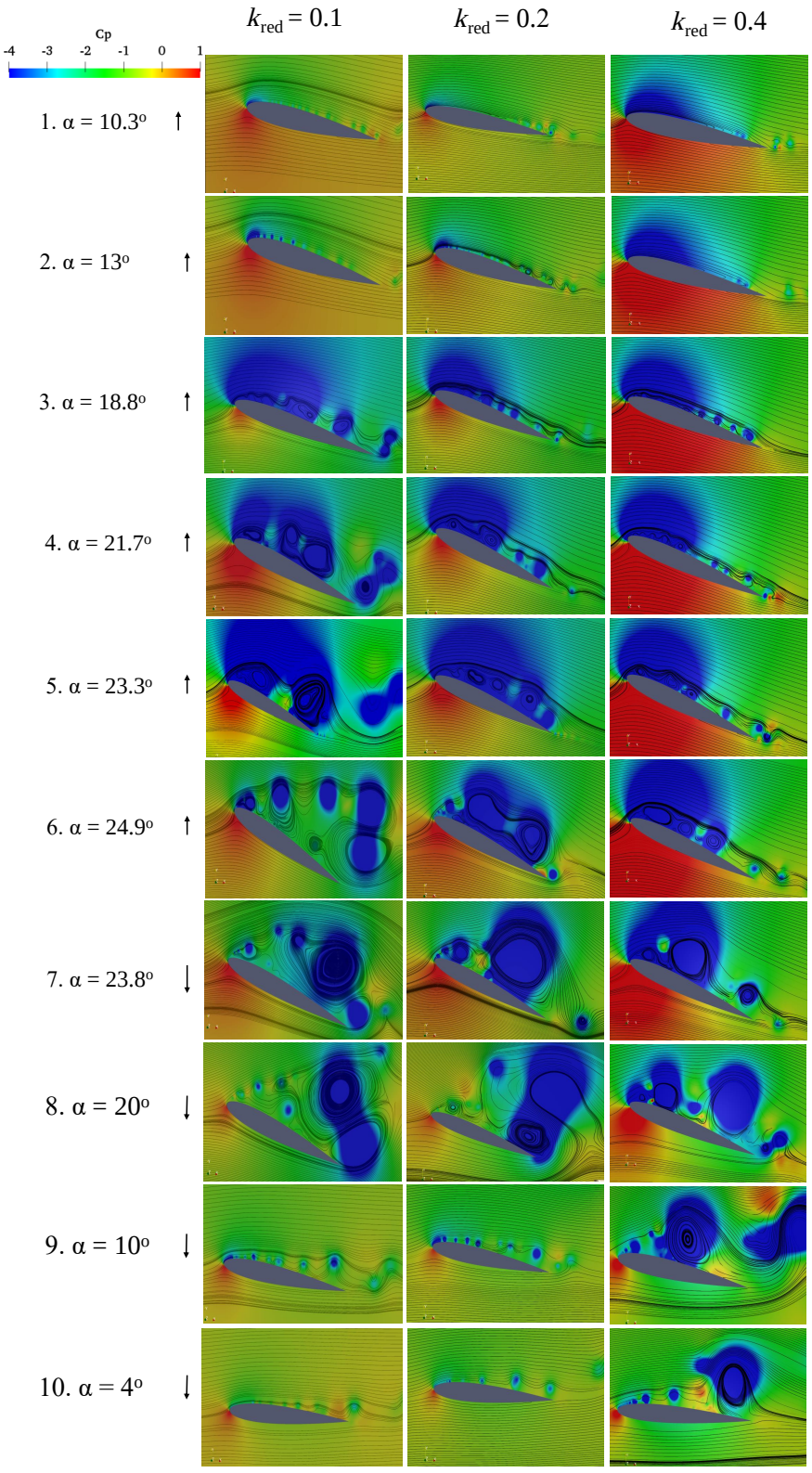

Figure 5.24: Instantaneous flow streamlines coloured by instantaneous pressure coefficient, for k_{red} 0.1 (left), 0.2 (middle) and 0.4 (right). The Identification numbers (ID=1,2...10) respectively correspond to 1Ds (1,2...10) marked with dot-lines in Fig. 5.12 (a).

For $k_{\text{red}} = 0.4$, the first LEV and other vortices are clearly visible, and remain attached, which continue increasing the lift coefficient (Fig. 5.12 (a) ID 6).

7. $\alpha = 23.3°$ at $119.5°\downarrow$. Figs. 5.23 and 5.24 shows a sudden reattachment of the third LEV for $k_{\text{red}} = 0.1$, resulting in a very small increase of lift (Fig. 5.12 ID 7). Similar phenomenon is observed for $k_{\text{red}} = 0.2$, which is due to the merging of LEVs. For $k_{\text{red}} = 0.4$ a full separation of the boundary layer is yet to start, resulting in sustaining a high lift coefficient during the early stage of downstroke (ref. Fig. 5.12 (a) ID 7). The LEVs remains well attached and convect downstream.

8. $\alpha = 20°$ at $\Psi = 140\downarrow$. $k_{\text{red}} = 0.1$. Figs. 5.23 and 5.24 shows a marginal increase of lift, which is due to the merging of the third and second LEVs and their interaction with the second TEV near the trailing edge. For $k_{\text{red}} = 0.2$, a complete separation of the boundary layer is evident. The large vortex merged from LEVs split away from the second TEV at the trailing edge and is shed into the wake, resulting in a rapid lift drop. For $k_{\text{red}} = 0.4$, the first LEV convects past the mid-chord but remains attached. The second LEV starts to develop at the LE.

9. $\alpha = 10°$ at $\Psi = 180°\downarrow$. Figs. 5.23 and 5.24 shows that the flow is reattached from the LE to the near mid-chord for $k_{\text{red}} = 0.1$. Similar phenomenon is observed for $k_{\text{red}} = 0.2$. For $k_{\text{red}} = 0.4$, the first LEV is shed into the wake (Fig. 5.12 (a) ID 9). The second LEV convects at the mid-chord and largely remains attached.

10. $\alpha = 4°$ at $\Psi = 200°\downarrow$. Figs. 5.23 and 5.24 shows that the flow is fully reattached for $k_{\text{red}} = 0.1$. A similar phenomenon is observed for $k_{\text{red}} = 0.2$. For $k_{\text{red}} = 0.4$, the second LEV starts to shed into the wake, which keeps the flow separate.

It should be noted that the highest reduced frequency $k_{\text{red}} = 0.4$ delays the detachment of the LEV up to $\alpha \leq 4°$ in the downstroke. This explains that the LEV have a short life-span on the suction side, which confirms the comments in [86]. The boundary layer reattachment during the downstroke is significantly delayed at the high reduced frequency. The merging of LEVs over the suction side during upstroke stroke enhances lift, whereas the splitting of LEV and TEV after their interaction causes rapid drop of lift during the downstroke.

5.5.5 Vortex shedding frequency

To estimate the non-dimensional shedding frequency, the Strouhal number (St) for the different reduced frequencies that range from 0.15 to 0.4 was studied.The probes (sensors) are placed at streamwise direction $x/c = 0.75$ and $x/c = 1$, and the crossflow direction position was $y/c = 0.1$. Both sensors locations are relative to the aerofoil motion. The time series of the instantaneous velocity at these probes locations are obtained for three to eight cycles for the different reduced frequencies $k_{\text{red}} = 0.15$ to 0.4 for the 3D simulations.

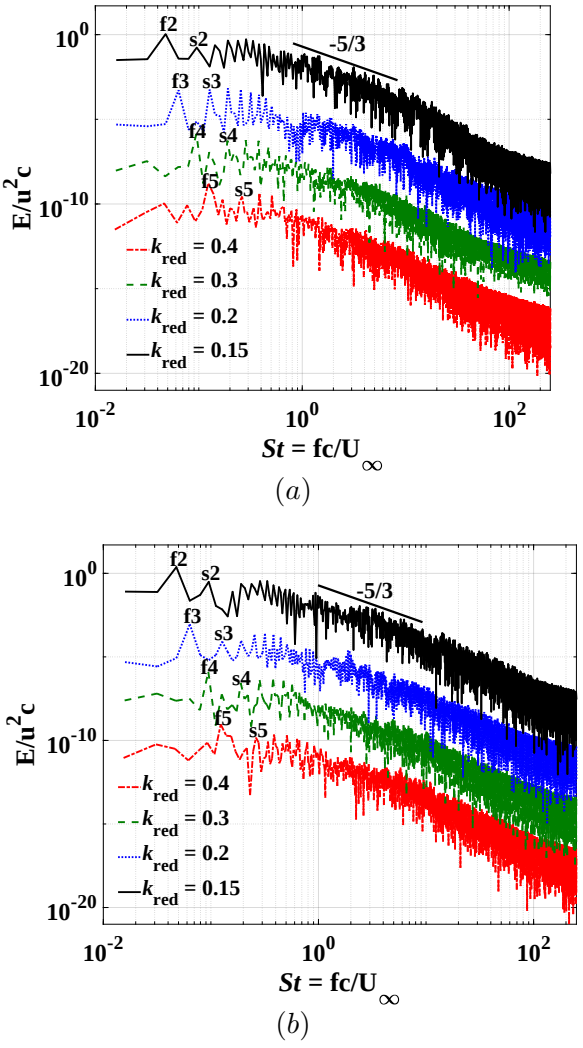

Figure 5.25: Power density spectra of the cross-flow velocity component. The spectra for $k_{\text{red}} = 0.2$, 0.3 and 0.4 are shifted by 3, 6 and 9 decades respectively. All sensors are placed on the middle span plane. (a) $x/c = 0.75$, $y/c = 0.1$; (b) $x/c = 1$, $y/c = 0.1$. The letters **f** and **s** denotes the first and second (primary vortex shedding frequency) peaks respectively.

Figure 5.25 shows the power density spectra for $k_{\text{red}} = 0.15$, 0.2, 0.3 and 0.4. The letters **f** and **s** on the figure denotes the first and second (primary vortex shedding frequency) peaks respectively, and the number **1** to **5** correspond to the five different simulated cases. Noted that $k_{\text{red}} = 0.1$ **f1** and **s1** are not shown in Fig. 5.25 due to insufficient data for a spectra analysis. The power density spectra were normalised with the velocity variance and the chord length. In Fig. 5.25 (a - b) the peaks, **f2**, **f3**, **f4** and **f5** correspond to the reduced frequencies at 0.15, 0.2, 0.3 and 0.4 respectively.

Table 5.5 show the primary vortex shedding frequency - second (**s**) peaks of the spectra (see Fig. 5.25 a - b), **s2**, **s3**, **s4** and **s5**, which correspond to the $St = 0.095$, 0.127, 0.19, and 0.25 respectively, and they are respectively for $k_{\text{red}} = 0.15$,

Table 5.5: Reduced frequency (k_{red}) and non-dimensional primary vortex shedding frequency (St).

$k_{\mathbf{red}}$ [·]	0.15	0.2	0.3	0.4
St [·]	0.095	0.127	0.19	0.25

0.2, 0.3 and 0.4. An LES study [4] reports that the average shedding frequency for a pitching aerofoil for $k_{\text{red}} = 0.025$ - 0.1 is averagely 0.1. The Strouhal number St of flow over a static aerofoil is relative to the angle of attack reported in [158], e.g. $St = 0.2$ for $\alpha \geq 18°$ (post-stall) and 0.02 for $\alpha \leq 15°$ (pre-stall). From, the power density spectra (Fig. 5.25 a - b), the vortex shedding frequency obtained for the different reduced frequencies falls only within post $-$stall angle of attack Strouhal number. For $k_{\text{red}} = 0.15$ - 0.4, the average Strouhal number is estimated $St = 0.17$.

The ratio between the aerofoil pitching frequency **f** and the primary non-dimensional vortex shedding frequency **s** in the spectra is estimated to be two (see Fig. 5.25 a - b)). The explains that the primary vortex shedding frequency (i.e. **s1 to s5**) is twice of their respective reduced frequencies. This means that at least two LEVs sheds sequentially per pitching cycle of aerofoil at different high phase angles.

5.6 Chapter summary

The effect of pitching motion at high reduced frequencies (i.e. $0.1 \leq k_{\text{red}} \leq 0.4$) on a wind turbine blade section under a deep dynamic stall is studied using 2D and 3D large-eddy simulation (LES). This study is focused on the effect of various high reduced frequencies induced on wind turbine blade sections at different span locations. From the results the author have drawn the following conclusions:

- The present 2D and 3D LES results, such as the lift, drag and moment coefficients, are in a reasonable agreement with the experimental and other numerical data in the references. In particular the excellent performance of the 2D LES at high reduced frequencies suggests that it could be a promising compromise to 3D LES for pitching aerofoil applications in terms of efficiency and accuracy. This is because the leading edge vortices (LEVs) are suppressed on the aerofoil suction side at a high reduced frequency, and the flow can be considered as quasi-two dimensional.
- The current LES data reveal that the force coefficients are evidently dependent on the pitching frequency. The lift coefficient at reduced frequency $k_{\text{red}} = 0.4$ increases up to 22% during the upstroke, and up to 64% during the downstroke compared with $k_{\text{red}} = 0.2$. The peak drag coefficient at reduced frequency $k_{\text{red}} = 0.4$ decreases up to 26% compared to $k_{\text{red}} = 0.2$. A dependency of the moment coefficient on the reduced frequency is noticeable - this

is primarily because the position of the aerodynamic force centre is affected by the pitching motion at different reduced frequencies. Overall the 2D LES data are consistent with the 3D LES data.

- Both the 2D and 3D data show that the dynamic stall occurs near the maximum angle of attack toward the downstroke within the range of reduced frequency $0.2 \leq k_{\text{red}} \leq 0.4$. This suggests that the dynamic stall angle for reduced frequency greater than 0.2 must be very close to the maximum angle of attack. The phase angle, at which the global minimum moment coefficient is predicted, shifts from the upper limit of the upstroke region into the deep downstroke region as the reduced frequency k_{red} increases from 0.1 to 0.4.
- Pitching motion at the high reduced frequency $k_{\text{red}} = 0.4$ significantly enhances the suppression of LEVs during the upstroke, and delays the reattachment of the boundary layer until a very low angle of attack in the downstroke. During the upstroke, the merging of LEVs within a chord length from the leading edge increases lift, while during the downstroke the splitting of LEV and trailing edge vortex (TEV) after their interaction causes a rapid drop of lift. It is also conclude that the interaction of LEV and TEV at a higher reduced frequency (e.g. $k_{\text{red}} = 0.4$) is weaker than that at a lower reduced frequency (e.g. $k_{\text{red}} = 0.2$).
- The primary vortex shedding frequency estimated from the power density spectra is twice the pitching frequency. This means that a minimum of two vortexes would be shad per pitching cycle of the aerofoil. In exception of $k_{\text{red}} = 0.1$ that the first LEV shed near the dynamic stall phase angle during the upstroke. All the other LEVs shed at high phase angles during the early part of the downstroke for reduced frequencies $k_{\text{red}} \geq 0.2$.

Overall, the effects of a pitching motion at high reduced frequencies on the aerodynamics of an aerofoil under a deep dynamic stall are evident. The provided more accurate aerodynamic force coefficients at various angles of attack, and reduced frequencies and the gained more understanding of physics from this study, can be used for improvement in the parameterisation of the operational blade element method (BEM). In addition, the 2D LES data demonstrate its fidelity compared to the 3D LES at high reduced frequencies, and suggest 2D LES be an efficient alternative for studying a section of a pitching wind turbine blade at high reduced frequencies.

In the next chapter, the turbulence inflow condition is applied to investigate the impact of large-scale turbulence on the aerodynamic characteristics and performance of the pitching blade section with a similar Reynolds number. This is crucial because the wind turbine aerodynamics is subject to freestream turbulence in the

atmospheric boundary layer. Such a study can also help to rule out uncertainties in the aspect of Reynolds number effect, as taking account of the freestream turbulence is effective to some extent modelling high Reynolds number effect.

Chapter 6

Turbulence inflow: impact of large-scale turbulence on a pitching wind turbine blade aerodynamics

6.1 Introduction

The impact of large-scale freestream turbulence on wind turbine blades is far to be understood, in particular, for a pitching blade, although, considerable experimental and numerical studies have been conducted for freestream turbulence effect on aerodynamic characteristics of static and pitching aerofoils as discussed in Subsection 2.3.2. For the latter, researchers focused on the effect of high turbulence intensity with small-scales turbulence ($\leq 0.1c$) [40, 4, 22]. They have concordantly inferred that an increase of the turbulence intensity increases the lift coefficients during the downstroke. It is to note that research on the effect of large-scale turbulence on the dynamic stall of a pitching turbine blade is not available in the literature. Table 2.3 summarised the recent available literature that reports on turbulence (small-scale) effect on pitching aerofoils aerodynamics.

Wind engineers for decades have conducted investigations on the effect of large-scale turbulence greater than the cross-section height of rectangular cylinders for the bluff body's aerodynamics [159, 160, 161, 162]. They reported that large-scale turbulence weakens the regular vortex shedding by reducing the spanwise correlation, and the pressure distribution is significantly affected by the incident flow of the incoming large-scale turbulence. Nevertheless, these findings are directly beneficial for designing high-rise buildings and long-span bridges aerodynamics.

In general, for static aerofoil, recent studies of the effect of large-scale turbulence on the aerodynamic characteristics and performance could not provide a consensus

view. The research works (e.g. [13, 12, 44]) supports the notion that large-scale eddy ($L_x \leq 1c$) significantly improve the aerodynamic performance of the blade by increasing the lift coefficient and lift-to-drag ratio. However, [42, 43, 45] argues that large-scale turbulence ($L_x \leq 0.4c$) adversely affects the aerodynamic characteristics and performance of a static aerofoil. These opposing views are from wind tunnel measurements [13, 12, 44, 43, 45] and LES study [42]. The discussion of detailed settings for these different studies are in Subsection 2.3.2. Indeed, numerical studies are required to give support to one side of the argument leading to a consensus.

It should be noted that the lack of consensus-view of large-scale turbulence effect on the aerodynamic performance for static aerofoil raises more questions than answers. Therefore, the need arises to investigate this critical research topic for clarification. Definitely, new numerical results of a pitching wind turbine blade that could account for the pre-stall and post-stall regime of a static aerofoil would provide a significant contribution to reaching a global consensus view for large-scale turbulence ($L_x \geq 1c$) effect on wind turbine aerodynamics. Appendix B presents preliminary findings obtained from the 2D LES approach of the topic in this chapter.

6.1.1 Outline of this chapter

In this chapter, the author aimed to numerically investigate the impact of large-scale inflow turbulence $L_x \geq 1c$, of which the chord length c is equal to 1 m of the studied pitching wind turbine blade section, and constant turbulence intensity ($TI = 11\%$) prescribed at the inflow inlet at a moderate Reynolds number $Re = 1.35 \times 10^5$. Section 6.2 describes the numerical settings, a brief overview of the synthetic inflow turbulence generation and modification of the mesh for easy application of inflow turbulence conditions. Section 6.3 presents verification of the prescribed inflow turbulence conditions used for the present study. This includes auto-correlation and two-point correlation functions and the turbulence kinetic energy (TKE) upstream of the computational domain.

Section 6.4 presents the validation of smooth inflow cases for reduced frequencies $k_{red} = 0.05$ and 0.1, spanwise domain-length sensitivity study with three different incoming large scales turbulence and a test case for the effect of small-scale turbulence with streamwise integral length-scale $L_x \leq 0.3c$ for $k_{red} = 0.1$. Section 6.5 presents the simulations of the impact of large-scale inflow turbulence on the aerodynamic characteristics and performance of a pitching blade for k_{red} 0.1 and 0.2, followed by the discussion of the results. In addition, a comparison of the surface pressure and skin-friction coefficients, also with snapshots of instantaneous vorticity contours for both the smooth inflow and large-scale inflow turbulence cases, to support the novel results obtained from the aerodynamic coefficients. Section 6.6

presents a new concept known as the dispersive (phase) shear stress to determine the contribution of the blade's motion to the mean flow in the wake of the wind turbine blade. Finally, the conclusions and summary of the novel contributions of this chapter were presented in Section 6.7.

Part of this work was presented in a conference paper published in the book of abstract (06A-1) by **T.E. Boye** and Z.T. Xie, UK Fluids Conference, University of Southampton, 8th - 10th September 2021 [50]. The results in this chapter were used to prepare a manuscript by **T.E. Boye** and Z.T. Xie "Impact of Large-Scale Turbulence on a Pitching Wind Turbine Blade Aerodynamics" to be submitted for paper publication in the Journal of Wind Engineering and Industrial Aerodynamics within the first quarter of 2022.

6.2 Numerical settings

The large-eddy simulation method discussed in Subsections 2.3.1.1 and 3.2.2, and Section 3.3 is adopted in this chapter. A synthetic upstream inflow turbulence generation approach denoted as XC [137] (developed in-house), which imposes correlations using an exponential function to satisfy the prescribed space and time integral length scales. The XC synthetic inflow turbulence generation is a synthetic digital filtering method for LES incompressible flow solvers. A minor modification to make the XC synthetic inflow turbulence generation code divergent-free gave birth to the new turbulence generation code denoted as XCDF [25, 163]. The detailed discussions for the inflow turbulence generation XC and XCDF methods are presented in Section 3.5. The XCDF synthetic inflow turbulence generation is then applied for all the large-scales turbulence simulations in the chapter.

The decision to adopt the XCDF for the present study is based on its efficiency crucially needed for the simulation of incoming large energetic eddies greater than $1c$ in size. Further details were discussed in the Subsection 3.5.2.

6.2.1 Adopted numerical settings

Similar numerical settings in Section 5.2 in Chapter 5 were applied for all the simulations in this chapter.

Figure 5.1, illustrates the motion of the pitching blade cross-section, a NACA 0012 profile at various phase angles Ψ. The pitching pivot was placed at $0.25c$ from the leading edge of the aerofoil. The pitching motion was described in Eq. 5.6 in Chapter 5. A similar Reynolds number $Re = 1.35 \times 10^5$ based on the chord length c is used in the present work. This is within the range of Reynolds numbers for small and medium wind turbines. Moreover, Reynolds number dependability is less on aerofoil subject to freestream turbulence than that of smooth inflow. Table 6.1 shows the pitching blade parameters.

Table 6.1: Parameters of the pitching blade

Profile	NACA 0012
Chord length	$1c$
Blade span length	$3c$
Re	1.35 $\times 10^5$
α_0	10°
α_1	15°
k_{red}	0.05, 0.1 and 0.2

Reduced frequency k_{red} was expressed in Eq. 2.1. The k_{red} = 0.05, 0.1 and 0.2 were examined in this chapter. The dynamic mesh technique [19] discussed in Subsection 3.4.3.5 was applied in Chapter 5 and is also adopted for the pitching motion of the wind turbine blade section in this chapter.

6.2.2 Mesh for turbulence inflow simulations

The inlet of mesh $3DM_3$ (see Table 5.2) is modified to form a new H-type structured mesh, which was generated in Pointwise V18 show in Fig. 6.1 (a), and used for the inflow turbulence simulations. The mesh used for the validation (smooth flow) was the original $3DM_3$ hybrid C-H type structured mesh (see mesh configurations in Table 5.2), which was used for the 3D simulations in Chapter 5. A skilful modification was performed in the construction of the upstream section of mesh $3DM_3$ for easy implementation of the visual plane of the inflow turbulence boundary conditions. It should be noted that imposing the inflow boundary condition, construction of the computational domain is essential to allow simple alignment of the inflow conditions at the inlet-plane [116].

The turbulence inflow 2D transverse plane (visual plane) is placed at x/c = -7 or -7c upstream from the leading edge of the turbine blade as shown in Fig. 6.1 (b) (a sketch of the new H-type computational domain (not to scale)). The leading edge of the aerofoil is located at $x/c = 0$, $y/c = 0$ and $z/c = 0$, which are the origin coordinates of the computational domain. The inflow plane location was derived from the sensitivity test conducted not shown in this thesis. The inflow plane location x/c = -7 is consistent with [4, 25] suggestion for similar computational domain streamwise-length, which ensure adequate development of the turbulence with less decay rate of the turbulence level before the flow reaches the specific area of interest (pitching blade).

Note that the boundary layer mesh-resolution is unchanged in the modified version of mesh $3DM_3$.

Tables 6.2 shows the boundary conditions imposed on the domain on both the hybrid C-H type and modified H-type meshes for laminar flow and turbulent flow simulations, respectively. The no-slip and symmetry boundary conditions are imposed on the wall (blade surfaces) and the lateral sides of the domain, respectively.

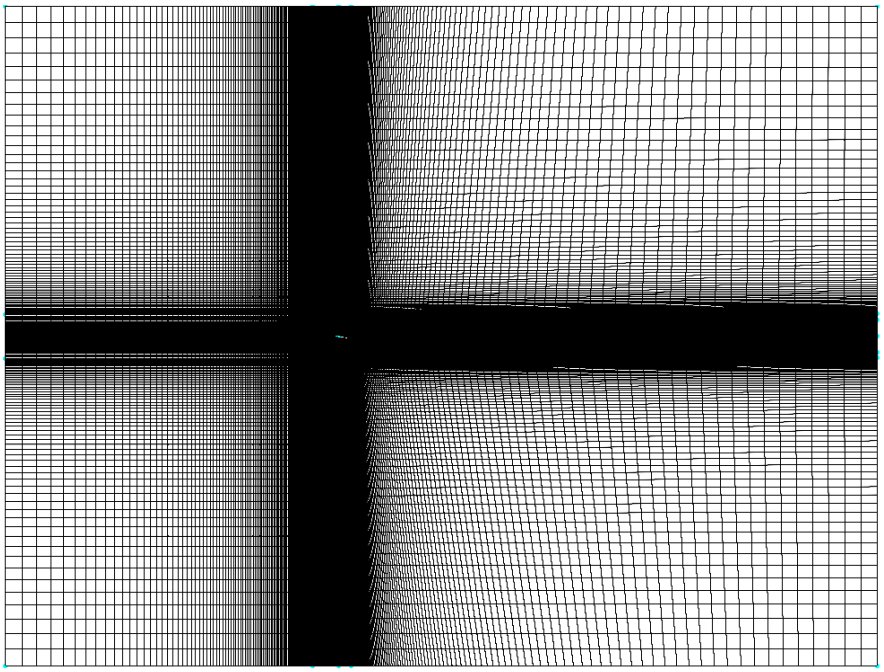

(*a*)

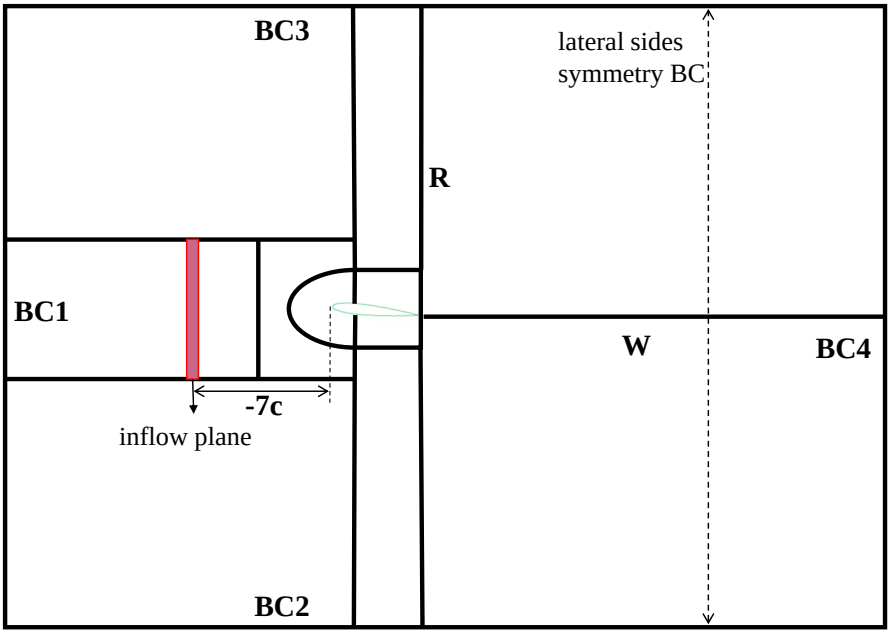

(*b*)

Figure 6.1: (a) Modified 3DM$_3$ mesh topology an H-type mesh. (b) A sketch of the modified computational domain (not to scale) , BC1, BC2, and BC3 inlet boundary conditions, while and BC4 is an outlet boundary condition, R is the radius, W is the wake, the symmetry BC on the lateral sides of the domain.

Table 6.2: Summary of the boundary condition BC. U_∞ is the freestream velocity and $\partial p/\partial n$ is the derivative to the boundary. x/c is the non-dimension location of visual plane for the synthetic inflow turbulence inlet. See Fig. 6.1 modified H-type mesh $3DM_3$ and Fig. 4.1 hybrid C-H type $3DM_3$ mesh in Chapter 5.

Mesh type	BC1	BC2	BC3	BC4	x/c
Hybrid C-type	$u_i = U_\infty$, $\partial p/\partial n = 0$	$u_i = U_\infty$, $\partial p/\partial n = 0$	$\partial u_i/\partial n = 0$, $p = p_\infty$	$\partial u_i/\partial n = 0$, $p = p_\infty$	n/a
Modified to H-type	$u_i = U_\infty$, $\partial p/\partial n = 0$	$u_i = U_\infty$, $\partial p/\partial n = 0$	$u_i = U_\infty$, $\partial p/\partial n = 0$	$du_i/dn = 0$, $p = p_\infty$	-7

The reasons discussed in Section 5.3 for the decision in symmetry boundary conditions on lateral sides of the domain is still valid.

6.2.3 Large-scale inflow turbulence parameters

Table 6.3 shows the turbulence parameters used to study the impact of large-scale inflow turbulence on wind turbine blade aerodynamics. The different turbulence length scales categorised are related to the streamwise integral length-scale L_x. In this chapter, large-scale turbulence is defined as the streamwise integral length-scale $L_x \geq 1c$ of the blade chord length. This definition is consistent with [103] characterisation of turbulence length scales in the atmospheric boundary layer. It is to be noted that the turbulence category defined as 'large-scale' (L_x) is one order of magnitude greater than those seen in relevant studies of small-scale turbulence (Table 2.3) effect on pitching aerofoil aerodynamics in the literature [e.g. 40, 15, 4, 14, 110, 22].

Table 6.3: Turbulence parameters adopted for the current study. L_x, L_y and L_z denotes integral length scales in the streamwise, cross-flow and spanwise directions respectively. TI denotes Turbulence intensity.

Turbulence Category	L_x	L_y	L_z	TI
Smooth inflow	-	-	-	0%
Small-scale	$0.3c$	$0.15c$	$0.15c$	11%
Large-scale	$1c$	$0.5c$	$0.5c$	11%
Large-scale	$1.5c$	$0.75c$	$0.75c$	11%

The XCDF method can generate synthetic turbulent eddies in Table 6.3 using Eqs. (3.48) - (3.53). By using exponential correlations, particularly, in the streamwise direction, it would significantly reduce the computational time compared to other digital filters methods [132].

The specific integral length scales and turbulence intensity (normal stresses) in all the three flow directions (x, y and z) are prescribed as the turbulence conditions

at the turbulence inflow-inlet (virtual plane) in the XCDF turbulence generation code. In order to generate synthetic isotropic large-scale turbulence in the domain, which is the focus of this study, the turbulence shear stress is set to zero.

6.3 Verification of the prescribed integral length-scale and turbulence kinetic energy

The integral length scales prescribed at the inflow inlet was verified for consistency with the actual turbulent eddies generated inside the domain by using the upstream turbulent fluctuations of the velocity u_i for correlation analysis. The integral time-scale (Eq. 1.1) auto-correlation function and two-point cross-correlation function (Eq. 1.2) were used for calculations of the effective integral length scales generated inside the domain. The former estimates integral length-scale in the streamwise direction while the latter estimates integral length-scale in the spanwise direction.

6.3.1 Auto-correlation

To obtain reasonable-converged correlation function, time series of 50,000 time-steps each from three different probe locations systematically arranged at middle-span section of the domain (i.e. $1.25 \leq z/c \leq 1.75$) upstream of the blade's leading edge was used for calculation of the correlation functions. Specifically, in the streamwise direction there are two probes at x/c = -7 and -3.5 while in cross-flow direction $y/c = 0$, and in the spanwise direction at z/c = 1.25, 1.5 and 1.75 respectively for both of the probes. The auto-correlation function for each of the three spanwise positions corresponding to the two probes at the streamwise locations was calculated and then spatially averaged $\langle\rangle$ to obtain an improved converged auto-correction function for each of the different streamwise locations at x/c = -7 and -3.5, respectively.

Figures 6.2 and 6.3 shows the integral time-scale - auto-correlation function for two large scales turbulence at the two different upstream locations inside the domain. To estimate the integral length-scale from the auto-correlation function. The correlation function was integrated until correlation dropped to a minimum value [164, 165], thereby, leads to a decision to cut-off at 0.25 of the correlation coefficient. This cut-off point would significantly reduce uncertainty compared to the zero-crossing approach for estimating the turbulence length-scale [166].

For the first prescribed lager-scale inflow turbulence ($L_x = 1c$) in the streamwise direction at the inflow inlet x/c = -7, the effective streamwise integral length scales inside the domain estimated from Fig. 6.2 (a-c) were $L_x = 1.05c$, $1.05c$ and $1.05c$ for the turbulent fluctuations u', v', and w' respectively. At x/c = -3.5 the

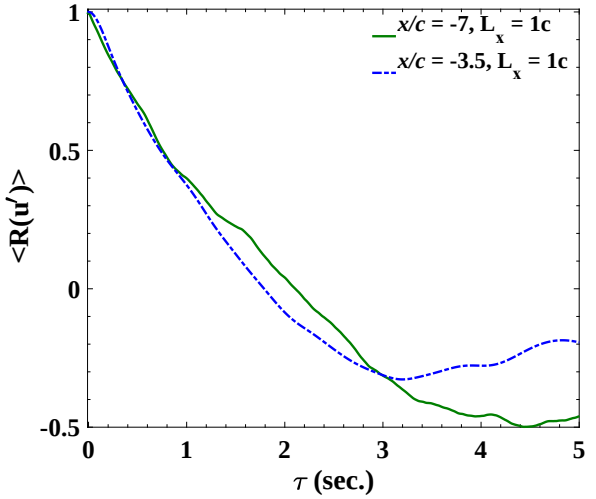

(a)

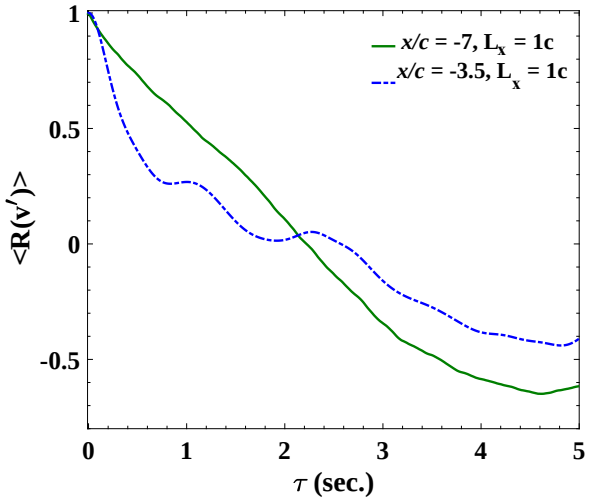

(b)

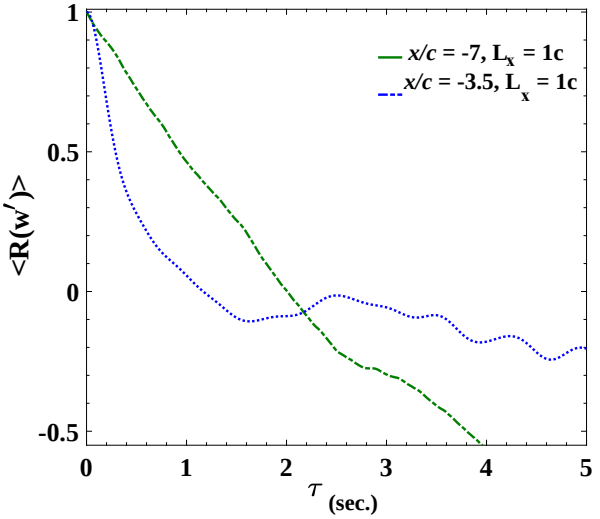

(c)

Figure 6.2: Integral time-scale auto-correlation function span averaged for the estimation of the streamwise integral length-scale $L_x = 1c$. (a) u′, (b) v′ and (c) w′.

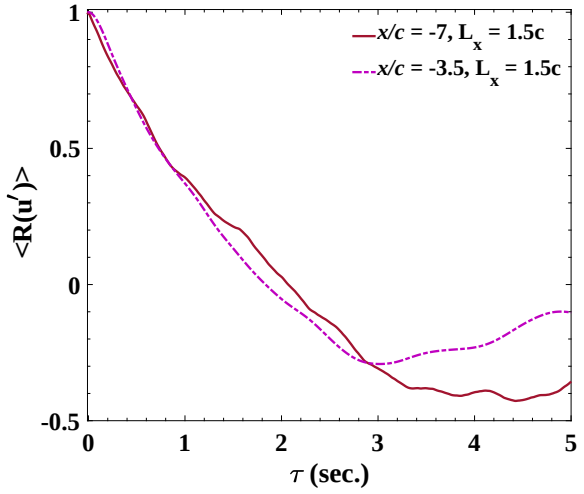

(*a*)

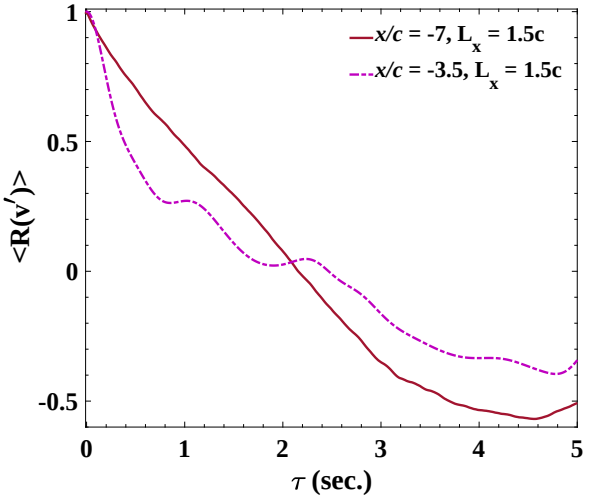

(*b*)

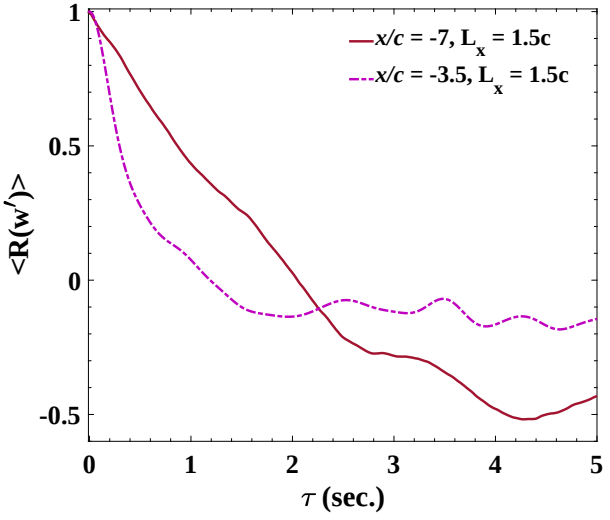

(*c*)

Figure 6.3: Integral time-scale auto-correlation function span averaged for the estimation of streamwise integral length-scale $L_x = 1.5c$. (a) u′, (b) v′ and (c) w′.

estimated integral length scales from Fig. 6.2 (a-c) were $L_x = 1c$, $0.93c$ and $0.55c$ for the turbulence fluctuations u′, v′, and w′ respectively.

For the second prescribed large-scale inflow turbulence ($L_x = 1.5c$) in the streamwise direction at the inflow inlet x/c = -7, the effective turbulence integral length scales in the domain estimated from Fig. 6.3 (a-c) were $L_x = 1.07c$, $1.15c$ and $0.95c$ for the turbulence fluctuations u′, v′, and w′ respectively, while at x/c = -3.5 the estimated integral length scales from Fig. 6.3 (a-c) were $L_x = 0.97c$, $0.95c$ and $0.55c$ for the turbulent fluctuations u′, v′, and w′ respectively.

It should be noted that the effective streamwise integral length scales in the domain are consistent with the ones prescribed at the inflow inlet-plane, particularly at location x/c = -7 (at the inflow inlet-plane location) in both the Figs. 6.2 (a-c) and 6.3 (a-c). However, the integral length scale of turbulent fluctuations v′ and w′ reduced noticeably as the flow developed and convect at location x/c = -3.5. The discrepancies at this location could be linked to the high angular velocity on the leading edge of the pitching blade motion. This could have an adverse influence on the developing turbulent flow streamwise, in particular on the turbulence fluctuations v′ and w′.

In addition, the effective integral length scales generated inside the domain at x/c = -7 shown in Fig. 6.3 (a-c) was different by an average of 34% compared to the second large-scale inflow turbulence ($L_x = 1.5c$) prescribed at the inflow inlet-plane. It should be noted that the present study is focused to generate streamwise large-scales inflow turbulence $L_x \geq 1c$ of which the effective turbulence length scales estimated in the domain fulfils this requirement, in particular at locations x/c = -7 and x/c = -3.5 shown in the both Figs. 6.2 (a) and 6.3 (a).

6.3.2 Two-point correlation

Figure 6.4 shows the effective spanwise integral length-scale L_z in a two-point correlation function at probe location x/c = -1, $y/c = 0$ and z/c = 1, 1.25, 1.5, 1.75 and 2. A similar spanwise averaging procedure described earlier for the auto-correlation function was employed to obtain an improved converged two-point cross-correlation function. The estimated effective spanwise integral length scales show in Fig. 6.4 are approximately $L_z = 0.51c$ and $0.575c$ for the first prescribed large-scale inflow turbulence ($L_x = 1c$, $L_y = 0.5c$, $L_z = 0.5c$) and the second prescribed large-scale inflow turbulence ($L_x = 1.5c$, $L_y = 0.75c$, $L_z = 0.75c$) respectively.

The effective spanwise integral length scale $L_z = 0.51c$ is consistent with the first prescribed large integral length scale while the other $L_z = 0.58c$ is approximately 24% less then the second prescribed large integral length scale. Given that the estimated effective spanwise integral length scales inside the domain are consistent with the prescribed ones, this gives confidence in the turbulence generation and is vital to commence the present study.

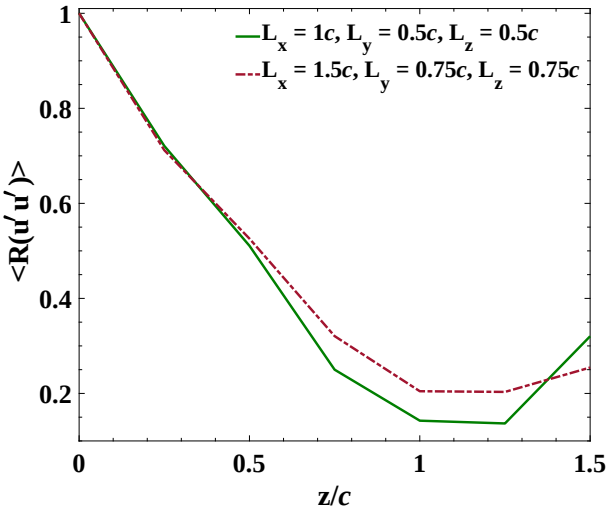

Figure 6.4: Two-point correlation of the streamwise instantaneous turbulent fluctuations at x/c = -1 for estimation of the integral length-scale L_z in the spanwise direction.

6.3.3 Turbulent kinetic energy (TKE)

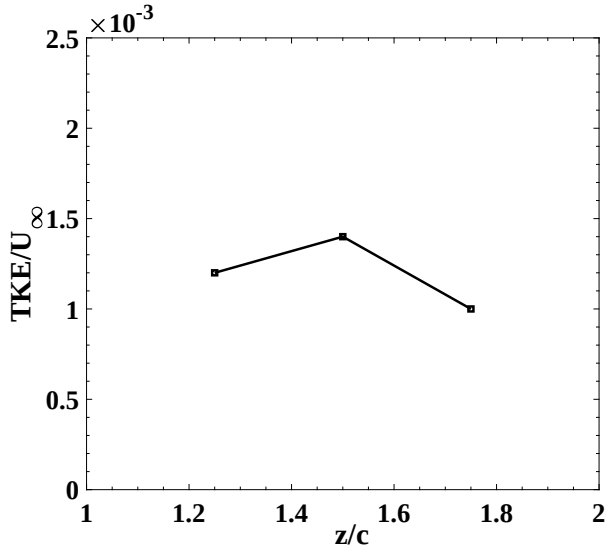

Figure 6.5: Turbulent kinetic energy (TKE) normalised by U_∞ at x/c = -3.5, $1.25 \leq$ z/c ≤ 1.75.

Another crucial characteristic of turbulence is that the turbulence intensity (IT) or turbulent kinetic energy (TKE) is assumed to be homogeneous in the spanwise direction. Therefore, the homogeneity of TKE on the blade's span is verified. Fig. 6.5 shows the turbulent kinetic energy (TKE) in the upstream location x/c = -3.5c and spanwise direction z/c = 1.25, 1.5 and 1.75. A similar spatial averaging procedure for the correlation functions was adopted to estimate the TKE at location x/c = -3.5. It is assumed that TKE is homogeneous in the middle 1c section of the

span i.e. $1 \leq z/c \leq 1.75$. However, the discrepancy observed between the middle point and the other points is due to uncertainty. In addition, Fig. 6.5 data confirm that the effect of the symmetry boundary conditions imposed on the lateral sides of the domain ($3c$) is small at the middle plane of the blade span .

It is to be noted that the synthetic inflow turbulence generation is simplified with the assumption of isotropy turbulence and, such an assumption is because the incoming flow Reynolds shear stresses are set to zero. Nevertheless, in physical flows, either in the wind or water tunnels, background turbulence is found to be isotropy and also, after a sufficiently long distance behind a passive grid [45, 167]. Indeed, the turbulence characteristics of isotropy turbulence generation by the XCDF method was examined in [25], and [130, 143] also showed that the power density spectral had a good agreement with von Karman wind spectral. Since these types of verifications of turbulence generation by the XCDF method is well tackled in other relevant studies then a similar analysis is therefore not required in the present study.

6.4 Baseline simulations

The validation of the aerodynamic coefficients for $k_{\text{red}} = 0.05$ and 0.1 in 3D smooth inflow is performed. In addition, the span-length sensitivity test for large-scale inflow turbulence is carry-out in this section. This is crucial to determine an optimal span length to accommodate large-scale turbulence greater than chord length. Furthermore, a test case simulation for small-scale turbulence for $k_{\text{red}} = 0.1$ is conducted for verification and to applying the inflow turbulence generation and for validation purposes.

6.4.1 Validation in smooth inflow

Figures 6.6 and 6.7 shows a comparison of the aerodynamic coefficients in smooth inflow between the present simulations and reference LES [22, 4], and experiment [21] for $k_{\text{red}} = 0.05$ and 0.1 respectively. The present results of the lift coefficient C_L (Fig. 6.6 (a)) agrees very well with the reference LES predictions [22]. It is also in good agreement with the wind tunnel measurements [21]. The present LES prediction of the first and second peaks of the lift, which is owing to sheds of the first and second LEVs near the maximum angle of attack in the early stage of the dynamic stall, are the same with the wind tunnel measurements [21]. The present drag coefficient C_D (Fig. 6.6 (b)) shows good agreement with those of the reference LES [4] and experiment [21].

Figure 6.7 shows a comparison of aerodynamic coefficients between the present results and reference LES [22] and experiment [21] for $k_{\text{red}} = 0.1$. The present LES results agree very well with the reference LES predictions [22]. They are also

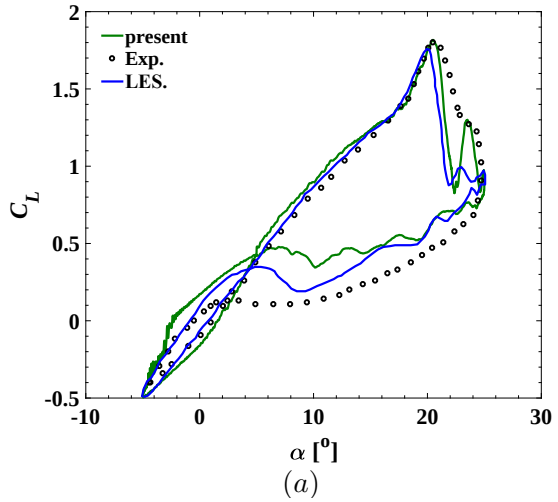

(*a*)

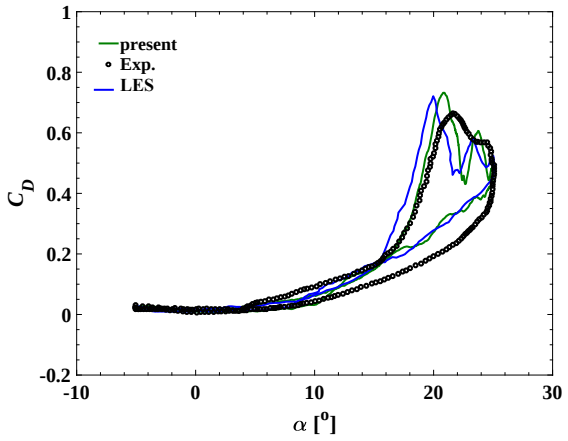

(*b*)

Figure 6.6: Aerodynamic coefficients (a) lift, (b) drag, $k_{\text{red}} = 0.05$. Exp. [21], LES C_L [22], C_D [4].

in good agreement with the wind tunnel measurements [21], except for the peak lift and minimum moment coefficients at the maximum α and at $\alpha \geq 20°\downarrow$. Note that the same reasons given for the discrepancies in the lift and moment coefficients for $k_{\text{red}} = 0.1$ in Section 5.4 are still valid. Therefore, no need for repetition in this chapter.

6.4.2 Span-length sensitivity study for large-scale turbulence

A span length twice the prescribed spanwise integral length-scale $\mathbf{L}_z$ is typical when studying turbulence effect on flows surrounding an aerofoil/blade to ensure accurate spatial correlation of the turbulent velocity in the spanwise direction. This setting appears to be the main advantage for small-scale turbulence numerical investigations, and it is due to the less computational cost overheads compared to the simulation of large-scale turbulence.

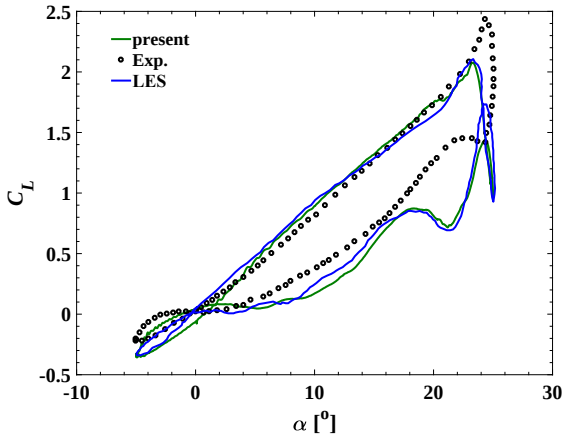

(a)

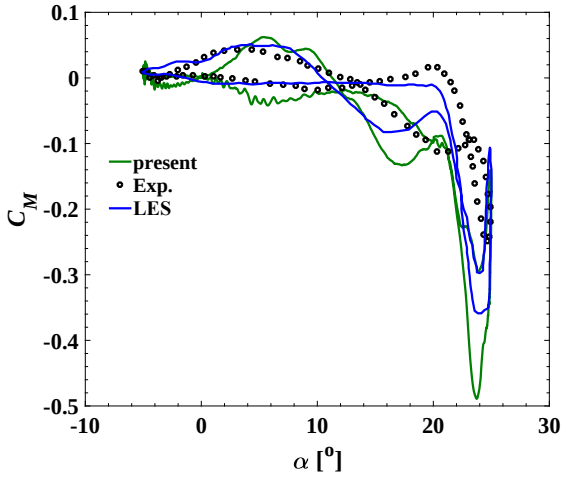

(b)

Figure 6.7: Aerodynamic coefficients (a) lift, (b) drag, $k_{\text{red}} = 0.1$. Exp. [21], LES [22].

A number of numerical studies that investigates small-scale structures uses span-length ranging between $0.2c$ and $0.5c$ [168, 169, 4, 106, 45]. However, considering realistic flow structures sizes in the ABL, it would be necessary to improve the spanwise settings greater than those seen in the literature. [170], and [171] postulated that small-scale structures tend to neutralise each other, while flow structures comparable to the chord length are the more influential and lead to quasi-static variations in the incoming flow. Indeed, this emphasises the importance to investigate large-scale turbulence effects in which only a very large span length is inevitable for use to ensure physical application and obtain quantitatively reliable data for turbulent flow.

In this section, three large scales inflow-turbulence for two different span lengths were used in performing the span-length sensitivity test. The same number of grid points were used to discretize the two different span lengths. Table 6.4 shows

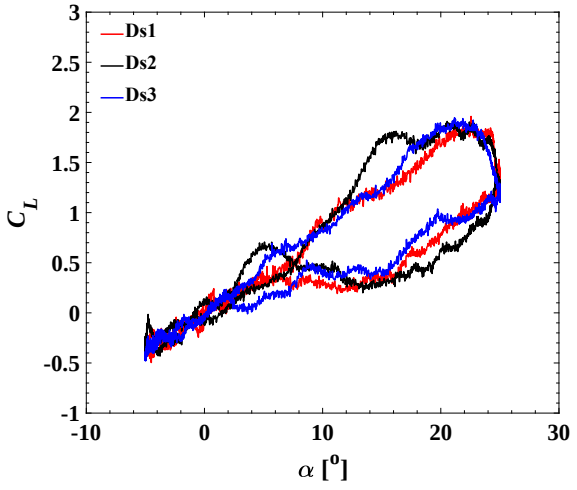

(*a*)

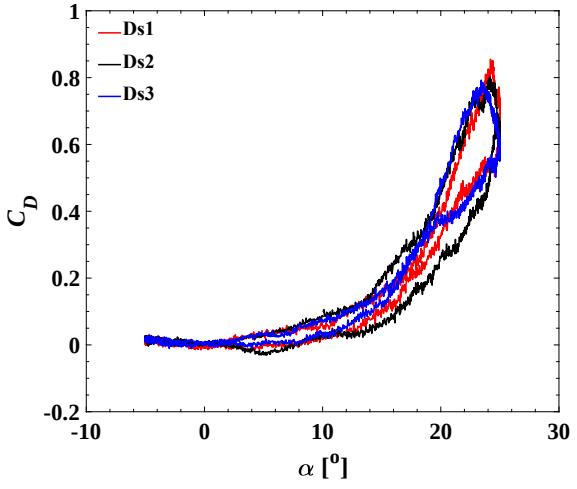

(*b*)

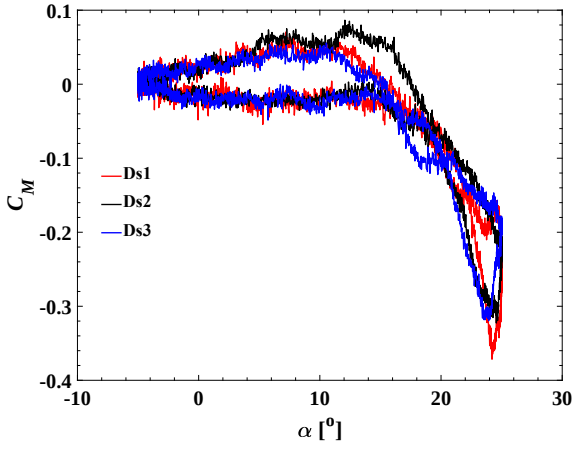

(*c*)

Figure 6.8: Effect of span-length on aerodynamic force coefficients (a) lift, (b) drag and (c) moment for large-scale inflow turbulence, $k_{\text{red}} = 0.1$.

Table 6.4: Span length and large-scale inflow turbulence parameters used for sensitivity study. Note **s** is the span-length, N_z is the number of grid points in the spanwise direction, c is the chord length and Ds1, Ds2 and Ds3 denote domain-span 1, 2 and 3 respectively. $\mathbf{L}_x$, $\mathbf{L}_y$, $\mathbf{L}_z$ for integral length-scale in streamwise, cross-flow and spanwise directions respectively. TI is Turbulent intensity.

case	**s**	N_z	$\mathbf{L}_x$	$\mathbf{L}_y$	$\mathbf{L}_z$	TI	**Category**
Ds1	$1.5c$	60	$1.2c$	$0.63c$	$0.6c$	11%	Large-scale
Ds2	$1.5c$	60	$1.25c$	$0.5c$	$0.625c$	11%	Large-scale
Ds3	$3c$	60	$1.5c$	$0.75c$	$0.75c$	11%	Large-scale

details of the different domains and inflow turbulence parameters for the sensitivity test.

The reduced frequency $k_{\text{red}} = 0.1$ is set for the motion of pitching blade. It is be noted that three cycles of the pitching blade were used for post-processing, such as phase averaging of the aerodynamic force coefficients, while only one cycle is used to initialise the simulation. Indeed, it is expected that more than three cycles for phase averaging would produce a better convergence of the numerical results. Nevertheless, a compromise between results accuracy and computational cost, three cycles are reasonable for post-processing the numerical data.

Figure 6.8 (a-c) shown the effect of domain span-length for large-scale inflow turbulence on aerodynamic force coefficients. The lift coefficient C_L for case Ds2 (s = $1.5c$) is affected by the span-length compared to the case Ds1 (s = $1.5c$) of which the integral length scales prescribed in the domains are of the same order. The difference between Ds1 and Ds2 spanwise integral length scales L_z is 4%. Moreover, the length scales L_z for cases Ds1 and Ds2 are slightly lesser than half of their respective span-length (s = $1.5c$). Fig. 6.8 (a) shows that case Ds2 have a big jump on the lift at $12°\uparrow \leq \alpha \leq 19°\uparrow$ and a broader lift hysteresis loop curve during the downstroke at a high angle of attack compared to cases Ds1 and Ds3. These differences were attributed to the limited span length, which is small to allow the natural growth of the separation bubble on the blade suction surface during the upstroke.

For case Ds3 (s = $3c$) the effect of the span-length is not visible on the lift coefficient shown in Fig. 6.8 (a). This is due to the longer span-length large enough to allow growth of the separation bubble comparable to chord-length with negligible spanwise blockage. Note that the spanwise integral length-scale $\mathrm{L}_z = 0.75c$ in Ds3 is 20% greater than case Ds2 spanwise integral length-scale $\mathrm{L}_z = 0.625c$.

For the drag and moment coefficients shown in Fig. 6.8 (b) and (c) respectively, similar domain effects were observed. Noted, that case Ds3 span-length is double of the cases Ds1 and Ds2 span lengths. Therefore, it can be deduced that a span-length four times greater than the spanwise integral length scale L_z must be used for the simulation of large-scale inflow turbulence effect. Otherwise, span-length

less than four times the spanwise integral length-scale might cause the results to be unpredictable.

To reduce uncertainty on the numerical solutions from the effect of span-length for large-scale turbulence simulations, the computational domain with span-length (s = $3c$) discretized with 120 grid points (e.g. H-type mesh $3DM_3$) is adopted for the rest of the simulations. Indeed, this means that the accuracy of the numerical results is prioritised than the high computational cost, which makes the task even more challenging.

6.4.3 Test case: effect of small-scale inflow turbulence

It is stated that small-scale inflow turbulence of integral length-scale $\leq 0.3c$ and TI = 10% increase the lift coefficient of a pitching aerofoil by 50% during the downstroke [4]. This was certain because the incoming turbulence breaks-down the separation bubble resulting in a reduced separation region, and the re-attachment occur earlier for low reduced frequency $k_{\text{red}} = 0.05$ [4] (Ref. Fig. 2.14). Nevertheless, uncertainties of the effect of small-scale inflow turbulence is yet unresolved from a numerical study perspective, for example flow of higher $k_{\text{red}} \geq = 0.1$ at α_0 = 10°and α_1 = 15°associated with deep stall.

More recently, [22] reported similar findings for the effect of small-scale inflow turbulence with the same order of integral length-scale [4] and TI = 5% on the lift coefficient during the downstroke for $k_{\text{red}} = 0.2$ at $\alpha_0 = 15°$and $\alpha_1 = 10°$. The study utilises the LES approach. Furthermore, these numerical studies inferred [4, 22] were consistent with an experimental [40] investigation conclusion.

In this subsection, it is aimed to numerically study the effect of small-scale inflow turbulence and TI = 11% on a pitching blade for high $k_{\text{red}} = 0.1$ at $\alpha_0 = 10°$and $\alpha_1 = 15°$. Therefore, this would bridge the gap between $k_{\text{red}} = 0.05$ and 0.2 of any uncertainties for the effect of small-scale turbulence in the literature. In addition, the results in this subsection will be used for comparison with relevant data in the literature and the results of the effect of large-scale turbulence simulations. The latter is the main focus of this chapter. Note that streamwise integral length-scale L_x is used to identify simulation cases and for easy reading except otherwise.

Figure 6.9 shows the effect of small-scale inflow turbulence of integral length-scale ($L_x = 0.3c$, $L_y = 0.15c$, $L_z = 0.15c$) and TI = 11% on the aerodynamic characteristics for $k_{\text{red}} = 0.1$. In general, there is no significant effect of the small-scale turbulence on the force and moment in the prescribed conditions. The peak lift, drag and minimum moment are quite similar as those of the smooth inflow case.

The most evident effect of freestream turbulence on the lift coefficient occurs during the downstroke (Fig. 6.9 (a)) when the lift coefficient increase approximately by

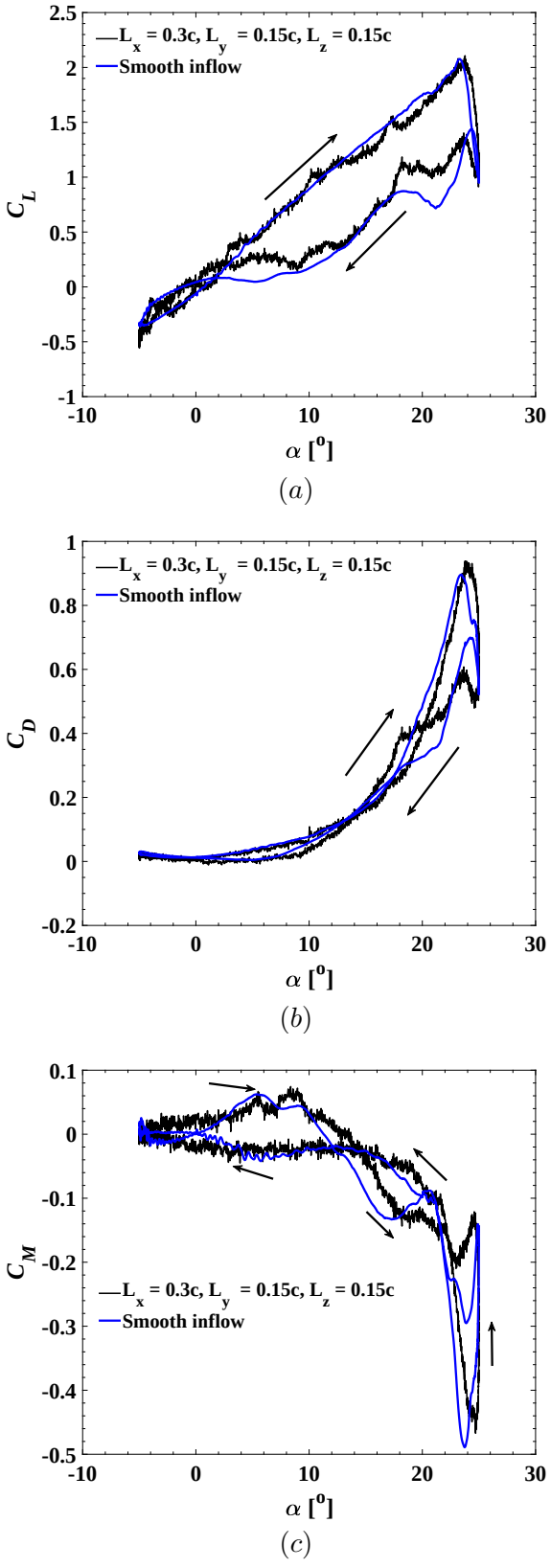

Figure 6.9: Effect of small-scale inflow turbulence on aerodynamic coefficients. (a) lift, (b) drag and (c) moment. $TI = 11\%$, $k_{\text{red}} = 0.1$.

45% compared to the smooth inflow case. This effect is due to the inflow turbulence suppression of the second LEV and TEV shed at the early stage of the dynamic stall procedure. Thus, leaves no clear evidence of two counter-rotating vortices on the lift coefficient as observed in the smooth inflow case at region $18°\downarrow \leq \alpha \leq 24°\downarrow$. At this region where the impact of inflow turbulence is evident on the lift coefficient, a similar effect is also visible on the drag and moment coefficients but in smaller magnitudes (Fig. 6.9 (b-c)). Another evident impact of the small-scale inflow turbulence is that reattachment of the flow occurs much earlier (e.g. approximately $\alpha = 7°\downarrow$) for inflow turbulence case ($L_x = 0.3c$) than that of the smooth inflow case $\alpha \approx 2°\downarrow$ during the downstroke. It is to be noted that the effect seen in Fig. 6.9 is attributed more to the turbulent intensity rather than the small integral length-scale. Because the results are consistent with data from small integral length-scale and high turbulent intensity in the literature, e.g. numerical studies - LES [4, 22] and experimental measurement - wind tunnel [40]. In addition, small-scale structures tend to neutralise each other.

The new results of the effect of small-scale inflow turbulence and high turbulence intensity on the aerodynamics characteristics obtained from $k_{\text{red}} = 0.1$ in the present study gives further confidence in the numerical settings and application of inflow turbulence generation to investigate the impact of large-scale inflow turbulence on a pitching wind turbine blade. Furthermore, these results bridges the research gap between $k_{\text{red}} = 0.05$ and 0.2 of any uncertainties for the effect of small-scale turbulence in the literature.

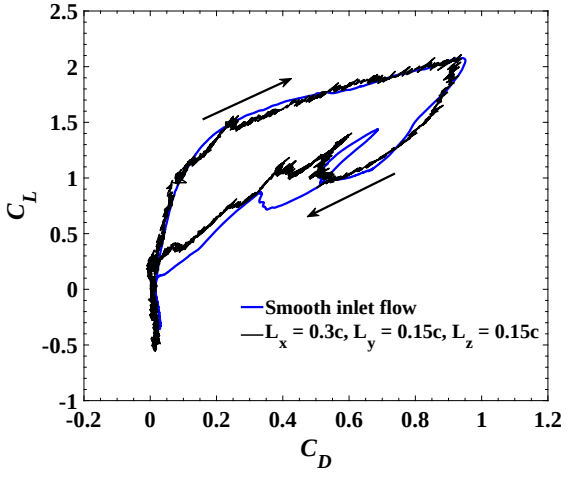

Figure 6.10: Drag polar for small-scale turbulence, $k_{\text{red}} = 0.1$.

Figure 6.10 shows the drag polar curve for small-scale turbulence $L_x = 0.3$, $TI = 11\%$. The maximum lift-to-drag ratio between the smooth inflow case and small-scale turbulence case are similar, which indicates that the maximum aerodynamic performance is not affected and a small increase ($\approx 20\%$) of the performance at the middle region of the downstroke with the given turbulence conditions.

6.5 Impact of large-scale inflow turbulence

In section 6.4.3 the of effect small-scale turbulence with integral length-scale $L_x = 0.3c$ and $TI = 11\%$ was conducted as a test case simulation for the present study. Wind turbine operates in the ABL where larger-scale turbulence or weather-scale flow structures are dominant. Therefore, realistic eddies size ($\geq$ 1 m) in the ABL are considered in the simulations of this section.

The large-scale turbulence category in Table 6.3 is the focus of this section. The reduced frequencies $k_{red} = 0.1$ and 0.2 are the cases to be investigated because they fall within unsteady flows motion [72, 74] usually the type of flows around wind turbine in operation. It should be noted that smooth inflow is referred to as flow with $TI = 0$ while large-scale inflow turbulence is referred to as turbulent flows with inflow conditions detailed in Table 6.3.

6.5.1 Effect on aerodynamic characteristics for $k_{red} = 0.1$

The effect of large-scale inflow turbulence on aerodynamic characteristics, performance, instantaneous vorticity field, pressure and skin-friction coefficients at different angles of attack for $k_{red} = 0.1$ are discussed and presented.

6.5.1.1 Phase-averaged aerodynamic coefficient

Figure 6.11 shows the effect of incoming large-scales turbulence on aerodynamic characteristics for $k_{red} = 0.1$. In general, the large-scale inflow turbulence does significantly change the force and moment hysteresis at the given conditions.

The angles for the maximum lift, drag and minimum moment are evidently different from those of the smooth inflow case. The magnitudes of the maximum lift and drag coefficients reduced noticeably, while the minimum global moment coefficient increased with the increased turbulence integral length-scales and a constant turbulence intensity. These effects are primarily due to the large integral length-scale, in contrast to the effect of small integral length-scale with the same turbulence intensity (see Fig. 6.9).

The most visible impact of large-scale inflow turbulence on the lift coefficient occurred near the maximum angle of attack during the upstroke and the downstroke just after the dynamic stall event (Fig. 6.11 (a)), when the lift coefficient reduced evidently as the integral length-scale increases. The average decrements for the different large-scales inflow turbulence cases are approximately 21% and 20% at the peak lift coefficients for cases $L_x = 1c$ and $L_x = 1.5c$ respectively. In addition, the lift coefficients are reduced by an average of 22% within $15°\downarrow \leq \alpha \leq 22°\downarrow$ during the downstroke for both the cases. The reason for this significant lift reduction seen on the peak lift and most phase angles at the early stage of the dynamic

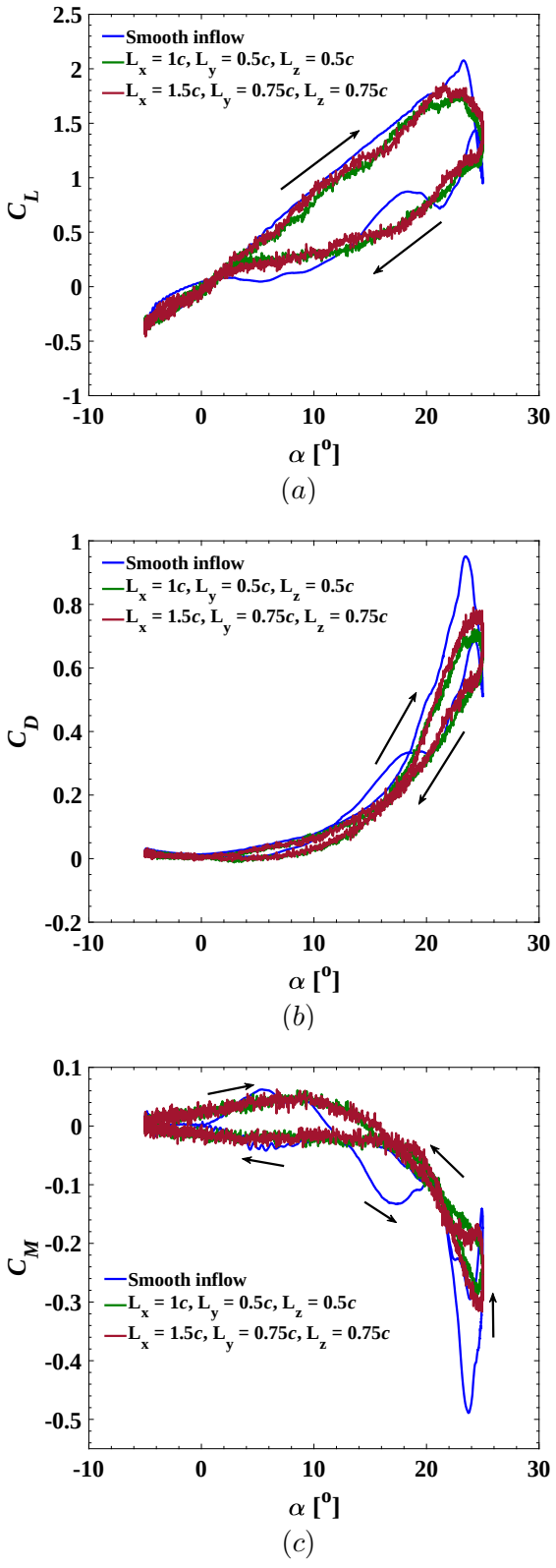

Figure 6.11: Effect of large-scale turbulence on aerodynamic coefficients. (a) lift, (b) drag and (c) moment, $k_{\text{red}} = 0.1$.

stall during the downstroke are owing to the disordered LEVs structures from an impingement of the incoming large-scale turbulence. For example, this could be described as turbulence entrainment - the process in which mass is transferred (e.g. large-scale inflow turbulence) from the external flow regime into the volume of turbulent flow (e.g. LEV generated by the pitching blade) from the background (see Fig. 6.13 (b) - (d) (middle) and (right)).

The effect of large-scale inflow turbulence on the lift coefficient is opposite to that of small scales turbulence [4, 22]. By using LES to studied small-scale turbulence of integral length-scale $\leq 0.3c$ and turbulence intensity 5% [22] and 10% [4] at reduced frequency 0.05 [4] and 0.2 [22]. They found that the peak lift angle showed little change during the upstroke, while an evident lift increment was seen during the downstroke as the turbulence intensity increased. A similar observation was recorded in Section 6.4.3 for the test case of small-scale turbulence effect on a pitching blade for $k_{\text{red}} = 0.1$.

In the present study, it should be noted that the variation at some phase angles during the upstroke and downstroke of the lift coefficients (Fig. 6.11 (a)) are within the range of uncertainties, specifically for the large-scale inflow turbulence cases. Another visible effect of large-scale inflow turbulence is the early re-attachment of the boundary layer flow occurs approximately at $\alpha = 11°\downarrow$ for both of the large-scale inflow turbulence cases compared to smooth inflow case, which occurs approximately at $\alpha = 2°\downarrow$ during the downstroke shown in Fig. 6.11 (a).

The peak drag coefficients for large-scale inflow turbulence cases evidently decreases compared to that of smooth inflow case shown in Fig. 6.11 (b). The difference of the drag coefficients for large-scale inflow turbulence cases compared to smooth inflow case is directly correlated to that of lift coefficient since the drag primarily consists of pressure forces compared to the skin-friction. It was observed that turbulence does not evidently enhance the drag coefficient. At most phase angles during pre-stall and post-stall, the drag coefficient of the smooth inflow case is higher than those of large-scale inflow turbulence cases. The average peak drag coefficients of the large-scale inflow turbulence cases decreased approximately by 21% than that of the smooth inflow case. This fundamental change of the peak drag coefficients was not observed in the small-scale turbulence effect in Section 6.4.3, and in the literature (e.g. [4, 22]).

The impact on the minimum moment coefficient by large-scale inflow turbulence is similar to the effects observed on the lift and drag coefficients. The most visible impact of turbulence on the moment coefficient occurs at dynamic stall angle and during the downstroke shown in Fig. 6.11 (c). The 'memory' (the area in the hysteresis loop) reduced significantly for both large-scales inflow turbulence cases, at high angle of attack and during the downstroke, where separated flows are dominant (see Fig. 6.13 (e) (middle) and (right)). This is owing to the suppressed

and shed LEVs, which are disordered by the impact of incoming turbulence. It can be deduced that the energy of LEVs shed in smooth inflow at the maximum angle of attack is higher than those of the large-scales inflow turbulence. This further shows the magnitude of impact on the LEV structures. Indeed, the average difference of the global minimum moment coefficients between the smooth inflow case and large-scale inflow turbulence cases is approximately 60%. This is because the moment coefficient absolute values are small results in higher uncertainty. Moreover, this suggests that the moment, which is very sensitive to LEVs shed due to the blade's motion, is impacted most compared to the lift and drag coefficients by large-scale turbulent flow. Furthermore, this gives more data and context for new design considerations of reducing fatigue and tackling issues due to wind turbulence on the wind turbine blades.

Overall, the data shown in Fig. 6.11 can draw a conclusion that the aerodynamics force coefficients change evidently under the impaction of large-scale inflow turbulence, e.g, integral length scales $L_x = 1c$ and $L_x = 1.5c$ for $k_{red} = 0.1$.

6.5.1.2 Aerodynamic performance - drag polar

The lift-to-drag ratio (drag polar) is a principal parameter for designing an efficient wind turbine blade. Fig. 6.12 shows a comparison of the phase averaged drag polar curves between smooth inflow and large-scales turbulence for one cycle of the blade for $k_{red} = 0.1$.

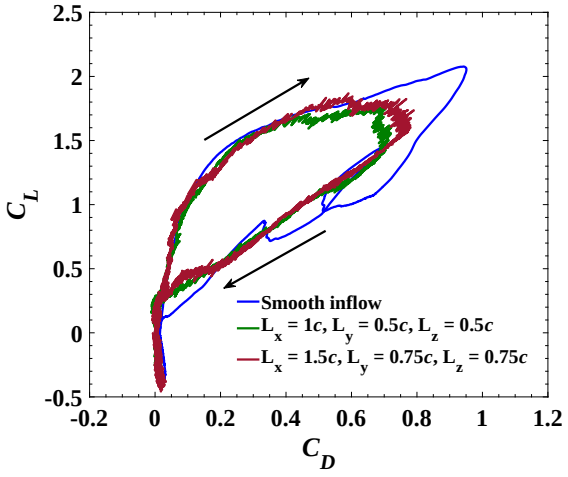

Figure 6.12: Aerodynamic performance - drag polar, $k_{red} = 0.1$.

There is a significant difference between the smooth inflow case and large-scale inflow turbulence cases. The evident difference occurs at the peak lift-to-drag ratio and some portion during the downstroke. The large-scale inflow turbulence cases lift-to-ratio declined sharply during the downstroke compared to the smooth inflow case, which has a small loop within the big polar drag curve. It was observed

that large-scale inflow turbulence cases stalls early but have a slightly high lift-to-drag ratio during the downstroke. Nevertheless, the aerodynamic performance of the pitching blade is severely affected by the large-scales inflow turbulence. In particular, at the peak polar drag, which is different compared to the small-scale turbulence drag polar data shown in Fig. 6.10.

The average difference between the smooth inflow and the large-scale inflow turbulence cases at the peak polar drag is within 18%. This is consistent with the average difference estimated from the lift and drag coefficients shown in Fig. 6.11 (a-b). Overall, the shape of polar drag curves loops of the large-scale inflow turbulence cases (Fig. 6.12) signifies reduced performance compared to the smooth inflow case.

To use a different approach to examine the impact of large-scale inflow turbulence on the aerodynamic performance and characteristics of the pitching wind turbine blade. Therefore, the vorticity contours for different angles of attack are presented in the proceed subsection.

6.5.1.3 Vorticity field

Figure 6.13 shows snapshots of the instantaneous spanwise component of vorticity at the mid-span plane with smooth inflow (left), large-scale inflow turbulence cases $L_x = 1c$ (middle) and $L_x = 1.5c$ (right) for $k_{red} = 0.1$.

In the smooth inflow case $\alpha = 15.8°\uparrow$ to $\alpha = 21.8°\uparrow$ (Fig. 6.13 (a) - (b) (left)), the boundary layer flow on suction side of the blade is largely attached and continuous growth of the first LEV is observed near the blade's leading edge. For both the large-scales inflow turbulence cases (Fig. 6.13 (a) - (b) (middle) and (right)), boundary layer separations are visible, while the first LEVs are difficult to discern due to their interaction with the large-scale inflow turbulence.

In Fig. 6.13 (c) (left), the first LEV has grown to maturity ready to detached, which resulted in a significant increment of the peak lift coefficient near the dynamic stall angle $\alpha \approx 23.3°\uparrow$. This is consistent with Fig. 6.11 (a). Such a phenomenon at this phase angle is not evident in both the large-scales inflow turbulence cases ((Fig. 6.13 (c) (middle) and (right)). This is because incoming large-scale turbulence breaks down and disorders the LEVs structures, which causes early stall, and significant changes in the aerodynamic force coefficients. This is again consistent with Figs. 6.11 (a) - (c) and 6.12. In addition, Fig. 6.14 (b) - (d) shows the pressure and skin-friction coefficients with further evidence of the LEVs suppression for large-scale inflow turbulence cases.

At $\alpha \approx 24.9°\uparrow$ near to the maximum angle of attack ((Fig. 6.13 (d) (left)) interaction between the first LEV and first TEV is observed for smooth inflow case, which makes the lift recover slightly (see the small loop in Fig. 6.12). Whereas,

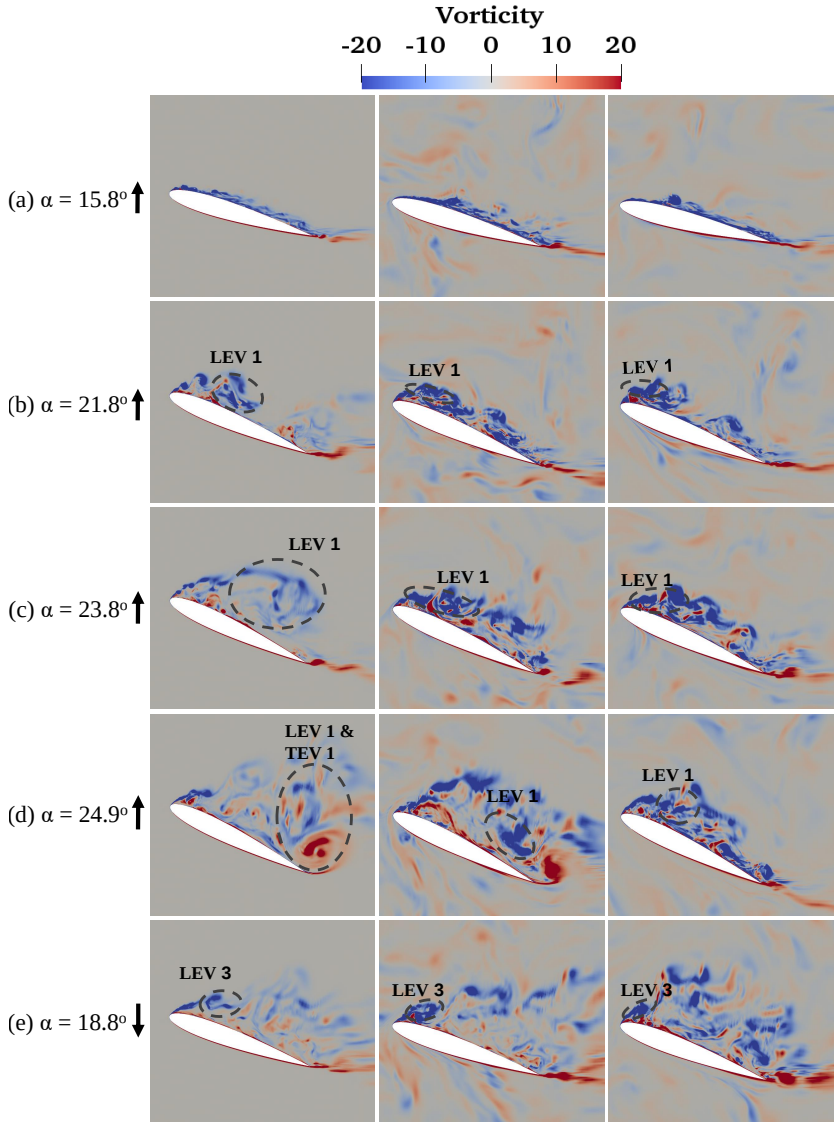

Figure 6.13: Snapshots of the instantaneous vorticity field contours normalised by c and U_∞. (left) smooth inflow, (middle) $L_x = 1c$, (right) $L_x = 1.5c$, $k_{red} = 0.1$. (a) $\alpha = 15.8°\uparrow$, (b) $\alpha = 21.8°\uparrow$, (c) $\alpha = 23.8°\uparrow$, (d) $\alpha = 24.9°\uparrow$, (e) $\alpha = 18.8°\downarrow$. The marked dash ellipse corresponds to the LEV's length and location in Fig. 6.14, in particular the skin-friction.

there is no evidence of the two counter-rotating vortices in both the large-scale inflow turbulence cases ((Fig. 6.13 (d) (middle) and (right)), which makes the lift coefficients drop sharply (see Figs. 6.11 (a) and 6.12).

At $\alpha = 18.8°\downarrow$ for the smooth inflow ((Fig. 6.13 (e) (left)) the third LEV (second LEV not show here, (see Fig. 5.23 (left) I.D. 7)) begins to form near the leading edge of the blade, which increases the lift slightly. However, for both the large-scale inflow turbulence cases ((Fig. 6.13 (e) (middle) and (right)) the third LEVs appears very small near the leading edge of the blades, and complete separation of the boundary layer flow mixing with the incoming large-scale turbulence

(like turbulent entrainment process) is evident. This causes large drop of the lift coefficients within this region $15° \downarrow \leq \alpha \leq 22° \downarrow$ (see Fig. 6.11 (a)).

The energetic large-scale inflow turbulence interaction with large flow structures (e.g. LEVs) results in significant break-down, disorder and suppression during the upstroke regime and disturb separated flows at most phase angles during the downstroke regime, which affects the aerodynamics characteristics of the pitching blade at $k_{\text{red}} = 0.1$. To get a further understanding of the impingement on LEVs by the energetic large-scale inflow turbulence, the surface pressure and skin-friction coefficients distributions around the pitching blade were analysed in the proceed subsubsection.

6.5.1.4 Blade surface pressure and skin-friction coefficients

The spanwise averaged surface pressure and skin-friction distributions are obtained for the smooth inflow case and large-scale inflow turbulence cases at different angles of attack that corresponds to those in Fig. 6.13.

Figure 6.14 shows comparison of the spanwise averaged pressure coefficient C_p (top) and skin-friction coefficient C_f (bottom) between smooth inflow case and large-scales inflow turbulence cases $\mathrm{L_x} = 1c$ and $\mathrm{L_x} = 1.5c$. In Fig. 6.14 (a) the emerging LEV is evident at $x/c \approx 0.05$ in the C_p (top) and C_f (bottom) for both the smooth inflow case and the large-scales inflow turbulence cases. Nevertheless, the case with integral length-scale $\mathrm{L_x} = 1.5c$ produced negative $C_p \approx$ -8 on the suction side. In addition, most values of C_p on the pressure side are negative, which means there is substantial surface pressure variation due to the impact of the larger-scale inflow turbulence. This confirms [162] reports, which state that a slight increase in integral length-scale (e.g. $\mathrm{L_x}$ = 1.7D to 2.3D) increased surface pressure variance on a square prism. It should be noted that the difference between the two large-scales inflow turbulence cases (Fig. 6.14 (a)) is simply due to the uncertainties (C_p and C_f were not phase averaged).

It is expected that the LEVs would grow and convect downstream the chord length as the angle of incidence increases. The peak of the LEV was observed at $x/c \approx 0.5$, which the separation point started at $x/c \approx 0.37$ and reattachment point at $x/c \approx 0.7$ for the smooth inflow C_p (top) and C_f (bottom) at $\alpha = 21.2°\uparrow$ as shown in Fig. 6.14 (b). For the large-scale inflow turbulence case $\mathrm{L_x} = 1c$ the LEV extents from $x/c \approx 0$ to 0.4 without convect further downstream, unlike what was observed in the smooth inflow case. The same phenomenon was observed in the other large-scale inflow turbulence case $\mathrm{L_x} = 1.5c$ and with a highly suppressed LEV. This is consistent with Fig. 6.13 (b). Furthermore, a similar phenomenon was observed in Fig. 6.14 (c) - (d). This further confirms the suppression, breakdown and disorder of the LEVs structure due to the impact of the incoming large-scale turbulence during the blade's pitching cycle, which is consistent with the

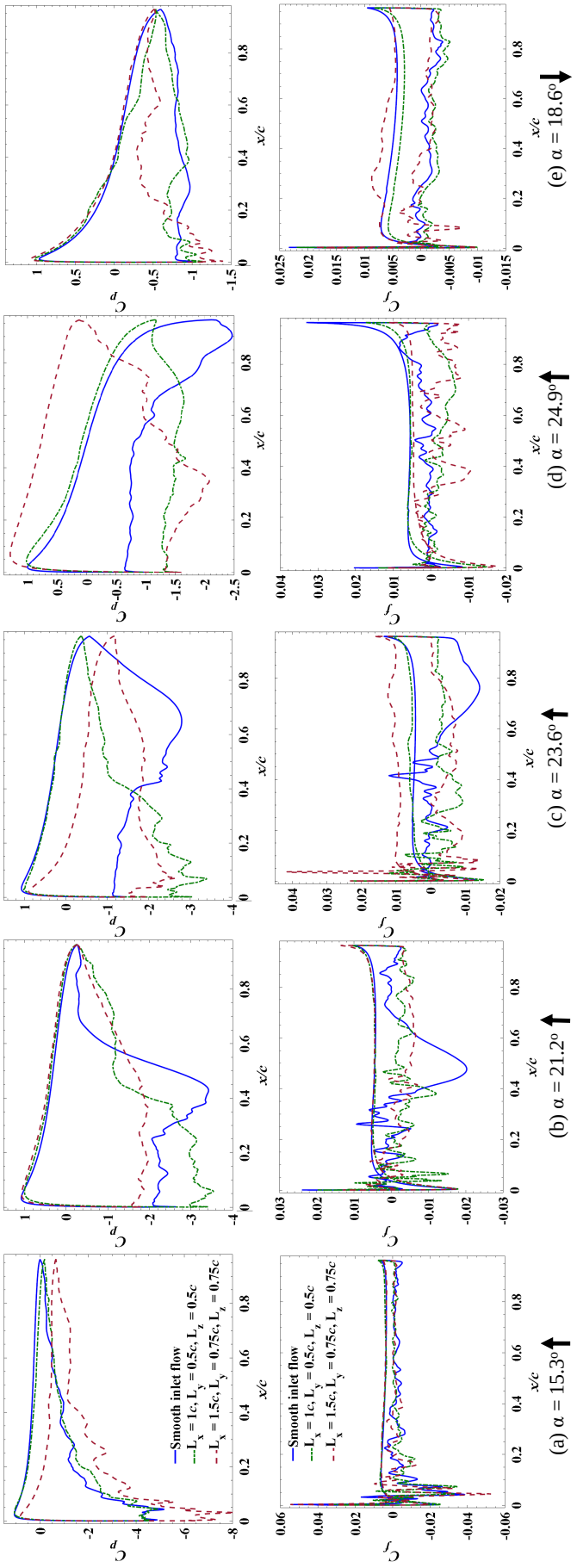

Figure 6.14: Surface forces spanwise-averaged. (top) Pressure coefficients, (bottom) Skin friction, $k_{\text{red}} = 0.1$. (a) $\alpha = 15.8°\uparrow$, (b) $\alpha = 21.8°\uparrow$, (c) $\alpha = 23.8°\uparrow$, (d) $\alpha = 24.9°\uparrow$, (e) $\alpha = 18.8°\downarrow$.

instantaneous vorticity contours taken at the mid-span plane shown in Fig. 6.13 (c) - (d). The LEV average size is estimated to be 0.52 (smooth inflow case) and 0.28 (large-scales inflow turbulence cases), which gives a difference of approximately 60%.

Another impact of the large-scale inflow turbulence on the LEVs during the upstroke is the slower speed to convect downstream compared to LEVs in smooth inflow case as the angle of incidence increases (Fig. 6.14 (d)). This is further confirmed with the pressure coefficient snapshots contours (Fig. 6.15). For the smooth inflow case (Fig. 6.14 (d)) the LEV convects downstream and begin to interact with the TEV at $0.8 \leq x/c \leq 0.95$, whereas for large-scale inflow turbulence cases, very weak LEVs are discern in Cp and C_f at $0.5 \leq x/c \leq 0.7$ for case $\mathrm{L_x} = 1c$, and at $0.3 \leq x/c \leq 0.45$ for case $\mathrm{L_x} = 1.5c$ (see Fig. 6.13 (d)). It is deduced that the large-scale inflow turbulence slowdown the LEV convecting speed downstream at high angles of attack (Figs. 6.13 (d) and 6.15). A low frequency is typical for large-scale turbulence momentum, which influences other large structures (e.g. LEVs) generated by the pitching blade.

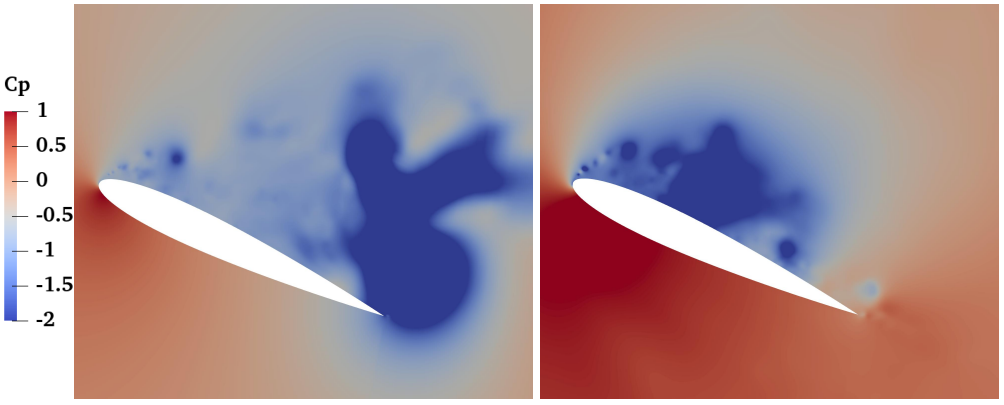

Figure 6.15: Snapshots of instantaneous pressure coefficient contours at $\alpha = 24.9°\uparrow$ for $k_{\mathrm{red}} = 0.1$. (a) smooth inflow, (b) $\mathrm{L_x} = 1.5c$.

The decrease of the lift observed at $\alpha = 18.6°\downarrow$ in Fig. 6.11 (a) for the large-scale inflow turbulence cases are consistent with Cp and C_f plots shown in Fig. 6.14 (e). In particular, for case $\mathrm{L_x} = 1.5c$ at $0.3 \leq x/c \leq 0.95$, which shows narrower pressure distribution curve loop. Moreover, case $\mathrm{L_x} = 1c$ shows little evidence of the LEV near the blade's leading edge at $\alpha = 18.6°\downarrow$.

To use various approaches in explaining the impact of large-scale inflow turbulence on the generated large structures (e.g. LEV) due to the blade's motion, iso-contours of the vorticity field are presented.

The Q-criterion is defined as $\frac{1}{2}\left(\Omega_{ij}\Omega_{ij} - S_{ij}S_{ij}\right)$, where $\Omega_{ij} = \frac{1}{2}\left(\frac{\partial u_i}{\partial x_j} - \frac{\partial u_j}{\partial x_i}\right)$, and $S_{ij} = \frac{1}{2}\left(\frac{\partial u_i}{\partial x_j} + \frac{\partial u_j}{\partial x_i}\right)$. Fig. 6.16 shows instantaneous snapshots of the iso-surface contours of the vorticity filed for smooth inflow case and large-scale turbulence

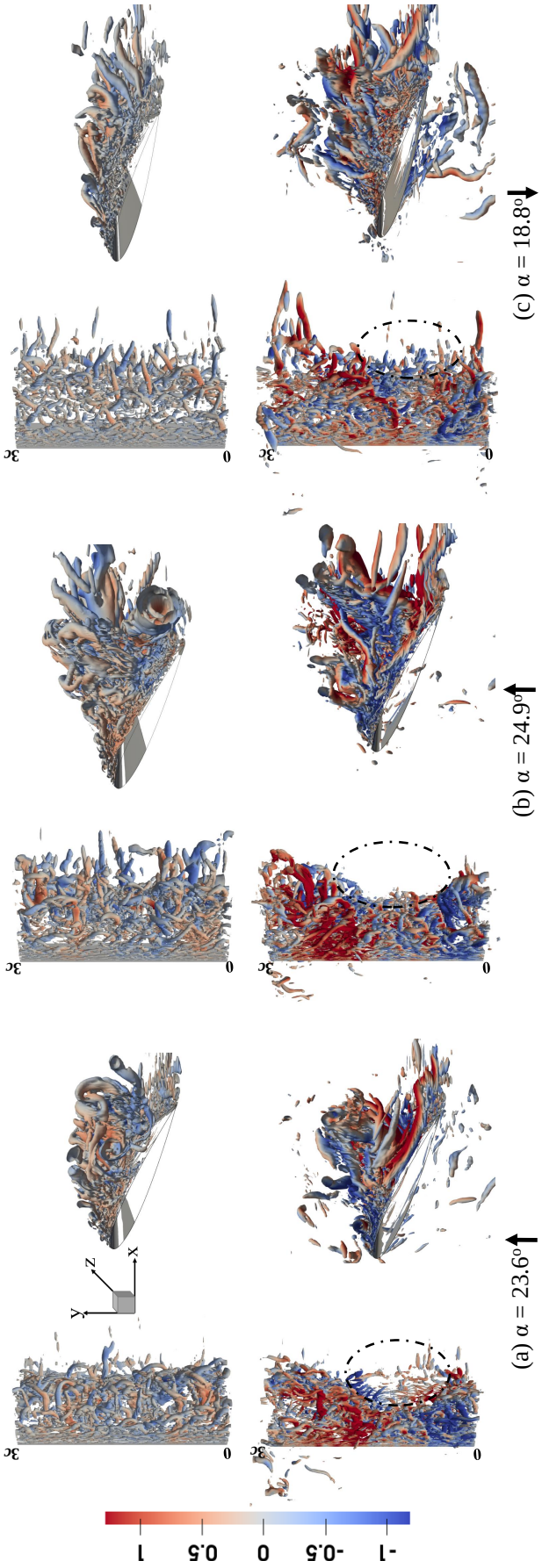

Figure 6.16: Instantaneous snapshots of the flow visualised Iso-surface (Q = 50) normalised by c and U_∞, coloured with the instantaneous streamwise velocity. (top) smooth inflow, (bottom) large-scale turbulence $L_x = 1.5c$, $k_{red} = 0.1$. (a) $\alpha = 23.6°\uparrow$, (b) $\alpha = 24.9°\uparrow$, (c) $\alpha = 18.8°\downarrow$.

case $L_x = 1.5c$ at various angles of incidence (e.g. $\alpha = 23.6°\uparrow$,$\alpha = 24.9°\uparrow$ and $\alpha = 18.8°$) for $k_{red} = 0.1$.

For the smooth inflow case, as the angle of attack increases, the LEV is generated at the blade's leading edge, grows and convects downstream along the suction side and finally detaches from the trailing edge shown in Fig. 6.16 (a) - (c) (top). However, this process of the LEV life-span is hard to discern for the large-scale inflow turbulence case shown in Fig. 6.16 (a) - (c) (bottom). The LEVs are dominant for the smooth inflow case, while interaction between LEVs and the incoming large-scale turbulence results in break-down and disorder structures of the LEV (Fig. 6.16 (a) - (c) (bottom) (x-y plane)). This gives more details on the break-down and disorder LEVs due to the impact of large-scale inflow turbulence, which was first highlighted in the vorticity contours shown in Fig. 6.13 (middle) and (right) ((b) - (d)).

The LEV size is comparable to the chord length [4, 63], which is confirm in Figs. 6.16 (a) (x-y plane) and 6.13 (c) (left) for the smooth inflow case, whereas for the large-scale inflow turbulence case the LEV size is short seen around the middle section of the blade-span (see the dash-dot ellipse in Fig. 6.16 (a) - (b) (bottom) z-x plane) as the angle of attack increases. This supports the vorticity field contours obtained at the mid-span plane shown in Fig. 6.13 (middle) and (right) ((c) - (e). It is deduced that short LEVs around the middle section of the span suggests a reduced size and uneven dominance in the blade span compared to the smooth inflow case. The less dominance of the LEV across the span at high angles of incidence results in early stall of the lift. This was evident in both the lagre-scales inflow turbulence cases $L_x = 1c$ and $L_x = 1.5c$ lift coefficients shown in Fig. 6.11.

Overall, large-scale inflow turbulence interaction with the LEVs results in break-down and disorder of its structure, which has an adverse effect on lift coefficients. Indeed, the LEV plays a dominant role by enhancing the lift coefficients of the pitching blade, particularly at a high angle of attack.

6.5.2 Effect on aerodynamic characteristics for $k_{red} = 0.2$

The effect of large-scale inflow turbulence on aerodynamic characteristics, performance, instantaneous vorticity field, pressure and skin-friction coefficients at different angles of attack at $k_{red} = 0.2$ is discussed and presented as follows:

6.5.2.1 Phase-averaged aerodynamic coefficient

Figure 6.17 shows the effect of large-scale inflow turbulence on aerodynamic characteristics of a pitching wind turbine blade for $k_{red} = 0.2$. In general, the large-scale inflow turbulence does not significantly change the lift hysteresis loop except for the drag and moment coefficients at the given conditions. The angles of the

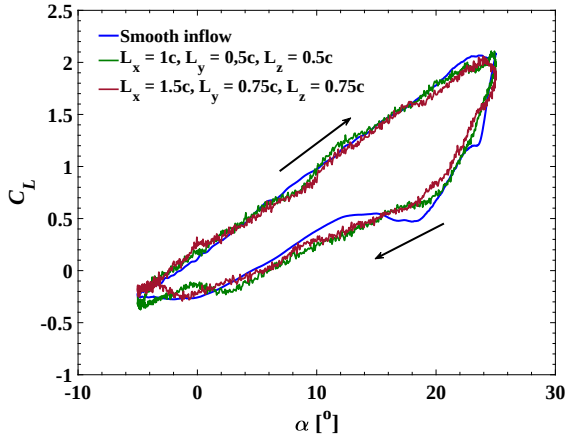

(*a*)

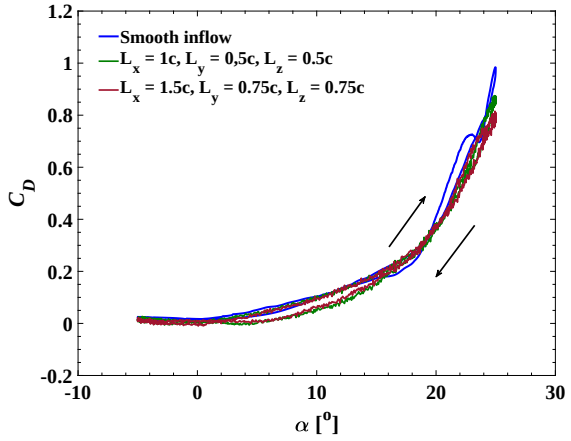

(*b*)

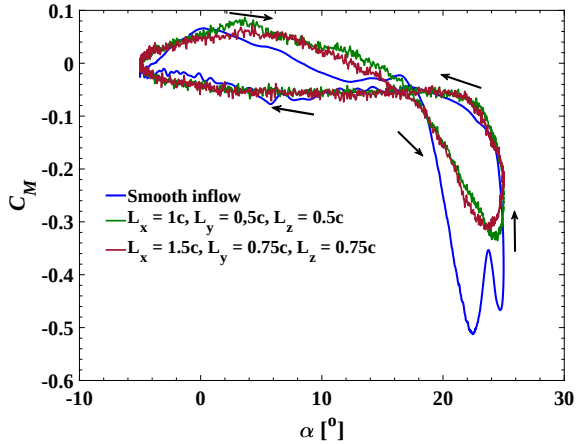

(*c*)

Figure 6.17: Effect of large scale turbulence on aerodynamic coefficients. (a) lift, (b) drag, and (c) moment, $k_{\text{red}} = 0.2$.

peak lift are almost the same compared to that of the smooth inflow case. There are small lift coefficients decrements during the downstroke, and noticeable drag reduction is evident with the increase of the integral length scales.

The drag coefficients decrease by an average of 15% for the large-scales inflow turbulence cases compared to the smooth inflow (Fig. 6.17 (b)). This effect is of lesser magnitude compared to the drag coefficient magnitude observed for $k_{\text{red}} = 0.1$ data (Subsection 6.5.1). The drag coefficients in the pre-stall phase show no visible difference between the smooth inflow case and large-scales inflow turbulence cases, while at the post-stall regime, the drag coefficients drop sharply from their peaks due to the impact of large-scale inflow turbulence. As earlier mentioned, the drag mainly consists of the pressure forces than skin-friction, so it only makes a small contribution to the drag coefficients.

The lift coefficients in the pre-stall and post-stall regimes do not change noticeably for large-scale inflow turbulence cases compared to the smooth inflow case. The large-scale inflow turbulence does not evidently affects the peak lift coefficients compared to those of $k_{\text{red}} = 0.1$ (Fig. 6.11 (a)). It was observed that for both $k_{\text{red}} = 0.1$ and 0.2 large-scale inflow turbulence does not consistently enhanced the lift coefficients during the downstroke, which is opposite to the lift coefficient increment observed for small-scale inflow turbulence effects reported in Subsection 6.4.3, wind tunnel test [40] and LES studies [4, 22]. In addition, the reason for a less visible effect on the lift coefficient hysteresis loop compared to that for $k_{\text{red}} = 0.1$ could be owing to the fast pitching motion, which breaks down the incoming large-scale eddies to much smaller ones and as a result, the impact on the LEV and its motion was weakened. Hence, the LEV could effectively play its role to some extent - primarily increment of the lift coefficient at high angles of attack during the upstroke. This is evidently shown in the lift coefficient C_L (Fig. 6.17 (a)) at maximum angle of incident and at $18°\downarrow \leq \alpha \leq 23°\downarrow$ during the downstroke. Unlike, for the case $k_{\text{red}} = 0.1$ that incoming large-scale eddies impacts the LEV structures and its dynamics significantly at the stall angle and most part of the downstroke shown in Fig. 6.11 (a).

The most evident impact of large-scale inflow turbulence for $k_{\text{red}} = 0.2$ is on the moment coefficient at the stall angle and during the downstroke. There is a significant increase of the global minimum moment coefficients for the large-scale inflow turbulence cases compared to the smooth inflow case shown in Fig. 6.17 (c). This is due to a slight shift of the aerodynamic force centre downstream of the blade, usually, for NACA 0012 aerofoil, the force centre is at a quarter chord length near the lead edge. The absolute minimum moment coefficient value increased as the integral length scale increased. The peak-to-peak difference between laminar and turbulence cases at the global minimum moment coefficients is an average of 56%. A similar impact on the moment coefficient was observed for $k_{\text{red}} = 0.1$ (Fig.

6.11 (c)), whereas such an impact was not seen in Fig. 6.9 (c)) for small-scale inflow turbulence effect.

It is to be noted that the moment is sensitive to LEV dynamics (i.e. growth, attachment, reattachment or detachment) near the leading edge of the blade. However, these processes were altered due to the impact of large-scale inflow turbulence. Thereby, show noticeable changes in the aerodynamics force centre of the pitching blade under the deep dynamic stall. Given that large-scale inflow turbulence has a considerable impact on the aerodynamic force centre (moment) of the pitching blade, therefore, it can be concluded that the global minimum moment coefficient is strongly dependent on the change of turbulence inflow conditions.

6.5.2.2 Aerodynamic performance - drag polar

Assessing the aerodynamic performance of a wind turbine blade is crucial for an efficient blade design. Fig. 6.18 shows the lift-to-drag ratio of the pitching wind turbine blade for smooth inflow case and large-scale inflow turbulence case for k_{red} = 0.2. Generally, it was evident that the large-scale inflow turbulence reduced the 'memory' of the polar drag curve loop. The peak polar drag reduces as the large-scale inflow turbulence increases, which means that the peak performance of the wind turbine blade decreases by interacting with large eddies in the ABL or during weather-scale conditions. The narrowed polar drag curves of the two large-scale inflow turbulence cases (i.e. $L_x = 1c$ and $L_x = 1.5c$) means a decrease in blade performance at the peak and a slight increase during the downstroke. A similar effect of large-scale inflow turbulence on the aerodynamic performance was observed for k_{red} = 0.1 with greater impact, shown in Fig. 6.12 in Subsection 6.5.1.2.

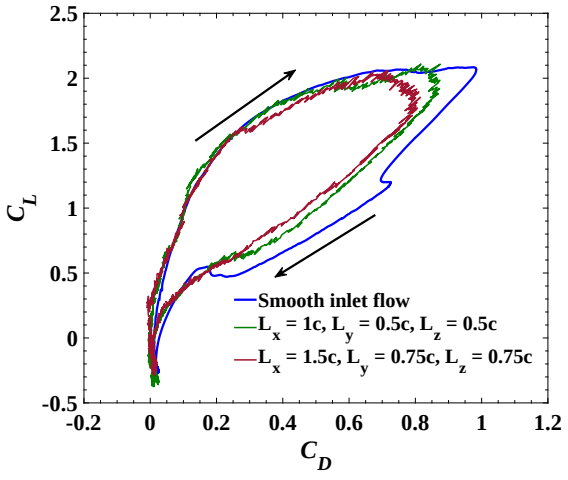

Figure 6.18: Aerodynamic performance - drag polar, k_{red} = 0.2

Overall, it was observed that high reduced frequency (e.g. $k_{\text{red}} = 0.2$) would not influence increase of the peak performance of the pitching blade under large-scale turbulent flow. This suggests that the impact of large-scale inflow turbulence on the aerodynamic performance is independent of the blade's motion.

6.5.2.3 Vorticity field

Figure 6.19 shows snapshots of the instantaneous spanwise component of vorticity at the mid-span plane with smooth inflow (left), large-scale turbulence $L_x = 1c$ (middle) and $L_x = 1.5c$ (right) for $k_{\text{red}} = 0.2$.

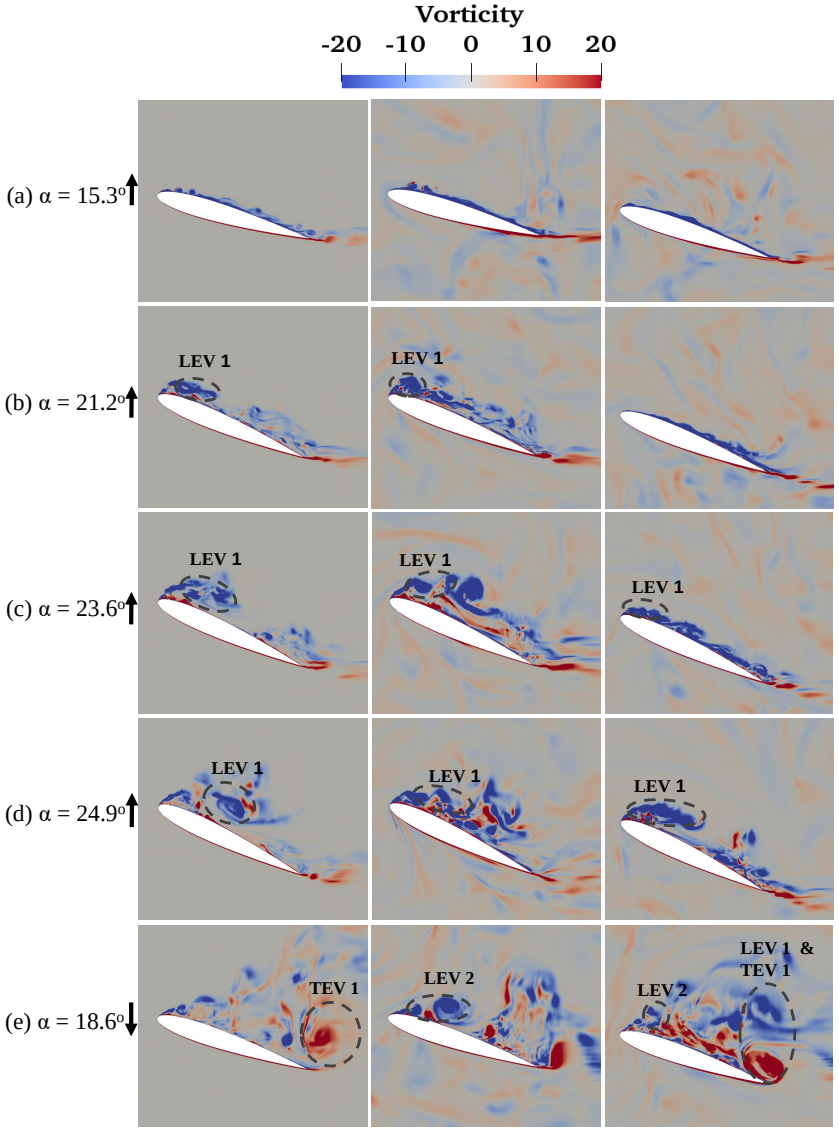

Figure 6.19: Snapshots of the instantaneous vorticity field contours normalised by c and U_∞. (left) smooth inflow, (middle) $L_x = 1c$, (right) $L_x = 1.5c$, $k_{\text{red}} = 0.2$. (a) $\alpha = 15.3°\uparrow$, (b) $\alpha = 21.2°\uparrow$, (c) $\alpha = 23.6°\uparrow$, (d) $\alpha = 24.9°\uparrow$, (e) $\alpha = 18.6°\downarrow$. The marked dash ellipse correspond to the LEV's length and location in Fig. 6.20, in particular the skin-friction.

In the smooth inflow case (Fig. 6.19 (a) - (d) (left)) the LEV grows and remains attached while for large-scales inflow turbulence cases (Fig. 6.19 (a) - (d) (middle) and (right)) the LEV are attached and slightly disordered. This confirms that the incoming large-scale turbulence does not significantly impact the LEVs structures due to the faster blade motion compared to $k_{\mathrm{red}} = 0.1$ turbulent flow cases (Fig. 6.13 (b) - (e) (middle) and (right)). This means that the fast blade motion energises the 'semi-disordered' LEVs, thereby improving its convection downstream as nearly the same as the LEV motion in smooth inflow (see Fig. 6.20) as the angle of attack increases.

The fully separated flow is evident for the smooth inflow case and large-scales inflow turbulence cases at $\alpha = 18.6°\downarrow$ shown in Fig. 6.13 (e)). In addition, the TEVs are visible, although for the large-scale inflow turbulence case $\mathrm{L_x} = 1c$ (middle), the TEV appears to be weak. It should be noted that the difference between weak TEV structure for turbulence case $\mathrm{L_x} = 1c$ (middle) and those of smooth inflow (left), and turbulence case $\mathrm{L_x} = 1.5c$ (right) is due to uncertainty since the instantaneous vorticity fields are not phase averaged.

To further describe the effect on LEVs for reduced frequency $k_{\mathrm{red}} = 0.2$, the surface pressure coefficients and skin-friction coefficients are presented in the proceed Subsubsection.

6.5.2.4 Blade surface pressure and skin-friction coefficients

The spanwise averaged surface pressure and skin-friction distributions are obtained for smooth inflow case, and the large-scale inflow turbulence cases at different angles of attack correspond to those in Fig. 6.19.

Figure 6.20 shows comparison of the spanwise averaged pressure coefficients C_p (top) and skin-friction coefficient C_f (bottom) between smooth inflow case and the large-scales inflow turbulence cases $\mathrm{L_x} = 1c$ and $\mathrm{L_x} = 1.5c$. For the smooth inflow case the LEV is slightly forward than those of the large-scale inflow turbulence cases while the LEVs sizes increase comparable to the smooth inflow LEV size with increase of the angle of incident ($\alpha = 15.5°\uparrow$ to $\alpha = 24.9°\uparrow$) (Fig. 6.20 (a) - (d)). The LEV average size is estimated to be 0.47 and 0.42 for the smooth inflow and both large-scales inflow turbulence cases respectively, this gives a difference of approximately 13%. Again, this confirms that the impact of the large-scale inflow turbulence on LEV structures gradually weakens as the angle of attack increases for high reduced frequency (e.g. $k_{\mathrm{red}} = 0.2$). Thereby, the lift coefficient is less affected.

It can be deduced that the LEV convection slowed down by interacting with incoming large-scale inflow turbulence. However, the suppression of LEVs gradually weakens as the blade approaches the maximum angle of incident. Therefore, the lift and drag coefficients for the large-scales inflow turbulence cases is comparable

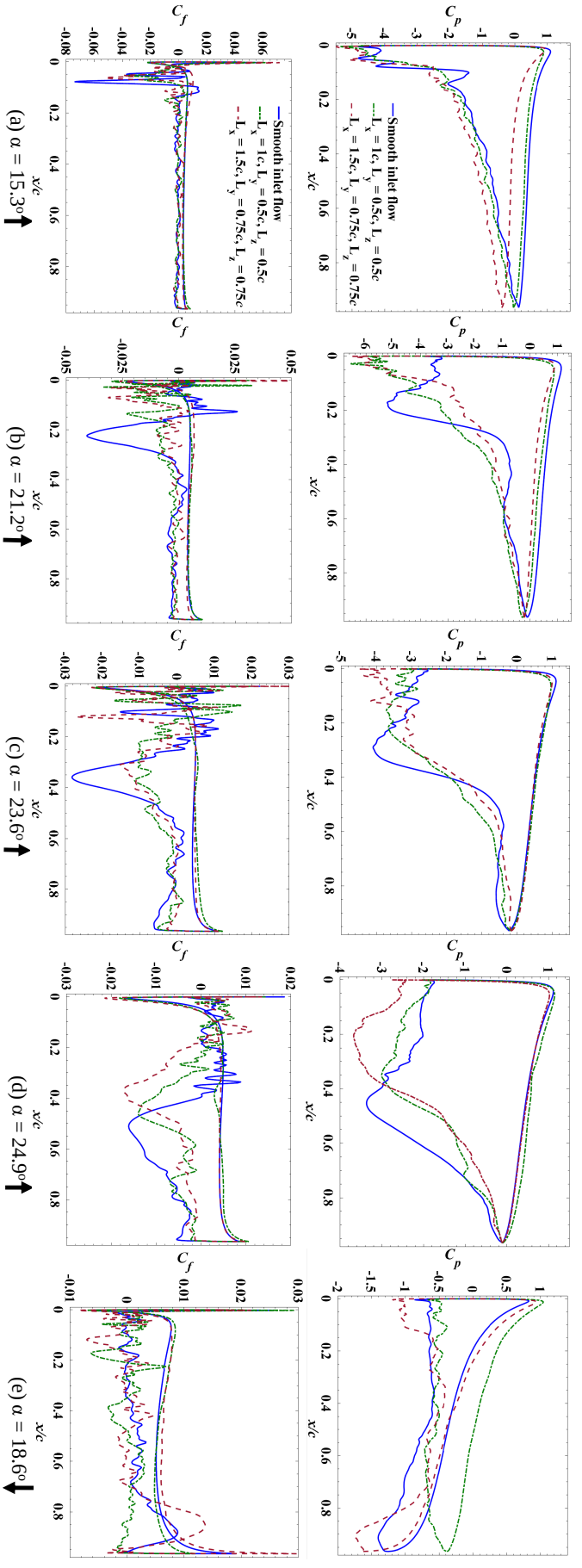

Figure 6.20: Surface forces spanwise-averaged, (top) Pressure coefficients, (bottom) Skin friction, $k_{\text{red}} = 0.2$. (a) $\alpha = 15.3°\uparrow$, (b) $\alpha = 21.2°\uparrow$, (c) $\alpha = 23.6°\uparrow$, (d) $\alpha = 24.9°\uparrow$, (e) $\alpha = 18.6°\downarrow$.

to that of the smooth inflow case at most phase angles of the entire pitching cycle of the blade except at the maximum angle of incident for the drag coefficient.

Fig. 6.20 (e) shows the LEV and TEV interaction for both smooth inflow and turbulence case $L_x = 1.5c$ (right), and a weak TEV of the other turbulence case $L_x = 1c$ (middle), which are consistent with Fig. 6.19 (e).

A vital inferred can be drawn from Fig. 6.20 that large-scale turbulence slowdown the LEV convection downstream. This phenomenon is consistent for both the reduced frequencies, $k_{\text{red}} = 0.1$ and 0.2. Overall, in conclusion, the high pitching motion of the blade mitigates the impact of large-scale inflow turbulence on the aerodynamic force coefficients, e.g. lift and to some extent on the drag for $k_{\text{red}} = 0.2$. The moment coefficient is significantly affected because it is dependent on the change of turbulence inflow conditions and independent of the blade's motion.

6.6 Dispersive shear stress in the wake

The dispersive or phase shear stress is the component of the momentum flux due to the phase average velocities. In other words, it can be referred to as the average of the production of the phase fluctuations of the phased averaged velocities components. The phase velocity fluctuation is the difference between phase-averaged velocity and the average of the mean velocity. Note that the average $\langle\rangle$ here is the average over a period of the blade pitching motion and $\tilde{}$ is the phase averaged operator. Mathematically, the dispersive shear stress can be derived as follow:

$$\mathrm{u}_{i(t)} = \langle\tilde{\mathrm{u}}_i\rangle + \hat{\mathrm{u}}_i + \mathrm{u}'_{i(t)}, \tag{6.1}$$

where $\mathrm{u}_{i(t)}$ is the instantaneous time velocity (i = u,v,w), $\langle\tilde{\mathrm{u}}_i\rangle$ is the average of the entire cycles of the phase average velocity (Eq.6.2), $\hat{\mathrm{u}}_i$ is the phase fluctuation of the phase averaged velocity (Eq. 6.3), $\tilde{\mathrm{u}}_i$ is the phase averaged velocity and $\mathrm{u}'_{i(t)}$ is the instantaneous time turbulence fluctuations (Eq. 6.4).

$$\langle\tilde{\mathrm{u}}_i\rangle = \frac{1}{\Psi}_n \int_{\Psi_n} \tilde{\mathrm{u}}(x, y, z)dxdy \tag{6.2}$$

$$\hat{\mathrm{u}}_i = \tilde{\mathrm{u}}_i - \langle\tilde{u}_i\rangle \tag{6.3}$$

$$\mathrm{u}'_{i(t)} = \mathrm{u}_{i(t)} - \tilde{\mathrm{u}}_i \tag{6.4}$$

Therefore, the production of phase fluctuation $\hat{u}\hat{u}$ and $\hat{u}\hat{v}$ are the dispersive normal stress and dispersive shear stress at every phase angle Ψ respectively. $\langle\hat{u}\hat{u}\rangle$ and $\langle\hat{u}\hat{v}\rangle$ are the dispersive normal stress and dispersive shear stress averaged of the

entire cycle respectively while $\widetilde{u'u'}$ and $\widetilde{u'v'}$ are the normal turbulent stress and turbulent shear stress phase averaged on every phase angle Ψ respectively.

The post-processing of the phase stresses data presented in this section was obtained from time series of 75,000 time-steps (3 cycles) each at five different probes locations, systematically arranged at middle - span section of the domain (i.e. $1 \leq z/c \leq 2$) in the wake $1c$ from the blade's trailing edge. Specifically, the coordinates of the probes were located at $x/c = 2$ in the streamwise direction, $y/c = 0$ in cross-flow direction, and in the spanwise direction at $z/c = 1$, 1.25, 1.5 1.75 and 2. At x/c = -3.5 upstream of the blade's leading edge, the similar coordinates of the probes were used in the cross-flow direction while the spanwise direction z/c = 1.25, 1.5 and 1.75, but with 50,000 time-steps each at the three different probes locations.

A total of 6 and 15 cycles of $u_{i(t)}$ was phase averaged to obtain the final phase-averaged velocity $\tilde{u}_i$ for a cycle in the upstream and in the wake locations respectively. To obtain the phase fluctuation $\hat{u}$, Eq. 6.3 was used, which is the difference between phase-averaged velocity $\tilde{u}_i$ and the average over the entire cycles $\langle \tilde{u}_i \rangle$. Thereafter, the product (e.g. $\hat{u}\hat{u}$ and $\hat{u}\hat{v}$) was phased-averaged on every phase angle (Ψ) of a cycle. A similar averaging and phase averaging procedures were used to obtain the phase averaged turbulent stress $\widetilde{u'v'}$ and phase averaged turbulent kinetic energy $\widetilde{TKE}$ show in the figures hereafter.

Figures 6.21 and 6.22 shows the time series for instantaneous velocities (u_i) for large-scale turbulence $L_x = 1c$ at $x/c = 2$, $y/c = 0$, for $z/c = 1$ to 1.25 and z/c = 1.5 to 2 respectively, for the 3 cycles. Similarly, Figs. 6.23 and 6.24 shows the time series for instantaneous velocities (u_i) for large-scale turbulence $L_x = 1.5c$ at probe location $x/c = 2$, $y/c = 0$, for $z/c = 1$ to 1.5 and $z/c = 1.75$ to 2 respectively, for the 3 cycles.

Figures 6.25 shows comparison between upstream location x/c = -3.5 and wake location $x/c = 2$ of the phase averaged velocity $\tilde{u}_i$ for cases $L_x = 1c$ (top) and $L_x = 1.5c$ (bottom) on every phase angle Ψ of a cycle. The streamwise phase averaged velocity $\tilde{u}$ oscillates within the mean velocity U on every phase angle Ψ of the cycle at the upstream x/c = -3.5 while at the wake $x/c = 2$ the periodical oscillation of $\tilde{u}$ diminished but, velocity deficit in the wake is evident in most phase angles of the cycle.

The profile of the streamwise phase averaged velocity $\tilde{u}$ at the upstream x/c = -3.5 compared to that of wake $x/c = 2$ is evident that the effect of blade's pitching motion further downstream on the incoming turbulence is negligible at this location (x/c = -3.5) and confirms that the turbulence is likely homogeneous (see Fig. 6.5) on the blade's span in a cycle. A similar trend is observed in both the cases $L_x = 1c$ and $L_x = 1.5c$.

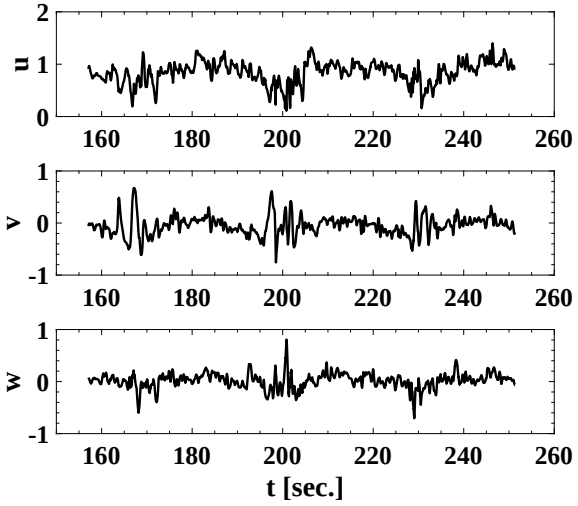

(*a*)

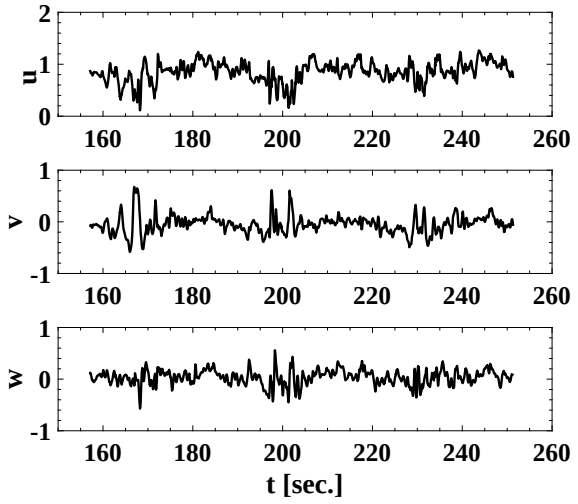

(*b*)

Figure 6.21: Time series of the instantaneous velocities (u_i) of Large-scale turbulence $L_x = 1c$ for 3 cycles at $x/c = 2$, $y/c = 0$. (a) $z/c = 1$, (b) $z/c = 1.25$, $k_{red} = 0.1$.

The cross-flow phase averaged velocity $\tilde{v}$ and spanwise phase averaged velocity $\tilde{w}$ are very small at every phase angles for both cases at the upstream locations (Fig. 6.25 (a) and (c)). Nevertheless, a clear pattern of the streamwise averaged velocity $\tilde{u}$ is seen on the cross-flow $\tilde{v}$ and spanwise $\tilde{w}$ phase averaged velocities, except in the wake location where $\tilde{v}$ show a negative peak value approximately -0.3 at $\Psi \approx 90°$in both the cases $L_x = 1c$ and $L_x = 1.5c$ respectively. Usually, the cross-flow velocity is very sensitive to the vortex shedding, e.g. at $\Psi \approx 90°$for $k_{red} = 0.1$ where the first LEV and first TEV detaches and sheds into the wake (Ref. Fig. 6.13 c (left)) and causes strong oscillation of the lift coefficient at this phase angle.

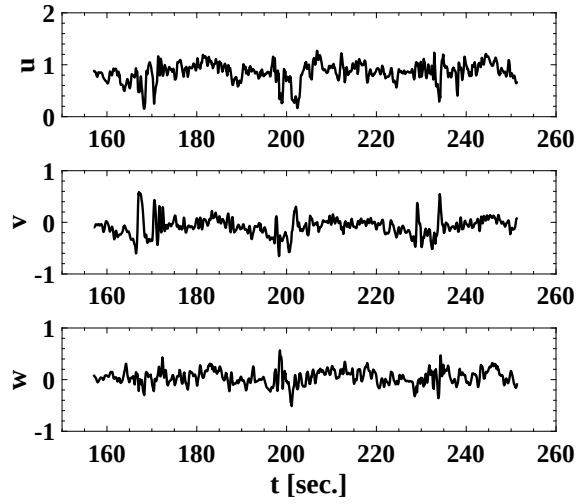

(*a*)

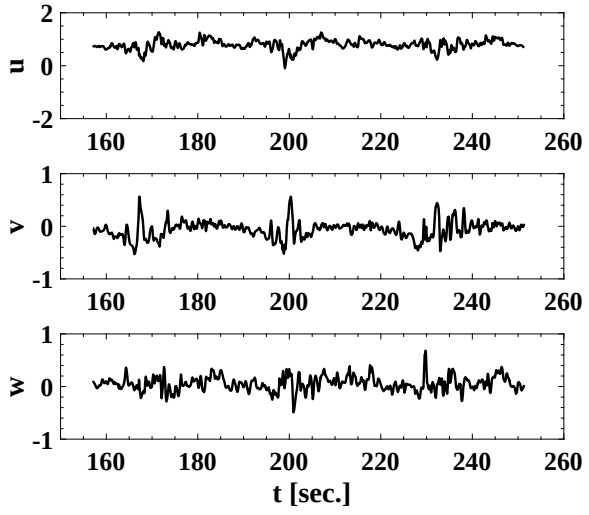

(*b*)

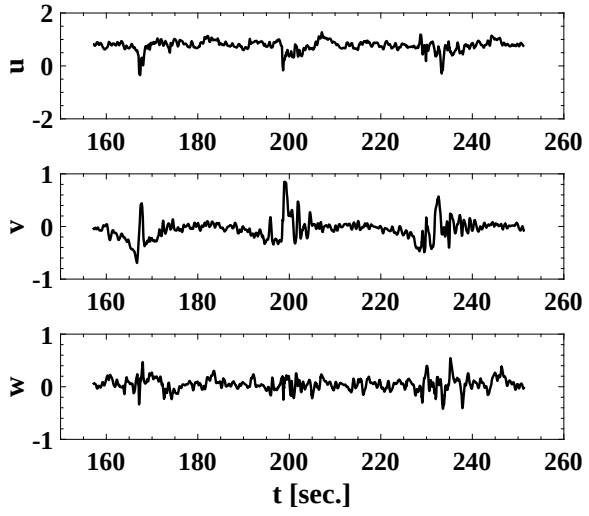

(*c*)

Figure 6.22: Time series of the instantaneous velocities (u_i) of Large-scale turbulence $L_x = 1c$ for 3 cycles at $x/c = 2$, $y/c = 0$. (a) $z/c = 1.5$, (b) $z/c = 1.75$, (c) $z/c = 2$, $k_{red} = 0.1$.

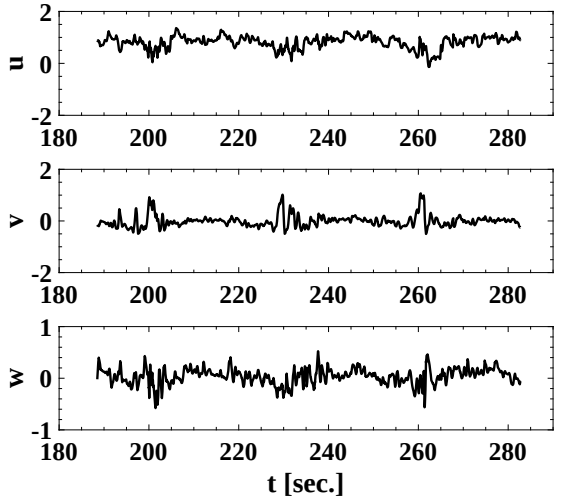

(*a*)

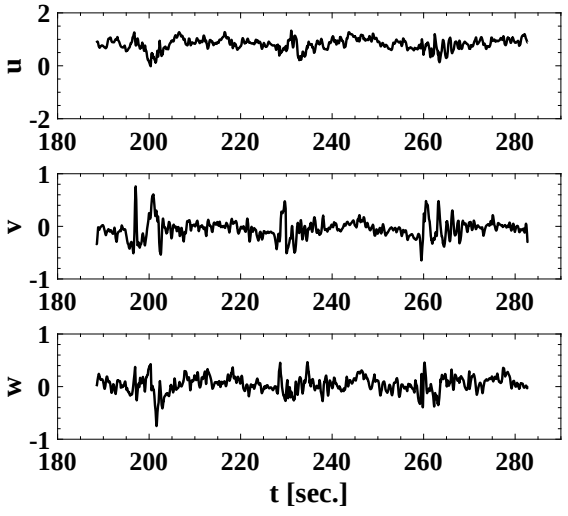

(*b*)

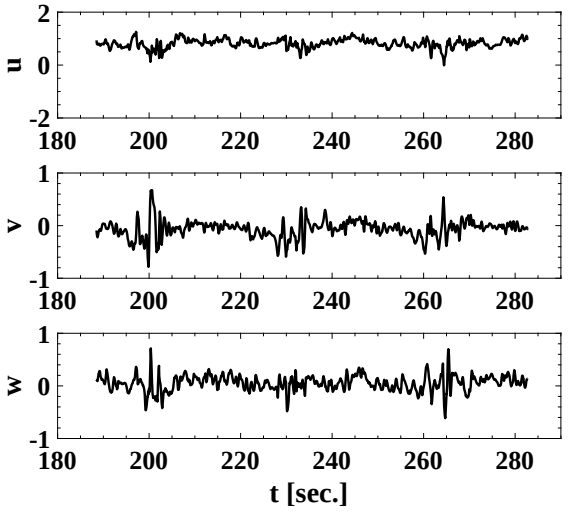

(*c*)

Figure 6.23: Time series of the instantaneous velocities (u_i) of Large-scale turbulence $L_x = 1.5c$ for 3 cycles at $x/c = 2$, $y/c = 0$. (a) $z/c = 1$, (b) $z/c = 1.25$, (c) $z/c = 1.5$, $k_{red} = 0.1$.

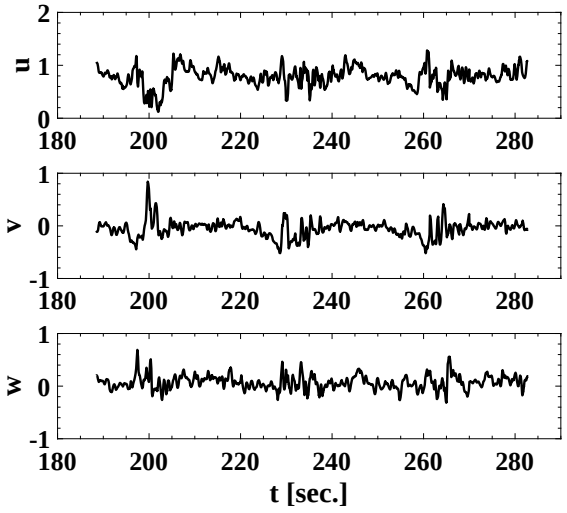

(*a*)

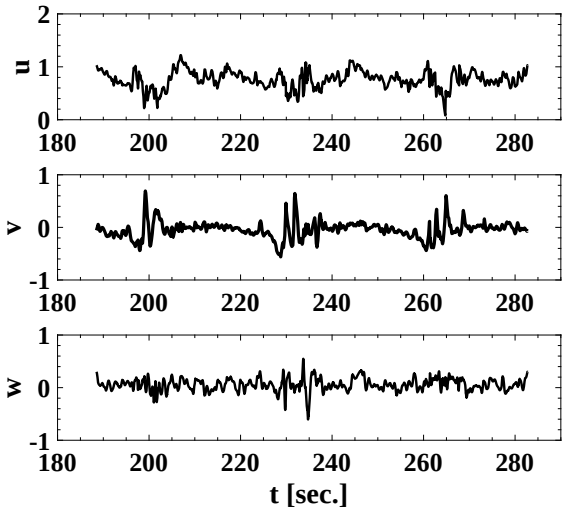

(*b*)

Figure 6.24: Time series of the instantaneous velocities (u_i) of Large-scale turbulence $L_x = 1.5c$ for 3 cycles at $x/c = 2$, $y/c = 0$. (a) $z/c = 1.75$, (b) $z/c = 2$,$k_{red} = 0.1$.

6.6.1 Phase angle dispersive shear stress

Figures 6.26 shows the dispersive shear stress $\hat{u}\hat{v}$, turbulent shear stress $\widetilde{u'v'}$ and turbulent kinetic energy $\widetilde{TKE}$ in the wake at $x/c = 2$ for the cases $L_x = 1c$ and $L_x = 1.5c$ phase averaged on every phase angle Ψ of a cycle.

In general, in the wake at $x/c = 2$ (Fig. 6.26 (a) and (b)) respectively for cases $L_x = 1c$ and $L_x = 1.5c$, the dispersive shear stress $\hat{u}\hat{v}$ and turbulent shear stress $\widetilde{u'v'}$ and $\widetilde{TKE}$ produced very small values at lower phase angles (i.e. during the upstroke), whereas at high phase angles (during the downstroke) significant changes of the values are observed. Specifically, the $\widetilde{TKE}$ considerably reduced at low phase

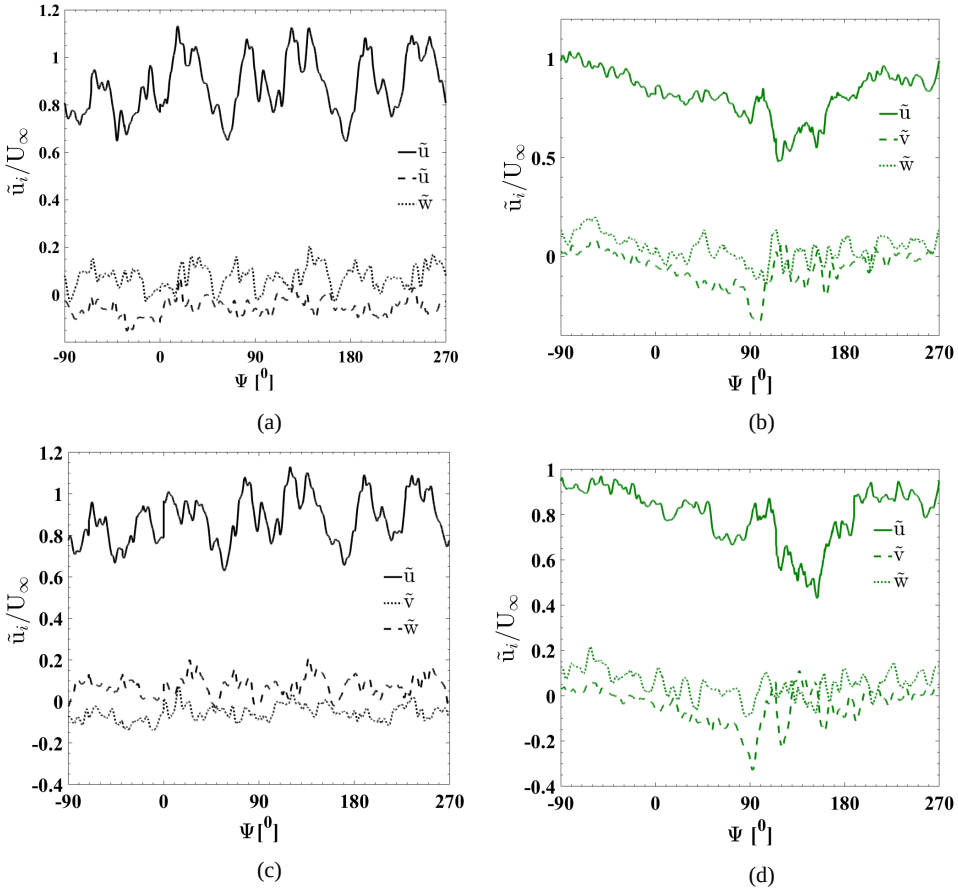

Figure 6.25: Phase averaged velocity $\tilde{u}_i$ normalised U_∞. Case $L_x = 1c$ (top) (a), x/c = -3.5 (b) $x/c = 2$, and case $L_x = 1.5c$ (bottom) (c) x/c = -3.5, (d) $x/c = 2$, $k_{red} = 0.1$.

angles ($-90° \uparrow\leq \Psi \leq 90° \uparrow$) while at high phase angles ($90° \uparrow\leq \Psi \leq 270° \downarrow$) the values of the $\widetilde{TKE}$ increased noticeably for both the cases $L_x = 1c$ and $L_x = 1.5c$. The $\widetilde{TKE}$ values are evidently larger at high phase angles compared to low phase angles. This can be attributed to the pitching downstroke motion of the blade, of which separated flows in the boundary layer and shear layer are dominant.

The dispersive shear stress $\hat{u}\hat{v}$ and turbulent shear stress $\widetilde{u'v'}$ in the wake in Fig. 6.26 (a) and (b) are evident at high phase angles ($90° \uparrow\leq \Psi \leq 270° \downarrow$).

The total shear stress (τ_{Tp}), which is the sum of the dispersive shear stress $\hat{u}\hat{v}$ and turbulent shear stress $\widetilde{u'v'}$ are -0.0037 and -0.0059 for cases $L_x = 1c$ and $L_x = 1.5c$ respectively. Total shear stress for $L_x = 1.5c$ increased by 60% compared to that of $L_x = 1c$. It is not surprising that a larger turbulence length-scale produces stronger shear stress in the wake.

The high value of total shear stress in the wake of the pitching wind turbine blade suggests that the pitching motion of the blade enhances the dispersive and Reynolds stresses in the wake region. In addition, this could mean that the dissipation rate of eddies in the wake would last even longer. To understand more

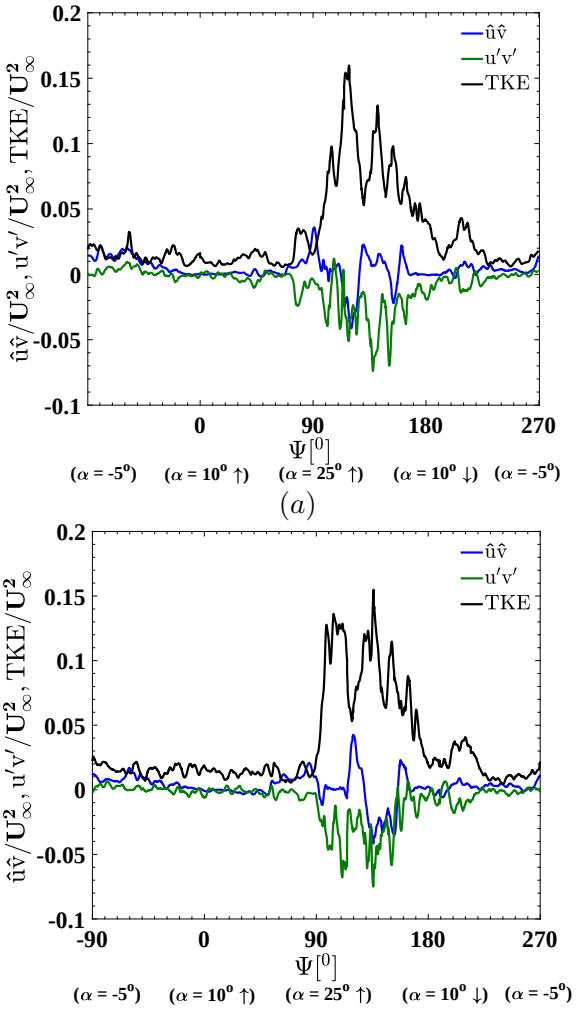

Figure 6.26: Dispersive shear stress ûv̂, turbulent shear stress $\widetilde{u'v'}$, and turbulent kinetic energy $\widetilde{TKE}$ normalised by U_∞^2 in the wake at location at $x/c = 2$. (a) case $L_x = 1c$, (b) case $L_x = 1.5c$, $k_{red} = 0.1$.

of the dispersive and turbulent shear stresses in the wake region, therefore, the straight forward quadrant analysis [172] is employed in the proceed subsection.

6.6.2 Quadrant analysis

The simple quadrant analysis is a useful tool to determine more insight into the fractional contribution of each of the four categories of turbulent shear stress and the bursting phenomenon. The four categories includes: Q1 $(+u', +v')$, Q2 $(-u', +v')$, Q3 $(-u', -v')$ and Q4 $(+u', -u')$, which are called quadrants of the Reynolds stress plane [172, 173]. The Q2 and Q4 relate to gradient-type motion, which is the ejection and sweep quadrants, and they make the largest contributions to the turbulent shear stress, while Q1 and Q3 relate to counter gradient-type motion, which is the outward and inward interactions quadrants. This quadrant

technique is applied for the phase averaged dispersive shear stress $\hat{u}\hat{v}$ and turbulent shear stress $u'v'$ in the wake of the pitching wind turbine blade.

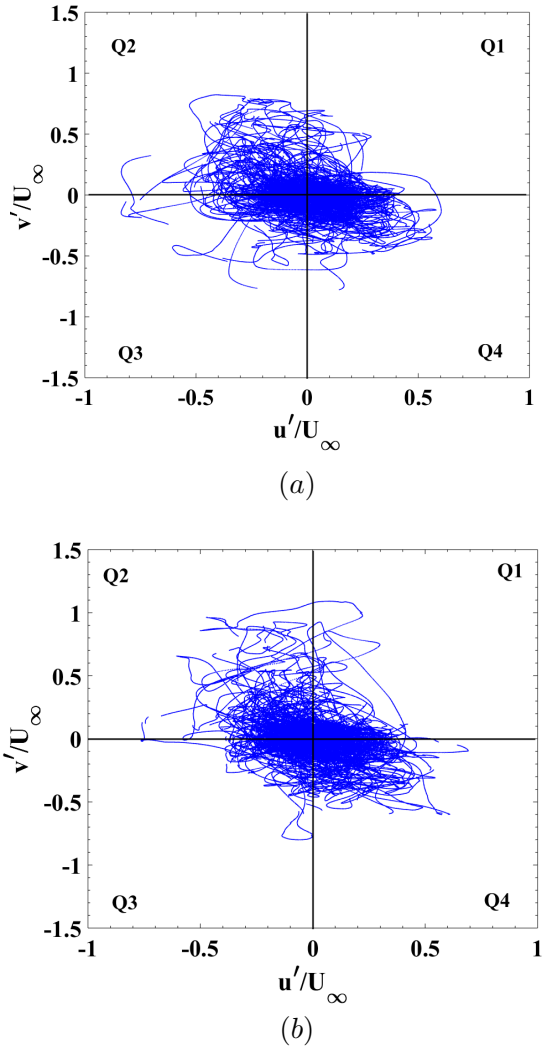

Figure 6.27: Quadrant for the instantaneous turbulence velocities u' and v' normalised by U_∞ at location $x/c = 2$ for 15 cycles. (a) case $L_x = 1c$, (b) case $L_x = 1.5c$, $k_{red} = 0.1$.

Figure 6.27 (a) and (b) shows the quadrants of the turbulent shear stress $u'v'$ in the wake for both the cases $L_x = 1c$ and $L_x = 1.5c$ respectively, obtained from 15 cycles. The quadrants Q2 and Q4 of the turbulent shear stress for case $L_x = 1c$ are evidently dominant compared to Q1 and Q3 (Fig. 6.27 (a)). This means that the ejection and sweep events are the largest contributors to the turbulent shear stress in the wake flows. However, the ejection event is slightly stronger than that of the sweep event. A similar phenomenon is evident for case $L_x = 1.5c$ (Fig. 6.27 (b)).

The turbulence shear stress $\langle\widetilde{u'v'}\rangle$ for the 15 cycles is estimated to be -0.0079 and -0.0083 for both the cases $L_x = 1c$ and $L_x = 1.5c$ respectively. The turbulence

shear stress values of both the cases are substantially high compared to that of the very rough wall observed in [174]. The dominant-negative values of the turbulent shear stress suggest flow resistance in the wake region.

For the dispersive shear stress $\hat{u}\hat{v}$ the quadrants Q1 and Q3 are the dominant events compared to the Q2 and Q4 for both the case $L_x = 1c$ and $L_x = 1.5c$ (Fig. 6.28 (a) and (b)). This means that the outward and inward events are the largest contributors to the dispersive shear stress in the wake of a pitching wind turbine blade.

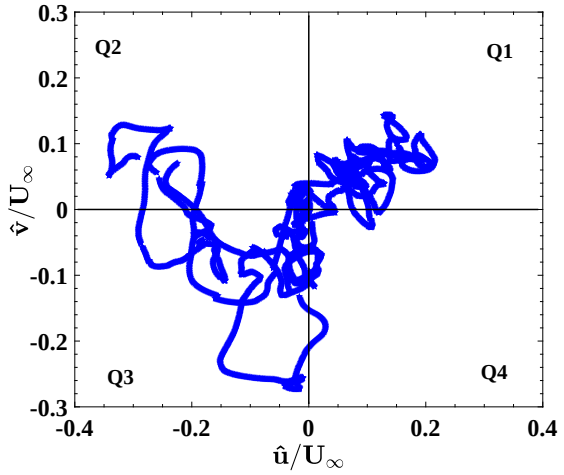

(*a*)

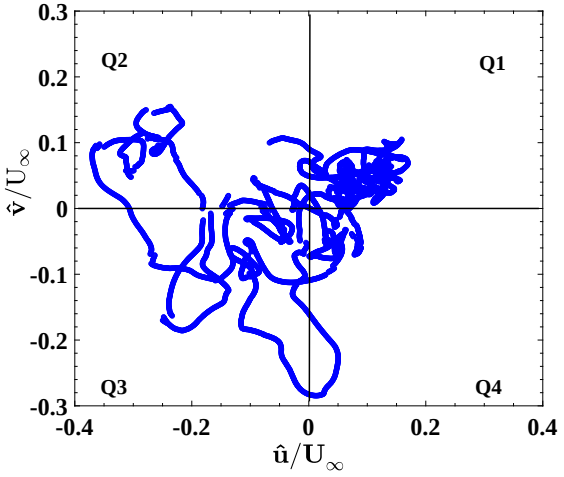

(*b*)

Figure 6.28: Quadrant for the phase fluctuation $\hat{u}$ and $\hat{v}$ normalised by U_∞ at location $x/c = 2$ for one cycle. (a) case $L_x = 1c$, (b) case $L_x = 1.5c$, $k_{red} = 0.1$.

The dominant quadrants events of the dispersive shear stress are directly opposite to that of the turbulent shear stress (Fig.6.27), is observed in the wake. In addition, the dispersive shear stress $\langle\hat{u}\hat{v}\rangle$ for the entire cycle is estimated to be 0.0042 and 0.0023 for both the cases $L_x = 1c$ and $L_x = 1.5c$ respectively. Therefore, the

positive dispersive shear stresses evident in both the large-scale inflow turbulence cases suggests flow propulsion in the wake of the pitching wind turbine blade. This propulsion phenomenon of the dispersive shear stress observed in Fig. 6.28 (a) and (b) could explain the reason wind turbine wake can travel very far away from its operational site or existence of non-turbulence unsteadiness in the wake of a wind turbine. Furthermore, Table 6.5 shows that the total shear stress in the wake region is negative, which support the flow resistance (drag) phenomenon in the wake of a wind turbine.

Table 6.5: Dispersive stress and turbulent shear stress in the wake of the pitching wind turbine blade at location $x/c = 2$ for large-scale inflow turbulence. $\langle \hat{u}\hat{v} \rangle$ and $\langle u'v' \rangle$ denotes average of the entire cycle for the dispersive stress and turbulent shear stress respectively.

case	$\langle \widetilde{u'v'} \rangle / U_\infty$	$\langle \hat{u}\hat{v} \rangle / U_\infty$	Total shear stress
$L_x = 1c$	-0.0079	0.0042	-0.0037
$L_x = 1.5c$	-0.0083	0.0023	-0.0059

Overall, the vital conclusions of this section include: 1.) The motion of the wind turbine significantly contributes to the total turbulent shear stress in the wake. Moreover, the larger the turbulence length scale, the higher the total shear stress in the wake. 2.) The quadrant analysis shows that the dispersive shear stress is positive while the turbulent shear stress is negative, which suggest propulsion and resistance respectively, in the wake flows of a pitching wind turbine blade. The total shear stress is the sum of the dispersive shear and turbulent shear stresses and was a negative value. This suggests a crucial phenomenon of wind turbine wake that can explain the slow dissipation of eddies downstream or the existence of non-turbulence unsteadiness in the wake and the tendency of those eddies to travel very far away from the wind turbine operational site.

6.7 Chapter summary

The impact of large-scale inflow turbulence on the aerodynamic characteristics of a pitching wind turbine blade has been studied. Large scale inflow turbulence equal to or greater than the blade chord length ($c = 1$ m), assumed to be the realistic size of eddies in the atmospheric boundary layer, is used for the numerical investigation, which makes the execution of the research work even more challenging. An efficient inflow turbulent generation approach for large-eddy simulation is employed to perform the numerical experiments of this specialised research topic. This chapter constitutes the central trust of this PhD research project, and the main conclusions are as follows:

– The domain span-length sensitivity study revealed that a span-length four times greater than the spanwise integral length scale (L_z) must be used for

the simulation of large-scale turbulence. Otherwise, span-length less than four times the spanwise integral length-scale might cause the results to be unpredictable.

- The small-scale turbulence with integral length-scale ($L_x = 0.3c$, $L_y = 0.15c$, $L_z = 0.15c$) and turbulent intensity $TI = 11\%$ increase the lift coefficient approximately by 45% during the downstroke compared to laminar flow for reduced frequency $k_{red} = 0.1$. The effects on the drag and minimum moment coefficients in the turbulence inflow case are small compared to those in the smooth inflow case. This new results bridge the gap between $k_{red} = 0.05$ (e.g. [4]) and 0.2 (e.g. [22]) of any uncertainties for the effect of small-scale turbulence on the aerodynamic coefficients.
- The impact of large-scale inflow turbulence of streamwise integral length-scale equal or greater than the chord length and $TI = 11\%$ is evident on the lift, drag and moment coefficients of the pitching wind turbine blade. The magnitude of the lift and drag decreases with the increase of integral length-scale while the minimum moment coefficient increase with the given inflow conditions. These impacts are attributed to the early separation of the boundary layer during the upstroke and disordered, break-down, and slow convection of the leading-edge vortex (LEV) by the impingement of the large-scale inflow turbulence for $k_{red} = 0.1$. The average difference of the lift coefficients at the maximum angle of attack (upstroke) and during the downstroke is 20% and 22%, respectively, while the maximum drag and global minimum moment coefficient average differences are 21% and 60% respectively compared to the smooth inflow case.

  The effect of the large-scale inflow turbulence on aerodynamic force coefficients and moment coefficient is found to be opposite the effect of small-scale turbulence presented in this chapter and the literature (e.g. [22, 4]). The snapshots of the vorticity flow field, surface pressure and skin-friction at different incidence also confirms that large-scale inflow turbulence has significant impact on the flow around the pitching blade. Indeed, the distorted LEVs with slow convection during the blade's pitching cycle is due to the interaction with energetic large-scale inflow turbulence, which leads to significant changes in the lift, drag and moment coeffcients.
- The increase of reduced frequency from 0.1 to 0.2 do not increase the lift coefficients during the upstroke and downstroke, while the peak drag coefficient decreased moderately and the absolute value of the minimum moment coefficient increased with large-scale inflow turbulence. This means that the high pitching motion of the blade mitigates the effect of large-scale inflow turbulence on the lift coefficients compared to the impact observed for $k_{red} = 0.1$. The effect on the drag and moment coefficients have an average of 15% and 54%, respectively compared to smooth inflow. The high pitching

motion of the blade mitigates the impact of large-scale inflow turbulence on the aerodynamic force coefficients, e.g. lift and to some extent on the drag for $k_{\text{red}} = 0.2$. Indeed, the moment is strongly dependent on the increase of the integral length-scale for both the reduced frequencies, $k_{\text{red}} = 0.1$ and 0.2. In addition, the snapshots of the vorticity flow field, surface pressure and skin-friction at different incidences support the results obtained from the simulations of high reduced frequency of the wind turbine blade in large-scale inflow turbulence.

- The lift-to-drag ratio showed shorter polar-drag curves with large-scale inflow turbulence, which significantly reduces the maximum aerodynamic performance of the pitching wind turbine blade. A similar trend was found in both the reduced frequencies 0.1 and 0.2, which means that the impact of large-scale inflow turbulence on the aerodynamic performance is independent of the blade pitching motion.
- The motion of the wind turbine significantly contributes to the total turbulent shear stress in the wake and the larger the turbulence length scale, the higher the total shear stress in the wake. The quadrant analysis revealed that the dispersive shear stress and total shear stress are positive and negative, respectively. This suggests propulsion and resistance in the wake flows of a pitching wind turbine blade. The new phenomenon is important to understand the mechanism of wind turbine wake travelling very far from its operation site, or the flow could be described as non-turbulence unsteadiness.

The new phenomena of large-scale inflow turbulence derived from this study provide a novel understanding needed to enhance the development of the innovative aerodynamic design for modern large wind turbine blades to withstand turbulent wind loading during their operational lifespan. In addition, the current study contributes relevant data of large-scale turbulence not seen in the literature to the turbulence research communities that will enhance the development of theoretical models for wind turbine research in particular. It is crucial to state that this is the first attempt that has numerically studied using LES to model the impact of integral length-scale greater than the pitching blade chord length of 1 m to the best of the author's knowledge.

Chapter 7

Conclusions and recommendations

The research key points are deduced for wind turbine blade aerodynamics in which large-eddy simulations are used. This thesis has sought to understand the impact of energetic large-scale inflow turbulence on wind turbine blade aerodynamics. The novel results are summarised, and recommendations are given for future work.

The topics of large-scale turbulence effect on wind turbine aerodynamics are explored by critical literature review in Chapter 2. The literature search indicated that the research area of large-scale turbulence is not well studied or documented in the field of wind turbine research, unlike high turbulence levels (turbulent intensity). Perhaps, this is due to the limitation of the wind tunnel experiment not being able to reproduce close to the realistic large turbulent scales (e.g. eddies size greater than 1 m) that exist in the height of the atmospheric boundary layer which large wind turbine operates. Arguably, this must-have contributed to why large-scale turbulence data for wind turbine aerodynamics are scarce in the literature. In particular, for a blade oscillating in pitching motion, which is typical to model non-uniform wind speed across the wind turbine height, highly unsteady incoming flows and at a yawed angle.

Moreover, there are opposing inferences of the effect of large-scale turbulence on the aerodynamics performance of a static aerofoil, majorly from experimental studies. Therefore, it is not clear whether the large incoming eddies improve the performance of the aerodynamic forces of a pitching aerofoil. Indeed, new numerical results of dynamic motion blades that could account for the pre-stall and post-stall regime of a static aerofoil would significantly contribute to reaching a global consensus for the effect of large-scale turbulence on wind turbine blade aerodynamics.

The advanced numerical modelling methods such as large-eddy simulation (LES) in Chapter 3 are promising to simulate highly unsteady flow and capture fundamental flow physics of large-scale eddies interactions with a pitching wind turbine blade and with high fidelity of the numerical solutions. However, the numerical approach poses new challenges for implementation, such as the massive computational resources required to run the 3D simulations using LES. The large scales turbulence are generated by the imposed inflow conditions, which must be adequately resolved spatially and temporally inside the computational domain. This makes the calculations very expensive. Thereby, strategies were developed to overcome the challenges as discussed in Subsection 2.4.2, Chapter 2.

7.1 Major conclusions

The initial phase of this work (Chapter 4) was to conduct sensitivity studies to obtain quality mesh resolution and to check the effect of LES SGS models on the numerical solutions to select an adequate SGS model for the current investigated topic using 2D and 3D LES of a static NACA 0012 aerofoil at $\alpha = 10°$. This work found and concludes that:

1. The SMT_{2D} is found to be of high quality and was used for the SGS model sensitivity test. The mixed time-scale (MTS) SGS model produced a better prediction of the separation bubble peak with 0.71% of the pressure coefficient and the reattachment point with 9% of the skin-friction coefficient compared to the wind tunnel measurement at Reynolds number $Re = 135{,}000$.
2. The MTS SGS model consistently outperformed the Smagorinsky SGS model by analysing the average lift-to-drag ratio with an average difference of 39%. The low performance of the Smagorinsky SGS model was attributed to the dissipation of excessive turbulence near the aerofoil surface, which suppresses the laminar separation bubble. Therefore, MTS was adopted for the simulations of the current study.

The simulation of the dynamic stall of a NACA 0012 aerofoil oscillating in pitching motion at various reduced frequencies $k_{\text{red}} = 0.1$, 0.15, 0.3 and 0.4 in smooth inflow (Chapter 5) was investigated for the study of the effect of high reduced frequency on the aerodynamic performance using 2D and 3D simulations. This study was to understand the global flow fields of the dynamic stall in smooth inflow before applying the inflow turbulence conditions to numerically study the impact of large-scale turbulence on the aerodynamic performance of a wind turbine blade. This work found and concludes that:

1. The present 2D LES and 3D LES results (such as the lift and moment coefficients) are in reasonable agreement with the experimental and other numerical data in the references. In the 3D LES, the lift hysteresis loop increase during the upstroke and downsroke of the pitching blade as the reduced frequency increases, while the peak drag coefficients decrease as the reduced frequency increases. The moment coefficient showed a strong dependency on the reduced frequency - this is primarily due to the position of the aerodynamic force centre being affected by the pitching motion at different pitching frequencies. In general, the 2D LES data are consistent with the 3D LES data.
2. The dynamic stall occurs near the maximum angle of attack toward the downstroke with the increase of the reduced frequency $k_{\mathrm{red}} = 0.2$ to 0.4, which implies that the dynamic stall angle for $\mathrm{k_{red}} \geq 0.2$ must be very close to the maximum angle of attack. The phase angle, which is used to predict the global minimum moment coefficient, showed a significant shift from the upper limit of the upstroke region into the deep downstroke region as the reduced frequency increases from $k_{\mathrm{red}} = 0.1$ to 0.4. These findings are consistent in both the 2D LES and 3D LES results.
3. Pitching motion at the high reduced frequencies significantly enhances suppression of the leading edge vortex (LEV) during the upstroke, which results in the delay of the reattachment of the boundary layer until at a lower angle of attack in the downstroke, e.g. for $k_{\mathrm{red}} = 0.4$. For the different reduced frequencies investigated, a new trend was identified as in the merging of LEVs within a chord length from the leading edge during upstroke stroke increases lift, while the splitting of LEV and trailing edge vortex (TEV) after their interaction causes a sharp decline of lift during the downstroke regime. But this trend was less visible for the higher reduced frequencies (e.g. $k_{\mathrm{red}} = 0.4$) because of weaker interaction of LEV and TEV compared to that at lower reduced frequencies.

The investigation of the impact of large-scale inflow turbulence on the aerodynamic characteristics and performance of a pitching wind turbine blade section for reduced frequencies $k_{\mathrm{red}} = 0.1$ and 0.2 was carried out (Chapter 6) by the imposition of an efficient and divergence-free inflow turbulence condition (XCDF) capable of generating synthetic large eddies inside the computational domain. The XCDF approach is applied upstream to the flow over a pitching blade with a NACA 0012 profile of chord length 1 m. Large-scale turbulence of streamwise integral length-scale ($\mathrm{L_x}$) ranging from $1c$ - $1.5c$ and constant turbulence intensity of 11% are studied. The core focus of this work is to reveal a new understanding and provide data for the impact of the large-scale inflow turbulence on the dynamic stall of the pitching blade. This work found and concludes that:

1. It was found that the effect of small-scale turbulence of streamwise integral length-scale ($L_x = 0.3c$) and turbulent intensity $TI = 11\%$ increase the lift coefficient approximately by 45% during the downstroke compared to smooth inflow for reduced frequency $k_{red} = 0.1$. The drag and minimum moment coefficients changes due to turbulence inflow are small compared to those in the smooth inflow. This current results bridges the research gap between reduced frequencies $k_{red} = 0.05$ (e.g. [4]) and 0.2 (e.g. [22]) of any uncertainties and establishes the effect of small-scale turbulence on the aerodynamic coefficients of a pitching blade under deep dynamic stall.

2. Large-scale inflow turbulence of integral length-scale equal or greater than the chord length ($c = 1$ m) and $TI = 11\%$ have an adverse impact on the lift, drag and moment coefficients during the upstroke and downstroke of the pitching wind turbine blade for both the cases $L_x = 1c$ and $L_x = 1.5c$. The effect on the maximum lift coefficient at the dynamic stall angle near the maximum angle of attack is by an average of 20% and during the downstroke is by an average of 22%, while the maximum drag and minimum moment coefficients have an average of 21% and 60%, respectively compared to the smooth inflow. This means that the lift and drag decrease with the increase of integral length-scale while the global minimum moment coefficient increase with the given inflow conditions. These impacts are mainly attributed to the early separation of the boundary layer during the upstroke and disordered, break-down, and slow convection of the lead-edge vortex by the impingement of the incoming large-scale turbulence, which is evident on the vorticity snapshots and pressure and skin-friction coefficients for this specific reduced frequency $k_{red} = 0.1$.

   It was found that the new results of the effect of the incoming large-scale turbulence on aerodynamic force coefficients and moment coefficients of a pitching blade are opposite to the effects of small-scale turbulence reported in this thesis and the literature (e.g. [22, 4]). The preliminary 2D LES study for $k_{red} = 0.1$ of the impact of large-scale inflow turbulence on the aerodynamic force coefficients in Appendix B are consistent with the 3D LES data of this work, which also supports [42, 45, 43] arguments that large-scale turbulence affects the aerodynamics performance of static aerofoils.

3. The impact of large-scale turbulence on the pitching blade at a high reduced frequency $k_{red} = 0.2$ does not increase the lift coefficient during the upstroke and downstroke, while the peak drag coefficient decreases and the absolute value of the minimum moment coefficient increases for both of the cases $L_x = 1c$ and $L_x = 1.5c$ compared to those of the smooth inflow. The fast blade motion energises the 'semi-disordered' LEVs, thereby improving its convection downstream as nearly the same as the LEV motion in smooth inflow as the angle of attack increases, which was evident in the snapshots of the vorticity flow field, surface pressure and skin-friction. This explains that the higher

pitching motion of the blade diminishes the effect of the incoming large-scale turbulence on lift coefficient than a lower pitching motion, e.g. $k_{\text{red}} = 0.1$. The effect on the drag and moment coefficients have an average of 15% and 54%, respectively, compared to smooth inflow.

4. The drag-polar (i.e. the lift-to-drag ratio) of both the reduced frequencies k_{red} = 0.1 and 0.2 shows a significant reduction of the maximum aerodynamic performance due to the impact of incoming large-scale turbulence, which suggests that this impact is independent of the blade's motion.

5. Additionally, the wake flow analysis revealed a new phenomenon of the wind turbine blade's motion contribution to the dispersive shear stress and turbulent shear stress downstream in the wake region. The downstroke, which is during high phase angles ($90 \uparrow \leq \Psi \leq 270 \downarrow$) of the pitching wind turbine blade, enhanced the turbulence shear stresses such as the dispersive shear stress, turbulent shear stress and turbulent kinetic energy downstream in the wake.

   The inward and outward quadrants events strongly influence the dispersive shear stress $\langle \hat{u}\hat{v} \rangle$, while turbulent shear stress $\langle \widetilde{u'v'} \rangle$ is dominated by the gradient-type motion such as sweep and ejection quadrants events. In addition, the dispersive shear stress $\langle \hat{u}\hat{v} \rangle$ is positive while the turbulent shear stress $\langle \widetilde{u'v'} \rangle$ stress is negative, which suggest propulsion and resistance (drag) respectively in the wake flows of a pitching wind turbine blade. However, the total shear stress, the sum of the dispersive shear and shear turbulent shear stresses, is a negative value, which supports flow resistance. This can explain a crucial phenomenon of wind turbine wake eddies slow dissipation, or the flow could be non-turbulence unsteadiness and the tendency of those eddies to travel very far away from their operational site.

In conclusion, there are evident effects of a pitching motion at high reduced frequencies on the aerodynamic characteristics such as the lift, drag and moment coefficients of an aerofoil under a deep dynamic stall. The 2D LES data demonstrate fidelity compared to the 3D LES results for high reduced frequencies and suggest that 2D LES is an affordable alternative approach when only limited computer resources are available.

The energetic large-scale inflow turbulence equal or greater than the chord length have a significant adverse effect on the aerodynamic force coefficients, moment coefficient and its performance during the upstroke and downstroke of the pitching wind turbine blade. A Higher pitching motion of the blade does not improve the aerodynamic characteristics and performance either. Furthermore, the dispersive shear stress and turbulent shear stress in the wake of the pitching wind turbine blade are positive and negative, which indicates flow propulsion and resistance, respectively, but the total turbulent shear stress is negative.

Finally, the data and knowledge derived from this current PhD thesis contribute to enhancing the innovative aerodynamic design for modern large wind turbine blades, and the accurate aerodynamic force coefficients data can be beneficial for improvement in the parameterisation of the operational blade element method (BEM) of wind turbine blades design. This is the first attempt that has numerically studied using large-eddy simulation (LES) to investigate the impact of large-scale freestream turbulence greater than the chord length of a pitching wind turbine blade at high reduced frequencies to the best of the author's knowledge.

7.2 Recommendation for future work

This work forms the basis of an initial investigation into the impact of large-scale inflow turbulence on moderate Reynolds number i.e. $Re = 135{,}000$ as applicable to wind turbine blade aerodynamics. While this work provided some substantial insight into the aerodynamic mechanisms in action, it is limited in scope, and there are a few points considered worthy for future work to improve the understanding of this specific research topic.

Possible areas for future work include:

1. Reynolds number 10^6 is one order of magnitude higher compared to the Reynolds number 135,000 used in this work is of great interest to investigate to rule out any uncertainty on this aspect. Because Reynolds number in the order of 10^6 is synonymous with the ones typical for modern large wind turbines, which will be of more benefit to the wind energy research community. Note that numerical study of such a higher Reynolds number using LES will be a challenging task due to the computational resources requirements.
2. The NACA 0012 profile is used for the blade cross-section in the current study because many details of reference data are available on these aerofoils and the fundamentals (effect of turbulence and effect of reduced frequency on the dynamic stall behaviour etc.) behind the aerofoil aerodynamics, are in principle, similar. It would be of great interest to conduct a study with aerofoil recommended by National Renewable Energy Laboratory (NREL) such as S809, S825 or S830, and NACA 44xx would have a more direct impact on wind turbine blade design.
3. A study for the impact of large-scale anisotropic turbulence, which is of more realistic turbulence in the height of atmospheric boundary layer - where large wind turbine operates is also of great interest. This includes the wind shear, gust and anisotropic effect.

4. The dispersive stress in the wake of the wind turbine blade in the current study used only 15 cycles for the analysis limits the convergence of the obtained data (e.g. phase averaged velocities, turbulence shear stress and dispersive shear stress). Therefore, the dispersive shear stress and phase averaged velocity analysis should use many more cycles well over 15 cycles is strongly recommended for the averaging procedure.

Appendix A

Wind turbine blade parameter

A.1 Damaged wind turbine blade due to turbulence

Figure A.1: Failed Wind turbine blades at the root and transition region obtain from google pictures, www.weatherguardwind.com/wind-turbine-blade-dielectric-protection/ date access 25th November 2020.

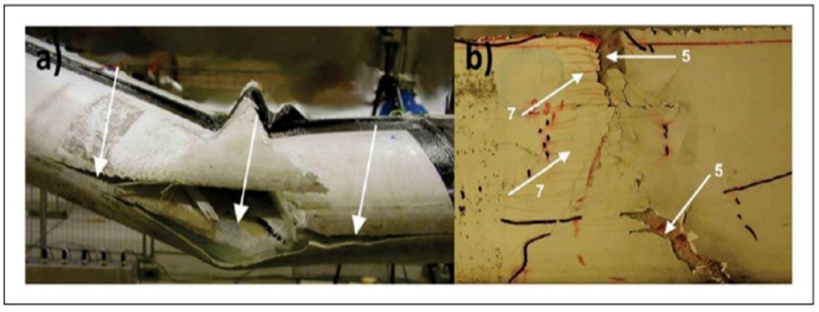

Figure A.2: (a) Type 2 damage (adhesive joint dailture between skins) [24] and (b) Type 5 damage (Laminate failure in compression) and Type 7 damage (gelcoat cracking) at the bottom of the leading at the leading edge [24].

Figure A.3: Heavy seas engulf the Black Island Wind Farm- the first US offshore wind farm. Five Halide 6MW turbines were installed by Deepwater Wind and began producing power in 2016. (Photo by Dennis Schroeder/NREL) Source: https://www.energy.gov/eere/articles/how-do-wind-turbines-survive-severe-storms date access 28th July 2021.

A.2 Wind turbine blade data

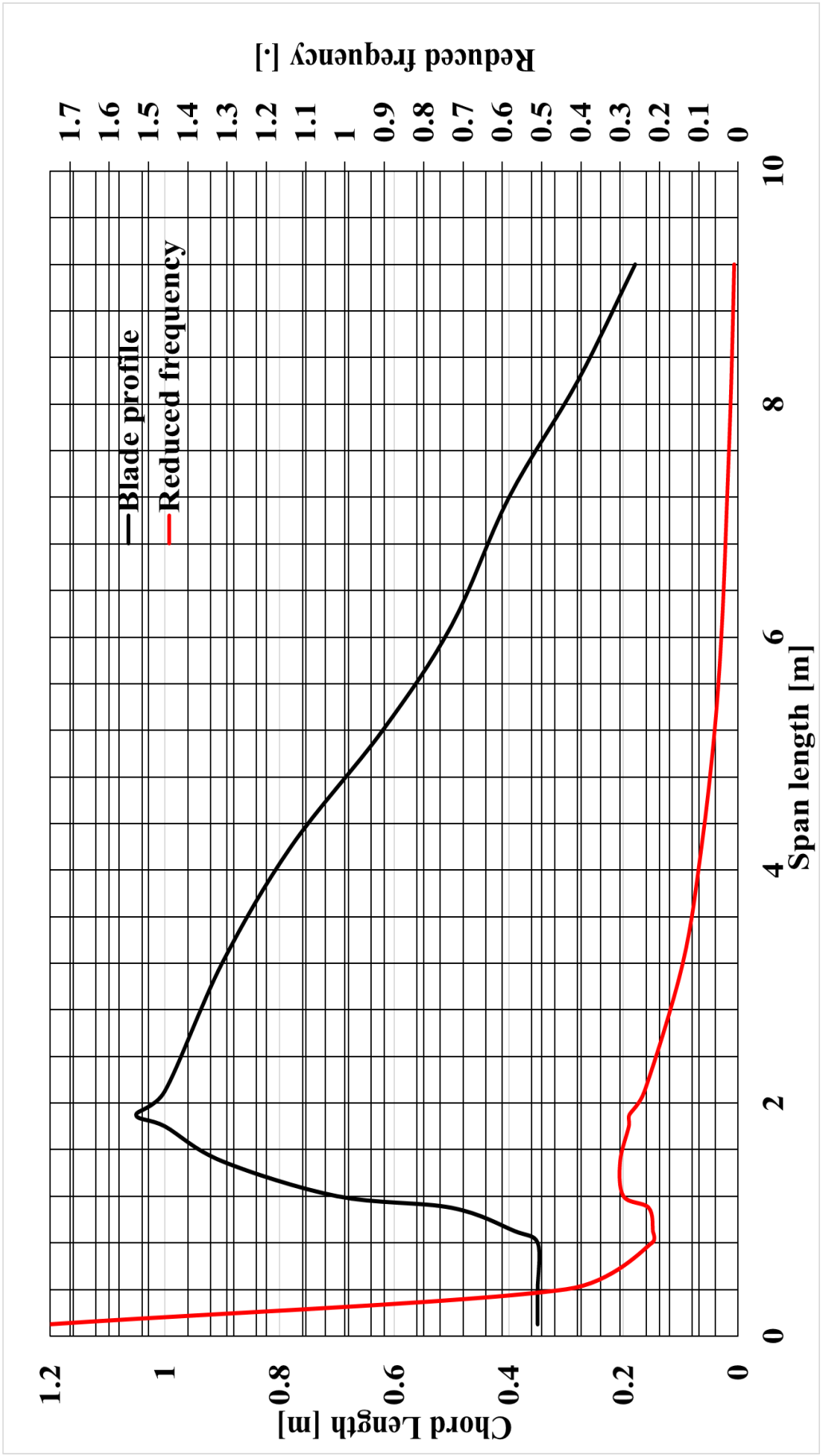

Figure A.4: Northern Power Systems (NPS) 100 kw 9.2-meter Wind Turbine blade profile and corresponding reduced frequencies along the blade chord sections.

Table A.1: Derived parameter from Northern Power Systems (NPS) 100 kw 9.2-meter Wind Turbine blade profile.

RMP [Rev/m]	**Omega** (ω) [rad/s]	**Chord** (c) [m]	**Radius** (r) [m]	U_∞[m/s]	$k_{\mathbf{red}}$	**period** (T) [sec.]	**Eddy size** [m]
	(RMP/60)2π	-	-	ω r	ωc/2U$_\infty$	$2\pi/\omega$	U_∞ T
25	2.6183	0.35	0.1	0.2618	1.75	2.4	0.62
25	2.6183	0.35	0.4	1.0473	0.43	2.4	2.51
25	2.6183	0.35	0.8	2.0946	0.21	2.4	5.02
25	2.6183	0.39	0.9	2.3565	0.21	2.4	5.65
25	2.6183	0.5	1.1	2.8801	0.22	2.4	6.91
25	2.6183	0.7	1.2	3.1420	0.29	2.4	7.53
25	2.6183	0.9	1.5	3.9275	0.3	2.4	9.4247
25	2.6183	1	1.8	4.7130	0.27	2.4	11.30
25	2.6183	1.01	1.9	4.9748	0.26	2.4	11.93
25	2.6183	1	2.1	5.4985	0.23	2.4	13.194
25	2.6183	0.9	3.2	8.3786	0.14	2.4	20.10
25	2.6183	0.78	4.2	10.997	0.09	2.4	26.38
25	2.6183	0.62	5.2	13.6153	0.05	2.4	32.67
25	2.6183	0.5	6.1	15.9718	0.04	2.4	38.32
25	2.6183	0.4	7.2	18.852	0.02	2.4	45.23
25	2.6183	0.28	8.2	21.4703	0.01	2.4	51.52
25	2.6183	0.18	9.2	24.0886	0.0097	2.4	57.80

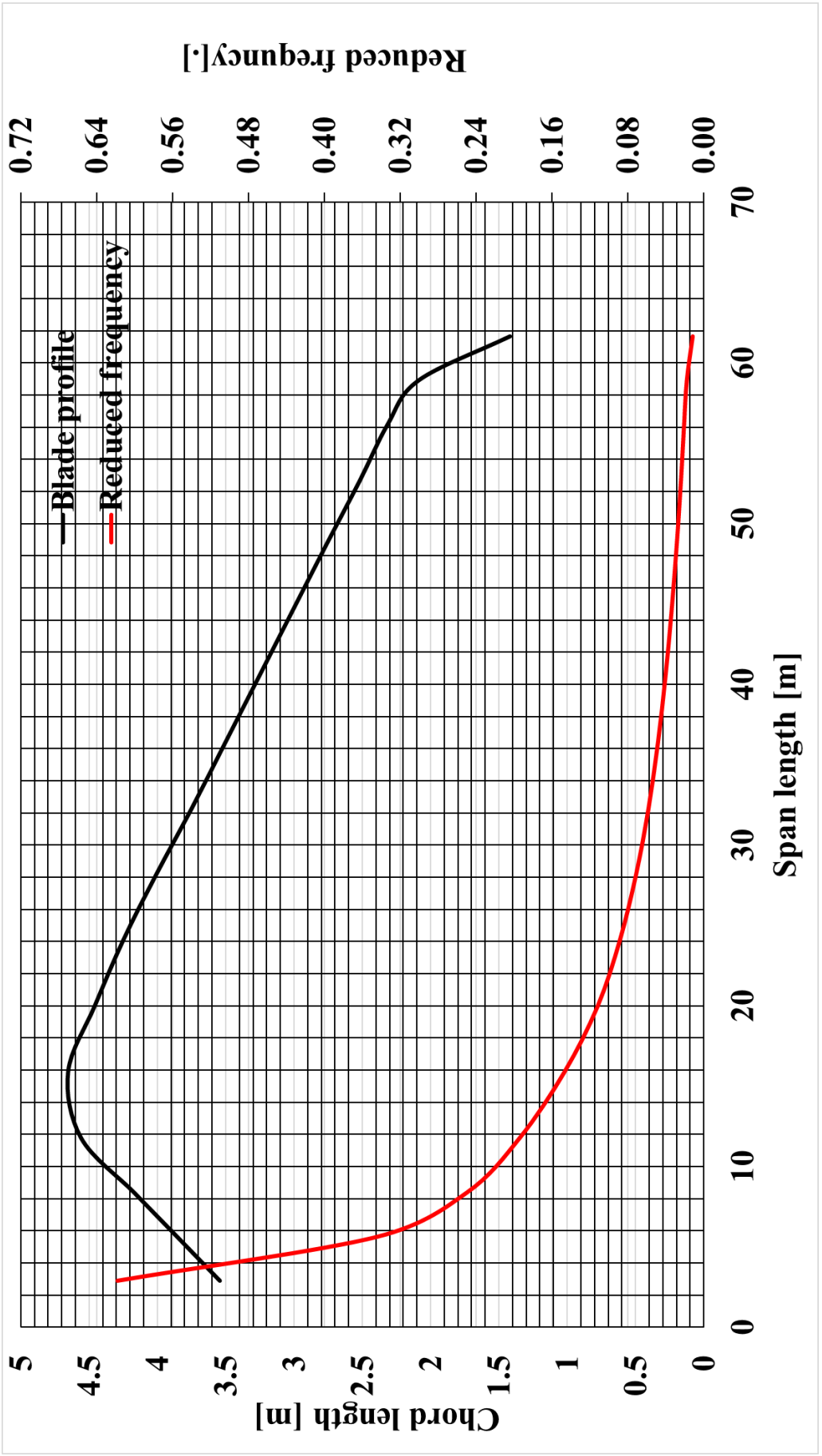

Figure A.5: NREL 5MW 61.63 - meter Wind Turbine blade profile and corresponding reduced frequencies along the blade chord sections.

Table A.2: Derived parameter from NREL 5MW 61.63 - meter Wind Turbine blade profile.

RMP [Rev/m]	**Omega** (ω) [rad/s]	**Chord** (c) [m]	**Radius** (r) [m]	U_∞[m/s]	$k_{\mathbf{red}}$	**period** (T) [sec.]	**Eddy size** [m]
	(RMP/60)2π	-	-	ω r	ωc/2U$_\infty$	$2\pi/\omega$	U_∞ T
12.1	1.2672	3.54	2.87	3.63	0.6177	4.96	18.01
12.1	1.2672	3.85	5.6	7.10	0.3441	4.96	35.19
12.1	1.2672	4.16	8.33	10.56	0.2500	4.96	52.36
12.1	1.2672	4.55	11.75	14.89	0.1939	4.96	73.83
12.1	1.2672	4.65	15.85	20.08	0.1467	4.96	99.60
12.1	1.2672	4.45	19.95	25.28	0.1117	4.96	125.36
12.1	1.2672	4.24	24.05	30.47	0.0883	4.96	151.13
12.1	1.2672	4	28.15	35.67	0.0711	4.96	176.89
12.1	1.2672	3.748	32.25	40.86	0.0581	4.96	202.65
12.1	1.2672	3.502	36.35	46.06	0.0481	4.96	228.42
12.1	1.2672	3.25	40.45	51.26	0.0402	4.96	254.18
12.1	1.2672	3.01	44.55	56.45	0.0337	4.96	279.95
12.1	1.2672	2.76	48.65	61.65	0.0284	4.96	305.71
12.1	1.2672	2.51	52.65	66.72	0.0239	4.96	330.85
12.1	1.2672	2.31	56.17	71.17	0.0205	4.96	352.95
12.1	1.2672	2.08	58.9	74.64	0.0177	4.96	370.12
12.1	1.2672	1.41	61.63	78.10	0.0115	4.96	387.30

Appendix B

2D LES approach: impact of large-scale inflow turbulence on a pitching aerofoil

B.1 Introduction

Large-scale inflow turbulence simulations were carried out in a modified 2D computational domain of mesh M1 in Chapter 5 to investigate the impact of the dynamic stall of a pitching aerofoil aerodynamics.

The motivation of this appendix chapter includes firstly - to use the 2D LES approach to simulate incoming large-scale turbulence impacting a pitching aerofoil at a reduced frequency, 0.1. This is one of the strategies adopted in Subsection 2.4.2 to get a quick insight into this research topic possible outcomes. The results help determine if it is worth carrying on with the research topic due to expensive simulations that will involve using 3D LES simulations with other technical issues, which has limited research in this specific area for decades. Secondly, the results help for the allocation of computational resources when the 3D LES computations for large-scale inflow turbulence impact on wind turbine blade aerodynamics are carried out in Chapter 6.

In this appendix chapter, the aim is to investigate the effect of integral length-scales on a pitching NACA 0012 aerofoil at a moderate Reynolds number Re = 1.35 $\times 10^5$ based on the chord length. Section B.2, covers the method and numerical settings briefly because it is similar to that of Chapter 5. In Section, B.3 the baseline simulation and case studies of the turbulence parameters used for the simulation of large-scale turbulence effect were given. In Section B.4, the effect of large-scale inflow turbulence on the aerodynamic performance of a pitching aerofoil is studied, and the results are analysed. Also included in this section are the vortex dynamics visualisation, pressure coefficient fluctuation - probability distribution function

(PDF) and the vortex shedding frequency in the wake. Section B.5 includes the summary and concluding remarks of this appendix chapter.

Part of this work was presented in a conference paper by **T.E Boye** and Z.T. Xie, UK Fluids, University of Cambridge, 2019 [47], and European Turbulence Conference ETC, 2019 [48].

B.2 Numerical settings

The governing equations are the unsteady filtered Navier-Stokes equations for an incompressibe flow is applied see Chapter 3, Eqs. (3.14 a - b), while for the sudgrid scale (SGS) is Eq. (3.17).

A divergence-free turbulence inflow condition method denoted as XCDF [25] for LES is applied to generate large-scale isotropic turbulence inside the computational domain. It is a synthetic inflow turbulence generation method. At the inflow inlet, integral length scales greater than the chord length is used for modelling the energetic large-eddies impacting on the pitching aerofoil at reduced frequencies k_{red} = 0.1. The detailed descriptions and suitability for applying XCDF in the current study have been discussed and justified in Subsections 3.5 and 3.5.2 respectively in Chapter 3.

The numerical settings used in this chapter is similar to Section 3.41 Chapter 5, for the pitching motion of the aerofoil. The additional numerical setting in this appendix chapter is the imposition of the inflow boundary condition in the computational domain. The transient incompressible solver from OpenFOAM 2.3.0 was used, and the PIMPLE algorithm is employed for the pressure-velocity coupling [142]. The decision to use the PIMPLE algorithm is based on its robustness and efficiency. PIMPLE is a combination of SIMPLE and PISO algorithm, and it could accommodate a larger time step, for example, if $CFL > 1$. Also, a second-order implicit scheme is implemented for the temporal discretization, and a Gamma differencing scheme (γ) a hybrid scheme developed by Jasak et al. (1999) [144] is used for the convective term. The time step (Δt) = 1.0 $\times 10^3$ which satisfies the mean CFL $\leq$ 1. The maximum value of CFL was thus within 2 for all cases. Also, recall that the outstanding performance of the mixed-time scale (MTS) SGS model [127] in the SGS models verification and validation in Subsection 4.4 of Chapter 4 , the MTS SGS model is thus, selected with model constant C_{MTS} = 0.03 and C_T = 10 [146]

A modified version of the H-type structured mesh was constructed in Pointwise V18 and used for the inflow turbulence cases simulation, while for the smooth inlet flow the hybrid C-H type structured mesh was used, both are from the mesh SMT_{2D} (M1), which was selected from the grid sensitivity study in Chapters 4 and 5. A skilful modification was performed in the construction of the upstream section

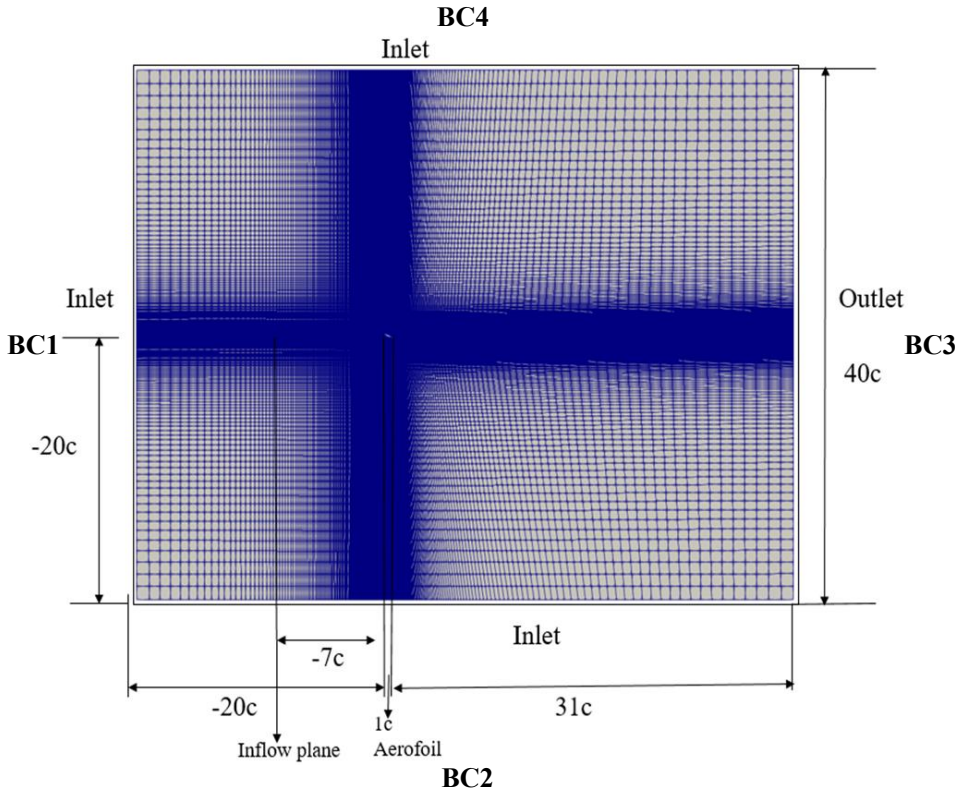

Figure B.1: Modified topology of H-type mesh with boundary condition and computational domain size. Also see Table 5.1 in Chapter 5.

of the computational domain inlet (see Fig. B.1) for easy implementation of the visual plane of the inflow turbulence boundary condition. Note that the boundary layer mesh is the same as mesh M1. It should be noted that to impose the inflow boundary condition, the construction of the computational domain is essential to allow simple alignment of the inflow condition inlet plane [116]. In that case, the turbulence inflow plane (x/c) was set for -7 upstream from the leading edge of the aerofoil. The inflow location was derived from a sensitivity test conducted not shown in the thesis. Also, [4, 25] proposed -7c upstream from the leading edge of the aerofoil is adequate for similar computational domain size to ensure less turbulence decay rate before the flow reaches the leading edge of the aerofoil.

B.3 Baseline simulations

The numerical set-up is described in Section B.2. Also, similar to that of Chapter 5 in Subsection 5.2.1 and maintained the dynamic aerofoil motion boundary condition imposed in the baseline simulations shown in Eq. 5.6. Generally, using LES calculation that needs many cycles of the pitching aerofoil for a 3D flow simulations to get statistical convergence of the solutions is usually time-consuming and

extremely expensive. Even so, the cost of computation would increase dramatically when large-scale turbulence is generated from the inflow boundary conditions that needs to be resolved in 3D spatially and temporally.

For that reason, 2D LES simulation is used to pilot the current simulations. Moreover, the justification of the adequacy and reliability of 2D LES results compared to 3D simulation results is reported in [175, 153, 129]. The verification and validation of 2D LES in Subsection 4.4, Chapter 4, and results produced in Chapter 5, demonstrated confidence on its adequacy, reliability and cost-effectiveness.

B.3.1 Smooth inflow validation

Tables B.1 captured the boundary conditions imposed on the domain on both the hybrid C-H type mesh and modified H-type mesh. The no-slip and symmetry boundary conditions are imposed on the wall (aerofoil) and the lateral sides of the domain, respectively. Recalled that an extensive convergence test had been conducted in Section in Chapter 5 for smooth inflow with the same Reynolds number, aerofoil profile, pitching motion, and reduced frequency $k_{\text{red}} = 0.1$. Hence there is no need to perform such a study again in this Appendix chapter.

Table B.1: Summary of the boundary condition (BC). U_∞ is the freestream velocity and $\partial p/\partial n$ is the derivative to the boundary. $x = x_0$ the location of visual plane of the synthetic inflow turbulence (XCDF [26]) is imposed. k_{red} is the reduced frequency. See Fig: B.1 modified H-type mesh and Fig. 4.1 hybrid C-H type mesh.

Mesh type	BC1	BC2	BC3	BC4	x_0/c
Hybrid C-type	$u_i = U_\infty$, $\partial p/\partial n = 0$	$u_i = U_\infty$, $\partial p/\partial n = 0$	$\partial u_i/\partial n = 0$, $p = p_\infty$	$\partial u_i/\partial n = 0$, $p = p_\infty$	n/a
Modified to H-type	$u_i = U_\infty$, $\partial p/\partial n = 0$	$u_i = U_\infty$, $\partial p/\partial n = 0$	$u_i = U_\infty$, $\partial p/\partial n = 0$	$du_i/dn = 0$, $p = p_\infty$	-7

The 2D case validated aerodynamic force such as the lift and drag coefficients (Mesh M1)for reduced frequency $k_{\text{red}} = 0.1$ in Fig. 5.5, Subsection 5.4, Chapter 5 and also reported by Boye and Xie [47] is adopted as the benchmark data for the comparison and analysis of the large-scale freestream turbulence effects. Therefore, further validation for the case with the same reduced frequency in this chapter would not be required. The aerofoil was set at a neutral angle of attack, $\alpha = 10°$ in the domain, i.e. at t = 0 and phase zero. The symbols '↑' and '↓' denotes pitching-upstroke and pitching-downstroke motion, respectively.

Table B.2: Pitching aerofoil parameters

Profile	NACA 0012
Re	1.35 $\times 10^5$
α_0	10°
α_1	15°
Chord length	1 m

B.3.2 Large-scale turbulence parameters for the case studies

Tables B.3 and B.4 captures the difference streamwise integral length-scales L_x for two case studies with high turbulence intensity of 11% and 20% respectively. Integral length-scale $L_x = 0.1c$ and $1c \leq L_x \leq 3c$ are categorised as small-scale and large-scale turbulence respectively. Large integral length scale in the study is referred to as streamwise integral length scale one order of magnitude higher than integral small-scale integral large-scale ($L_x = 0.1c$). Note that henceforth, integral length-scale and large-scale inflow turbulence would be used interchangeably in the Appendix chapter.

The turbulence intensity is kept constant for both the $TI = 11\%$ and 20% case studies because the focus here is on revealing the effects of the large integral length-scales on the dynamic stall of the pitching aerofoil through the lift and drag coefficients as well as corresponding flow-field of the large-scale turbulence structures. These are presented in the following sections.

Table B.3: Turbulence parameters for case with $TI = 11\%$

Flow with TI = 11%	L_x **[m]**	L_x **[.]**	**Category**
Smooth inlet	-	-	-
Case 1	0.1	0.1c	Small-scale
Case 2	1	1c	Large-scale
Case 3	2	2c	Large-scale
Case 4	3	3c	Large-scale

Table B.4: Turbulence parameters for $TI = 20\%$

Flow with TI = 11%	L_x **[m]**	L_x **[.]**	**Category**
Smooth inlet	-	-	-
Case 1	0.1	0.1c	Small-scale
Case 2	1	1c	Large-scale
Case 3	2	2c	Large-scale
Case 4	3	3c	Large-scale

B.4 Large-scale inflow turbulence effect

The numerical experiments using 2D LES method was commenced with the modelling of small-scale turbulence $L_x = 0.1c$ for both case study with $TI = 11\%$ and 20% respectively. The results are compared with smooth inflow to estimate the effect on the aerodynamic force coefficients, such as the lift and drag. This strategy employed for this initial study is first to gain confidence in the inflow turbulence cases numerical settings and secondly to use the results as reference data for the large-scale turbulence effect scenario. It should be noted that all simulated cases run for a minimum of 20 pitching cycles of the aerofoil, which are used for phase averaged of the lift, drag and moment coefficients after initialising with the first 10 cycles.

B.4.1 Effect of small-scale inflow turbulence on the aerodynamic characteristics of a pitching aerofoil

Again, note that integral length-scale $L_x = 0.1c$ is categorised as small-scale while $1c \leq L_x \leq 3c$ are categorised as large-scale turbulence in the current study. Fig. B.2 shows the lift and drag coefficients of the hysteresis loop on the dynamic stall of the NACA 0012 pitching aerofoil at $k_{red} = 0.1$ in small-scale freestream turbulence for case 1 with $TI = 11\%$ and case 1 with $TI = 20\%$ compared with smooth inflow data.

The effect of the small-scale freestream turbulence on the aerodynamic characteristics does not significantly change forces hysteresis at any given conditions. The linear region of the lift coefficients and angle of the maximum lift and drag are nearly the same as those of the smooth inflow. The increase of $TI = 11\%$ to higher $TI = 20\%$ with the same integral length-scale not do cause any change to the aerodynamic performance of the pitching aerofoil in these cases. The results in Fig. B.2 (a - b) shows consistency during the upstroke of the lift coefficients with similar results reported by Kim and Xie [4] that used LES to model the effect of small-scale freestream turbulence ($k_{red} = 0.05$ and $TI = 10\%$) flow over a pitching NACA 0012. Other groups that perform wind tunnel tests [110, 40] also reported a similar effect of small-scale freestream turbulence on the lift coefficient during the upstroke.

The effect of inflow turbulence in the downstroke observed in the lift and drag for both cases at $\approx 15^\circ \downarrow \leq \alpha \leq 20^\circ \downarrow$ is small compared to the smooth inflow. There is a small reduction of the lift coefficients within those pitching regions of the aerofoil motion before recovering. This can be attributed to the interaction of the incoming small-eddies with the second leading-edge vortex during the downstroke, typical for k_{red} =0.1.

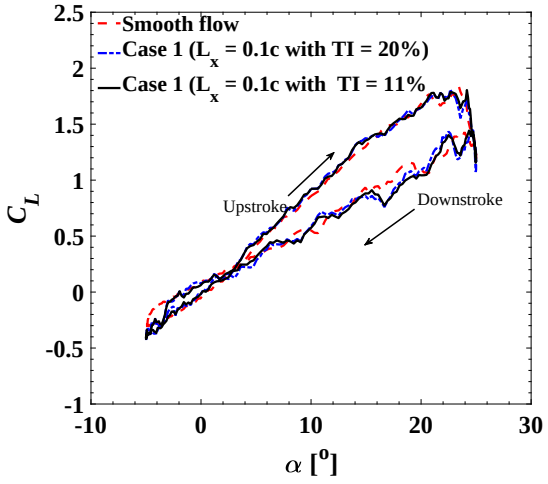

(*a*)

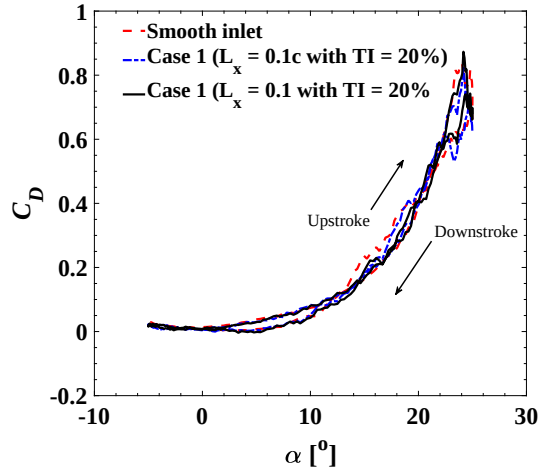

(*b*)

Figure B.2: Small-scale turbulence $L_x = 0.1c$ for both case study of $TI = 11\%$ and 20% phase averaged aerodynamics coefficients (a) Lift, (b) Drag, $k_{red} = 0.1$.

It should be noted that the small-scale turbulence effect results combined with that of smooth inflow results for $k_{red} = 0.1$ are used as reference data for comparison of large-scale turbulence effect on the aerodynamic performance of the pitching aerofoil going forward.

B.4.2 Effect of large-scale turbulence on the aerodynamic characteristics of a pitching aerofoil

Figure B.3 (a-c) shows the effect of large scales freestream turbulence with $TI = 11\%$ on aerodynamic characteristics such as the lift, drag and moment coefficients respectively. During the upstroke regime, the effect of the large-scale freestream

turbulence with $TI = 11\%$ on the aerodynamic force coefficients was observed to be insignificant compared to smooth inflow and small-scale turbulence.

In general, it is hard to estimate the effect of the large-scale inflow turbulence during the downstroke regime due to the complexity of the aerodynamic force profiles in the downstroke, which is characterised by the non-linearity of the highly separated flow of the boundary layer of the pitching aerofoil and free shear flow. Therefore, in order to give a good estimation on the effect of the large-scales turbulence on the lift, drag and moment coefficients. The data of cases 2 to 4 in Fig. B.3 (a-c) were assembled and averaged to get a new single large-scale turbulence effect profile with $TI = 11\%$ for the lift, drag and moment coefficients show in Fig. B.5 (a-c). This new assembled averaged data is denoted as assemble aved. large integral length-scale with $TI = 11\%$.

Fig. B.4 (a-c) shows the effect of large-scales freestream turbulence with $TI = 20\%$ on aerodynamic characteristics such as the lift, drag and moment coefficients respectively. Significant effect of the large-scale turbulence is observed on the lift, drag and moment coefficients. The most evident impact of the large-scale freestream turbulence is on the lift coefficient that occurred during the upstroke compared to the smooth inflow and small-scale integral length-scale. In addition, a noticeable effect is observed during the downstroke. The lift coefficient during the upstroke of the various large length scales in Fig. B.4 (a) have non-linear profiles, and the downstroke profiles are very complicated to estimate the impact. This is due to the early rapid separated flow within the boundary layer vicinity (see Fig. B.6 a - b), which results to surface pressure fluctuations during the upstroke.

A similar assembled averaged procedure performed for large-scale turbulence cases study with $TI = 11$ % is applied of for the lift, drag and moment coefficients of cases 2 - 4 in Fig. B.4 (a-c) and a new single large-scale freestream turbulence effect profile with $TI = 20\%$ is obtained for the lift, drag and moment coefficients respectively as shown in Fig. B.5 (a - c) and denoted as assemble aved. large integral length-scale with $TI = 20\%$.

The assembled averaged lift, drag and moment coefficients of the large scales inflow turbulence effect on the dynamic stall is shown in Fig. B.5 (a-c) respectively. It was found that large-scale inflow turbulence case study with $TI = 11\%$ (pink dot-dash line) in Fig. B.5 (a) indicates a marginal effect on the lift hysteresis loop during the upstroke, i.e. the lift coefficient dropped marginally during the upstroke and the downstroke compared to smooth inflow case. This suggests that the effect large-scale turbulence is relative to the energy it contains, which is evident in the case study with $TI = 20\%$ in Fig. B.5 (a). The solid blue line in Fig. B.5 (a) shows the effect of large-scale turbulence for case study with $TI = 20\%$.

From the data in Fig. B.5 (a), it was found that large-scale turbulence has a significant adverse effect on the lift coefficient during the upstroke and a noticeable

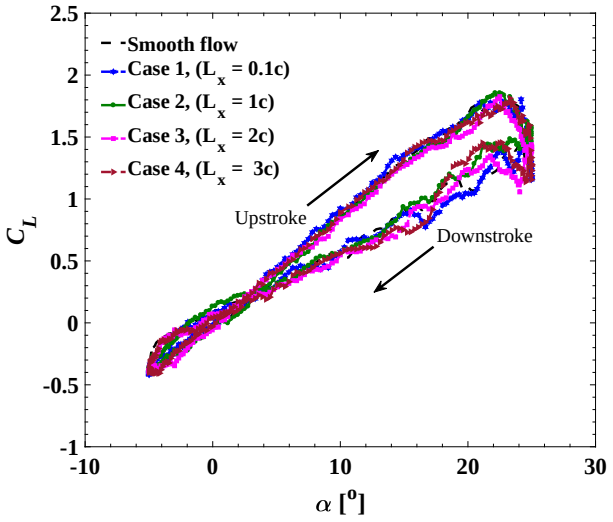

(a)

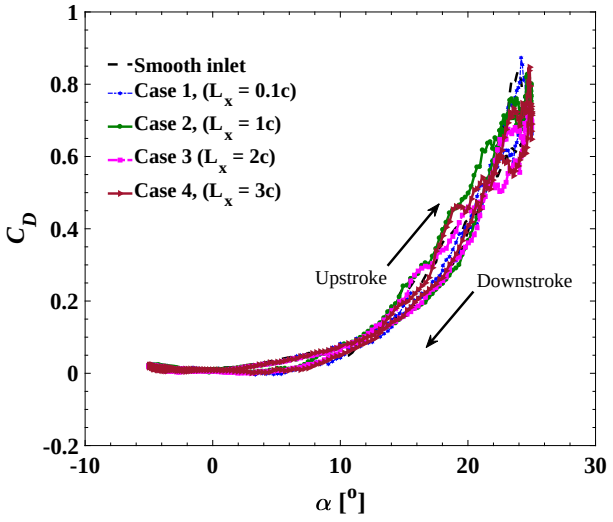

(b)

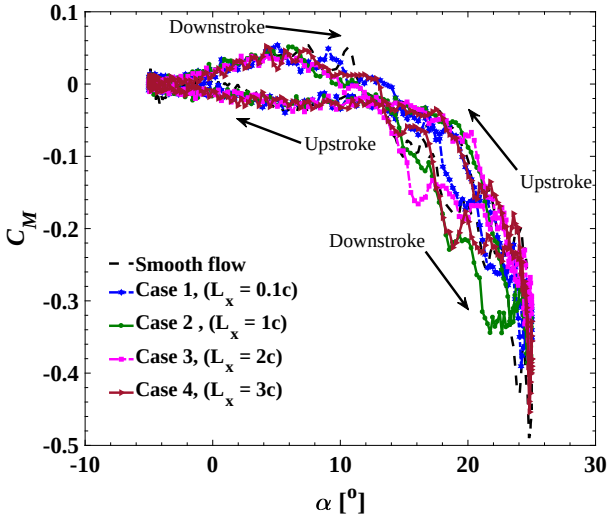

(c)

Figure B.3: Large-scale turbulence $1c \leq \mathrm{L_x} \leq 3c$ with $TI = 11\%$ phase averaged aerodynamics coefficients (a) Lift, (b) Drag, (c) moment, $k_{\mathrm{red}} = 0.1$.

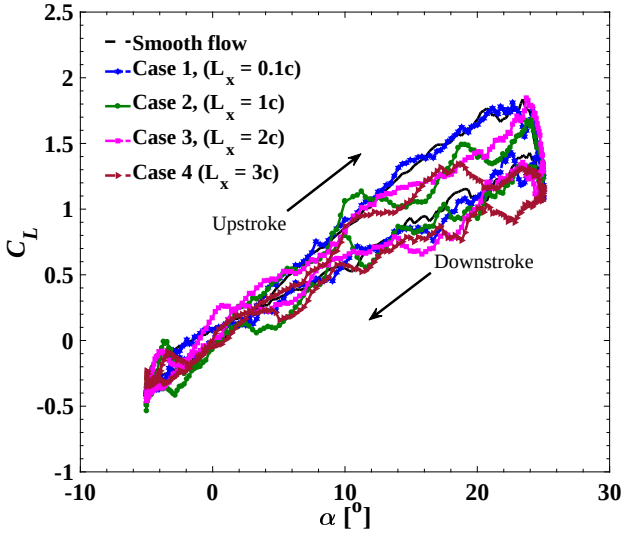

(a)

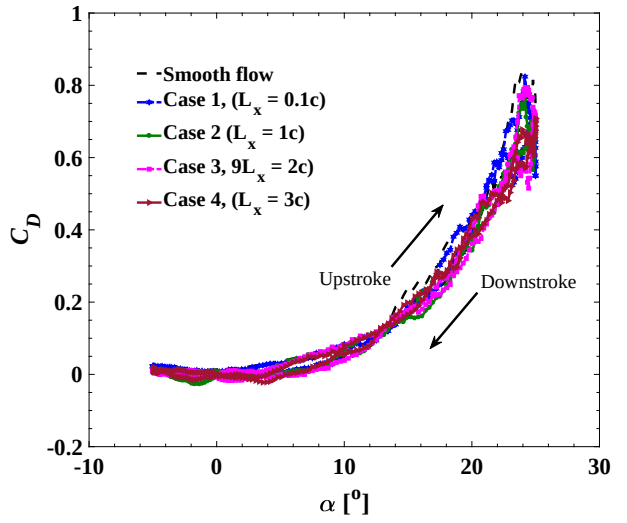

(b)

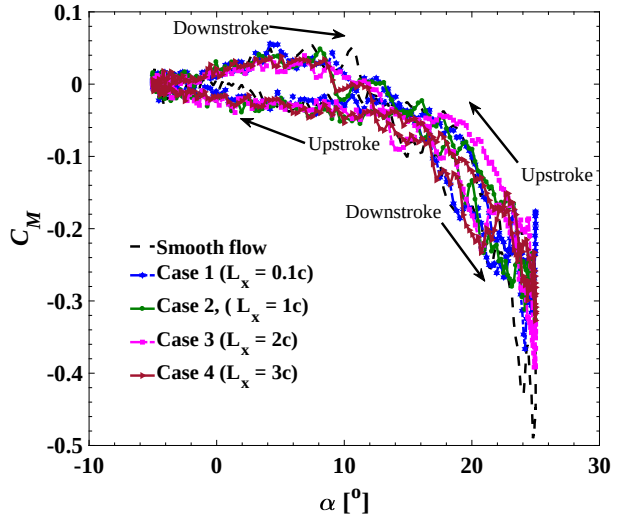

(c)

Figure B.4: Large-scale turbulence $1c \leq \mathrm{L_x} \leq 3\mathrm{c}$ with $TI = 20\%$ phase averaged aerodynamics coefficients (a) Lift, (b) Drag, (c) moment, $k_{\mathrm{red}} = 0.1$.

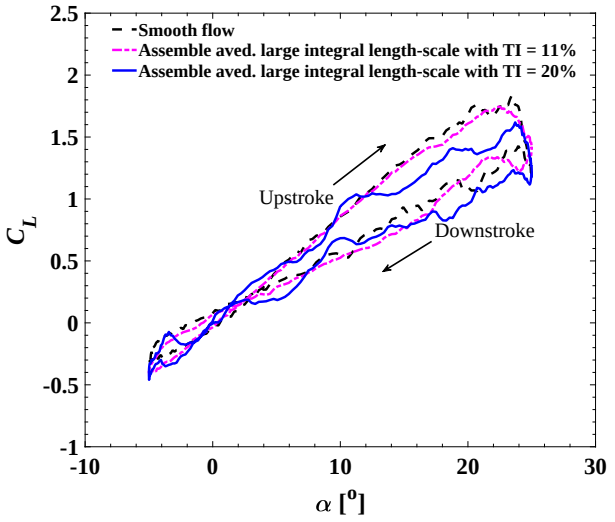

(*a*)

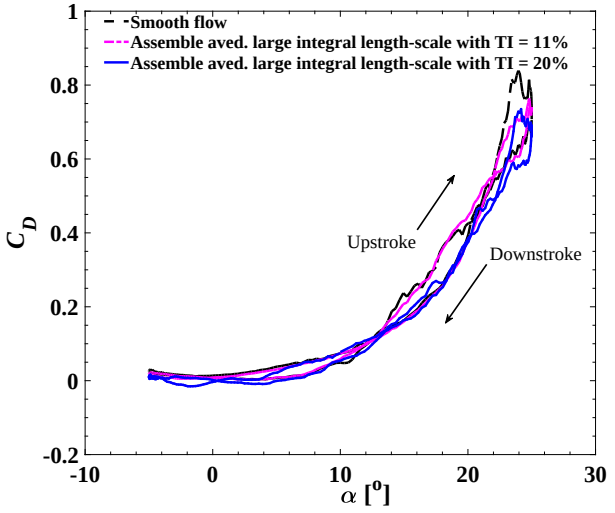

(*b*)

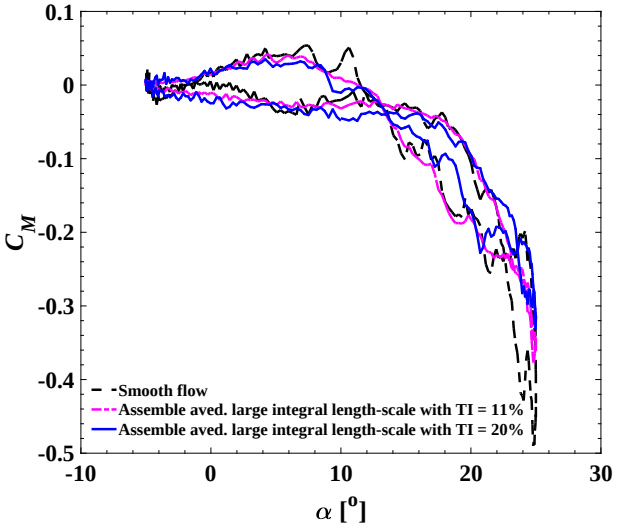

(*c*)

Figure B.5: Assembled phase averaged of large-scale turbulence aerodynamics coefficients (a) Lift, (b) Drag, (c) moment, $k_{\text{red}} = 0.1$.

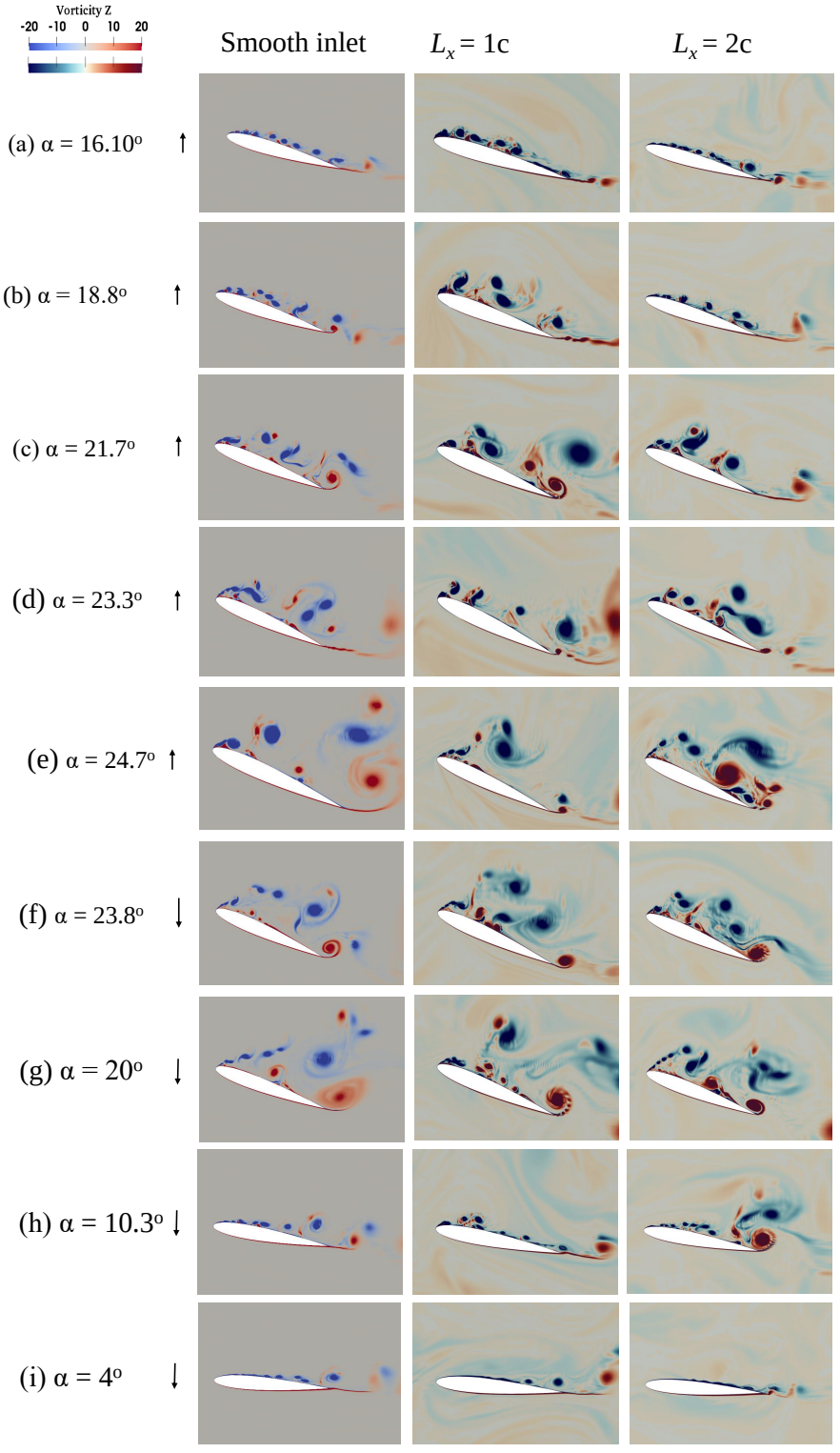

Figure B.6: The instantaneous 2D vorticity flow field normalised by c and U_∞ for smooth flow in (left), Large-scale $L_x = 1c$, $TI = 20\%$ (middle) and Large-scale $L_x = 2c$, $TI = 20\%$ (right). $Re = 1.35 \times 10^5$, $\alpha(t) = 10° + 15° \sin(\omega t)$ and $k_{red} = 0.1$

effect on the downstroke. Similarly, the flow memory is reduced substantially (the solid blue line compared with the black-dash line at $12°\uparrow \downarrow \leq \alpha \leq 25°\uparrow \downarrow$ and $\downarrow$) in Fig: B.5 (a-c). This is due to the incoming energetic large eddies interaction with the leading-edge vortex; as a result, break-down the leading-edge vortex near the leading edge of the pitching aerofoil to smaller structures during the upstroke and alters the flow of the coherent structures of the leading-edge vortex. (see Fig: B.6 (c - e)). Fig. B.7 clearly shows the effect of the incoming energetic large-scale turbulence on the leading-edge vortex at the maximum angle of attack $\alpha = 25°$.

An experimental result of the short laminar separation bubble of the leading edge on static aerofoil is due to large-scale eddies, which was reported by [106]. Moreover, the incoming inflow energetic turbulence's promotes early separation of the boundary layer of the pitching aerofoil during the upstroke regime, which is evident in the snapshots of the vorticity flow field shown in Fig: B.6 (a-c). Another effect of the large-scale turbulence with $TI = 20\%$ is early re-attachment of the boundary layer during the downstroke with evidence shown in the snapshots of the vorticity flow field (Fig. B.6 (e - i)).

The magnitude of the maximum drag coefficient slightly decrease in both large scales turbulence case studies with $TI = 11\%$ and 20%, However, the minimum moment coefficient significantly decrease in both large scales turbulence case studies with $TI = 11\%$ and 20% compared to smooth inflow case shown in Fig: B.5 (c). This is interesting because it is observed that energetic large-scale turbulence increased the minimum moment coefficients and the variation of the pitching moment during the dynamic stall process.

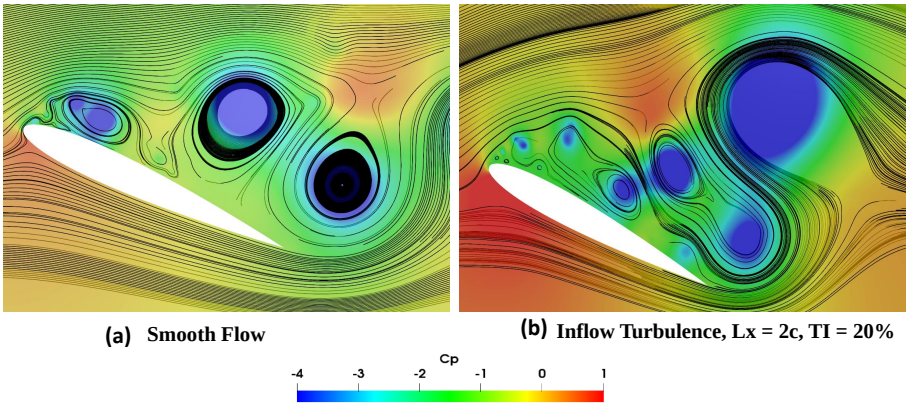

Figure B.7: Pressure coefficient contour superimpose with instantaneous velocity streamline at $\alpha = 25°$(Maximum angle of attack). (a) Smooth inflow, (b) Inflow turbulence, $L_x = 2c$ with $TI = 20\%$

Fig. B.7 shows the impact of leading-edge vortex and increase pressure fluctuations at the maximum angle of attack $\alpha = 25°$. It is interesting to note that at the maximum angle of attack, a large negative pressure/vortex structure is observed

near the leading-edge of the pitching aerofoil in the smooth inflow case B.7 (a). For the large-scale turbulence case, no visible negative pressure/vortex other than a weaker and smaller vortex structure is observed within the mid-chord of the pitching aerofoil. This also supports the earlier suggestion that large-scale inflow turbulence breaks down the generated large leading-edge vortex structure to small structures at the leading edge of the pitching aerofoil and increases the pressure fluctuations within the boundary layer vicinity of the upper and bottom surfaces of the aerofoil. As a result, the lift coefficient performance is affected significantly during the upstroke of the dynamic stall procedures.

The case study of large scales inflow turbulence with $TI = 20\%$ produced more interesting results on the effect of the aerodynamic performance of the pitching aerofoil than the case study of large scales inflow turbulence with $TI = 11\%$. Therefore, the further analysis focuses on the case study of large scales turbulence with $TI = 20\%$ for the remaining section of this appendix chapter.

B.4.3 Probability distribution function (PDF) of the pressure coefficient fluctuations

A statistics tool such as the probability density function (PDF) is used to analyse the surface pressure fluctuations near the surface of the pitching aerofoil at different locations of streamwise chord length. Fig. B.8 shows the PDF of the surface pressure coefficient fluctuations $Cp^{'}$ at $x/c = 0.1$, 0.25, 0.75 and 1 and $y/c = 0.1$ on the suction side of the pitching aerofoil. Note that the probes move relatively with the aerofoil motion, and data for two pitching cycles are used for the sampling of the $Cp^{'}$ data.

The PDF shows the positively skewed distribution of the $Cp^{'}$, which is from the low-pressure generated on the suction surface of the pitching aerofoil. At these locations x/c = 0.1 and 0.25 within the leading edge of the aerofoil, it is observed that large-scale turbulence of $L_x = 1c$ and $2c$ PDFs are bimodal and multimodal, respectively. The smooth inflow case and small-scale turbulence $L_x = 0.1c$ case have a single-mode each. However, it was found that large-scale turbulence of $L_x = 3c$ tents to a single-mode probability density function. This is an indication of the pressure fluctuation of large-scale turbulence, e.g. $L_x = 3c$ at location $x/c = 0.1$ and 0.25 for the current study tents to go back and resemble smooth inflow PDF profile. Haan Jr et al. [162, 12] reports similar experimental results of the effect on large scale turbulence much greater than the rectangle prism length and flat plate respectively.

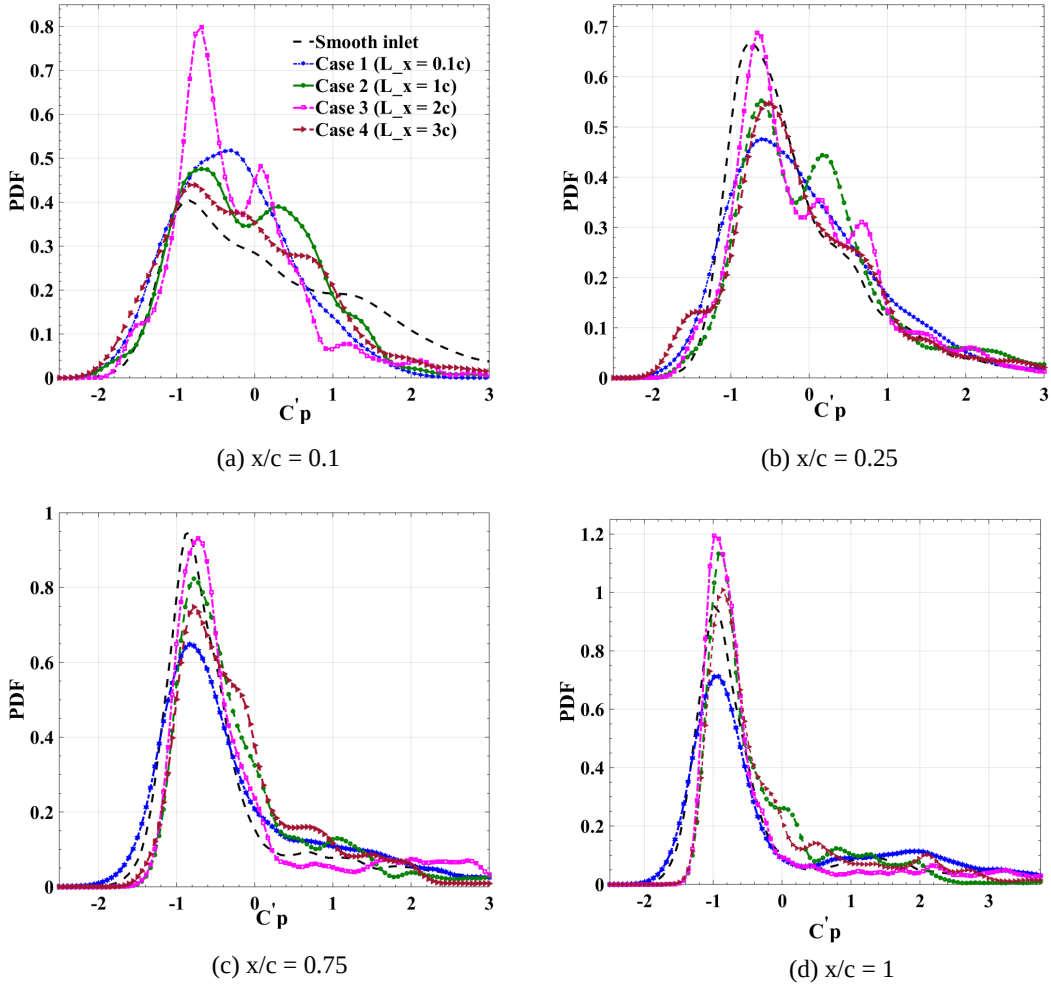

(a) x/c = 0.1

(b) x/c = 0.25

(c) x/c = 0.75

(d) x/c = 1

Figure B.8: PDF of Cp′. Large-scale turbulence turbulence $0.5c \leq \mathrm{L_x} \leq 3c$ with $TI = 20\%$ over the suction-side of the pitching aerofoil chord length at probe location $\mathrm{x}/c = 0.1$, 0.25, 0.75 and 1, $\mathrm{y}/c = 0.1$ for two pitching cycle.

B.4.4 Effect on the vortex shedding frequency near the wake

Figs. B.9 and B.10 shows the power spectral density (PSD) of smooth inflow and large-scale turbulence effect respectively. The data sampling points are at location $\mathrm{x}/c = 0.75$ and $\mathrm{y}/c = 0.1$ near the trailing edge. The power spectral density of the smooth inflow is first compared with that of the small-scale inflow turbulence scale $\mathrm{L_x} = 0.1\mathrm{c}$ with $TI = 20\%$. Fig. B.9 shows that the first peak corresponds to the pitching frequency of the aerofoil (see Subsection 5.5.5 in Chapter 5), and the second peak corresponds to the non-dimensional vortex shedding frequency. The strouhal number (St) for both the smooth inflow and the small-scale inflow turbulence is similar, which correlates with the aerodynamic coefficients of small-scale effect in Subsection B.4.1.

Fig. B.10 shows the PSD of the large scales turbulence compared to small scale inflow turbulence. Similar to Fig. B.9 the first peak corresponds to the pitching

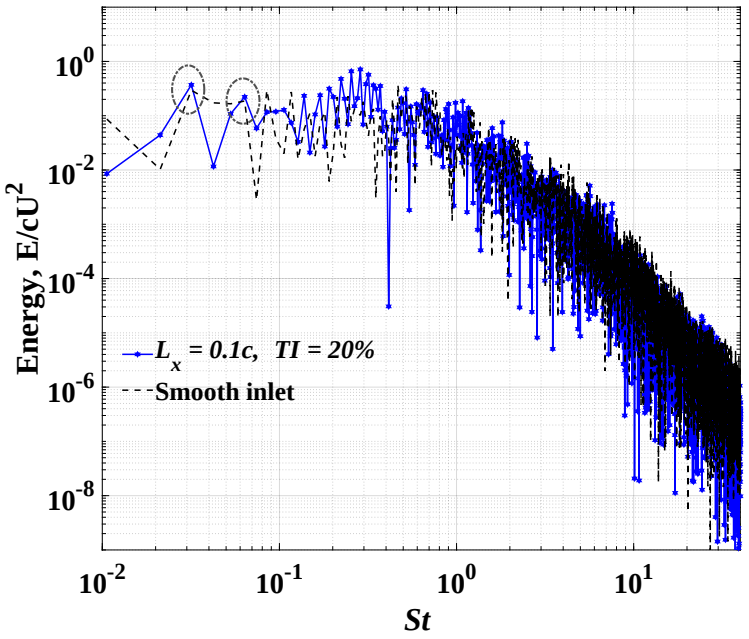

Figure B.9: Power spectral density of the cross-flow velocity normalised by the chord length and fluctuation U^2 at $0.75c$ upper surface of the aerofoil the trail edge for small-scale turbulence.

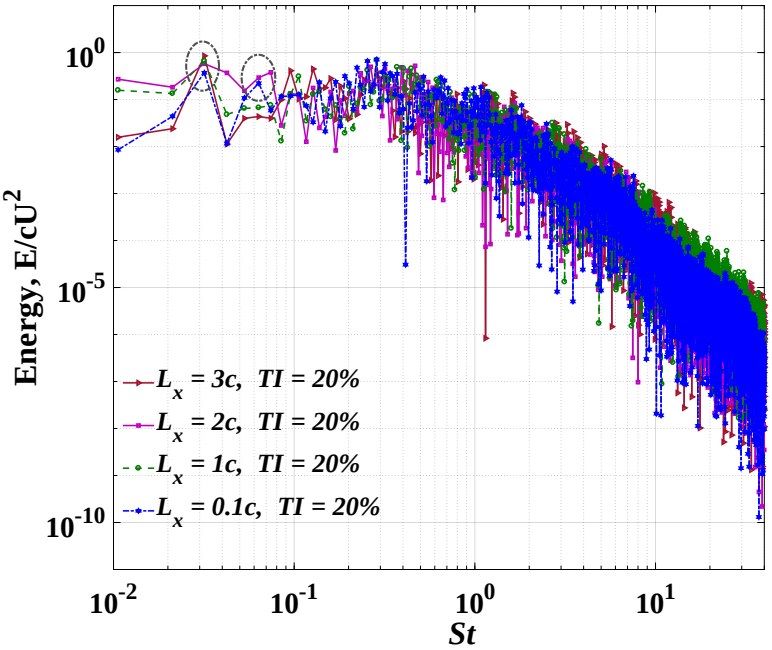

Figure B.10: Power spectral density of the cross-flow velocity normalised by the chord length and fluctuation U^2 at $0.75c$ upper surface of the aerofoil the trail edge for large-scale turbulence.

frequency of the aerofoil, while the second peak corresponds to the non-dimensional vortex shedding frequency. The magnitude of the first peaks of the large scales turbulence is consistently higher than the small-scale turbulence case, which suggests considerable energy is transferred from the incoming energetic large-eddies to the pitching aerofoil during their interaction.

The second peak in PSD in Fig: B.10 of each large-scale turbulence case, which is the vortex shedding frequency, shows that large-scale turbulence $L_x = 2c$ has the higher peak magnitude than small integral length-scale whereas, for $L_x = 1c$ and $3c$ did not show any visible peak within this vortex shedding frequency region. It is unclear why the inconsistency of vortex shedding frequency both length-scales, this could be as a result of the complete breakdown of the leading vortex at a higher angle of attack during the upstroke as observed in the lift coefficient hysteresis loop in Fig. B.4 - (a). However, close observation in the frequency domain of large scales turbulence larger than the chord length, and length-scale with the same chord length was reported by Ravi et al. [12, 44].

B.5 Appendix chapter summary

The dynamic stall of a pitching aerofoil in large-scale freestream turbulence has been revealed to some extent using the 2D LES approach. This Appendix chapter is the forerunner study of Chapter 6 of this PhD thesis to determine the possible outcomes for the investigation of the impact of large-scale inflow turbulence on pitching wind turbine blades aerodynamics. Therefore, large-scale turbulence greater the aerofoil chord length, which is the dominant realistic eddy-size in the atmospheric boundary layer, was simulated. The XCDF, an efficient and divergence-free inflow condition for LES for incompressible flow solver, was used to generate large-scale isotropic turbulence inside the computational domain.

The results produced from the numerical study and the analysis of the data begets to following conclusion:

- Energetic large-scale turbulence in order of the chord length has an adverse effect on the lift coefficient of a pitching aerofoil during the up-stroke regime.
- It is evident that the leading-edge vortex significant breaks down during the dynamic stall procedure, in particular during the upstroke, which is attributed to the interaction between the energetic incoming large-scale turbulence and leading-edge vortex.
- The energetic large-scale inflow turbulence promotes early separation of the boundary layer during the upstroke and enhances early reattachment of the boundary layer at a low angle of attack during the downstroke.

– The effect of energetic large-scale freestream turbulence observed in the current study supports the experimental results for static aerofoil reported by Mahmoodilari et al. [176].

Finally, the data derived from this study provide some evidence for the impact of energetic large-scale turbulence on the aerodynamics of a pitching aerofoil in 2D LES, which is vital for the decision to further this investigation using 3D LES (Chapter 6). In addition, the results of this Appendix chapter gives some crucial insights into what to expect using the 3D simulations for the reduced frequency of 0.1. Hence, the 2D LES approach is a practical strategy for efficient simulations at the preliminary stage of the research topic despite its limits to simulate highly unsteady flows of a pitching aerofoil at a low reduced frequency used in this Appendix chapter.

References

[1] IRENA. Global energy transformation: A roadmap to 2050. Technical report, The International Renewable Energy Agency (IRENA), 2019.

[2] Qing'an L., K. Yi, M. Takao, M. Junsuke, and Y. Nishida. Effect of turbulence on power performance of a horizontal axis wind turbine in yawed and no-yawed flow conditions. *Energy*, 109:703–711, 2016.

[3] H. R. Karbasian, JA Esfahani, and E. Barati. Effect of acceleration on dynamic stall of airfoil in unsteady operating conditions. *Wind Energy*, 19(1):17–33, 2016.

[4] Y. Kim and Z. T. Xie. Modelling the effect of freestream turbulence on dynamic stall of wind turbine blades. *Comput. Fluids*, 129:53–66, 2016.

[5] L. W. Carr. Dynamic stall progress in analysis and prediction. *J. Aircr.*, 25(1):6–17, 1985.

[6] J. Locke and U. Valencia. Design studies for twist-coupled wind turbine blades. Technical Report June, Wichita State University, National Institute for Aviation Research, Wichita, Kansas 67260-0093, 2004.

[7] I. Van der Hoven. Power spectrum of horizontal wind speed in the frequency range from 0.0007 to 900 cycles per hour. *Journal of Atmospheric Sciences*, 14(2):160–164, 1957.

[8] A. Sneed. World largest wind turbine, https://www.scientificamerican.com/article/world-rsquo-s-largest-wind-turbine-would-be-taller-than-the-empire-state-building/(Date accessed: 01.04.2018).

[9] J. Teixeira and S. Cheinet. A simple mixing length formulation for the eddy-diffusivity parameterization of dry convection. *Boundary-Layer Meteorol.*, 110(3):435–453, 2004.

[10] R. B. Stull. *An introduction to boundary layer meteorology*. Kluwer Academic Publishers, 1988.

[11] S. B. Pope. *Turbulence Flows*. Cambridge University Press, 2000.

[12] S. Ravi, S. Watkins, J. Watmuff, K. Massey, P. Peterson, and M. Marino. Influence of Large-Scale Freestream Turbulence on the Performance of a Thin Airfoil. *AIAA J.*, 50(11):2448–2459, 2012.

[13] V. Maldonado, L. Castillo, A. Thormann, and C. Meneveau. The role of free stream turbulence with large integral scale on the aerodynamic performance of an experimental low Reynolds number S809 wind turbine blade. *J. Wind Eng. Ind. Aerodyn.*, 142:246–257, 2015.

[14] J. M. Yu, T. S. Leu, and J. J. Maiu. Investigation of reduced frequency and freestream turbulence effects on dynamic stall of a pitching airfoil. *J. Vis.*, 20(1):31–44, 2017.

[15] S. Wang, D. B. Ingham, L. Ma, M. Pourkashanian, and Z. Tao. Turbulence modeling of deep dynamic stall at relatively low Reynolds number. *J. Fluids Struct.*, 33:191–209, 2012.

[16] A. Laing and J.L. Evans. *Introduction to Tropical Meteorology.* The COMET, 2 edition, 2011.

[17] U. Piomelli. Large-eddy simulation: achievements and challenges. *Prog. Aerosp. Sci.*, 35(4):335–362, 1999.

[18] ANSYS Fluent. ANSYS Fluent 14.0 Theory Guide, 2018.

[19] H. Jasak and Ž. Tuković. Automatic mesh motion for the unstructured Finite Volume Method. *Trans. Famena*, 30(2):1–20, 2004.

[20] K. Rinoie and N. Takemura. Oscillating behaviour of laminar separation bubble formed on an aerofoil near stall. *Aeronaut. J.*, 108(1081):153–163, 2004.

[21] T. Lee and P. Gerontakos. Investigation of flow over an oscillating airfoil. *J. Fluid Mech.*, 512:313–341, 2004.

[22] X. Huang, M. Albers, P. S. Meysonnat, M. Meinke, and W. Schröder. Analysis of the effect of freestream turbulence on dynamic stall of wind turbine blades. *Int. J. Heat Fluid Flow*, 85, 2020.

[23] D. M. Sharma and K. Poddar. Investigation of dynamic stall characteristics for flow past an oscillating airfoil at various reduced frequencies by simultaneous PIV and surface pressure measurements. *PIV 13, 10th Int. Symp. Part. Image Velocim. Delft.*, 2013.

[24] B. F. Sørensen, E. Joergensen, C. P. Debel, F. M. Jensen, H. M. Jensen, T. Jacobsen, and K. M. Halling. Improved design of large wind turbine blade of fibre composites based on studies of scale effects (phase 1)-summary report. 2004.

[25] Y. Kim. *Wind Turbine Aerodynamics in Freestream Turbulence*. PhD thesis, University of Southampton, 2013.

[26] Y. Kim, I. P. Castro, and Z. T. Xie. Computers & Fluids Divergence-free turbulence inflow conditions for large-eddy simulations with incompressible flow solvers. *Comput. Fluids*, 84:56–68, 2013.

[27] J. Flores, M. Laura Cunico, M. A. Rodriguez, and A. Vecchietti. Optimizing the energy production infrastructure considering uncertainty in fossil resource availability. *Ind. Eng. Chem. Res.*, 53(44):16984–17001, 2014.

[28] P. R. Ehelich and J. P. Holdeen. Impact of population growth. *Obstet. Gynecol. Surv.*, 26(11):769, 1971.

[29] UN-DESA Population Division. World Population Prospects: The 2017 Revision. Technical report, Methodlofy of the United Nations Population Estimates and Projecttions, United Nations New York, 2017.

[30] J. Mohtasham. Review Article-Renewable Energies. *Energy Procedia*, 74:1289–1297, 2015.

[31] J. N. Sørensen. Aerodynamic Aspects of Wind Energy Conversion. *Annu. Rev. Fluid Mech.*, 43(1):427–448, 2011.

[32] M. O. L. Hansen, J. N. Sørensen, S. Voutsinas, N. Sørensen, and H. A. Madsen. State of the art in wind turbine aerodynamics and aeroelasticity. *Prog. Aerosp. Sci.*, 42(4):285–330, 2006.

[33] E. Dogan, R. E. Hanson, and B. Ganapathisubramani. Interactions of large-scale free-stream turbulence with turbulent boundary layers. *J. Fluid Mech.*, 802:79–107, 2016.

[34] A. C. Hansen and C. P. Butterfield. Aerodynamics of Horizont Al-Axis Wind. *Renew. Energy*, 25:115–149, 1993.

[35] R. Wiser, Z. Yang, M. Hand, O. Hohmeyer, D. Infi eld, P. H. Jensen, V. Nikolaev, M. O'Malley, G. Sinden, and A. Zervos. Wind Energy. Technical report, In IPCC Special Report on Renewable Energy Sources and Climate Change Mitigation [O. Edenhofer, R. Pichs-Madruga, Y. Sokona, K. Seyboth, P. Matschoss, S. Kadner, T. Zwickel, P. Eickemeier, G. Hansen, S. Schlömer, C. von Stechow (eds)], Cambridge Universit, 2011.

[36] J. C. Kaimal and Finnigan J. J. *Atmospheric boundary layer flows: their structure and measurement*, volume 32. Oxford University press., 1994.

[37] M. S. Shohag, E. C. Hammel, D. O. Olawale, and O. Okoli. Damage mitigation techniques in wind turbine blades: A review. *Wind Engineering*, 41(3):185–210, 2017.

[38] M. M. Hand. *Mitigation of wind turbine/vortex interaction using disturbance accommodating control*. University of Colorado at Boulder, 2004.

[39] A. Gandhi, B. Merrill, and Y. Peet. Effect of reduced frequency on dynamic stall of a pitching airfoil in a turbulent wake. *AIAA SciTech Forum - 55th AIAA Aerosp. Sci. Meet.*, pages 1–15, 2017.

[40] X. Amandolèse and E. Széchényi. Experimental study of the effect of turbulence on a section model blade oscillating in stall. *Wind Energy*, 7(4):267–282, 2004.

[41] J. Stack. Test in the variable density tunnel to investigate the effect of scale and turbulence on airfoil characteristics. Technical Report 364, National Advisory Committee for Aeronautics, NACA Technical Note. 364, Washington, 1931.

[42] R. Wang and Z. Xiao. Influence of free-stream turbulence on the aerodynamic performance of a three-dimensional airfoil. *AIP Advances*, 11(7):075304, 2021.

[43] M. Mahmoodilari. *The Effect of Turbulent Flow on Wind Turbine Loading and Performance*. PhD thesis, University of Manchester, 2012.

[44] S. Ravi, S. Watkins, J. Watmuff, and A. Fisher. Transient loads occurring over a thin airfoil subjected to large-scale freestream turbulence. *AIAA J.*, 51(6):1473–1485, 2013.

[45] S. L. Herbst, C. J. Kähler, and R. Hain. Influence of large-scale free-stream turbulence on an SD7003 airfoil at low reynolds numbers. *2018 Appl. Aerodyn. Conf.*, 2018.

[46] K. Gharali and D.A. Johnson. Dynamic stall simulation of a pitching airfoil under unsteady freestream velocity. *J. Fluids Struct.*, 42:228–244, 2013.

[47] T. E. Boye and Z. T. Xie. Modelling dynamic stall of a pitching aerofil in large-scale freestream turbulence (Part 1). In *UK Fluid Conf. List Abstr. tallk 1.3 Univ. Cambridge*, pages 15 – 16, 2019.

[48] T. E. Boye and Z. T. Xie. Modelling dynamic stall of a pitching aerofil in large-scale freestream turbulence (Part 2). In *Eur. Turbul. Conf. Torino, Italy.*, Torino, 2019.

[49] ThankGod E Boye and Zheng-Tong Xie. Aerodynamics of a pitching wind turbine blade at high reduced frequencies. *Journal of Wind Engineering and Industrial Aerodynamics*, 223:104935, 2022.

[50] T. E. Boye and Z. T. Xie. The Effect of Large Scale Incoming Turbulence on Wind-Turbine-Blade. In *UK Fluid Conf. List Abstr. tallk 06A-1 Univ. Southampton*, page 99, 2021.

[51] T. E. Boye, T. C. Nwaoha, O. D. Samuel, and F. I. Ashiedu. A validation method of computational fluid dynamics (CFD) simulation against experimental data of transient flow in pipes system. *American Journal of Engineering Research (AJER)*, 6(6):67–79, 2017.

[52] T. E. Boye and O. D. Samuel. Computer-based method of design and modeling of transient flow in crude oil pipeline system. *Journal of Engineering Research*, 8(3), 2020.

[53] B. Raverdy, I. Mary, P. Sagaut, and N. Liamis. High-resolution large-eddy simulation of flow around low-pressure turbine blade. *AIAA J.*, 41(3):390–397, 2003.

[54] A. Jimenez, A. Crespo, E. Migoya, and J. Garcia. Advances in large-eddy simulation of a wind turbine wake. *J. Phys. Conf. Ser.*, 75(1):0–13, 2007.

[55] R. Howell, N. Qin, J. Edwards, and N. Durrani. Wind tunnel and numerical study of a small vertical axis wind turbine. *Renew. Energy*, 35(2):412–422, 2010.

[56] Y. T. Wu and F. Porté-Agel. Large-Eddy Simulation of Wind-Turbine Wakes: Evaluation of Turbine Parametrisations. *Boundary-Layer Meteorol.*, 138(3):345–366, 2011.

[57] A. M. Chowdhury, H. Akimoto, and Y. Hara. Comparative CFD analysis of Vertical Axis Wind Turbine in upright and tilted configuration. *Renew. Energy*, 85:327–337, 2016.

[58] M. R. Visbal and D. J. Garmann. Analysis of dynamic stall on a pitching airfoil using high-fidelity large-eddy simulations. *AIAA J.*, 56(1):46–63, 2018.

[59] M. J. Churchfield, S. Lee, J. Michalakes, and P. J. Moriarty. A numerical study of the effects of atmospheric and wake turbulence on wind turbine dynamics. *J. Turbul.*, 13:1–32, 2012.

[60] C. H. Kuo and J. K. Hsieh. Unsteady flow structure and vorticity convection over the airfoil oscillating at high reduced frequency. *Exp. Therm. Fluid Sci.*, 24(3-4):117–129, 2001.

[61] I. H. Tuncer, J. C. Wu, and C. M. Wang. Theoretical and numerical studies of oscillating airfoils. *AIAA J.*, 28(9):1615–1624, 1990.

[62] G. N. Barakos and D. Drikakis. Unsteady separated flows over manoeuvring lifting surfaces. *Philos. Trans. R. Soc. A Math. Phys. Eng. Sci.*, 358(1777):3279–3291, 2000.

[63] S. Wang, D. B. Ingham, L. Ma, M. Pourkashanian, and Z. Tao. Numerical investigations on dynamic stall of low Reynolds number flow around oscillating airfoils. *Comput. Fluids*, 39(9):1529–1541, 2010.

[64] Y. S. Baik, L. P. Bernal, K. Granlund, and M. V. Ol. Unsteady force generation and vortex dynamics of pitching and plunging aerofoils. *J. Fluid Mech.*, 709:37–68, 2012.

[65] W. J. McCroskey, L. W. Carr, and K. W. McAlister. Dynamic stall experiments on oscillating airfoils. *AIAA J.*, 14(1):57–63, 1976.

[66] B. J. Pruski and R. D. W. Bowersox. Leading-edge flow structure of a dynamically pitching NACA 0012 airfoil. *AIAA J.*, 51(5):1042–1053, 2013.

[67] A. Choudhry, M. Arjomandi, and R. Kelso. Methods to control dynamic stall for wind turbine applications. *Renew. Energy*, 86:26–37, 2016.

[68] J. M. Yu, T. S. Leu, and J. J. Miau. Investigation of reduced frequency and freestream turbulence effects on dynamic stall of a pitching airfoil. *J. Vis.*, 20(1):31–44, 2017.

[69] B. Johan, D. Grigorios, and A. Xavier. Dynamic stall onset variation with reduced frequency for three stall mechanisms. In *17th Int. Forum Aeroelasticity Struct. Dyn.*, pages 1–15, 2017.

[70] M. Thakor, G. Kumar, D. Das, and A. De. Investigation of asymmetrically pitching airfoil at high reduced frequency. *Phys. Fluids*, 32(5), 2020.

[71] M. H. Hansen, A. Hansen, J. T. Larsen, S. Øye, P. Sørensen, and P. Fuglsang. Control design for a pitch-regulated variable speed wind turbine. Technical Report No. 1500(EN), Denmark. Forskningscenter. Risoe-R, 2005.

[72] J. G. Leishman. Challenges in modeling the unsteady aerodynamics of wind turbines. In *21st ASME Wind Energy Symp. 40th AIAA Aerosp. Sci. Meet. Reno, NV.*, pages 141–167, 2002.

[73] C. Diego, A. E. Alejandro, E. Hugo, J. A. Juan, A. Horacio, M. Piergiovanni, and O. Probst. Numerical validation of a finite element thin-walled beam model of a composite wind turbine blade. *Wind Energy*, pages 203–223, 2012.

[74] K. Gharali, E. Gharaei, M. Soltani, and K. Raahemifar. Reduced frequency effects on combined oscillations, angle of attack and free stream oscillations, for a wind turbine blade element. *Renew. Energy*, 115:252–259, 2018.

[75] R. A. Mcd. Galbraith, D. E. Shipley, and M. S. Miller. Unsteady Aerodynamics of Wind Turbines. In *33rd Aerosp. Sci. Meet. Exhib. AIAA*, 1995.

[76] S. A. Huyer, D. Simms, and M. C. Robinson. Unsteady aerodynamics associated with a horizontal-axis wind turbine. *AIAA J.*, 34(7):1410–1419, 1996.

[77] M. Ghasemian, Z. N. Ashrafi, and A. Sedaghat. A review on computational fluid dynamic simulation techniques for Darrieus vertical axis wind turbines. *Energy Convers. Manag.*, 149:87–100, 2017.

[78] A. Rezaeiha, H. Montazeri, and B. Blocken. On the accuracy of turbulence models for CFD simulations of vertical axis wind turbines. *Energy*, 180:838–857, 2019.

[79] A. J. Torregrosa, A. Gil, P. Quintero, and A. Tiseira. Enhanced design methodology of a low power stall regulated wind turbine. BEMT and MRF-RANS combination and comparison with existing designs. *J. Wind Eng. Ind. Aerodyn.*, 190:230–244, 2019.

[80] Z. T. Xie and I. P. Castro. LES and RANS for turbulent flow over arrays of wall-mounted obstacles. *Flow, Turbul. Combust.*, 76(3):291–312, 2006.

[81] M. R. Visbal and J. S. Shang. Investigation of the flow structure around a rapidly pitching airfoil. *AIAA J.*, 27(8):1044–1051, 1989.

[82] P. G. Choudluri and D. D. Knight. Effects of compressibility, pitch rate and reynolds number on unsteady incipient boundary layer separation over a pitching airfoil. *J. Fluid Mech*, 308, 1996.

[83] M. R. Amiralaei, H. Alighanbari, and S. M. Hashemi. An investigation into the effects of unsteady parameters on the aerodynamics of a low Reynolds number pitching airfoil. *J. Fluids Struct.*, 26(6):979–993, 2010.

[84] K. Gharali and D.A. Johnson. Numerical modeling of an S809 airfoil under dynamic stall, erosion and high reduced frequencies. *Appl. Energy*, 93:45–52, 2012.

[85] R. R. Leknys, M. Arjomandi, R. M. Kelso, and C. Birzer. Dynamic- and post-stall characteristics of pitching airfoils at extreme conditions. *Proc. Inst. Mech. Eng. Part G J. Aerosp. Eng.*, 232(6):1171–1185, 2018.

[86] N. Guillaud, G. Balarac, and E. Goncalvès. Large Eddy Simulations on a pitching airfoil: Analysis of the reduced frequency influence. *Comput. Fluids*, 161:1–13, 2018.

[87] S. Li, L. Zhang, K. Yang, J. Xu, and X. Li. Aerodynamic performance of wind turbine airfoil DU 91-W2-250 under dynamic stall. *Appl. Sci.*, 8(7), 2018.

[88] H. Z. Eslami, A. R. Davari, and M. R. Soltani. Impact of reduced frequency on the time lag in pressure distribution over a supercritical airfoil in a pitch-pause-return motion. *Chinese J. Aeronaut.*, 32(2):243–252, 2019.

[89] W. J. McCroskey. Unsteady airfoils. *Annual review of fluid mechanics*, 14(1):285–311, 1982.

[90] K. Ohmi, M. Coutanceau, T. P. Loc, and A. Dulieu. Vortex formation around an oscillating and translating airfoil at large incidences. *Journal of Fluid Mechanics*, 211:37–60, 1990.

[91] J. M. Anderson, K. Streitlien, D. S. Barrett, and M.l S. Triantafyllou. Oscillating foils of high propulsive efficiency. *Journal of Fluid mechanics*, 360:41–72, 1998.

[92] V. R. Kasibhotla and D. Tafti. Dynamic stall simulation of flow over naca0012 airfoil at 1 million reynolds number. In *ASME International Mechanical Engineering Congress and Exposition*, volume 57465, page V07AT09A020. American Society of Mechanical Engineers, 2015.

[93] A. Frangoul. Plans for world's 'largest and most powerful' offshore wind turbine unveiled, https://www.cnbc.com/2018/03/01/plans-for-worlds-largest-and-most-powerful-offshore-wind-turbine-unveiled.htmlm (Date accessed: 2018-07-04).

[94] J. Ambrose. General Electric to trial world's largest wind turbines in the UK, https://www.telegraph.co.uk/business/2018/04/24/general-electric-trial-worlds-largest-wind-turbines-uk/ (Date accessed 02 Oct. 2018).

[95] J. R. Garratt. Review: the atmospheric boundary layer. *Earth Sci. Rev.*, 37(1-2):89–134, 1994.

[96] L. C. Cheung, S. Premasuthan, S. Davoust, and D. Von Terzi. A Simple Model for the Turbulence Intensity Distribution in Atmospheric Boundary Layers. In *J. Phys. Conf. Ser.*, volume 753, 2016.

[97] M. R. Visbal. Numerical exploration of flow control for delay of dynamic stall on a pitching airfoil. *32nd AIAA Appl. Aerodyn. Conf.*, 2014.

[98] R. A. Houze. *Cloud Dynamics*. International Geophysics, 2 edition, 2014.

[99] P. Sagaut. *Large Eddy Simulation for Incompressible Flows*. Springer Berlin Heidelberg, 2006.

[100] J. A. Ekaterinaris and F. R. Menter. Computation of oscillating airfoil flows with one- and two-equation turbulence models. *AIAA J.*, 32(12):2359–2365, 1994.

[101] P. E. Hancock and P. Bradshaw. The effect of free-stream turbulence on turbulent boundary layers. *J. Fluids Eng. Trans. ASME*, 105(3):284–289, 1983.

[102] F. E. Ames and M. W. Plesniak. The Influence of Large-Scale, High-Intensity Turbulence on Vane Aerodynamic Losses, Wake Growth, and the Exit Turbulence Parameters. *Journal of Turbomachinery*, 119(2):182–192, 04 1997.

[103] C. Sicot, S. Aubrun, S. Loyer, and P. Devinant. Unsteady characteristics of the static stall of an airfoil subjected to freestream turbulence level up to 16%. *Exp. Fluids*, 41(4):641–648, 2006.

[104] N. Cao. *Effects of turbulence intensity and integral length scale on an asymmetric airfoil at low Reynolds numbers.* Electronic theses and dissertations, University of Windsor, 2010.

[105] S. Torres-Nieves, V. Maldonado, H.S. Kang, C. Meneveau, and L. Castillo. Effect of free-stream turbulence on the flow around a S809 wind turbine blade. *50th AIAA Aerosp. Sci. Meet. Incl. New Horizons Forum Aerosp. Expo.*, pages 275–276, 2012.

[106] S. L. Herbst, C. J. Kähler, and R. Hain. Laminar separation bubble on an SD7003 airfoil under large-scale turbulent inflow conditions. *5th International Conference on Experimental Fluid Mechanics ICEFM 2018, Munich, Germany*, 2018.

[107] Q. Wang and Q. Zhao. Experiments on unsteady vortex flowfield of typical rotor airfoils under dynamic stall conditions. *Chinese J. Aeronaut.*, 29(2):358–374, 2016.

[108] S. Xiao, H. Geng, and G. Yang. Non-linear pitch control of wind turbines for tower load reduction. *IET Renew. Power Gener.*, 8(7):786–794, sep 2014.

[109] M. Noda and R. G. J. Flay. A simulation model for wind turbine blade fatigue loads. *J. Wind Eng. Ind. Aerodyn.*, 83(1-3):527–540, 1999.

[110] S. Algozino, J. Marañón Di Leo, J. S. Delnero, and G. Capittini. Turbulence effect on flat plate pitching airfoil. *2018 Fluid Dyn. Conf.*, pages 1–11, 2018.

[111] A. Gandhi, B. Merrill, and Y. Peet. Effect of reduced frequency on dynamic stall of a pitching airfoil in a turbulent wake. *AIAA SciTech Forum - 55th AIAA Aerosp. Sci. Meet.*, pages 1–15, 2017.

[112] M. R. Visbal and D. J. Garmann. Numerical investigation of spanwise end effects on dynamic stall of a pitching NACA 0012 wing. *AIAA SciTech Forum - 55th AIAA Aerosp. Sci. Meet.*, pages 1–22, 2017.

[113] H. K. Versteeg, W. Malalasekera, G. Orsi, J. H. Ferziger, A. W. Date, and J. D. Anderson. *An Introduction to Computational Fluid Dynamics - The Finite Volume Method*. Pearson Education Limited, second edi edition, 1995.

[114] A. Leonard. *Energy cascade in large-eddy simulations of turbulent fluid flows*, volume 18. Advances in Geophysics, 1975.

[115] J. H. Ferziger. Large Eddy Numerical Simulations of Turbulent Flows. *AIAA J.*, 15(9):1261–1267, 1977.

[116] N. J. Georgiadis, D. P. Rizzetta, and C. Fureby. Large-eddy simulation: Current capabilities, recommended practices, and future research. *AIAA J.*, 48(8):1772–1784, 2010.

[117] J. Smagorinsky. General Circulation Experiments With the Primitive Equations. *Mon. Weather Rev.*, 91(3):99–164, 1963.

[118] P. Roger and K. Egon. *Advanced Turbulent Flow Computations*. Springer-Verlag Wien, 1 edition, 2000.

[119] D. K. Lilly. On the Application of the Eddy Viscosity Concept in the Inertial Sub-range of Turbulence. Technical report, NCAR Report, Boulder, Colorado, 1966.

[120] D. G. Fox and Douglas K Lilly. Numerical simulation of turbulent flows. *Reviews of Geophysics*, 10(1):51–72, 1972.

[121] J. W. Deardorff. A numerical study of three-dimensional turbulent channel flow at large Reynolds numbers. *J. Fluid Mech.*, 41(2):453–480, 1970.

[122] H. Schmidt and U. Schumann. Coherent structure of the convective boundary layer derived from large-eddy simulations. *J. Fluid Mech.*, 200(D11):511–562, 1989.

[123] J. Bardina, J Ferziger, and W.C. Reynolds. Improved subgrid-scale models for large-eddy simulation. In *13th fluid and plasmadynamics conference*, page 1357, 1980.

[124] M. Germano. A proposal for a redefinition of the turbulent stresses in the filtered Navier–Stokes equations. *Phys. Fluids*, 29(7):2323, 1986.

[125] M. Germano, U. Piomelli, P. Moin, and W.H. Cabot. A dynamic subgrid-scale eddy viscosity model. *Phys. Fluids A*, 1991.

[126] D. K. Lilly. A proposed modification of the Germano subgrid-scale closure method. *Phys. Fluids A*, 4(3):633–635, 1992.

[127] M. Inagaki, T. Kondoh, and Y. Nagano. A mixed-time-scale SGS model with fixed model-parameters for practical LES. *J. Fluids Eng. Trans. ASME*, 127(1):1–13, 2005.

[128] C. E. Badoe, Z. T. Xie, and N. D. Sandham. Performance analysis of a plunging wing at low reynolds number. *6th European Conference on Computational Mechanics (ECCM)*, 2018.

[129] X. Wang and Z. T. Xie. Large eddy simulation of a heaving wing in freestream turbulent flow. In *11th Int. Symp. Turbul. Shear Flow Phenomena, TSFP 2019*, pages 1–6, 2019.

[130] S. J. Daniels, I. P. Castro, and Z. T. Xie. Peak loading and surface pressure fluctuations of a tall model building. *J. Wind Eng. Ind. Aerodyn.*, 120:19–28, 2013.

[131] S. J. Daniels, I. P. Castro, and Z. T. Xie. Numerical analysis of freestream turbulence effects on the vortex-induced vibrations of a rectangular cylinder. *J. Wind Eng. Ind. Aerodyn.*, 153:13–25, 2016.

[132] X. Wu. Inflow Turbulence Generation Methods. *Annu. Rev. Fluid Mech.*, 49(1):23–49, 2017.

[133] F. Bazdidi-Tehrani, M. Kiamansouri, and M. Jadidi. Inflow turbulence generation techniques for large eddy simulation of flow and dispersion around a model building in a turbulent atmospheric boundary layer. *J. Build. Perform. Simul.*, 9(6):680–698, 2016.

[134] P. R. Spalart. Direct simulation of a turbulent boundary layer up to Rθ= 1410. *J. Fluid Mech.*, 187(-1):61–98, 1988.

[135] T. S. Lund, X. Wu, and K. D. Squires. Generation of inflow data for spatially-developing turbulent boundary layer simulations. *J. Comput. Phys.*, 144:233, 1998.

[136] P. Sagaut, E. Garnier, E. Tromeur, L. Larchevêque, and E. Labourasse. Turbulent Inflow Conditions for Large-Eddy Simulation of Compressible Wall-Bounded Flows. *AIAA J.*, 42(3):469–477, 2004.

[137] Z. T. Xie and I. P. Castro. Efficient generation of inflow conditions for large eddy simulation of street-scale flows. *Flow, Turbul. Combust.*, 81(3):449–470, 2008.

[138] N. Jarrin. *Syntethic Inflow Boundary Conditions for the Numerical Simulation of Turbulence*. PhD thesis, The University of Manchester, 2008.

[139] J. W. Patterson, R. Balin, and K. E. Jansen. Assessing and improving the accuracy of synthetic turbulence generation. *J. Fluid Mech.*, 906:1–15, 2021.

[140] K. M. Bercin, Z. T. Xie, and S. R. Turnock. Exploration of digital-filter and forward-stepwise synthetic turbulence generators and an improvement for their skewness-kurtosis. *Comput. Fluids*, 172:443–466, 2018.

[141] L. Prandtl. Bericht über untersuchungen zur ausgebildeten turbulenz. *ZAMM-Journal of Applied Mathematics and Mechanics/Zeitschrift für Angewandte Mathematik und Mechanik*, 5(2):136–139, 1925.

[142] C. J. Greenshields. OpenFOAM user guide version 5. Technical Report July, 2017.

[143] S. J. Daniels and Z.T. Xie. Free-stream turbulence effects on long-span bridge aerodynamics. *Procedia Engineering*, 126:199–203, 2015.

[144] H. Jasak, H. G. Weller, and A. D. Gosman. High resolution NVD differencing scheme for arbitrarily unstructured meshes. *Int. J. Numer. Methods Fluids*, 31(2):431–449, 1999.

[145] P. H. Gaskell and A. K. C. Lau. Curvature-compensated convective transport: SMART, A new boundedness- preserving transport algorithm. *Int. J. Numer. Methods Fluids*, 8(6):617–641, 1988.

[146] L. Krishnan, N. D. Sandham, and J. Steelant. Shock-wave/boundary-layer interactions in a model scramjet intake. *AIAA J.*, 47(7):1680–1691, 2009.

[147] C. E. Badoe, Z. T. Xie, and N. D. Sandham. Large Eddy simulation of a heaving wing on the Cusp of transition to turbulence. *Comput. Fluids*, 184:64–77, 2019.

[148] P. B. S. Lissaman. Low-reynolds-number airfoils. *Annual review of fluid mechanics*, 15(1):223–239, 1983.

[149] W. J McCroskey, K. W. McAlister, L. W. Carr, and S. L. Pucci. An experimental study of dynamic stall on advanced airfoil sections. volume 1. summary of the experiment. Technical report, TR-82-A-8. NASA., 1982.

[150] S. I. Benton and M. R. Visbal. The onset of dynamic stall at a high, transitional reynolds number. *Journal of Fluid Mechanics*, 861:860–885, 2019.

[151] S. Wang, Derek B. Ingham, L. Ma, M. Pourkashanian, and Z. Tao. Turbulence modeling of deep dynamic stall at relatively low reynolds number. *Journal of Fluids and Structures*, 33:191–209, 2012.

[152] D. Bouris and G. Bergeles. 2D LES of vortex shedding from a square cylinder. *J. Wind Eng. Ind. Aerodyn.*, 80(1-2):31–46, 1999.

[153] S. Suryanarayanan and R. Narasimha. Insights into the growth rate of spatially evolving plane turbulent free-shear layers from 2d vortex-gas simulations. *Phys. Fluids*, 29(020708), 2017.

[154] C. E. Badoe, Z. T. Xie, and N. D. Sandham. Large Eddy simulation of a heaving wing on the Cusp of transition to turbulence. *Comput. Fluids*, 184:64–77, 2019.

[155] M. K. Ng, R. H. Chan, and W. C. Tang. A fast algorithm for deblurring models with neumann boundary conditions. *SIAM Journal on Scientific Computing*, 21(3):851–866, 1999.

[156] F. Geng, I. Kalkman, A. S. J. Suiker, and B. Blocken. Sensitivity analysis of airfoil aerodynamics during pitching motion at a Reynolds number of 135,000. *J. Wind Eng. Ind. Aerodyn.*, 183:315–332, 2018.

[157] P. Ouro, T. Stoesser, and L. Ramírez. Effect of Blade Cambering on Dynamic Stall in View of Designing Vertical Axis Turbines. *J. Fluids Eng.*, 140(6):61104, 2018.

[158] J. Zman and B. K. Panda. Experimental investigation of the flow field of an oscillating airfoil and estimation of lift from wake surveys. *J. Fluid Mech.*, 265:65–95, 1994.

[159] A. Laneville and C. D. Williams. *Effect of Intensity and Large-Scale Turbulence on the Mean Pressure and Drag Coefficients of 2D Rectangular Cylinders.*, volume 1. Pergamon Press Ltd, 1980.

[160] D. G. Petty. The effect of turbulence intensity and scale on the flow past square prisms. *J. Wind Eng. Ind. Aerodyn.*, 4(3-4):247–252, 1979.

[161] Y. Nakamura and S. Ozono. The effects of turbulence on a separated and reattaching flow. *J. Fluid Mech.*, 178:477–490, 1987.

[162] F. L. Haan, A. Kareem, and A.A. Szewczyk. The effects of turbulence on the pressure distribution around a rectangular prism. *J. Wind Eng. Ind. Aerodyn.*, 77-78:381–392, 1998.

[163] Y. Kim, I.P. Castro, and Z.T. Xie. Divergence-free turbulence inflow conditions for large-eddy simulations with incompressible flow solvers. *Comput. Fluids*, 84:56–68, 2013.

[164] R. G. J. Flay and D. C. Stevenson. Integral length scales in an atmospheric boundary-layer near the ground. In *Australasian Fluid Mechanics Conference, 9 th, Auckland, New Zealand*, pages 464–467, 1987.

[165] D. J. Tritton. *Physical fluid dynamics*. Springer Science & Business Media, 2012.

[166] A. Trush, S. Pospíšil, and H. Kozmar. Comparison of turbulence integral length scale determination methods. *WIT Transactions on Engineering Sciences*, 128:113–123, 2020.

[167] M. S. Mohamed and J. C. Larue. The decay power law in grid-generated turbulence. *Journal of Fluid Mechanics*, 219:195–214, 1990.

[168] L. E. Jones, R. D. Sandberg, and N. D. Sandham. Direct numerical simulations of forced and unforced separation bubbles on an airfoil at incidence. *Journal of Fluid Mechanics*, 602:175–207, 2008.

[169] L. E. Jones, N. D. Sandham, and R. D. Sandberg. Acoustic source identification for transitional airfoil flows using cross correlations. *AIAA journal*, 48(10):2299–2312, 2010.

[170] A. Fisher. *The effect of freestream turbulence on fixed and flapping micro air vehicle wings*. PhD thesis, RMIT University, 2013.

[171] B. Loxton. *An experimental investigation into the effects of atmospheric turbulence on the aerodynamics of micro air vehicle wings*. PhD thesis, RMIT University, 2011.

[172] J. M. Wallace, H. Eckelmann, and R. S. Brodkey. The wall region in turbulent shear flow. *Journal of Fluid Mechanics*, 54(1):39–48, 1972.

[173] J. M. Wallace. Quadrant analysis in turbulence research: history and evolution. *Annual Review of Fluid Mechanics*, 48:131–158, 2016.

[174] Z. T. Xie, P. R Voke, P. Hayden, and A. G. Robins. Large-eddy simulation of turbulent flow over a rough surface. *Boundary-layer meteorology*, 111(3):417–440, 2004.

[175] C. S. Martha, G. A. Blaisdell, and A. S. Lyrintzis. Large eddy simulations of 2-D and 3-D spatially developing mixing layers. *Aerosp. Sci. Technol.*, 31(1):59–72, 2013.

[176] M. Mahmoodilari and K. Kontis. Effect of Turbulence Loading on a 2-D Aerofoil. In *49th AIAA Aerosp. Sci. Meet. Incl. new Horizons Forum Aerosp. Expo.* AIAA, 2011.